

Dissertation for the Ph.D in Science

**Observational Studies on the High-Latitude
Ionospheric Plasma Irregularities**

Keisuke Hosokawa

Department of Earth and Planetary Science,
Graduate School of Science,
Kyoto University

December 2002

Abstract

This thesis is based on the data obtained from the coherent HF radars of the Super Dual Auroral Radar Network (SuperDARN). The radars are designed to employ the field-aligned irregularities (FAIs) as tracers of the bulk plasma motion under the influence of the convection electric field. Since 1980's, there have been a number of studies that investigate morphological feature and generation process of the high-latitude F region FAIs. However, there still exist many questions and debates. In this thesis, we investigate why the FAIs appear, what kind of geophysical characteristics their properties reflect. In particular, we are aimed at disclosing how their characteristics can be utilized to identify atmospheric, ionospheric and magnetospheric regions, boundaries and physical processes. There are three major targets of this thesis, subauroral FAIs (Part II), FAIs within the dayside polar cap (Part III), and peculiar near range echoes (Part IV). The background and objectives of this study are explained in Part I. In the following, the abstract of the main body of this thesis is provided.

Part II Subauroral Irregularities as a Tracer for Longitudinal Extent of the Midlatitude Trough: Morphological feature of the subauroral FAIs has been investigated in relation to the several phenomena and processes in the subauroral ionosphere. At the first step, we have investigated spatial distribution of the subauroral F region FAIs in a statistical fashion. Consequently, we found that a distinct backscatter feature known as the dusk scatter event (DUSE, first explored by Ruohoniemi *et al.*, 1988) has a close relationship with the duskside end (i.e., sunward edge) of the midlatitude trough. This suggests that an electron density gradient at the sunward edge of the trough is an important factor for the generation of DUSE. It was shown that the model which employs the sunward density gradient at the sunward edge of the trough together with an ambient poleward electric field is most favorable for the generation of DUSE. Another important finding was that, in disturbed conditions, DUSE appears at earlier local times compared with those in quiet conditions. This implies that the trough also extends into the dayside across the terminator during disturbed conditions. In order to testify the model deduced from the statistical analysis, we have examined two DUSE events that occurred during disturbed conditions. Background electron density, electric field and plasma temperature obtained from the EISCAT incoherent scatter radar were employed. Consequently, when DUSE was observed by the SuperDARN radar, the EISCAT observed sunward directed density gradient and poleward electric field in the vicinity of DUSE. This evidenced that geometry of the parameters is quite consistent with the proposed model. During the interval of both events, DUSE appeared at earlier local time and the sunward edge of the trough was found to extend into the dayside. This suggests that DUSE can be used as a tracer for the sunward edge of the trough during both quiet and disturbed conditions. The other important finding was that the electric field observed by the EISCAT was more intense than that expected. In addition, ion temperature was significantly enhanced in the region of the strong electric field. These observations suggest a possibility that an enhanced recombination in the region of intense electric field through the ion-frictional heating contributes to the dayside extension of the midlatitude trough.

Part III Dayside High-Latitude Irregularities as a Proxy for the Polar Cap Boundary: FAIs in the dayside high-latitude ionosphere are known to have broad Doppler spectra which are distinct from those in the other regions. We examine the origin of these broad spectra, and then discuss how they can be applied to the studies of the magnetosphere-ionosphere coupling system. At the first step, statistical characteristics of the spectral width distribution were investigated using data from a pair of conjugate SuperDARN radars. Three types of spectral width distribution were identified in both hemispheres, (i) an exponential-like distribution in the lower magnetic latitudes (below 72°), (ii) a Gaussian-like distribution around a few degrees magnetic latitude centered on 78° , and (iii) another type of distribution in the higher magnetic latitudes (above 80°). The first two correspond respectively to the spectral width distributions within the LLBL and the cusp classified by Baker *et al.* (1995). Most important finding was that the spectral width is also narrow in the region poleward of the cusp (above 80°). These spectral width features are obtained in wide magnetic local time sector of at least 6 hours from 09 to 15 MLT. Next we have tried to disclose the origin of these broad Doppler spectral widths on the dayside polar region. Simulation study by André *et al.* (1999, 2000a, 2000b) pointed out that the broad spectral widths observed in the dayside high-latitude ionosphere result predominantly from time-varying electric field in

the Pc1-2 frequency range. However, no substantial observation has supported their prediction. We have performed a case study of a favorable conjunction of overpass of the Oersted satellite with the field-of-view of the SuperDARN Syowa-East radar during an interval of the southward IMF Bz. At the time, the radar observed L-shell aligned boundary in the spectral width around the dayside ionosphere. High-frequency (0.2-5 Hz) magnetic field fluctuations were simultaneously observed by the Oersted satellite high time resolution magnetometer. These magnetic field fluctuations are considered to be Alfvén wave possibly associated with the particle which precipitates into the ionosphere when magnetic reconnection occurs. Our observation clearly demonstrates that the boundary between narrow and broad spectral widths (spectral width boundary) was well corresponding to the boundary in the level of the fluctuations. This observation provides a direct evidence for the previous theoretical prediction. A close relationship between the electric and magnetic field fluctuations and the cusp particle precipitations during southward IMF conditions has been confirmed by many authors. The present observation suggests that the spectral width boundary observed in the dayside ionosphere is connected with the signature of the open/closed field line boundary such as the cusp particle precipitations and the red line (630 nm) auroral emissions via electric and magnetic field fluctuations for the case of the negative IMF Bz conditions. Hence, it is implied that the spectral width boundary can be used as a proxy for the open/closed field line boundary in the dayside ionosphere. Finally, we presented a case study which employed magnetically conjugate SuperDARN radars and made an interhemispheric comparison of the location and variation of the spectral width boundaries. Agreement between the magnetic latitudes of the boundaries in both hemispheres was remarkable. Correlation coefficients between the latitudes of the boundaries were larger than 0.70 for all conjugate beam pairs employed in this study. The temporal variation of the magnetic latitude of the spectral width boundary followed the same equatorward trend in both hemispheres. This signature is consistent with the accumulation of open flux in the polar cap by the dayside equatorial magnetopause reconnection, which is expected when IMF Bz is negative. Boundaries in both hemispheres also exhibited short-lived poleward motions superposed on the general equatorward trend, which followed the onset of substorm expansion phase and temporary northward excursion of IMF Bz during substorm recovery phase. These characteristics can be interpreted as a manifestation of the expanding and contracting polar cap due to the dayside and nightside reconnections. In addition, there was an interhemispheric difference in response time to the substorm occurrence between two hemispheres such that the spectral width boundary in the Southern Hemisphere started to move poleward 10 minutes earlier than that in the Northern Hemisphere. We discussed this difference in terms of interhemispheric asymmetry of the substorm breakup region associated with the effect of IMF By component. This case study has confirmed that the Doppler spectral characteristics of the FAIs is very useful to study the structures and processes in the dayside ionosphere.

Part IV Mesospheric Irregularities as an Indicator of the Global Environmental Change: Recently, peculiar echoes have been explored in near range observations of the SuperDARN HF radars (Ogawa *et al.*, 2002a; 2002b). We have investigated statistical characteristics of these peculiar near range echoes using 46 months of the SuperDARN Syowa-East radar data. Most important finding was that the echoes appeared predominantly in summer months from November to February. This strong seasonal dependence is consistent with those of Polar Mesosphere Summer Echoes (PMSE). It was also reported that the local time distribution of the echo appearance is basically similar to that of PMSE. Ogawa *et al.* (2002a) concluded that these peculiar near range echoes correspond to PMSE at HF frequencies, because they can not explained them by the other backscatter targets such as the E region FAIs and meteor trails. However, the amount of the dataset was insufficient to acquire final conclusion. Our study indicated that statistical characteristics of the echo are quite consistent with those of PMSE. Then, it was confirmed that the peculiar near range echoes are actually PMSE. Long-term variability of the echo occurrence probability was also examined. Echo occurrence probability seems to increase year by year. This might imply that the conditions for generating PMSE (mesopause temperature and water vapor concentration) are becoming more suitable in the recent years. However, amount of the data employed in this study was not sufficient to extract essential long-term trend of PMSE due to the contamination of the biases such as the increasing mesospheric ionization level. Thus, the occurrence probability must be investigated over the period longer than at least one solar cycle (11 years) in order to extract the pure long-term trend of PMSE activity.

Acknowledgements

The author would like to express his greatest gratitude to Prof. Toshihiko Iyemori at Data Analysis Center for Geomagnetism and Space Magnetism, Kyoto University, for being a fantastic supervisor. The author has learned many things from him such as the way of thinking with geophysics, how to proceed research, the attitude for being original. This thesis could not be completed without his supervision. Prof. Natsuo Sato at National Institute of Polar Research (NIPR) is acknowledged for many reasons. His continuous encouragement with useful advice on author's study was essential for completion of this thesis. He provided opportunities to work at Univ. of Leicester for the author. This thesis could not be completed without this experience. The author wishes to express his special thanks to Dr. Akira Sessai Yukimatu at NIPR for his continuous distribution of the SuperDARN data and rapid technical supports. His heartfelt advice and supports had greatly encouraged the author during this thesis work. The author would like to sincerely acknowledge to Prof. Mark Lester at Radio and Space Plasma Physics Group (RSPPG), Department of Physics and Astronomy, Univ. of Leicester in UK for giving the author a wonderful chance for collaboration work. His educative guidance and thoughtful encouragement during the author's stay at RSPPG were extremely useful for him to proceed this research. Dr. Emma Woodfield at RSPPG (now at High Altitude Observatory, National Center for Atmospheric Research in USA) is also greatly encouraged. She always inspired the author to advance the study through many valuable suggestions impressing the author with her way of living and positive thinking. The author would like to express his hearty thanks to Dr. Steve Milan at RSPPG for his kind and useful help as well as stimulating discussions during the author's stay at RSPPG. The author could not complete this study without kind and appropriate instruction in the EISCAT data processing by Dr. Masahiko Sugino and Dr. Satonori Nozawa at Solar-Terrestrial Environment Laboratory (STEL), Nagoya Univ. Prof. Tadahiko Ogawa at STEL is also greatly acknowledged for giving the author a chance to study Polar Mesosphere Summer Echoes. His valuable comments and continuous encouragement greatly helped the author to proceed this study. This study could not be completed without high-quality magnetic field data provided by the Oersted mission. The author wishes to express his hearty thanks to Mr. Satoru Yamasita at Solar-Planetary Electromagnetism Lab. (SPEL), Department of Geophysics, Kyoto Univ. for his useful instruction in the data processing. The author would like to express his sincerely acknowledgement to Dr. Peter Stauning at Danish Meteorological Institute (DMI) for providing the Oersted data for the author. Mr. Ryuho Kataoka at Department of Geophysics, Tohoku Univ. is also acknowledged. Discussion with him was always interesting and stimulating. The author is also indebted to Prof. Tohru Araki, Prof. Shinobu Machida, Mr. Toyo Kamei, Dr. Masahiko Takeda, Dr. Akinori Saito, and Dr. Masahito Nosé for their valuable comments and helpful suggestions. Thanks are also due to all the members in SPEL for their useful comments. The author thanks all the staff who contributed to the operation of the SuperDARN radars. Especially, the author wishes to express his greatest thanks to the staff who contributed to the construction and daily operation of the SENSU (Syowa-East radar of Syowa-South & East HF Radars of NIPR for SuperDARN) radars. The author is indebted to the director and staff of EISCAT for operating the facility and supplying the data. EISCAT is an International Association supported by Finland (SA), France (CNRS), the Federal Republic of Germany (MPG), Japan (NIPR), Norway (NFR), Sweden (NFR) and the United Kingdom (PPARC). The author would like to thank N. Ness at Bartol Research Institute and CDAWeb for access to key parameter data from the MFI instrument on-board the ACE spacecraft. The author also thanks the principle investigator, Prof. R. P. Lepping, for the use of key parameters from the Wind MFI instruments. Dr. D. Hardy of Phillips Laboratory designed and built the DMSP SSJ/4 particle detectors employed in this study. The CANOPUS instrument array is constructed, maintained and operated by the Canadian Space Agency. The author is grateful for the support of the Oersted Project Office and the Oersted Science Data Centre at Danish Meteorological Institute. The Oersted Project is funded by the Danish Ministry of Transport, Ministry of Research and Information Technology, and Ministry of Trade and Industry. Additional support was provided by National Aeronautics and Space Administration (NASA), European Space Agency (ESA), Centre Nationale d'Etudes Spatiales (CNES), and Deutsche Agentur für Raumfahrtangelegenheiten (DARA). The author is supported by a grant of Research Fellowships of the Japan Society for the Promotion of Science (JSPS) for Young Scientists.

Contents

Part I	General Introduction	8
Chapter 1	Territory of the Earth	9
1.1	Solar Wind and the Earth's Magnetosphere	9
1.2	Ionosphere	11
1.3	Earth's Atmosphere	13
Chapter 2	Structures in Polar Ionosphere	14
2.1	Ionospheric Convection in the High-Latitude	14
2.2	Magnetospheric Substorms	15
2.3	Auroral Particle Precipitation and Field-Aligned Current	16
Chapter 3	Field-Aligned Plasma Irregularities	17
3.1	Generation Mechanism	17
3.2	FAIs in the High-Latitude F Region Ionosphere	18
Chapter 4	Super Dual Auroral Radar Network	19
4.1	Volume Scattering Process	19
4.2	Coherent HF Backscatter Radar	20
4.3	Overview of the Network	21
4.4	Radar Facility	22
4.5	Operation	22
4.6	Data	23
Chapter 5	Organization of This Thesis	24
5.1	Philosophy of This Thesis	24
5.2	Targets of This Thesis	24
5.3	Outline of This Thesis	25
Part II	Subauroral Irregularities as a Tracer for the Midlatitude Density Trough	26
Chapter 1	Overview	27
1.1	Midlatitude Trough	27
1.2	Subauroral Ion Drift	29
1.3	Irregularities in the Subauroral Region	31
1.4	Organization of This Part	31

Chapter 2 Statistical Analysis of Field-Aligned Irregularities in the Subauroral F Region as Observed by the SuperDARN Radars	32
2.1 Introduction	32
2.2 The SuperDARN Radars and Statistics Data Set	33
2.2.1 SuperDARN Radars	33
2.2.2 Statistics Data Set	34
2.3 Method of Statistics	34
2.3.1 Data Selection	34
2.3.2 Scattering Occurrence Percentage	35
2.4 Statistical Results	36
2.4.1 Statistical Signature of DUSE	36
2.4.2 Feature of the DUSE in Each Radar	37
2.4.3 Seasonal Variation of DUSE	40
2.4.4 Relationship with the Sunward Edge of Trough	41
2.5 Discussion	45
2.5.1 Plasma Instabilities	45
2.5.2 Source Region of DUSE	46
2.5.3 Estimation of the Linear Growth Rate of FAIs	48
2.6 Summary	50
Chapter 3 Simultaneous Measurement of Subauroral Irregularities from SuperDARN Radar and EISCAT UHF System	51
3.1 Introduction	51
3.2 Experimental Arrangements	53
3.3 Observations	54
3.3.1 CUTLASS Finland Observations	54
3.3.2 EISCAT Observations	57
3.3.3 Plasma Drift Observation by the CUTLASS Finland Radar	61
3.3.4 Ground Magnetometer Observations	62
3.4 Discussion	62
3.4.1 The Model	62
3.4.2 Generation Mechanisms of the Trough	64
3.4.3 Relationship with the Other Phenomena	65
3.5 Summary	67
Chapter 4 Conclusions, Speculations, and Future Directions	68
Part III Dayside High-Latitude Irregularities as a Proxy for the Polar Cap Boundary	70
Chapter 1 Overview	71
1.1 Geophysical Characteristics within the Dayside Ionosphere	71
1.1.1 Structures Defined with Particle Precipitation	71
1.1.2 Dayside Auroral Morphology	73
1.1.3 The Cusp as a Source of Intense Electric and Magnetic Field Fluctuations	74

1.2	Coherent HF Radar Observation of the Cusp	74
1.2.1	Broad Doppler Spectral Width	74
1.2.2	Relationship between the Broad Spectra and Other Features	76
1.2.3	Application of the Broad Doppler Spectral Width	77
1.3	Cause of the Broad Doppler Spectra: Theoretical Approach	80
1.4	Interhemispheric Study: What is Conjugacy?	83
1.5	Organization of This Part	84
Chapter 2 Statistical Characteristics of Doppler Spectral Width as Observed by the Conjugate SuperDARN Radars		85
2.1	Introduction	85
2.2	Database and Analysis	86
2.2.1	Statistics Database	86
2.2.2	Geophysical Bias	87
2.3	Statistical Results	89
2.3.1	Latitudinal Variation of the Spectral Width Distribution	89
2.3.2	Longitudinal Variation of the Spectral Width Distribution	90
2.3.3	Form of the Spectral Width Distribution	90
2.4	Discussion	93
2.4.1	Generation Mechanisms of Broad Spectral Width	93
2.4.2	Interhemispheric Differences in Spectral Width Values	94
2.4.3	Comparison with the Other Observations	95
2.5	Summary	96
Chapter 3 Origin of the SuperDARN Broad Doppler Spectra: First Observational Evidence from Oersted Satellite Magnetometer		97
3.1	Introduction	97
3.2	Instrumentations	98
3.3	Observations	98
3.4	Discussion	100
3.5	Summary	103
Chapter 4 Interhemispheric Comparison of Spectral Width Boundary as Observed by the SuperDARN Radars		104
4.1	Introduction	104
4.2	Experimental Arrangement	105
4.3	Observations	106
4.3.1	Determining Spectral Width Boundary	106
4.3.2	Low Latitude Particle Precipitation	107
4.3.3	Interhemispheric Comparison of the Spectral Width Boundary	109
4.3.4	Response to the IMF and Substorm Activity	110
4.4	Discussion	113
4.4.1	Interhemispheric Collocation of the Boundaries	113
4.4.2	Response to the Changes of IMF Bz and Substorm	114

4.4.3	Interhemispheric Asymmetry in Response to the Substorms	115
4.5	Summary	117
Chapter 5	Conclusion and Future Directions	118
Part IV	Mesospheric Irregularities as an Indicator of the Global Climate Change	120
Chapter 1	Overview	121
1.1	Polar Mesosphere Summer Echoes: PMSE	121
1.2	Peculiar Near Range Echoes Detected with SuperDARN	122
1.3	Organization of This Part	124
Chapter 2	A Statistical Study of Antarctic Polar Mesosphere Summer Echoes Observed with the Syowa Station HF Radar	125
2.1	Introduction	125
2.2	Brief Description of the Radar	125
2.3	Event Selection	126
2.4	Seasonal Dependence	129
2.5	Local Time Dependence	130
2.6	Long-Term Variabilities	132
2.7	Summary	133
Chapter 3	Conclusion and Future Directions	134
Part V	Appendix	136
Chapter A	Techniques for Doppler Spectral Analysis of Coherent Backscatters in the High-Latitude Ionosphere	137
A.1	Introduction	137
A.2	Extraction of Doppler Component (in analog part)	138
A.3	Calculating Auto Correlation Function (ACF)	139
A.3.1	Brief Tutorial for Spectrum Analysis Using ACF	139
A.3.2	Single Pulse Observation	141
A.3.3	Correlation Time	142
A.3.4	Multiple Pulse Observation	142
A.4	Fitted Parameter Derivation	144
A.4.1	Noise Reduction	145
A.4.2	Doppler Velocity	146
A.4.3	Backscatter Power and Doppler Spectral Width	147
Chapter B	Linear Theory of Gradient-Drift Instabilities	148
B.1	Basic Equations of the Gradient-Drift Instabilities	148
B.2	Linear Growth Rate of the Gradient-Drift Instabilities	149
Part VI	List of References	150

Part I

General Introduction

Chapter 1

Territory of the Earth

Before describing background and objectives of this thesis in detail, it may be helpful to give a brief overview of the structures surrounding the Earth.

1.1 Solar Wind and the Earth's Magnetosphere

Through the interaction between the solar wind and the Earth's magnetic field, its sphere of influence known as the *magnetosphere* is formed. The axis of geomagnetic dipole is toward the southward direction roughly perpendicular to the ecliptic plane. Most of the particles inside the magnetosphere are ionized and their motion are dominated by the strong geomagnetic field. These plasmas are generally tenuous, less than 1 cm^{-3} in outer magnetosphere, while the temperature is high. The solar wind consists of supersonic (superAlfvénic in the magnetohydrodynamics) plasmas radially outflowing from the coronal regions. Near the orbit of the Earth, the typical solar wind density, flow velocity, and the temperature are $\approx 1\text{-}20 \text{ cm}^{-3}$, $\approx 400\text{-}450 \text{ km s}^{-1}$, and $\approx 10 \text{ eV}$, respectively. The interplanetary magnetic field (IMF) carried by the solar wind is generally weak, but its direction frequently varies.

Since the frozen-in solar wind plasma cannot flow across the magnetic field, the Earth's field acts as a hard obstacle to the solar wind, and the bulk of the solar wind flow is deflected around the Earth. When the solar wind strikes the Earth's magnetic field, standing shock wave called the *bow shock* is formed. The position of the shock is determined by a balance between the solar wind dynamic pressure and the magnetic pressure of the compressed Earth's magnetic field. The average location of the closest point of the shock surface is approximately 13 Earth radius (R_E). As the solar wind passes through the bow shock, it is decelerated, heated, and deflected around the magnetosphere in a region called the *magnetosheath*. Thickness of the magnetosheath is approximately $3 R_E$ near the subsolar point. After being decelerated by the bow shock, the heated solar wind plasma is accelerated again from subAlfvénic to superAlfvénic as it moves past the Earth. The large dynamic pressure of the solar wind presses the Earth's magnetic field and confined it to a magnetospheric cavity that has a long tail, which is called the *magnetotail*, in the anti-sunward direction. Figure I-1.1 shows a three-dimensional sketch of the configuration of the Earth's magnetosphere widely accepted.

The boundary layer that separates the magnetized plasma in the solar wind from the plasma confined by the Earth's magnetic field is called the *magnetopause*. The magnetopause is generally very thin, approximately 100 km, and its location is determined by a balance between the dynamic pressure of the solar wind and the magnetic pressure of the geomagnetic field. Along the Sun-Earth line on the dayside, the magnetopause position is approximately at $10 R_E$. Large-scale electric currents flow along the magnetopause, which separates the solar wind magnetic field from the Earth's magnetic field. On the front of the magnetopause, the current flow is

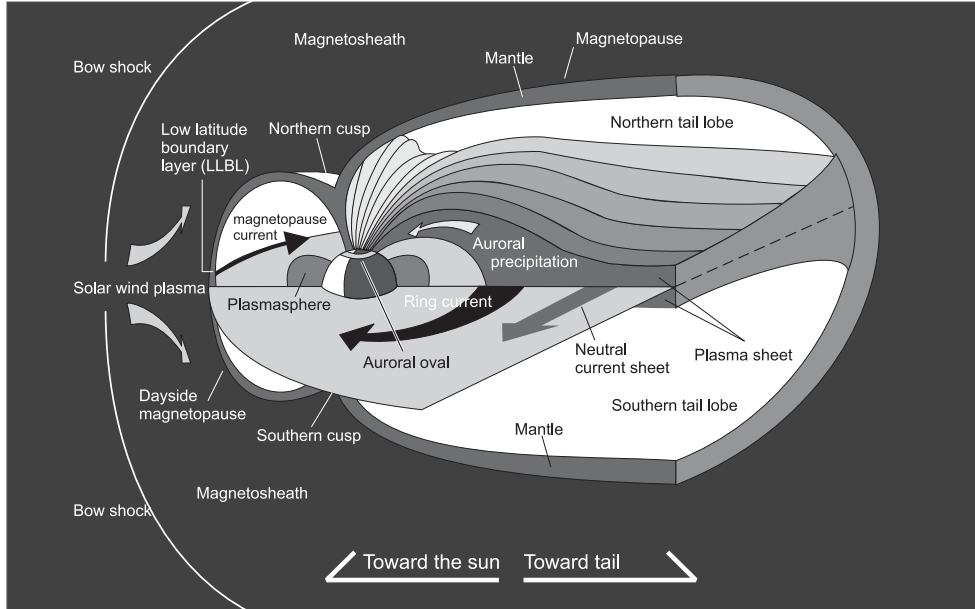


Figure I-1.1: A three-dimensional cutaway of the magnetosphere, where various characteristics and boundaries are indicated.

primarily from dawn to dusk, but it acquires an increasing meridional (north-south) component as it flows around and past the Earth.

Although the bulk of the solar wind particles are deflected around the Earth in the magnetosheath, some of them can cross the magnetopause and enter the magnetosphere. Direct entry of the solar wind plasma occurs on the dayside in the vicinity of the *cusp*. At low altitudes, the cusp occupies a narrow latitudinal band that is centered near noon. Within this region, the solar wind particles can travel along geomagnetic field lines and deposit their energy on the upper atmosphere. There exists another important layer just inside the magnetopause in terms of the energy and momentum transfer from the solar wind into the magnetosphere. The layer is called the *low-latitude boundary layer* (LLBL). The plasma flow in this region resembles that in the magnetosheath, which indicates that the plasmas of solar wind and magnetosphere origins are mixed in this region. The *plasma mantle* is another boundary layer where the plasmas of solar wind and magnetosphere origins are mixed. The plasma mantle is located in a region of open magnetic field lines in the magnetotail. The density in this region decreases from the magnetosheath value, but the flow is primarily parallel to the magnetosheath flow with a small inward component. The presence of these boundary layers indicates that the magnetopause is not a perfect shielding layer and that the solar wind plasma can get into the magnetosphere. However, the question of how and where the magnetosheath plasma crosses the magnetopause is still controversial.

The plasmas of solar wind origin populate a narrow region in and near the equatorial plane of the magnetotail, which is called the *plasma sheet*. The plasma sheet particles have an average energy 10 times larger than that found in the magnetosheath (a few keV) and a density there is lower by a factor of 10 to 100 ($\approx 0.1 \text{ cm}^{-3}$). Both the northward and southward regions of the plasma sheet have strong magnetic field components, called *lobe* regions. The lobes are generally considered to consist of tenuous plasmas ($< 0.01 \text{ cm}^{-3}$). The particles in the plasma sheet are not trapped, but have direct access to the Earth's upper atmosphere on the nightside along the magnetic field lines. At low altitude, these field lines converge on a region narrow in latitude, but longitudinally extended. This ring shaped region is known as the *auroral oval*. Particles in the plasma sheet

get accelerated and collide with the Earth's upper atmosphere, which produces the aurora visible for us.

In addition to the plasma sheet flow toward the Earth on the magnetic field lines connecting to the auroral oval, there is another large-scale current flow across the plasma sheet from dawn to dusk, which is called *neutral current sheet*. This dawn to dusk current separates the two regions of oppositely directed magnetic fields in the lobes, i.e., the fields toward the Earth in the northern lobe and those away from the Earth in the southern lobe. These field lines are highly stretched and extend deep into the magnetotail. Near the magnetopause, they are connected with the interplanetary magnetic field. This magnetic connection generates potential drops across the magnetotail, which is mapped down to the region poleward of the auroral oval, called the *polar cap*. The electric field generated by this potential drop points from dawn to dusk across the polar cap. As will be discussed in the next chapter, this electric field has a major impact on the plasmas in the high-latitude ionosphere.

The energetic particles near the center of the plasma sheet drift closer to the Earth due to magnetospheric electric fields and then get trapped on closed magnetic field lines. These trapped energetic particles drift in an azimuthal direction around the Earth due to gradients in the geomagnetic field, although the electrons and protons drift in opposite directions. These particles of the magnetotail origin result in a large-scale current that encircles the Earth, which is called the *ring current*. The ring current is primarily composed of geomagnetically trapped 10 to 200 keV particles (H^+ and O^+) bouncing along closed geomagnetic field lines. It is typically located between 3 and 6 R_E . A fraction of the ring current is carried by relativistic electrons and very energetic ions (an order of MeV). These particles penetrate deep into dense materials and thus cause radiation damage to spacecraft systems. The trapping region of these high energy particles is called the *radiation belt* or *Van Allen belt*. An important aspect of these trapped particles is that they prevent the high-latitude electric field from penetrating to middle and low-latitudes. In short, in response to the penetration of the high-latitude electric fields, the trapped ions and electrons polarize and set up oppositely directed electric field that effectively cancels the high-altitude electric field. Hence, except for the phenomena of transient feature, the middle and low-latitude regions are generally not affected by the magnetospheric electric fields.

More closer to the Earth, there exists a torus shaped region that surrounds the Earth, which is called the *plasmasphere*. The plasmasphere contains a relatively cool (≈ 5000 K) and dense plasma ($\approx 10^2$ cm $^{-3}$). The origin of the plasma in this region is basically the Earth's ionosphere. The plasma in this region corotates with the Earth, but it can bounce along closed magnetic fields from one hemisphere to the other. The outer boundary of the plasmasphere, which is called the *plasmopause*. The plasmopause is typically marked by a sharp decrease in plasma density. Its radial distance depends on magnetic activity. The plasmopause separates the plasma corotating with the Earth and the plasma that is influenced by the magnetospheric electric fields.

1.2 Ionosphere

There are ions and electrons at all altitudes of the terrestrial atmosphere. Below about 60 km, charged particles do not play any significant role in determining the chemical or physical properties of the atmosphere. Above about 60 km, however, the presence of electrons and ions becomes increasingly important with height. This region of the upper atmosphere is called the *ionosphere*. The research field of this thesis is the terrestrial ionosphere in the high-latitude. Here, only the vertical structure of the ionosphere is briefly introduced. Detailed description of the horizontal characteristics of the high-latitude ionosphere will be given in the next chapter.

The ionosphere can be divided into three main regions, (i) D region between 60 and 90 km, (ii) E region between approximately 90 and 180 km, and (iii) F region above 180 km. Chemical processes and physical properties, such as plasma density, plasma temperature, and electrical conductivity, are employed to distinguish

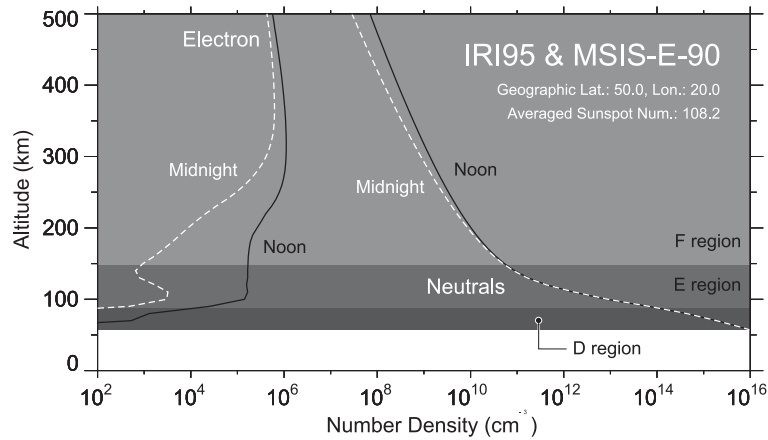


Figure I-1.2: Typical vertical profile of the electron density in the midlatitude ionosphere (deduced from IRI 95 model). For comparison, density of the neutral particles deduced from MSIS-E 90 model is also shown.

these regions. The vertical electron density profile deduced from the International Reference Ionosphere (IRI) 95 model (Bilitza, 1997) at middle latitudes is presented in Figure I-1.2, which illustrates roughly where these ionospheric regions exist. The profile is directly related to chemical processes in the ionosphere. The ionospheric electron concentration depends largely on photo-ionization of the neutral particles by solar EUV. The diurnal variation exhibits an increase of electron concentration during the day and a decrease at night. The concentration of electrons also varies with the solar cycle. During the solar maximum, the electron density can be larger by more than an order of magnitude than that in the solar minimum. Precipitating particles from the magnetosphere also cause ionization, especially in the auroral zone. The depth of the penetration of the magnetospheric particles into the ionosphere depends on their energy and on their pitch angle. The particles with energies of about 100 eV deposit their energy in the F region, while the particles with energies around 10 keV can penetrate into the lower E region.

Horizontal electric current is determined by both imposed electric field and ionospheric conductivity. The electric conductivity is an altitude-dependent quantity that varies significantly between the ionospheric layers, i.e., it depends upon the plasma density and the gyrofrequency of the constituent particles of the ionospheric plasma. In the E region, the motion of the ions is controlled largely by collisions with the neutrals, while the electrons are magnetically controlled. In the F region, both the ions and electrons are magnetically controlled and therefore both drift at the $\mathbf{E} \times \mathbf{B}$ drift velocity, where \mathbf{E} is the electric field and \mathbf{B} is the magnetic field. The *Hall* conductivity, which refers to horizontal currents in the direction perpendicular to the electric field and is due mainly to electrons, has its maximum in the E region at approximately 110 km. It is in this region where the ions drift slowly because they are collision-controlled, while the electrons Hall drift. This specific layer is called *dynamo region* and creates main part of the magnetic field perturbations observed at the ground-based observatories. Higher in the E region, between approximately 125 and 130 km, where the gyrofrequency of the ions is equal to the ion-neutral collision frequency, there is a peak in the ion-controlled *Pedersen* conductivity. The net current at this altitude flows along the electric field. In the ionosphere above about 140 km both the electrons and the ions drift in Hall direction. Hence, no net Hall current flows there although a small amount of Pedersen current can flow. Above approximately 150 km, the conductivity along the magnetic field is the only significant component, then the field-aligned currents are the prevailing current systems.

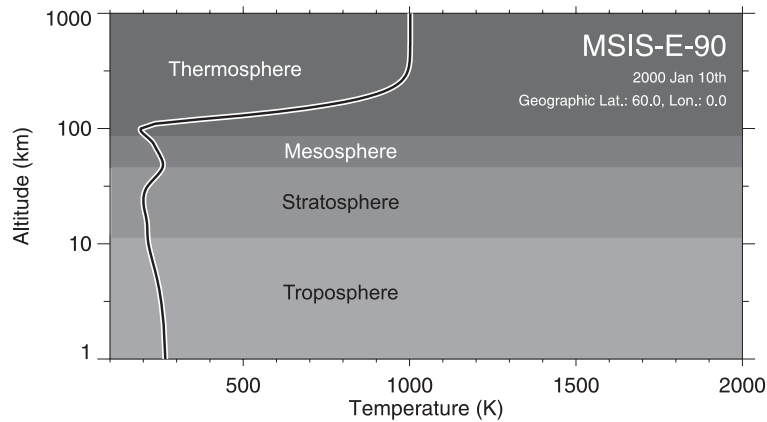


Figure I-1.3: Typical profile of the neutral atmospheric temperature in the midlatitude with the various atmospheric layers (deduced from MSIS-E 90 model).

1.3 Earth's Atmosphere

The Earth's atmosphere is the primary source of the ionospheric plasma. It extends from the Earth's surface to the altitudes beyond 1000 km. Neutral atmosphere has several distinct structures as well as the ionized atmosphere. The classification is primarily based on the variation of temperature with altitude. Figure I-1.3 shows typical profile of neutral atmospheric temperature with the various layers, which is derived from the MSIS-E 90 model (Hedin, 1991). In this system the regions are called *spheres* and the boundaries between the regions are called *pauses*.

The *troposphere* is the lowest atmospheric region. This region is normally associated with atmospheric weather. It begins at the surface and extends to about 10-12 km. This region is mainly characterized by a negative temperature gradient ($\approx -10 \text{ K km}^{-1}$). The troposphere is bounded by the *tropopause*, where the temperature is about 100-200 K. Above this boundary is the *stratosphere*, which extends from about 10 to 45 km and is the region where the ozone layer exists. In this region the temperature increases about 2 K km^{-1} due to the absorption of solar UV radiation by the ozone. The stratospheric ozone is particularly important because it absorbs UV radiation harmful to life. The local maximum temperature ($\approx 270 \text{ K}$) is reached at the stratopause, which is located at around 50 km altitude. Above the stratosphere the *mesosphere* lies, where the temperature again decreases with altitude. The temperature reaches its minimum ($\approx 180 \text{ K}$) at the mesopause, located at an altitude of about 85 km. The mesopause is the coldest region in the terrestrial atmosphere. The mesosphere contains complex chemical and aeronautical processes and thus the region of increasing interest. In these three lower regions, the atmosphere is well mixed and the relative composition of the major constituents (N_2 , O_2 , Ar, CO_2) is essentially constant.

Above the mesopause the solar UV radiation is fairly efficiently absorbed, while the reradiation processes are rather inefficient. The unbalance between these processes results in a drastic increase of temperature. This region is called the *thermosphere*. The thermospheric temperature eventually becomes nearly constant at values that are usually well over 1,000 K. This is the hottest part of the terrestrial atmosphere. In the thermosphere, the mixing of constituents is relatively rare because of the positive temperature gradient. Therefore, the various constituents may separate due to gravity, which produces significant compositional change with altitude. Above about 600 km altitude, individual atoms can escape from the Earth's gravitational field without collisions. This region is called the *exosphere*.

Chapter 2

Structures in Polar Ionosphere

2.1 Ionospheric Convection in the High-Latitude

Since the ionosphere and the magnetosphere are connected via the magnetic field lines, plasma convection inside the magnetosphere drives the plasma flows seen in the high-latitude ionosphere. From ground-based observations of the magnetic field and other ionospheric parameters, it has become a common knowledge that the flow pattern in the polar ionosphere has double vortices during the period of the southward IMF. The plasma flows from dayside to midnight over the polar cap and returns back toward the dayside at lower latitudes on both the dawn and dusk sides. Figure I-2.1 shows one of the most widely used models of the ionospheric convection pattern derived by Heppner and Maynard (1987). The convection pattern can be distributed symmetrically or asymmetrically between the two cells depending on the IMF B_y component. For the case of non-zero B_y , the two cell convection pattern is asymmetric, with enhanced convection in the dawn (dusk) cell for positive (negative) B_y conditions. Also, the entry of the flow into the polar cap is in the prenoon (postnoon) sector for positive (negative) B_y . These dependences on the IMF B_y are reversed in the Southern Hemisphere.

An explanation for the high-latitude plasma convection pattern was first proposed by Dungey (1961). Dungey's model attributed the momentum transfer from the solar wind into the magnetosphere to the *magnetic reconnection* at the dayside subsolar magnetopause. For the sake of simplicity, we now consider the case of almost southward IMF conditions. The magnetic field in the magnetosheath is roughly anti-parallel to the Earth's dipole field at the subsolar magnetopause. If these two anti-parallel magnetic fields reconnect and form a magnetic X-line, two field lines whose one end is connected to the dayside ionosphere and the other end is

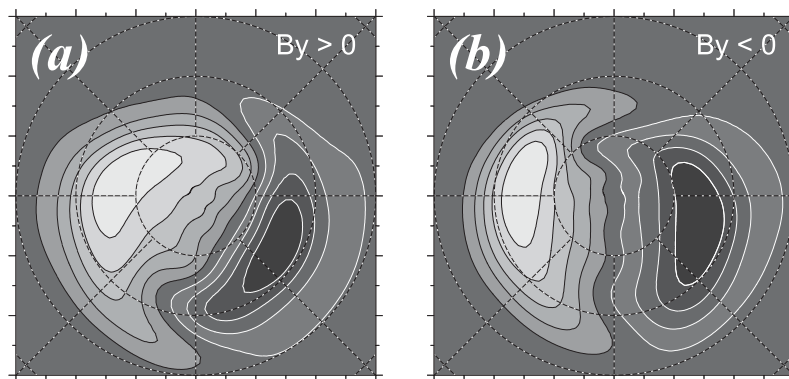


Figure I-2.1: Plasma convection patterns in the northern polar region for southward IMF and for both positive (left) and negative (right) IMF B_y components (from Heppner and Maynard, 1987). Corotation electric field is not included.

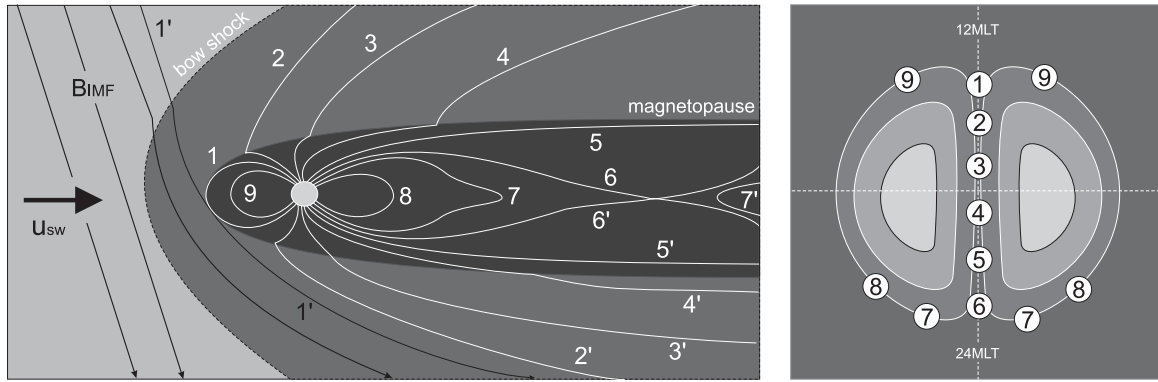


Figure I-2.2: (Left) schematic diagram illustrating how the magnetic fields are reconnected and convected in the framework of Dungey's concept. (Right) corresponding plasma convection as seen in the polar ionosphere.

stretching out into the interplanetary space are created. The solar wind flow in the magnetosheath drags the reconnected field lines in anti-sunward direction. Then, it becomes possible that the solar wind electric field penetrates into the magnetosphere and drives the plasma convection within the high-latitude ionosphere. The Dungey's model in the noon-midnight meridian for the southward IMF condition is shown in the left panel of Figure I-2.2. The numbered field lines show how the field lines are transported from the dayside magnetopause (field line 1-1') to the tail (field line 5-5'). This anti-sunward advection of the magnetic field lines can be traced into the polar ionosphere as shown in the right panel of Figure I-2.2.

Next we consider the origin of the return flow part of the ionospheric convection at lower latitudes. This sunward plasma flow is primarily caused by the reconnection at another X-line in the plasma sheet. In this case, anti-parallel field lines from the northern and southern lobes (field line 6-6') reconnect in the magnetotail and form a newly created closed geomagnetic field (field line 7). This reconnection also creates detached field line that will flow away in the anti-sunward direction (field line 7'). The newly created closed geomagnetic field line is highly stretched, and it relaxes by flowing earthward (field line 8). Near the earth, the field line moves around the earth and eventually returns to the dayside (field line 9). This earthward magnetospheric convection corresponds to the sunward flow in the ionosphere at lower latitudes. Although this description is oversimplified, the Dungey's concept of the open magnetosphere becomes a key when we consider energy input from the solar wind into the magnetosphere-ionosphere coupling system. In some part of this thesis, this framework known as the Dungey's cycle is employed to interpret the various kinds of ionospheric phenomena.

2.2 Magnetospheric Substorms

As noted before, the magnetic reconnection occurs at the dayside magnetopause, then newly created open field lines are dragged antisunward by the solar wind around the Earth. The plasmas and energies can enter into the magnetotail along the open field lines and are stored in the magnetotail. Then, they are released explosively into the inner magnetosphere, ionosphere and also into the solar wind. Simply speaking, the disturbances associated with this explosive energy release are the magnetospheric *substorms*.

Substorms have three phases, i.e, growth, expansion, and recovery phases. The growth phase is generally defined as a period during which the energy accumulates in the form of magnetic field in the magnetotail. When the energy in the magnetotail accumulates in excess or external conditions change, a rapid catastrophic instability or reconfiguration occurs. This causes a release and dissipation of the stored energy, namely, the

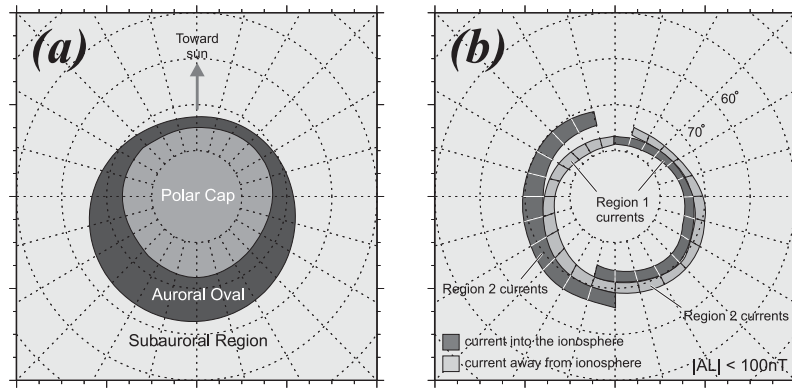


Figure I-2.3: (a) model of the auroral oval (Feldstein and Starkov, 1967) as modeled by Holzworth and Meng (1975) for quiet conditions, (b) distribution of the field-aligned currents (taken from Iijima and Potemura, 1978).

substorm expansion onset. In the recovery phase the magnetosphere returns to its ground state. Substorm includes at least one auroral breakup followed by a poleward expansion. During substorms various kinds of phenomena occur in the magnetosphere, ionosphere, and on the ground, such as dipolarization of the magnetic field, the formation of the current wedges, the energetic particle injection around the geosynchronous orbit, the ejection of plasmoid, the bursty bulk flow, the auroral breakup, the westward electrojet, and the Pi2 pulsation.

2.3 Auroral Particle Precipitation and Field-Aligned Current

Particle precipitation is another important mechanism that connects the magnetosphere and ionosphere at the high-latitudes. Energetic electrons precipitation in the auroral oval is not only the source of the optical emissions, but also (i) a source of ionization due to electron impact on the neutral atmosphere, (ii) a source of heating for both the ionosphere and atmosphere. The electron precipitation occurs in distinct regions in the auroral oval. Figure I-2.3 (a) shows model of the auroral oval (Feldstein and Starkov, 1967) as modeled by Holzworth and Meng (1975). The auroral oval divides the polar ionosphere into three categories, subauroral region, auroral oval, and polar cap. In general, the particle precipitation in the auroral zone is structured and highly time dependent. This acts to produce large-scale structure in ionization as well as important temporal variations particularly in the lower part of the ionosphere.

The precipitating auroral electrons are responsible for the upward field-aligned current (FAC). Associated with these precipitating magnetospheric electrons, ionospheric electrons are upflowing, which provides for a downward current. These upward and downward flowing FACs have been observed with satellite magnetometers and their average characteristics have been well investigated (e.g., Iijima and Potemura, 1978). Figure I-2.3 (b) shows statistical patterns of the FACs for quiet conditions. The FACs are concentrated into two principal circumpolar areas centered on the geomagnetic pole. The poleward part of the currents flows into the ionosphere in the morning sector and away from the ionosphere in the evening sector, which is called *Region 1 current*. The equatorward part of the currents, called *Region 2 current*, flows in the direction opposite to that of Region 1 at a given local time. The Region 1 and 2 FACs are considered to be connected via horizontal currents that flow in the lower ionosphere. These large-scale currents, including horizontal and field-aligned, and the conductivity structure due to the precipitating electrons and solar radiation, and the convection electric field are not independent but are closely related each other.

Chapter 3

Field-Aligned Plasma Irregularities

All of the structures described in this part so far are large in scale whose longitudinal and latitudinal distances are hundreds and thousands of kilometers. In this chapter, we turn to describe structure on smaller scales, which is the main target of this thesis, called *field-aligned plasma irregularities* (FAIs). The scale of the structures ranges from meters to kilometers. FAIs are detected and studied by using three main techniques, (i) direct measurement with satellite probes, (ii) their effect on radio signal (scintillation), and (iii) coherent backscatter radar. Since this thesis is mainly based on the coherent HF radar observation of the FAIs in the high-latitude upper atmosphere, a historical review of the FAIs detected with the coherent radars is given after a brief description of the generation mechanism of the FAIs.

3.1 Generation Mechanism

FAIs are produced in plasma instability processes such as two-stream instability, and gradient-drift instability (Fejer and Kelley, 1980; Keskinen and Ossakow, 1983; Tsunoda, 1988). At F region altitudes, the ion-neutral collision frequency is low, so ions and electrons move together with $\mathbf{E} \times \mathbf{B}$ drift velocity. Thus, the two-stream instability is not generated in these altitudes. Then, the gradient-drift instability is the major generation mechanism of the FAIs in the F region. Here, we show how the gradient-drift instabilities produce the irregular structure in plasma density.

If the medium becomes perturbed by some external influence, the perturbation will in turn disturb other aspects of the medium. If these consequences have the effect of enhancing the original perturbation, positive feedback will be introduced and the initial perturbation will tend to grow larger. This is the essence of the instabilities. The theory of instabilities tends to be mathematically complex, hence we overview some of the simpler aspects here and detailed description will be provided in Appendix B.

The gradient-drift instability is similar to the Rayleigh-Taylor instability. Schematic diagram of the gradient-drift instability is shown in Figure I-3.1. Plasma density falls off in $-y$ direction. A force acts from one side and it is assumed that small perturbations appear spontaneously at the contours of constant plasma density. Collision frequency at F region altitudes is generally very small but not zero. Then the positive ions and negative electrons have a relative motion in x direction. This motion, combined with the spatial inhomogeneity of the plasma density in x direction within the perturbation, produces net positive and negative charge at the contours of constant plasma density. This charge separation then makes polarization electric field $\delta\mathbf{E}$ in x or $-x$ direction. Due to the presence of the magnetic field, there emerges an additional force $\delta\mathbf{E} \times \mathbf{B}$ acting in the y or $-y$ direction. If the geometry of the parameters is favorable, this force can amplify the initial small perturbations. If the perturbation grows in amplitude as $\exp^{\gamma t}$, the growth rate, γ , is given in its simplest form

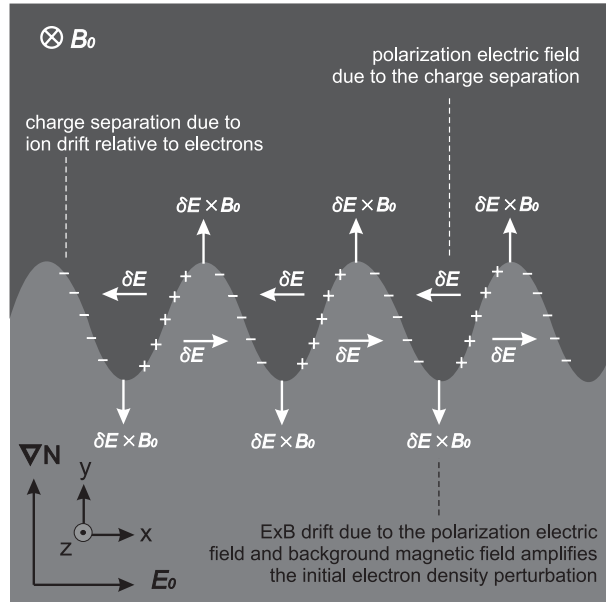


Figure I-3.1: Schematic diagram showing how the original perturbation grows by the gradient-drift instability process in the high-latitude geometry.

by

$$\gamma = \frac{E_0}{B_0} \cdot \frac{1}{n} \cdot \frac{dn}{dy}$$

3.2 FAIs in the High-Latitude F Region Ionosphere

F region FAIs in the equatorial zone have been studied since early 1970's in relation to the phenomena known as the spread F. Farley *et al.* (1970) first observed the overall structure of the FAIs by the Jicamarca radar at Peru. Later on, generalized Rayleigh-Taylor instability including the contribution of the electric field and neutral wind has been employed to explain the data.

In contrast to the equatorial zone, research of the FAIs in the high-latitude F region ionosphere has not progressed rapidly. One reason is that the observational data using ground-based radars were not large enough. In the equatorial case the Jicamarca can easily obtain backscatters from the F region FAIs since the wave vector is perpendicular to the local magnetic field. At the high-latitude, however, the geometrically is impossible to obtain the appropriate backscatter angle (normality condition, see the next chapter in detail) at the F region altitudes using VHF and UHF systems. Radar observations of the F region FAIs had become possible at HF frequencies since ionospheric refraction can be used to bend the radar signals and attain a scattering geometry nearly perpendicular to magnetic field. Successful measurements have been made in Scandinavia (Villain *et al.*, 1985) and in Goose Bay, Canada (Greenwald *et al.*, 1983). These preliminary results have shown that the echoes are indeed received in the tens of meters wavelength but a detailed interpretation does not exist for the scattering structures. Cerisier *et al.* (1985) investigated satellite observation of the electron density fluctuation, which is considered to be the FAIs, at F region altitude. They reported that the fluctuation occurs preferentially on only one sense of the large-scale density gradient. The same profile had already been obtained in the equatorial zone (Kelley *et al.*, 1982). This suggests that the generalized Rayleigh-Taylor instability employed in the equatorial zone is also applicable at high-latitudes.

Chapter 4

Super Dual Auroral Radar Network

This thesis is based on the observation of the Super Dual Auroral Radar Network (SuperDARN), which is a network of coherent HF backscatter radar located in the northern and southern high-latitude zones. In this chapter, a detailed description of the coherent HF backscatter radar is given first. Second, the history of the SuperDARN project, radar facility, operation, and data production are briefly introduced.

4.1 Volume Scattering Process

Transmitted signal is backscattered when the FAIs are present on the path of the signal. This process, called *volume scattering*, is essentially one kind of the partial reflection at the refractive index discontinuities due to the FAIs. Simplified theory of the partial reflection is as follows. The reflection and transmission coefficients at a sharp boundary are determined by the condition that the tangential components of the \mathbf{E} and \mathbf{H} vectors must be continuous across the boundary. Consider that a linearly polarized wave in a medium of refractive index n_1 is normally incident on a boundary with a medium of refractive index n_2 . The electric vectors of the incident, transmitted and reflected waves are respectively E_I , E_T and E_R , respectively (these vectors are assumed to be parallel each other for simplicity, hence they are described in scalar form). Then, for continuity,

$$E_T = E_I + E_R$$

For the magnetic components, due to the relationship between the directions of \mathbf{E} and \mathbf{H} , H_R is opposite to H_I because the reflected wave propagates in the opposite direction (see the left panel of Figure I-4.1). Thus,

$$H_T = H_I - H_R$$

In a non-magnetized medium,

$$\frac{H}{E} = \frac{n}{\sqrt{\epsilon_0 \mu_0}}$$

Therefore, by substitution,

$$E_T n_2 = E_I n_1 - E_R n_1$$

and replacing E_T from E_I and E_R ,

$$\frac{E_R}{E_I} = \frac{n_2 - n_1}{n_2 + n_1}$$

The fraction of power reflected is

$$\left(\frac{E_R}{E_I}\right)^2 = \frac{(n_2 - n_1)^2}{(n_2 + n_1)^2}$$

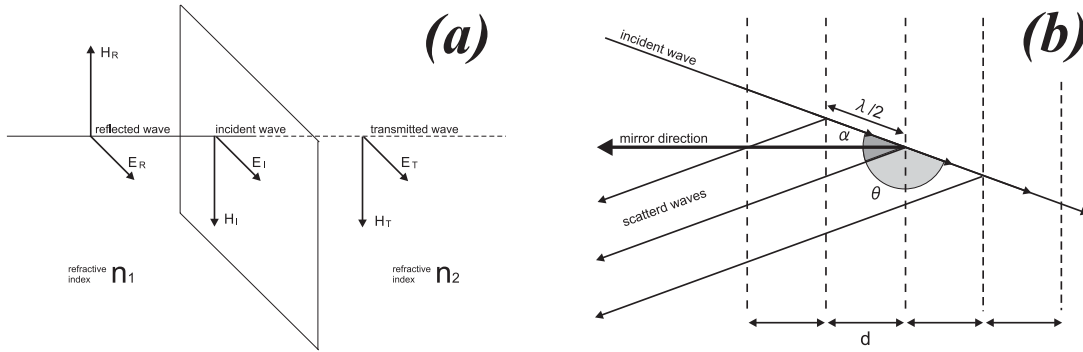


Figure I-4.1: (a) Continuity of electric and magnetic vectors at a sharp boundary. (b) Schematic drawing of volume scattering. A signal of wavelength λ , scattering through angle θ , selects spatial period $d = \frac{1}{2}\lambda \sin \frac{\theta}{2}$.

Hence, power of reflected wave is dependent on how sharp the refractive index discontinuity is. Whether ionized or not, the atmosphere contains irregularities of many different scales, and a small fraction of the incident energy is scattered in all directions at each boundaries. Signals scattered from irregularities spaced by half a wavelength will reinforce in the direction back to the radar. However, it is not necessary for the scattering structures to be regularly spaced. Signal of wavelength λ will effectively select the spatial component of period $\lambda/2$, ignoring the others. Referring to Figure I-4.1 (b), the signals from two scattering planes reinforce when their path difference is λ . Therefore the separation between the plane is

$$d = \frac{\lambda}{2} \cdot \cos\left(\frac{\alpha}{2}\right) = \frac{\lambda}{2} \cdot \sin\left(\frac{\theta}{2}\right)$$

where θ is the angle between incident and scatter waves. The normal to the scattering plane is called the *mirror direction*. The intensity of the return will be related to the strength of the scattering mechanism, and its frequency will show Doppler shift according to the line-of-sight velocity of the scattering volume. The shape of the echo spectrum may also contain valuable information about the medium, such as its spatial structure and temporal variabilities.

4.2 Coherent HF Backscatter Radar

A radar designed to receive echoes backscattered by the volume scattering process is usually called a *coherent scatter radar*. Different systems are required for the E and F regions observations. In the E region, they are used to observe the FAIs associated with the auroral electrojet, so-called *radio aurora*. These systems are normally operated in the VHF frequency band. The E region FAIs are formed when an electrojet flows in the auroral E region, generating instabilities by the two-stream or the gradient-drift mechanisms. Auroral electrojets are generally flowing almost perpendicular to the geomagnetic field, thus the E region FAIs are basically field-aligned. To obtain the strongest echoes the transmitted signal from the radar must be in the plane normal to the direction of the local geomagnetic field at E region altitudes (*normality condition*). Since the geomagnetic field is more vertical than horizontal in the case of the high-latitude ionosphere, the radars of VHF band meet the normality condition in the E region and can obtain significant backscatter from the E region FAIs.

F region FAIs are also observable by the coherent radars. However, F region FAIs are also field-aligned due to the larger plasma diffusion along the direction of the geomagnetic field, then it is impossible for the VHF radars to satisfy the normality condition within the high-latitude ionosphere. The solution is to operate

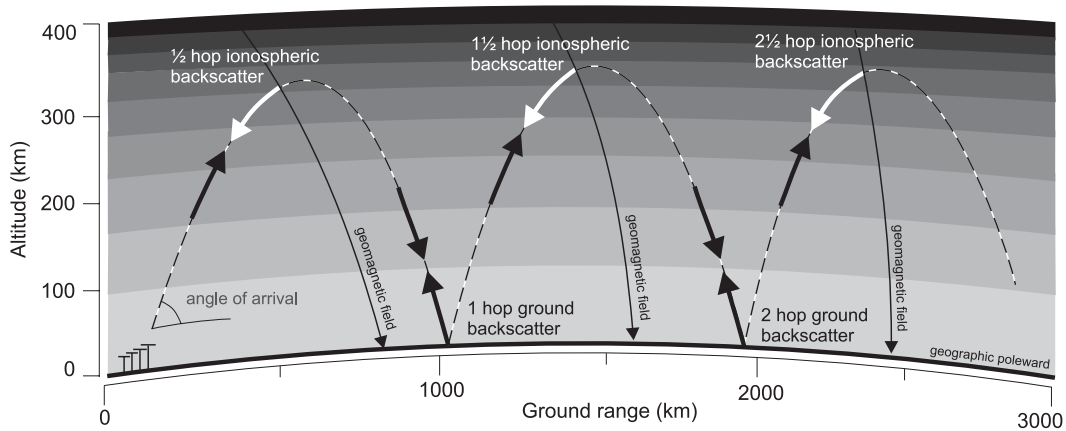


Figure I-4.2: Schematic illustration of the curved path of the HF wave transmitted from and received by the radar.

the radar in the high frequency (HF) band, covering frequencies between 3 and 30 MHz. The waves in HF band are gradually refracted as they experience vertical change in the refractive index. This modification of the raypath enables the waves to meet the normality condition when they inject the FAIs at F region altitudes, hence the coherent HF radar obtains significant backscatter echoes from F region FAIs. Schematic illustration of the curved path of the HF wave is shown in Figure I-4.2.

One big difference between E region and F region backscatter echoes is that the echo from the F region FAIs carries an information about the horizontal drift velocity of the ionospheric plasma. Ruohoniemi *et al.* (1987) have shown that line-of-sight velocities derived from the Doppler shift of the returned HF signal well agree with those obtained from the incoherent scatter radar. Later on, many authors have shown that the plasma velocities deduced from the coherent HF radar are quite consistent with those obtained from the other observation techniques. This advantage leads a number of scientists and scientific groups to construct the coherent HF radar system in the northern and southern high-latitude zones.

4.3 Overview of the Network

The concept of the SuperDARN (Greenwald *et al.*, 1995) evolved from discussions among scientists interested in radar remote sensing of the ionosphere in 1991. At the time, it was recognized that a network of paired HF radars could provide extensive spatial coverage and high temporal resolution measurements of plasma convection in the upper atmosphere. A plan was developed to share the responsibility for the development of the new radars and the participants began to prepare proposals to their various funding agencies. By late 1992, five new radars were at various levels of construction. The first new pair of radars began operation in 1993 at Saskatoon and Kapuskasing in Canada. Later on 15 radars have begun operation in the Northern and Southern Hemispheres. The fields-of-view of the radars are presented in Figure I-4.3.

SuperDARN is an excellent example of international collaboration in scientific research. At the present time, Australia, Britain, Canada, Finland, France, Japan, South Africa, Sweden, and the United States are contributing to the international effort. A unique feature of the SuperDARN is that all radars are very similar and have been developed to operate from a common radar control software. Thus, the data products from the various radars are fully compatible and can easily be investigated by using common analysis software. The full data products are copied and distributed to the SuperDARN community for scientific analysis.

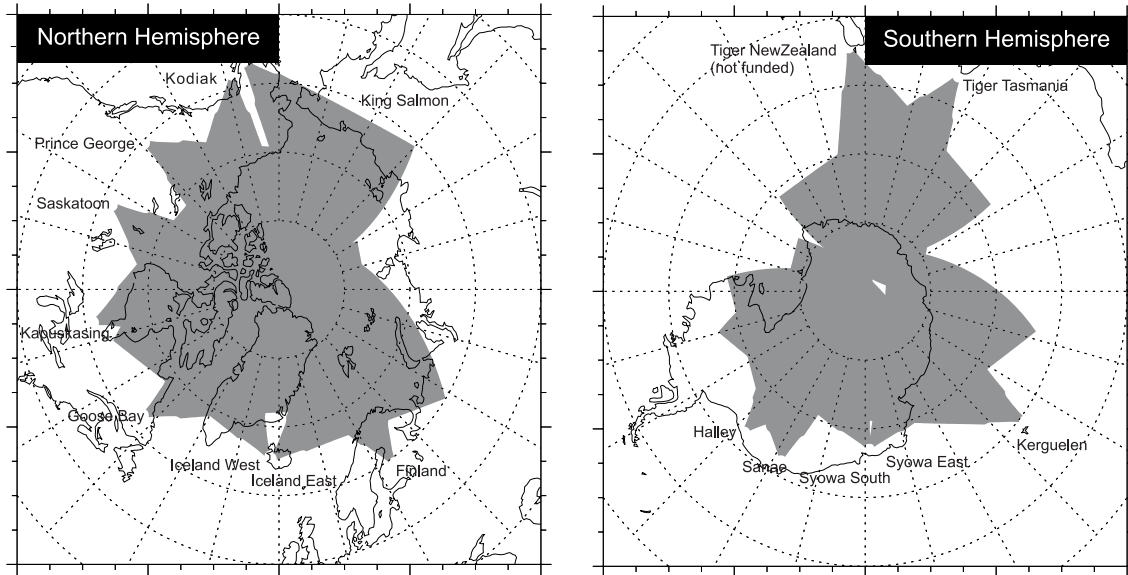


Figure I-4.3: The fields-of-view of the radars currently operative in the Northern Hemisphere (left) and in the Southern Hemisphere (right). Dotted circles represent 40° , 50° , 60° , 70° and 80° magnetic latitudes.

4.4 Radar Facility

Each of the SuperDARN radars has a design heritage that evolved from the Goose Bay HF radar. All radars have a main antenna array consisting of 16 log-periodic antennas that operate over the frequency range from 8 to 20 MHz. Signals from or to these antennas are phased with electronically-controlled time-delay phasing elements that allow the beam to be steered into 16 directions covering a nominal 52° azimuth sector. The direction of the measurements is independent of operating frequency, however, the azimuthal width of the beams is dependent on frequency. It ranges from 2.5° at 20 MHz to 6° at 8 MHz. Since most of the observations are made in the frequency range from 10 to 14 MHz, the nominal azimuthal resolution of the radar is approximately 4° . At a range of 1500 km, this corresponds to a transverse spatial dimension of about 100 km.

In addition to the main antenna array, a secondary, parallel array of 4 antennas is used to determine the vertical angle of the backscatter signal. The second array also uses a phasing matrix and is located 100 m in front of or behind the main antenna array. It functions as an interferometer to determine the relative phases of the backscattered signals arriving at the two arrays. This phase information is converted to an elevation angle, which is used to determine the propagation modes of the returning signals as well as the approximate altitude of the scatters.

4.5 Operation

SuperDARN electronic steering occurs in microsecond time scales, which allows the radar to scan rapidly through a number of beams or to dwell for an extended period on a single beam. The radars typically scan in a sequential fashion with a dwell of 7 s in each beam direction. All of the radars are synchronized to begin each scan on two minute boundaries. The basic Northern Hemisphere scan pattern for a pair of radars is such that the more westward radar to scan in a clockwise direction and the more eastward radar to scan in a counterclockwise direction, which enables the looking directions of the pair radars to overlap more simultaneously. The sense of the scans is reversed for the Southern Hemisphere radars. With synchronization of the viewing direction of the

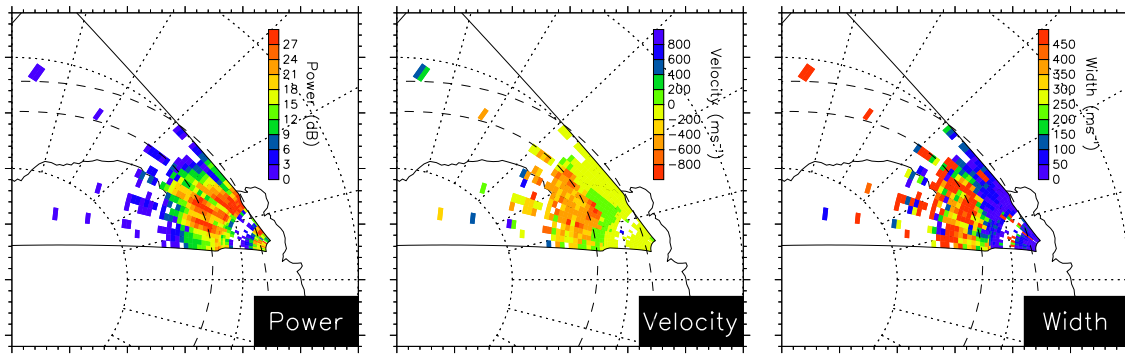


Figure I-4.4: Maps of the backscatter power (left), Doppler velocity (center) and Doppler spectral width (right) for one complete sweep of the 16 beams (2 min). The data are plotted on the magnetic coordinate system.

radars, the instantaneous common viewing area will track from north to south during each scan.

Important feature of the SuperDARN is that all of the radars operate continuously. 50% of the monthly operation is devoted to a common program that scans each radar 16 adjacent viewing directions on a two minutes schedule. 20% of the operation is devoted to special operating modes proposed by members of the SuperDARN community. For example, the radars might make high temporal resolution observations in a specific viewing direction while scanning through the full azimuth sector more slowly. Finally, 30% of the operation is discretionary to the individual Principal Investigators (PIs) and the data obtained during these intervals are initially proprietary. The schedules are generally prepared two months in advance of the month in which they are carried out.

Most of the radars use broadband (8-20 MHz) solid state transmitters at the base of each antenna of the main array. Each transmitter has an peak output power ranging from 500 to 800 W across the frequency band and a duty cycle of up to 6%. The typical pulse length of the transmitted signal is 300 μ s, yielding a range resolution of 45 km. The SuperDARN radars use a number of different multipulse transmission sequences consisting of 7 pulses transmitted over 100 ms time period. Detailed information about the coded multiple pulse used in the SuperDARN is given in Appendix A.

4.6 Data

The backscatter returns from these pulses are sampled and processed to produce multi-lag autocorrelation functions (ACFs) as a function of range. The ACFs are fitted to determine the backscatter power, the mean Doppler velocity, and the width of the Doppler power spectrum for each range gate where there are significant returns. Detail of the data production procedure is described in Appendix A. Figure I-4.4 shows examples of maps of the backscatter power, Doppler velocity and Doppler spectral width for one complete sweep of the 16 directions within 2 min.

Chapter 5

Organization of This Thesis

5.1 Philosophy of This Thesis

This thesis is based on the data obtained from the SuperDARN coherent HF radar network. There seem to exist two different ways to utilize the SuperDARN data. The radars are designed to employ the FAIs as tracers of the bulk plasma motion under the influence of the convection electric field. Thus, the first way is to employ the Doppler velocity data as a diagnostic tool for the ionospheric convection. SuperDARN covers the vast area in the northern and southern polar latitudes. Hence, the previous works using Doppler velocity have provided important insights into the studies of the large-scale phenomena in the magnetosphere-ionosphere coupling system. The other way is to examine the FAIs itself. Since 1980's, there have been a number of studies that investigate morphological feature and generation process of the high-latitude F region FAIs. However, there still exist many questions and debates. In this thesis, we investigate why the FAIs appear, what kind of geophysical characteristics their properties reflect. In particular, we are aimed at disclosing how their characteristics except for the Doppler velocity can be utilized to identify atmospheric, ionospheric and magnetospheric regions and processes. This is the philosophy of this thesis, which might be an antithesis to the studies using Doppler velocity. However, FAIs are very interesting scientific subject worth to be investigated and there could be many applications to the studies of magnetosphere-ionosphere-atmosphere coupling system.

5.2 Targets of This Thesis

There are three major targets of this thesis, (i) subauroral FAIs, (ii) FAIs within the dayside polar cap, and (iii) peculiar near range echoes. Figure I-5.1 presents a statistical map illustrating the occurrence distribution of the FAIs observed by the SuperDARN radars during winter, in which the first two targets of this thesis are indicated. Brief introductions of these targets are as follows:

(i) Subauroral FAIs

FAIs observed outside of the equatorward edge of the oval model. Unfortunately, the SuperDARN radars have not been designed to observe this region. Hence, there are few studies that have investigated FAIs in this region. However, as shown in Figure I-5.1, the peak of the FAI occurrence in the subauroral region is very sharp and very localized. Morphological feature of these FAIs is investigated in relation to the several phenomena and processes in the subauroral ionosphere.

(ii) FAIs within the dayside polar cap

These echoes are known to have spectral characteristics distinct from those in the other regions. Many authors have investigated these FAIs, but there are many aspects that remains unclear. We examine the

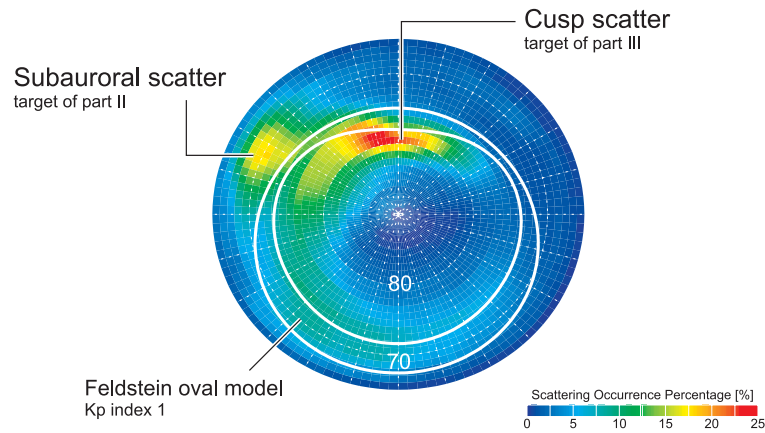


Figure I-5.1: Statistical map illustrating the occurrence distribution of the radar backscatter, in which some of the targets of this thesis are indicated. Occurrence is mapped into the magnetic coordinate system.

origin of these distinct spectral characteristics, and then discuss how they can be applied to the studies of the magnetosphere-ionosphere coupling system.

(iii) Peculiar near range echoes

Peculiar radar echoes appear at slant ranges very near to the radar site (say 180-315 km). Recently, these echoes have been found to be a backscatter from the mesospheric altitudes. We report detailed characteristics of these echoes and discuss their origin.

5.3 Outline of This Thesis

Outline of this thesis is as follows:

Part II. Statistical properties of the subauroral FAIs are presented, and a model that can explain their generation is proposed. In order to evidence the proposed model, simultaneous observation of the subauroral FAIs with the coherent and incoherent scattering radars is conducted. Then, it is reported that the subauroral FAIs can be used as a good indicator of the ionospheric boundaries and energy input processes from the magnetosphere into the ionosphere.

Part III. We have examined the dayside high-latitude FAIs known to have broad spectral width. Statistical distribution of these broad spectral width FAIs is clarified first. Next, conjugate observation of the broad spectra and magnetic field observation by the satellite is reported. Then, the origin of the broad spectral width is discussed. At last, it is confirmed from an interhemispheric event study that these FAIs can be used as a good proxy for the processes that occurs within the dayside ionosphere.

Part IV. Characteristics of the peculiar near range echoes detected with the SuperDARN Syowa-East radar are investigated in a statistical fashion. Seasonal and local time dependences of the echo occurrence distribution are reported. Long-term variabilities of the echo occurrence probability are also discussed.

Part V. Techniques for processing the radar data and linear theory of the gradient-drift instability are briefly introduced as an appendices.

Part VI. List of references is provided.

Part II
Subauroral Irregularities
as a Tracer for the Midlatitude Density Trough

Chapter 1

Overview

Target of the analysis presented in this part is field-aligned plasma irregularities (FAIs) in the subauroral F region ionosphere as observed by the SuperDARN coherent HF radars. As is already noted in the general introduction part (section I-2.3), the subauroral region is defined to lie equatorward of the energetic electron precipitation of the auroral oval. Plasma convection in this region is mostly zonal, i.e., the sunward return flow part of the high-latitude convection. Various kinds of geophysical characteristics, such as the midlatitude plasma density trough, subauroral ion drift (SAID), and stable auroral red (SAR) arcs, are observed in this region. Magnetic field lines in the subauroral region are basically closed. Thus, geophysical phenomena in this region are not always a direct manifestation of the magnetic reconnections that occur during substorm cycles. However, some of them are as dynamic as reconnection induced transient features and they could be understood in the framework of the magnetosphere-ionosphere coupling system during substorm cycles. The analysis presented here is aimed at describing physical characteristics of the subauroral FAIs in terms of the possible connection with the other ionospheric and magnetospheric processes that occur on the field lines in the subauroral latitudes.

1.1 Midlatitude Trough

Clearly, one of the most important features in the subauroral region is the plasma density depleted structure called the midlatitude (plasma density) trough. We define the midlatitude trough as the region of low plasma concentration at F region altitudes that appears just outside of the equatorward boundary of the auroral oval. This feature was first explored by Muldrew (1965) and Sharp (1966). Later on, its morphological characteristics have been investigated by using the data from the polar-orbiting satellites, incoherent scatter (IS) radars (see reviews by Moffett and Quegan, 1983, Rodger *et al.*, 1992 and references therein). The satellites observe density depleted structure when they overpass the subauroral latitudes meridionally (e.g., Spiro *et al.*, 1978). Here, snapshot of the midlatitude trough in latitude versus altitude plane obtained from the Millstone Hill IS radar is presented in Figure II-1.1 (taken from Foster, 2000) as a representative of the past observations. In the top panel, clear signature of the electron density depletion can be seen between 40° and 43° geodetic latitude at F region altitudes. Bottom panel shows the latitudinal gradient of the total electron content (TEC) obtained at the same time over the Millstone Hill. Steep gradient of TEC is in good agreement with the density depletion observed by the radar. The main characteristics of the midlatitude trough deduced from the past observations can be summarized as follows:

1. The midlatitude trough is primarily a nightside and late afternoon (dusk sector) phenomenon and it has been observed infrequently at all local times (Spiro *et al.*, 1978; Quegan *et al.*, 1982).
2. The midlatitude trough is most regularly seen in winter and during equinox, and its occurrence is rare

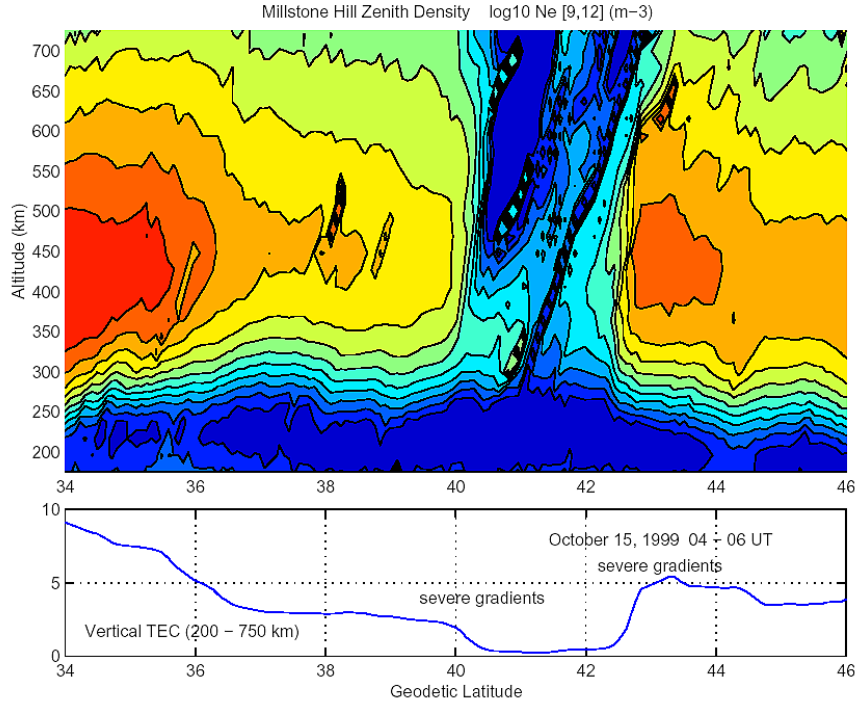


Figure II-1.1: (Top) geodetic latitude versus altitude profile of the electron density observed by the Millstone Hill incoherent scatter radar (42.5°N , 288.5°E). (Bottom) latitudinal gradient of total electron content (TEC) at the same time period over the Millstone Hill (taken from Foster, 2000).

and mainly restricted to the midnight sector in summer (Watkins, 1978, Sojka *et al.*, 1981).

3. The poleward edge of the trough lies close to the equatorward boundary of the diffuse aurora (corresponding to the central plasma sheet precipitation) (Sojka *et al.*, 1981; Quegan *et al.*, 1982).
4. The midlatitude trough in the dusk sector extends equatorward with increasing local time (Quegan *et al.*, 1982; Collis and Haggstrom 1988; Hargreaves and Burns, 1996).
5. During periods of increased geomagnetic activity, the midlatitude trough is observed at lower latitude for a given local time (Sojka *et al.*, 1981; Dudeney *et al.*, 1983).

Schematic illustration of the midlatitude trough is presented in Figure II-1.2 (a). The trough is found to be a circumpolar structure surrounding the auroral oval from dusk to dawn through midnight. For comparison, Figure II-1.2 (b) gives the field-aligned current system taken from Iijima and Potemura (1978).

Formation process of the trough is still controversial. There exist at least two competing theories. Some authors (Knudsen, 1974; Knudsen *et al.*, 1977; Spiro *et al.*, 1978) suggested that the midlatitude trough is primarily created by an ordinary loss through recombination in darkened regions of stagnated plasma flow (stagnation trough theory). At the subauroral latitudes, the earth corotation and magnetospheric electric field induced convection compete, which produces region of stagnated plasma flow in the evening sector. Flux tubes filled with F region plasma are confined to this stagnation region and spend many hours. The decay of ionization in these flux tubes leads to the formation of trough. Other authors (Evans *et al.*, 1983; Holt *et al.*, 1983; Providakes *et al.*, 1989) have pointed out that the trough is formed by an enhanced recombination in regions of rapid subauroral plasma drift through ion-frictional heating process (Schunk *et al.*, 1975) (enhanced

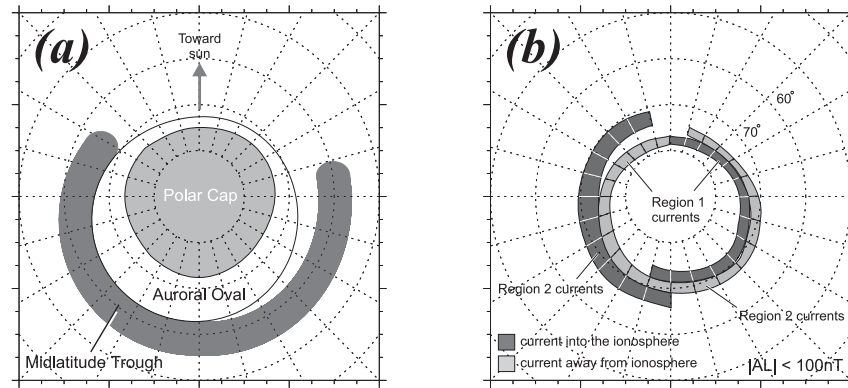


Figure II-1.2: (a) Schematic illustration of the midlatitude trough, (b) distribution of the field-aligned current during quiet conditions (taken from Iijima and Potemura, 1978).

recombination trough theory).

The observational and modeling results from the previous studies have clarified important characteristics of the midlatitude trough, especially its latitudinal structure is well understood. However, longitudinal distribution of the trough is relatively unclear. There has been only one study that presents how wide the longitudinal extent of the trough is (Halcrow and Nisbet, 1977). This unique study claimed that the longitudinal extent of the trough is controlled by the solar zenith angle and the level of geomagnetic disturbance as estimated by Kp index. However, the authors have not discussed at all why this clear relationship is introduced. This issue must be discussed in terms of the formation process of the trough during disturbed conditions. Combined observations of the electric field, electron density and plasma temperature within the trough are desired to answer this unresolved question.

1.2 Subauroral Ion Drift

Subauroral ion drift (SAID) is a region of high-speed westward ion flow channel confined to a narrow range of subauroral latitudes. In contrast to the narrow structure in latitude, the SAID extends over wide range of longitudes. It was first identified by Galperin *et al.* (1973) and subsequently by several other authors. Most observations of the SAID have been made using drift meters on-board polar-orbiting satellites (Smiddy *et al.*, 1977; Rich *et al.*, 1980; Anderson *et al.*, 1991, 1993, 2001; Karlsson *et al.*, 1998), although a few ground-based radar observations have also been reported (Providakes *et al.*, 1989; Yeh *et al.*, 1991). Figure II-1.3 shows an example of the SAID observed by the satellite electric field measurements (taken from Anderson *et al.*, 2001). On the day presented, EXOS-D and DMSP satellites have favorable conjunction for the multisatellite observation of the SAID. Both satellites observed strong westward ion drift over 1.5 km s^{-1} at the subauroral latitudes. Latitude of maximum drift is closely corresponding to the equatorward edge of the electron precipitation in the auroral oval. The typical characteristics of the SAID deduced from the past observations are summarized as follows:

1. SAID is a region of rapid westward flow at least 1 km s^{-1} up to 4 km s^{-1} , confined to a narrow range of latitudes ($1\text{-}2^\circ$) in the duskside subauroral region (Spiro *et al.*, 1979; Anderson *et al.*, 1991).
2. SAID is observed adjacent to the poleward boundary of the trough or sometimes overlapping the equatorward edge of the diffuse aurora (electron precipitation) (Providakes *et al.*, 1989; Anderson *et al.*, 2001).

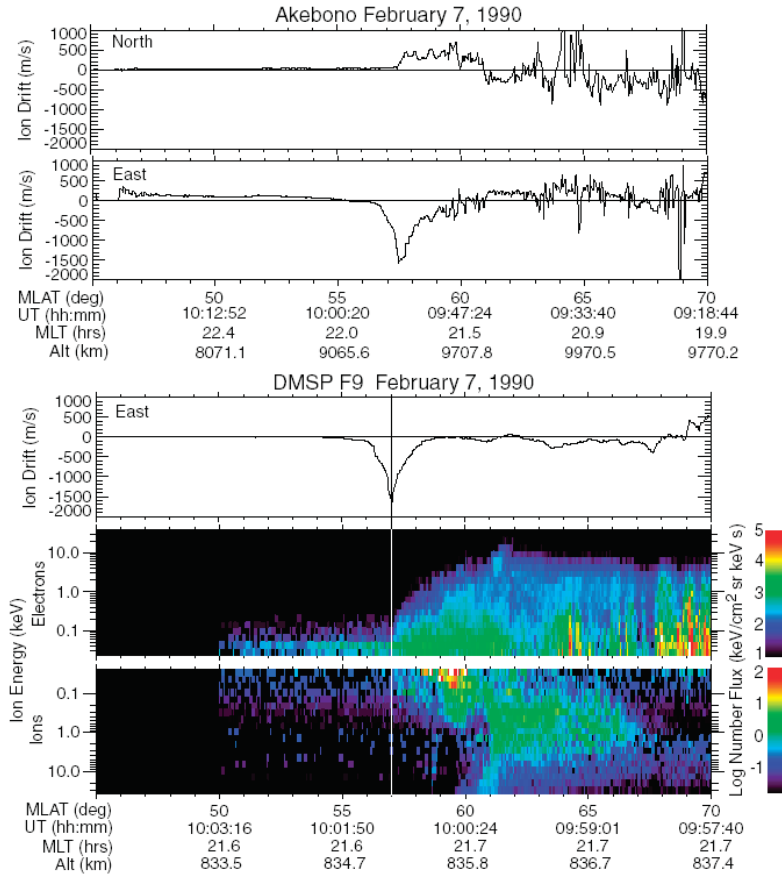


Figure II-1.3: (Top two panels) north-south and east-west components of ion drift observed by the EXOS-D EFD electric field measurements. (Bottom three panels) cross satellite track ion drift observed by the DMSP spacecraft. Colour-coded spectrogram of precipitating ions and electrons are also shown in the bottom two panels (taken from Anderson *et al.*, 2001).

3. Within the SAID, the ion temperature is elevated. In contrast, the electron temperature is not enhanced significantly. Major compositional changes and large field-aligned flows are observed in the vicinity of the SAID (Anderson *et al.*, 1991). These signatures could be the consequences of ion-frictional heating (Heelis *et al.*, 1993).
4. The lifetime of the SAID is uncertain, however, in the range from 30 min to 3 hours, commencing during substorm recovery phase. Any events are not observed within 30 min after substorm onset (Anderson *et al.*, 1991; Karlsson *et al.*, 1998).

Generation of the SAID is still a considerable debate. Southwood and Wolf (1978) suggested that the SAID is generated as a result of the establishment of low-latitude shielding of substorm-enhanced electric fields. An increase in the cross-tail magnetospheric electric field induces an electric field between the inner edges of the electron and proton ring currents when their separation is small. Recently, De Keyser *et al.* (1998) and De Keyser (1999) proposed that an intense radial electric field is generated by a thermoelectric effect across the interface between cold corotating plasma and hot plasma injected from the plasma sheet after substorm onset. Charge separation develops because the two particle populations have different energies and different gyro radii. The polarization electric field can be mapped into the subauroral ionosphere and the SAID is formed. Anderson *et al.* (1993) emphasized the importance of ion-frictional heating in the ionosphere, which causes a

reduction of the conductivity. The magnetospheric driver supplies the poleward electric field via field-aligned current. The current must close via Pedersen current in the ionosphere. If the conductivity reduces through ion-frictional heating, the electric field must increase in order to satisfy current continuity. This mechanism could also contribute to the generation and maintenance of the SAID.

Spacecraft observations have provided important insights into the characteristics of the SAID. They have obtained high-time resolution measurement of the SAID along single orbit overpassing the events. However, because of the typical period of the orbit (≈ 90 min for most cases), spacecraft observations have a limitations to observe the SAID continuously. Then, ground-based radar observations of the SAID are desirable to disclose the spatial extent of the SAID and to obtain more conclusive answer for the generation mechanism of the SAID.

1.3 Irregularities in the Subauroral Region

As introduced in the previous part (section I-3.1), most major generation mechanism of the FAIs at F region altitudes is thought to be the gradient-drift instability. It employs gradient in the electron density, electric and magnetic fields which are perpendicular each other. The midlatitude trough has a steep horizontal gradient in electron density at its edges. Large electric fields such as the SAID are often observed well after the substorm expansion. Obviously, geometry of the background parameters could favorable for the instability process to occur in the subauroral F region ionosphere. However, there have been few studies of the FAIs in the subauroral F region. Hower *et al.* (1966) have shown a pronounced peak in the occurrence of HF radar echoes from FAIs near the time of local sunset. This peak of occurrence rate is located at a geomagnetic latitude of 54° . The occurrence of these echoes is relatively independent of magnetic activity as estimated by Kp index. Backscatter from the FAIs in the midlatitude trough was examined by Moller and Tauriainen (1975). They reported that the intense FAIs appear poleward edge of the mid-latitude trough.

The fields-of-view of the SuperDARN radars are initially designed to cover the region between the equatorward edge of the auroral oval and polar cap in both the dayside and the nightside ionospheric F region. Then, the subauroral region is basically out of scope of the project. However, there has been only one paper investigating the subauroral F region FAIs using SuperDARN radar (Ruohoniemi *et al.*, 1988). They identified a distinctive backscatter feature known as the dusk scatter event (DUSE). They investigated DUSE during quiet geomagnetic conditions over a period of 5 months centered on winter solstice. They have reported that it appears when the solar zenith angle is near 95° and its source lies in the magnetic latitudes equatorward of the auroral oval. They proposed several models to explain the enhancement of FAIs in this region. However, the generation mechanism of FAIs responsible for DUSE is still an open question and the morphological feature of DUSE during disturbed condition has not been unresolved.

1.4 Organization of This Part

Organization of this part is as follows: In chapter 2, spatial distribution of the subauroral F region FAIs as observed by the SuperDARN HF radars is investigated in a statistical fashion. Then, possible generation mechanisms of the subauroral FAIs are proposed. In chapter 3, we discuss which of the mechanisms proposed in chapter 2 is relatively important on the basis of the simultaneous observation of the background parameters of the FAIs from the EISCAT UHF system. Relationship between the subauroral FAIs and the other ionospheric phenomena such as the SAID is discussed and practical applications of the subauroral FAIs to the study of the magnetosphere-ionosphere coupling system are proposed.

Chapter 2

Statistical Analysis of Field-Aligned Irregularities in the Subauroral F Region as Observed by the SuperDARN Radars

2.1 Introduction

The HF radars of SuperDARN transmit radio waves whose frequency ranges from 8 to 20 MHz. As the waves traverse the E and F regions of the ionosphere, they are scattered backward by the decameter-scale field-aligned irregularities (FAIs) when the Bragg condition is satisfied; i.e., significant backscatter is generated only if the radar wave k vector lies in the plane perpendicular to the structure of FAIs. Normally, the radars are used to obtain the ionospheric convection velocity by observing the drift motion of these FAIs (Ruohoniemi *et al.*, 1987; Ruohoniemi and Greenwald, 1996). The data of SuperDARN are also useful for the study of FAIs in the high-latitude ionosphere. The scattering occurrence depends on both the existence of FAIs and the conditions of HF wave propagation. Hence, the observed ‘scattering occurrence percentage’ is considered to be a lower bound on the actual ‘occurrence percentage of FAIs’, which provides important information about the distribution of FAIs and their generation mechanism.

Recently, several statistical studies of scattering occurrence using SuperDARN have been carried out. Ruohoniemi and Greenwald (1997) have investigated the scattering occurrence of 5.5 years of SuperDARN Goose Bay radar observations. In their study, a seasonal variation and a solar cycle dependence of the scattering occurrence are reported. The relationship with the auroral oval and the cusp region is also discussed. Milan *et al.* (1997) have analyzed the scattering occurrence of SuperDARN Iceland-East and Finland radars statistically. They have shown that FAIs are frequently generated around the dayside cusp in winter and within the nightside auroral oval in summer. In both papers, however, the occurrence distribution of the FAIs in the subauroral region has not been examined in detail.

Ruohoniemi *et al.* (1988) had earlier focused on the radar echoes in the subauroral F region and identified a distinctive backscatter feature that appeared in the dusk sector over a period of 5 months centered on winter solstice. This activity, which was called the dusk scatter event (DUSE), was investigated for magnetically undisturbed conditions using the data of SuperDARN Goose Bay radar. They reported that it appears when the solar zenith angle is near 95° . In addition, the source of DUSE lies in the magnetic latitudes equatorward of the auroral oval (i.e., near the poleward edge of the midlatitude trough). They proposed several mechanisms to explain the enhancement of FAIs in this region. However, the generation mechanism of FAIs responsible for DUSE is still an open question. Moreover, Ruohoniemi *et al.* (1988) did not analyze DUSE during disturbed conditions. Then, the morphological features of DUSE during disturbed conditions should be investigated as well.

In this study we extend the work of Ruohoniemi *et al.* (1988) by analyzing the scattering occurrence per-

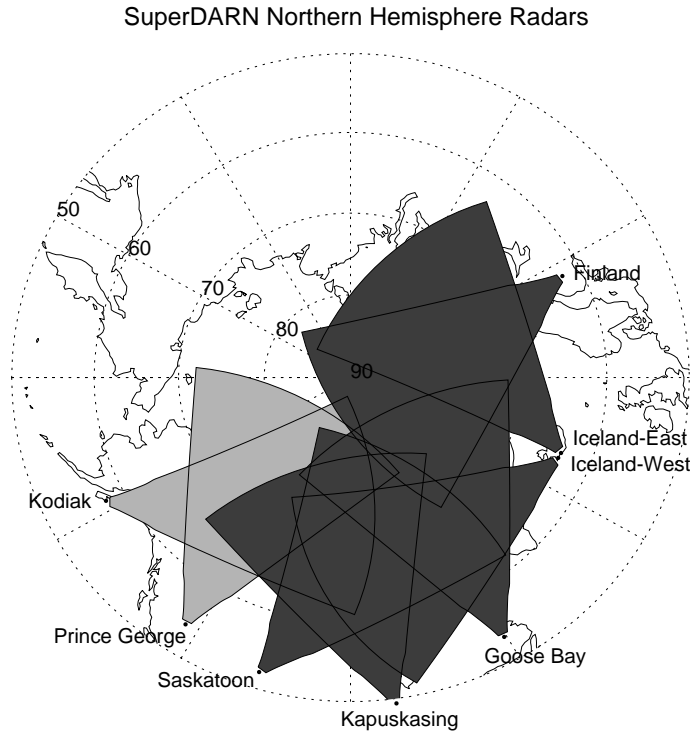


Figure II-2.1: Fields-of-view of the Northern Hemisphere SuperDARN radars (Kodiak, Prince George, Saskatoon, Kapuskasing, Goose Bay, Iceland-West, Iceland-East and Finland) in the geographic coordinate system. Shaded fields-of-view indicate the radars employed in the statistical analysis.

centage of Northern Hemisphere SuperDARN radars statistically. First, we clarify the distribution of subauroral FAIs in each radar and examine whether DUSE is a common feature of all the Northern Hemisphere SuperDARN radars. We also identify a distinctive backscatter feature around sunrise in the subauroral ionosphere, which is termed the dawn scatter event (DASE) in this paper. The seasonal variations of DUSE and DASE in both geographic and magnetic coordinate systems are presented. In particular, we examine the characteristics of DUSE during summer months. Finally, we investigate the relationship with the sunward edges of the midlatitude trough for both quiet and disturbed conditions. Consequently, the sources of DUSE and DASE are determined, and a new formation mechanism of FAIs based on the gradient-drift instability is proposed.

2.2 The SuperDARN Radars and Statistics Data Set

2.2.1 SuperDARN Radars

The radars of SuperDARN in the Northern Hemisphere conform to the basic operating design of the first facility which was built at Goose Bay in 1983. A detailed description of the Goose Bay radar has been given by Greenwald *et al.* (1985). The SuperDARN radars comprise two arrays of log-periodic antennas, one is a main array of 16 antennas with both transmission and reception capability, and the other is an interferometer array of 4 antennas with reception capability only. The radar frequency could be set anywhere from 8 to 20 MHz, but most often it is set between 10 and 15 MHz.

The radars operate on a 24-hours, 365-days-a-year basis, under the control of the operating program. The operation program is separated into three types, common time, special time and discretionary time. The data used in the statistics are taken from periods when the radars were running in the common time normal scan mode (50% of the whole operation time, see Greenwald *et al.*, 1995). In the current version of common time

Radar	Affiliation	Geographic Latitude, deg	Geographic Longitude, deg	Start Date
Saskatoon	University of Saskatchewan	+52.16	-106.53	Sept. 1993
Kapuskasings	Johns Hopkins University Applied Physics Laboratory	+49.39	-82.32	Sept. 1993
Goose Bay	Johns Hopkins University Applied Physics Laboratory	+53.32	-60.46	June 1983
Iceland-West	Centre National de la Recherche Scientifique	+63.86	-22.02	Oct. 1994
Iceland-East	University of Leicester	+63.77	-20.54	Nov. 1995
Finland	University of Leicester	+62.32	+26.61	Feb. 1995

Table II-2.1: Location and affiliation of the Northern Hemisphere SuperDARN radars used in the statistics.

normal scan mode the radars carry out azimuthal sweeps through discrete beam pointing directions that are numbered 0-15 with a step in azimuth of approximately 3.2° . It takes approximately 7 s to integrate backscatter returns in one direction and about 2 min are needed to complete all directions. In general, 75 range gates are sampled for each beam with a pulse length of $300 \mu\text{s}$, which is equivalent to a gate length of 45 km, and a lag to the first gate of $1200 \mu\text{s}$ (180 km). In this configuration the maximum range of the radars is approximately 3550 km. Hence the radar field-of-view in each scan contains 1200 cells ($75 \text{ ranges} \times 16 \text{ beams}$).

2.2.2 Statistics Data Set

Eight SuperDARN radars are currently under operation in the Northern Hemisphere (their fields-of-view are shown in Figure II-2.1). The Kodiak and Prince George radars started operation in the beginning of 2000. We used the data from six Northern Hemisphere SuperDARN radars, Saskatoon, Kapuskasing, Goose Bay, Iceland-West, Iceland-East and Finland (listed in Table II-2.1, shaded fields-of-view in Figure II-2.1). The study period encompassed 39 months from July 1995 to September 1998, which corresponds to the most recent period of solar cycle minimum. All radars except for Iceland-East started operation before July 1995. In the case of Iceland-East, the use of the data is limited to 35 months because this radar has been operational only since mid-November 1995. The number of days used in the statistics is approximately 15 days in each month.

2.3 Method of Statistics

2.3.1 Data Selection

The purpose of this study is to reveal the spatial distribution of FAIs in the subauroral F region. In particular, we aim at a detailed understanding of the morphological feature, the source region, and the formation process of DUSE. Hence, we need to deal with reliable echoes from F region FAIs. The main targets of the SuperDARN HF radars are the F region FAIs. The radars, however, also receive backscatter echoes from E region FAIs and from the ground as well as ghost scatter that is due to radio interference. We must exclude these echoes from the scattering occurrence statistics. In the SuperDARN observations, the radar echoes whose range is less than 600 km are regarded as being due to E region scatter, while echoes returned from ranges larger than 900 km are considered to be due to F region scatter (Ruohoniemi *et al.*, 1988). Hence data obtained from ranges greater than 900 km are taken in the statistics. Echoes that are considered to be ground scatter are excluded on the

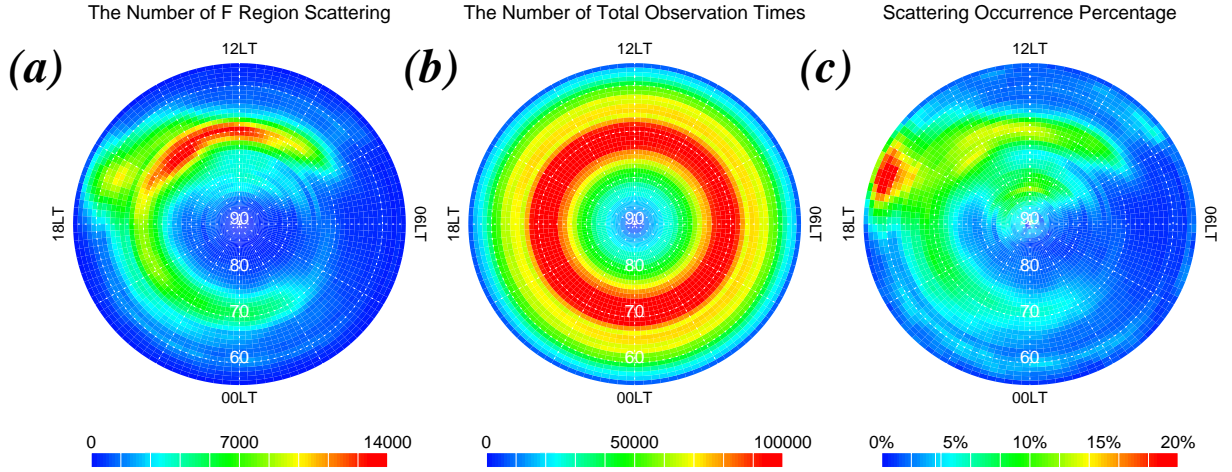


Figure II-2.2: (a) Total number of F region scattering in January between 1996 and 1998 as mapped into the geographic coordinate system. (b) Total number of observation times during the same period as (a). (c) Scattering occurrence percentage obtained by dividing values of (a) by those of (b).

basis of their line-of-sight velocity magnitude and spectral width (criteria is $V_{\text{los}} < 30 \text{ m s}^{-1}$ and spectral width $< 30 \text{ m s}^{-1}$). Finally, we remove the echoes which do not have sufficiently strong signal ($< 3 \text{ dB}$ signal-to-noise ratio) in order to eliminate much of the ghost scatter due to radio interference. Consequently, we constructed a database of F region FAIs which is uncontaminated by E region scatter, interference, or groundscatter.

2.3.2 Scattering Occurrence Percentage

After the noise reduction process described above, velocity data of the radars are mapped into both geographic (geographic latitude/local time) and magnetic (magnetic latitude/magnetic local time) coordinate systems. Here, Altitude Adjusted Corrected Geomagnetic Coordinates (AACGM) coordinate system (based on the work of Baker and Wing, 1989) is used to calculate magnetic latitude and magnetic local time. We sorted the filtered data into $1^\circ \times 3^\circ$ latitude/local time bins, indexed by (i, j) , in both coordinate systems for each month period. Then, we can compute the total number of F region scattering, $N_{\text{fai}}(i, j)$, and the total number of observation times, $N_{\text{obs}}(i, j)$, in each bin. The following formula provides the scattering occurrence percentage, \mathfrak{R} , in each coordinate system,

$$\mathfrak{R} = \frac{N_{\text{fai}}(i, j)}{N_{\text{obs}}(i, j)} \times 100$$

Figure II-2.2 (a) and (b) show the distribution of the total number of F region scattering, N_{fai} , and the total number of observation times, N_{obs} , respectively, which are deduced from the data of six Northern Hemisphere radars collected in January between 1996 and 1998. Figure II-2.2 (c) shows the scattering occurrence percentage, \mathfrak{R} , calculated by dividing the values of (a) by those of (b). The scattering occurrence distribution in the magnetic coordinate system is obtained by the same procedure. In the next section, we will show the monthly scattering occurrence percentage in both coordinate systems and discuss the relationship with several boundaries of plasma density in the subauroral F region. As will be described in more detail later, we relate our results to the morphology of the midlatitude trough, whose location depends on solar zenith angle (which is best described in a geographic coordinate system), and the position of the auroral oval (best described in geomagnetic coordinate). For this reason, we find it useful to plot our scattering occurrence statistics in both geographic and geomagnetic coordinate systems.

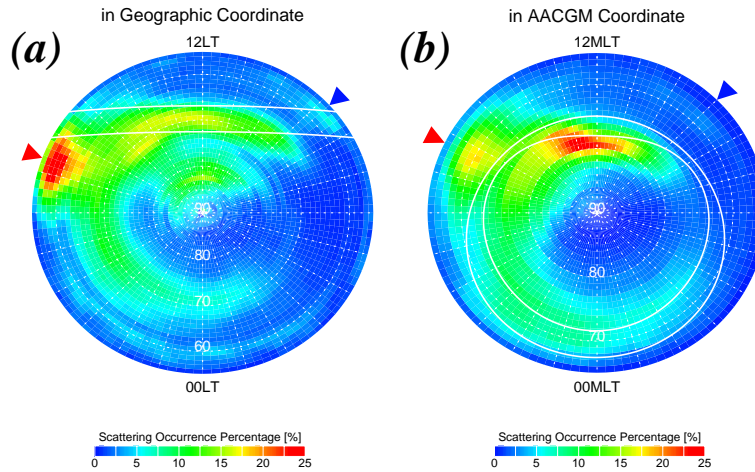


Figure II-2.3: Scattering occurrence percentage of all six radars in January between 1996 and 1998: (a) as mapped into the geographic coordinate system and (b) as mapped into the magnetic coordinate system (AACGM coordinates). In panel (a), two white lines represent the points where the solar zenith angle is equal to 90° at the start of the month and the end of the month. In panel (b), two white circles indicate the equatorward and poleward edge of the auroral oval (Feldstein and Starkov, 1967) as modeled by Holzworth and Meng (1975) for $Q = 1$ (quiet conditions).

2.4 Statistical Results

2.4.1 Statistical Signature of DUSE

Figure II-2.3 shows the scattering occurrence percentage mapped into (a) a geographic coordinate system (55° - 90°) and (b) a magnetic coordinate system (65° - 90°). These results are deduced from the observation of six Northern Hemisphere radars in January between 1996 and 1998.

In the geographic coordinate system (panel (a) of Figure II-2.3), two white lines represent the points where the solar zenith angle (SZA) is equal to 90° at the start of the month and the end of the month. A distinct peak in the scattering occurrence ($\approx 25\%$) is found in the eveningside of dusk as defined by the SZA 90° lines. This peak extends from 1530 LT to 1730 LT (the center of the peak is indicated by a red triangle) and its latitudinal location ranges from 55° to 65° . Another peak is seen around the dawnside SZA 90° lines (indicated by a blue triangle), whose latitudinal location also ranges from 55° to 65° . Its occurrence percentage is, however, smaller ($\approx 7\%$) in comparison with that in the dusk side, which suggests that there exists a marked asymmetry of the FAI occurrence between sunrise and sunset.

In the magnetic coordinate system (panel (b) of Figure II-2.3), two white circles indicate the equatorward and poleward edges of the auroral oval (Feldstein and Starkov, 1967) as modeled by Holzworth and Meng (1975) for $Q = 1$ (quiet conditions). A peak of scattering occurrence rate ($\approx 18\%$) is seen in the dusk meridian between 1500 MLT and 1800 MLT (the center of the peak is indicated by a red triangle). The magnetic latitudes of the peak in the dusk meridian are slightly lower than the equatorward edges of the auroral oval and coincide with the regions of density depletion called the midlatitude trough (Spiro *et al.*, 1978; Moffett and Quegan, 1983; Rodger *et al.*, 1992).

Furthermore, a weak enhancement of scattering occurrence ($\approx 4\%$) is also seen between 0800 MLT and 1000 MLT on the dawnside (indicated by a blue triangle). The magnetic latitudes of the peak are lower than the Feldstein oval, however, there is a little offset between the magnetic latitudes of the dawnside activity and those of the equatorward edge of the oval (about 5° in magnetic latitude). The model of the midlatitude trough

by Collis and Haggstrom (1988) and the two-dimensional electron density profile reported by Holt *et al.* (1983) suggest that the magnetic latitudes of the midlatitude trough have a dawn/dusk asymmetry, i.e., the latitudes of the dawnside trough are relatively lower in comparison with those of the dusk side trough. This feature of the trough might cause the offset between the latitudes of the dawn activity and those of the Feldstein oval.

Ruohoniemi *et al.* (1988) reported that DUSE appears when the solar zenith angle ranges between 95° and 105° . It was also pointed out that the source of DUSE lies in the midlatitude trough. The statistical features of the peak in the dusk sector in Figure II-2.3 satisfies these conditions, which means that we can discuss the morphology of DUSE using the statistics of the scattering occurrence. Furthermore, the activity around sunrise (hereinafter called “dawn scatter event” and referred to as DASE) is one of the new results found in this analysis, which has not previously been discussed.

Another clear peak is seen in the local noon sector (0900-1600 MLT) between 76° and 82° latitudes (panel (b) of Figure II-2.3), which is considered to be associated with the cusp region and has already been reported by Ruohoniemi and Greenwald (1997) and Milan *et al.* (1997). Radar echoes in this region are characterized by broad Doppler spectral width (Baker *et al.*, 1990; Baker *et al.*, 1995; Rodger *et al.*, 1995; Yeoman *et al.*, 1997; Milan *et al.*, 1998; Milan *et al.*, 1999). It is worth pointing out that DUSE and DASE are more prominent for mapping in geographic coordinates, while the cusp scatter feature is more prominent in geomagnetic coordinates. This suggests that the degree of solar EUV influence on DUSE and DASE is stronger than that on the cusp echoes. The characteristics of cusp scatter are still an open question. However, our interest here is primarily in the behavior of the subauroral FAIs, thus we do not discuss the enhancement of scattering occurrence around cusp in this chapter.

2.4.2 Feature of the DUSE in Each Radar

In the previous section, we have shown that the peak of scattering occurrence, which is regarded as the statistical signature of DUSE, appears around sunset within the midlatitude trough. However, we have not ascertained whether or not this is a common feature among the Northern Hemisphere SuperDARN radars. Here we investigate the scattering occurrence distribution of each Northern Hemisphere radar individually and confirm that DUSE is a feature that is commonly observed by all radars.

Figure II-2.4 shows the scattering occurrence percentage of each radar in January between 1996 and 1998 as mapped into the magnetic coordinate system. Two white lines indicate the Feldstein oval during quiet periods. In all panels, there exists a peak of scattering occurrence around dusk meridian (between 1500 MLT and 1800 MLT; the center of the peak is indicated by a red triangle) outside of the auroral oval, which confirms that DUSE is a common feature of the Northern Hemisphere SuperDARN radars. However, the percentage of the peak region is different among the radars. The maximum percentage is obtained in Kapuskasing ($\approx 25\%$) and the minimum percentage is in Finland ($\approx 15\%$). DUSE is more pronounced for Kapuskasing and Goose Bay. Thus there exists a clear UT effect in the characteristics of DUSE, such that the activity of DUSE is more pronounced for universal times corresponding to dusk on the prime magnetic meridian (0° longitude). We can identify the universal times where the activity of DUSE is most intense as a function of season. DUSE is more pronounced during UT times between 0100 UT and 0300 UT in summer, and 2200 UT and 2400 UT in winter.

There could be several reasons for this dependence. One is an actual UT dependence in the intensity of irregularity formation in the dusk sector, which might be caused by a UT dependence in the background ionization level or convection electric field. Or it might be due to a propagation effect. That is, the ray-path or aspect condition is more favorable for the scattering within the subauroral F region in the case of Kapuskasing

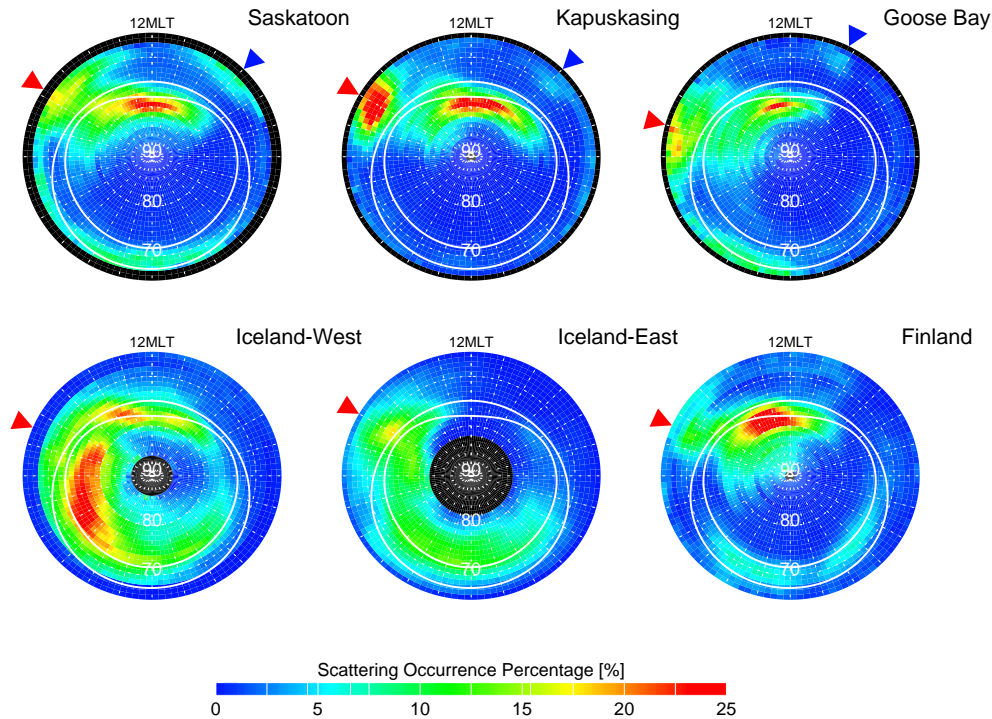


Figure II-2.4: Scattering occurrence percentage of each radar in January between 1996 and 1998 as mapped into the magnetic coordinate system. Two white lines indicate the poleward and equatorward edge of the Feldstein oval as before.

and Goose Bay, which is probably because the relationship between the magnetic field configuration and vertical plasma density profile is more suitable for scattering in these magnetic longitudes. The geographic latitudes of the Kapuskasing and Finland radars differ by 13° (49.3° versus 62.3°), which suggests that the level of background ionization at dusk will be higher at Kapuskasing. The density gradients associated with solar EUV radiation will also be stronger at Kapuskasing. These differences might cause the UT dependence in the activity of DUSE through their influence on irregularity formation or propagation condition.

Another peak around sunrise, which is identical to DASE, is seen in the Canadian radars (Saskatoon, Kapuskasing and Goose Bay), the center of the peak being indicated by a blue triangle. On the other hand, non-Canadian radars cannot observe it. Even for the Canadian radars, DASE does not appear until fairly late in the morning, which suggests that it takes a while for background ionization levels or density gradient to build up to some level in the dawn sector. For the non-Canadian radars, ionization and density gradient might not reach this level in January, which could cause the absence of DASE for them. The Iceland-West radar has echo characteristics different from the other radars. For example, the scattering occurrence is strongly enhanced in the domain poleward of the dusk side auroral oval, which is not seen in the other radars. We suppose that this difference is due to the beam direction of Iceland-West. As shown in Figure II-2.1, Iceland-West radar is directed considerably westward, which may affect the enhancement of scattering occurrence poleward of the auroral oval.

Figure II-2.5 shows range-time-parameter plots of the line-of-sight Doppler velocity observed by the six Northern Hemisphere radars on November 1, 1997. Only the data with backscattered power greater than 3 dB are shown. The gray area indicates ground scatter region. The level of geomagnetic disturbance is relatively quiet during this period (the Kp index ranged from 1+ to 2 over 1200-2400 UT). During this day, all six radars observed the echoes regarded as DUSE, which is enclosed by red squares in each panel. DUSE in Figure II-2.5

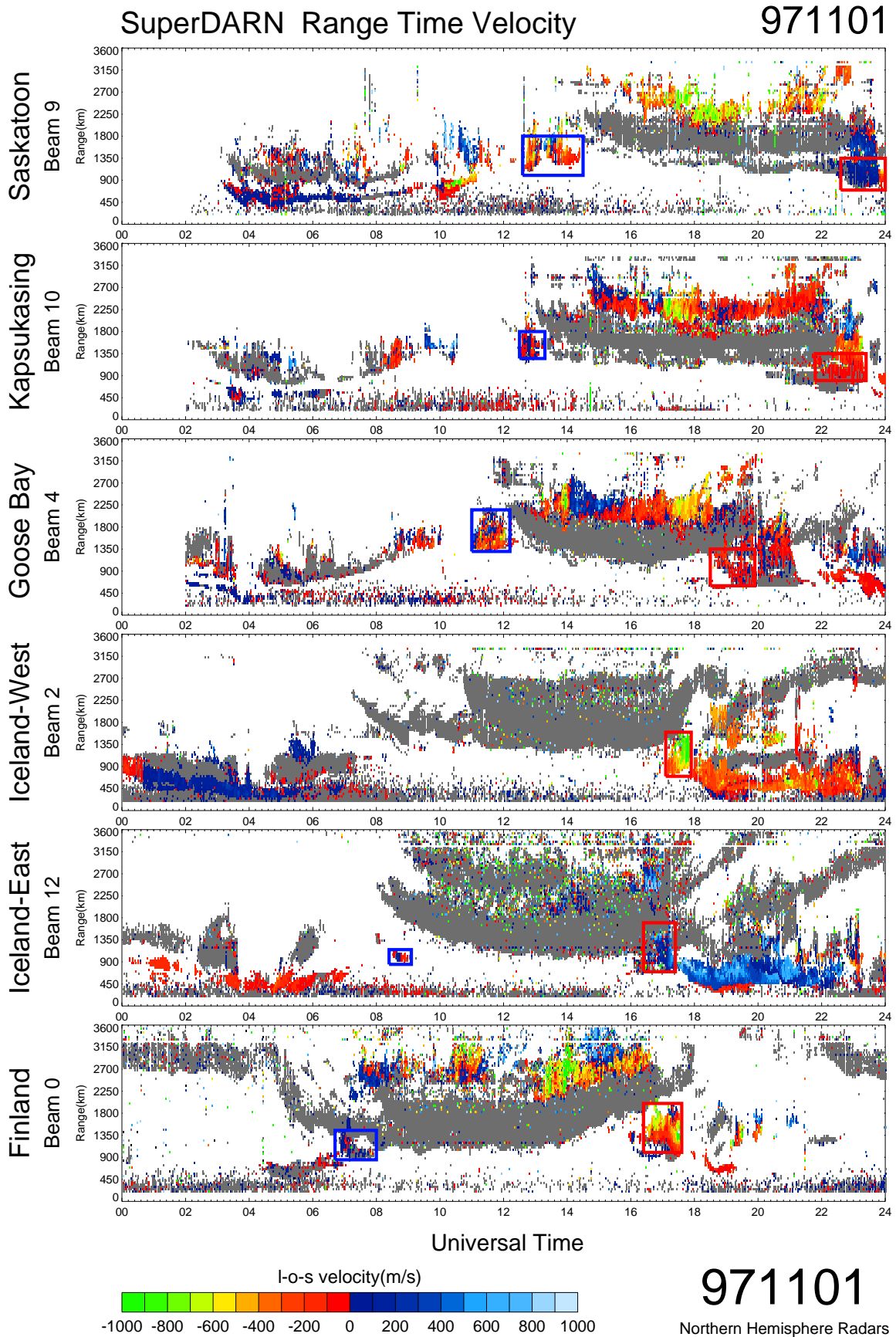


Figure II-2.5: Range-time-parameter plots of the line-of-sight Doppler velocities observed by the six Northern Hemisphere radars on November 1, 1997. DUSE is indicated by a red square in each panel and DASE indicated by a blue square.

present the clearest example from the period of our study. The UT of the DUSE increased systematically with increasing westward longitude beginning with Finland radar. The Canadian radars (Saskatoon, Kapuskasing and Goose Bay) observed the clear signature of DASE, which is enclosed by blue rectangles. Iceland-East and Finland radars also observed some dawn activity regarded as DASE around 0800 UT. However, the signature of DASE in Iceland-East and Finland is rather weak, which is not intense enough to be identified in our statistical analysis. The UT of the DASE also increased from Finland to Saskatoon with increasing westward longitude. These characteristics of DUSE and DASE agrees with the statistical results shown in Figure II-2.4. After all, the signature of DUSE and DASE in our statistics is most clearly seen in the Canadian radars (Saskatoon, Kapuskasing and Goose Bay). After this, we discuss the scattering occurrence statistics deduced from the Canadian radars.

2.4.3 Seasonal Variation of DUSE

All statistical results presented in the previous section are derived from the observations in winter. The morphological characteristics of DUSE during winter have already investigated by Ruohoniemi *et al.* (1988) in detail. They, however, did not detect DUSE during summer, so the morphology of DUSE during summer should be examined. In general, the midlatitude trough in the dusk sector extends equatorward with increasing local time in accordance with the shape of the auroral oval (Collis and Haggstrom, 1988; Rodger *et al.*, 1992; Hargreaves and Burns, 1996). Thus, the cross section of the midlatitude trough at sunset also moves equatorward during summer, which could be the reason why SuperDARN Goose Bay radar cannot observe DUSE in summer (Ruohoniemi *et al.*, 1988). Here we present the monthly scattering occurrence distribution deduced from the Canadian radars and clarify the seasonal variation of DUSE. Since the fields-of-view of Saskatoon and Kapuskasing radars are located at slightly lower latitudes than that of Goose Bay, it is expected that the signature of DUSE may be found even in summer.

Figure II-2.6 (a) shows the maps of monthly scattering occurrence percentage as a function of geographic latitude and local time, which are derived from the data of Canadian radars. As noted above, two white lines represent the points where the solar zenith angle is equal to 90° at the start of the month and the end of the month. The scattering occurrence percentage peaks in the lower latitude region within a few hours of local time on the eveningside of the SZA 90° lines. This tendency is found throughout the year, and the peak moves with the SZA 90° lines month by month. Scattering occurrence percentage in this area reaches its maximum in both winter and summer ($\approx 25\%$), with a minimum in spring ($\approx 17\%$). The occurrence of DUSE is rivaled only by that of the cusp feature in winter, which indicates that DUSE is one of the most reproducible features in the radar observations. The latitudinal width of the peak region is large in winter (from 55° to 70°) and small (from 55° to 62°) in summer. On the other hand, the longitudinal scale is wide in summer and narrow in winter. During winter months (November, December and January) there is a weak enhancement of scattering occurrence, whose occurrence rate is less than 7%, around the SZA 90° lines between 0800 LT and 1000 LT.

Figure II-2.6 (b) shows maps of monthly scattering occurrence rate as a function of magnetic latitude and magnetic local time, which is deduced from the same dataset as that used in Figure II-2.6 (a). In all months, a clear peak of scattering occurrence is seen in the dusk meridian whose magnetic latitude is slightly lower than the equatorward edge of the auroral oval. These peak regions are considered to be the same as those seen around sunset in the geographic coordinate system. In addition, a weak peak of scattering occurrence is also seen in the dawn side around 0900 MLT in the winter months. Overall, we find that the characteristics of DUSE in summer are the same as those in the other seasons; i.e., the statistical signature of DUSE is located on the

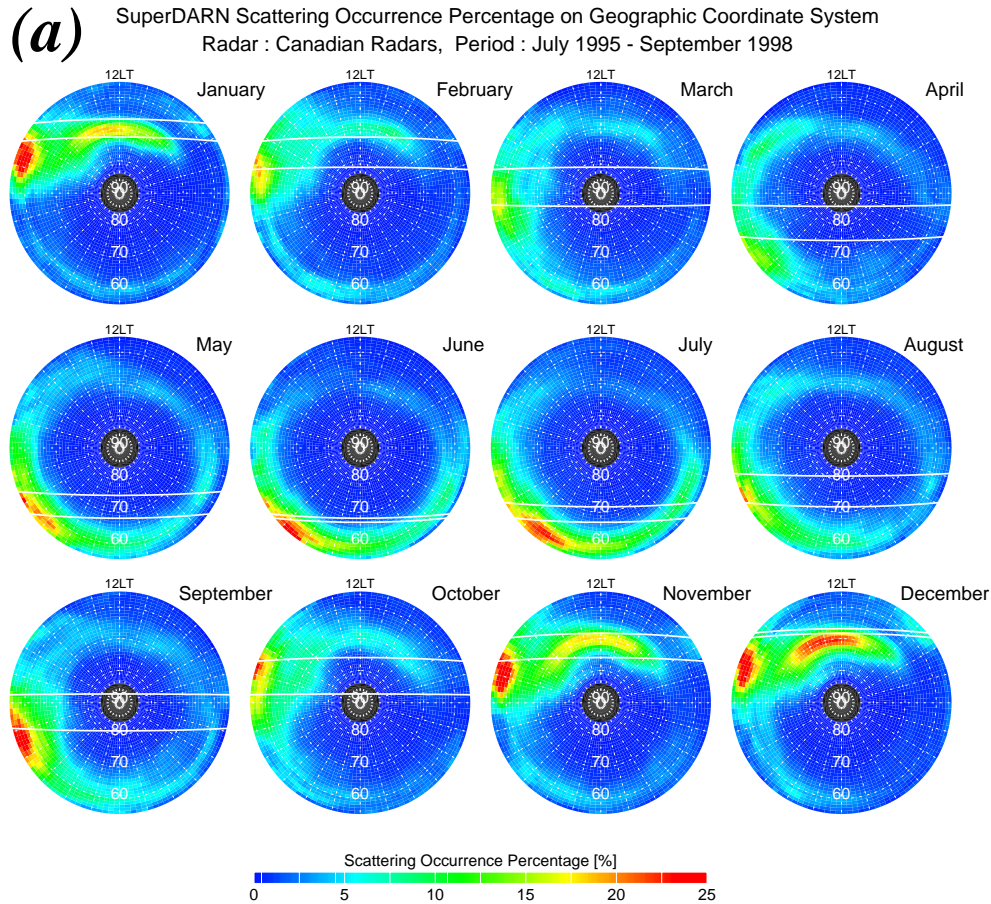


Figure II-2.6: Monthly scattering occurrence percentage as a function of (a) geographic latitude and local time and (b) magnetic latitude and magnetic local time (AACGM coordinates).

eveningside of the SZA 90° lines within the midlatitude trough throughout the year.

2.4.4 Relationship with the Sunward Edge of Trough

Our statistical analysis confirmed the basic feature of DUSE reported by Ruohoniemi *et al.* (1988), especially the relationship between DUSE and the latitudinal location of the midlatitude trough. The midlatitude trough is primarily a nightside phenomenon, though it extends into the dawn and dusk sectors (Rodger *et al.*, 1992). Halcrow and Nisbet (1977) investigated the data from low-altitude satellites and reported that the duskside and dawnside ends of the midlatitude trough in the longitudinal direction (hereafter this boundary is termed the sunward edge of the trough) are controlled by the solar zenith angle and geomagnetic disturbance level as estimated by the K_p index. They constructed a model of the sunward edge of the midlatitude trough as a function of solar zenith angle and K_p index. At the sunward edge of the trough, there exists a steep plasma density gradient directed sunward.

Whalen (1987, 1989) also detected the longitudinal extent of the midlatitude trough using the global ionosonde network and clarified where the sunward edge of the trough is located, obtaining basically the same results as Halcrow and Nisbet (1977). Sojka *et al.* (1990) also demonstrated that the longitudinal extent of the midlatitude trough is controlled by the solar radiation and magnetic activity using their time-dependent ionospheric model (TDIM). In the following, we shall pay attention to the sunward edge of the midlatitude trough and investigate its relationship with DUSE and DASE, which was not considered by Ruohoniemi *et al.*

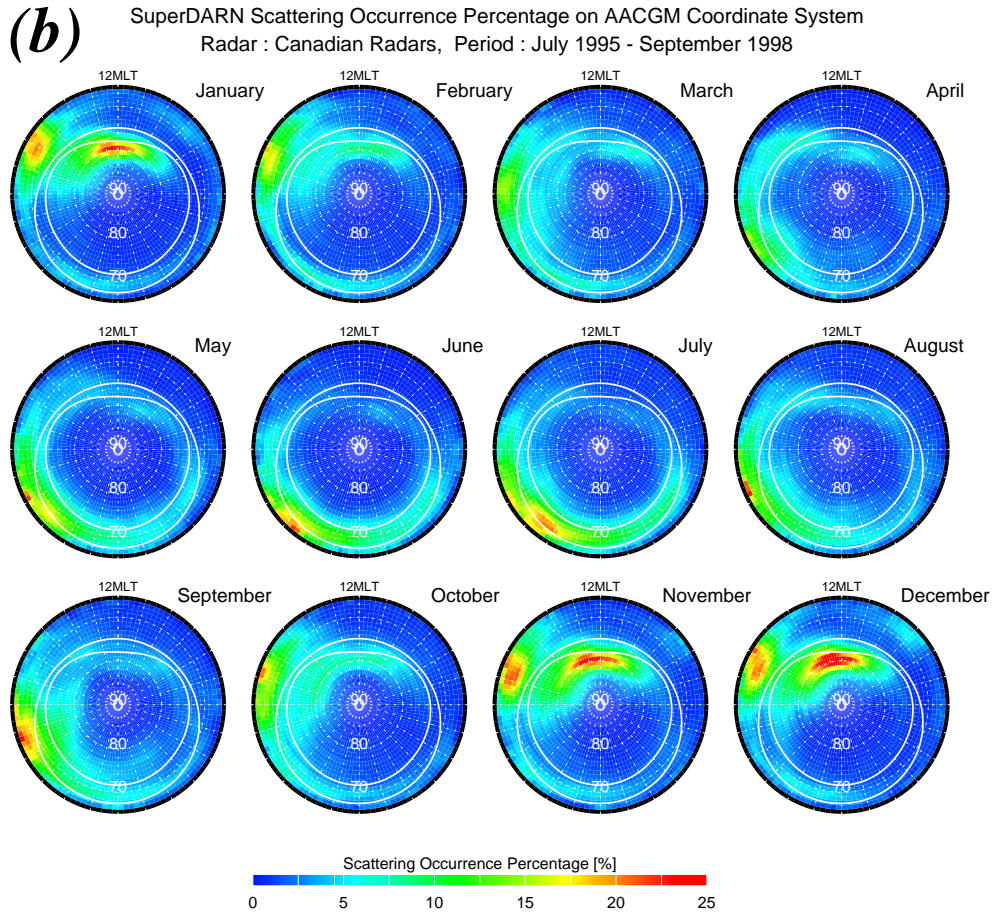


Figure II-2.6: (continued)

(1988). Here we employ the model of Halcrow and Nisbet (1977) and compare the areas where DUSE and DASE occur with the sunward edges of the midlatitude trough.

According to the model of Halcrow and Nisbet (1977), the top and bottom limits of the sunrise wall (dawnside sunward edge) are specified in terms of the solar zenith angle:

$$\text{Top : SZA} = 87^\circ$$

$$\text{Bottom : SZA} = 95^\circ$$

Here top means the point where depletion of plasma density starts, similarly bottom means the point where the plasma density decrease ends. That is, sunward electron density gradient is considered to be strong between the top and the bottom of the sunward edge. In the case of sunset, the end of the trough is quite sensitive to magnetic activity. The sunset wall of the trough (duskside sunward edge of trough) is prolonged far across the SZA 90° line during disturbed conditions. Hence it is necessary to incorporate a magnetic activity correction. Furthermore, the local time of the sunward edge is delayed by 1.5 hours compared with the dawnside.

$$\text{Top : SZA(LT} - 1.5) = 87^\circ - 3^\circ(Kp - 1/3)$$

$$\text{Bottom : SZA(LT} - 1.5) = 91^\circ - 3^\circ(Kp - 1/3)$$

The local time of the sunset edge predicted by this set of equations has to be delayed by 1.5 hours in practical use.

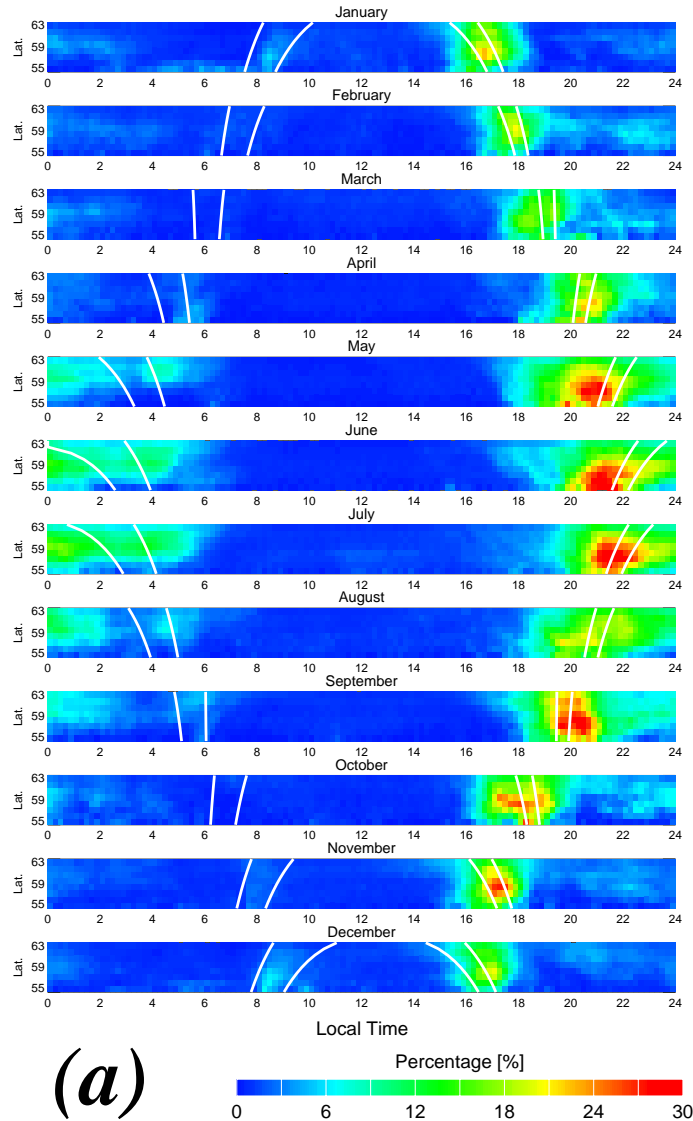


Figure II-2.7: Monthly scattering occurrence percentage as a function of geographic latitude and local time during (a) quiet condition ($0 \leq Kp \leq 1+$), (b) moderately disturbed condition ($2- \leq Kp \leq 3+$) and (c) severely disturbed condition ($4- \leq Kp \leq 9$). Two white lines indicate the top and bottom of the sunward edge of the midlatitude trough modeled by Halcrow and Nisbet (1977).

Figure II-2.7 shows the monthly scattering occurrence profile of Canadian radars (a) during quiet conditions ($0 \leq Kp \leq 1+$), (b) during moderately disturbed conditions ($2- \leq Kp \leq 3+$), and (c) during severely disturbed condition ($4- \leq Kp \leq 9$). Here, only the scattering occurrence percentages between 55° and 63° in geographic latitude are presented. Two white lines in each panel show the top and the bottom of the sunward edge of the trough modeled by Halcrow and Nisbet (1977) where Kp value is set to 0. In quiet condition (panel (a) of Figure II-2.7), it is clearly seen that peak of scattering occurrence lies in the region between the top and the bottom of the sunward edge of the trough in the dusk meridian for all months.

During moderately disturbed conditions (panel (b) of Figure II-2.7), we can find several characteristics which are not seen in quiet conditions. First, it is found that the area of higher occurrence extends to the dayside in all month periods. This signature is seen in both dawn and dusk sectors. The scale of the transition, however, is small in winter months (November, December and January). Second, the center of the scattering occurrence peak shifts equatorward in all month periods. Especially in summer, the clear peak seems to escape

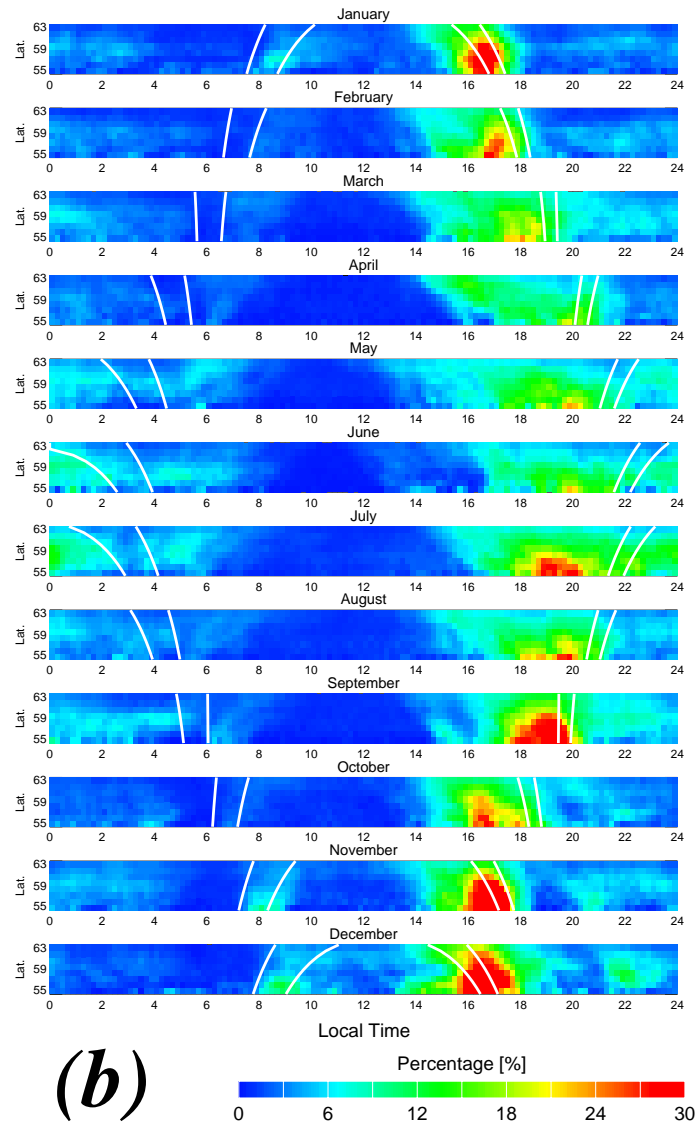


Figure II-2.7: (continued)

to latitudes below the equatorward edge of the SuperDARN fields-of-view. In severely disturbed conditions (panel (c) of Figure II-2.7), peak of scattering occurrence appears in earlier local time sectors. In addition, no clear peak of scattering occurrence is found in the periods except for winter months.

Halcrow and Nisbet (1977) and other papers treating the position of the trough (e.g., Collis and Hagstrom 1988, Rodger *et al.*, 1992 and references therein) reported that the trough appears at lower latitudes with increasing local time in the dusk sector. Since dusk occurs at later local time sectors in summer, the intersection with the trough occurs at lower latitude. Moreover, they indicated that the midlatitude trough shifts equatorward according to the shape of the auroral oval during disturbed conditions. These characteristics of the trough indicate that the intersection of sunset and the midlatitude trough is located equatorward of the SuperDARN fields-of-view during disturbed conditions in summer. This is the reason why the strong DUSE signature disappears for disturbed conditions in summer. Furthermore, the occurrence percentage of the peak during disturbed conditions is enhanced in comparison with that in quiet conditions. For example, the occurrence percentage during moderately disturbed conditions is 1.5 times of that during quiet conditions in the case of December. This increase may be due to the enhancement of plasma flow and associated electric field

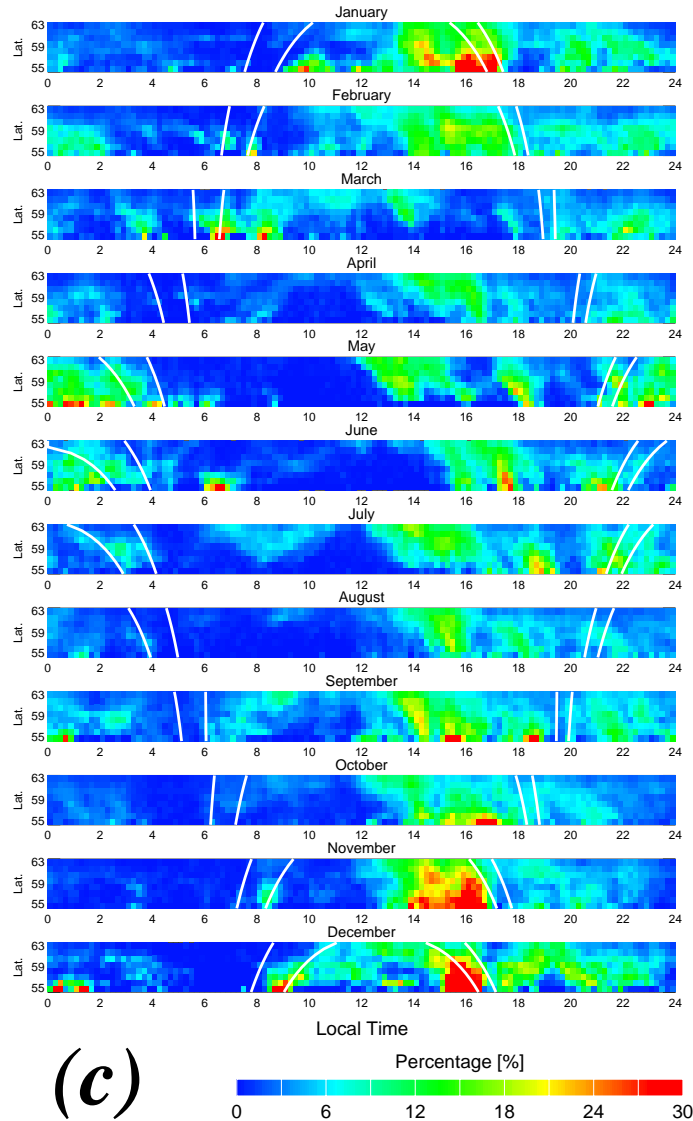


Figure II-2.7: (continued)

in disturbed conditions.

2.5 Discussion

2.5.1 Plasma Instabilities

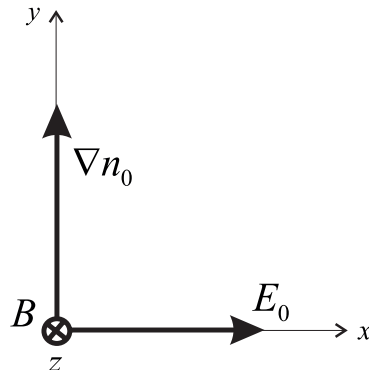
Ionospheric FAIs are density fluctuations which have been amplified in plasma instability processes such as two-stream instability, current-convective instability and gradient-drift instability (Fejer and Kelley, 1980; Keskinen and Ossakow, 1983; Tsunoda, 1988). At F region altitudes, the ion-neutral collision frequency is low, so ions and electrons move together with $\mathbf{E} \times \mathbf{B}$ drift velocity. Thus, the two-stream instability is not generated in these altitudes. The current-convective instability is often employed to explain the generation of FAIs in association with particle precipitation and field-aligned currents. In the subauroral region, however, particle precipitation and field-aligned currents are not so significant. Hence the gradient-drift instability is considered to dominate the generation of FAIs in the subauroral F region ionosphere.

A schematic diagram of the gradient-drift instability is described in Figure II-2.8. If the plasma density gradient is directed in the y direction, an applied background electric field in the x direction, and the geomagnetic

Linear Growth Rate of Gradient Drift Instability

$$\gamma \propto \frac{V_0}{L}$$

$$V_0 = \frac{E_0}{B}$$

$$L = \frac{n_0}{\nabla n_0}$$


B : Geomagnetic field
*n*₀ : Background plasma density
*E*₀ : Electric Field in the plane perpendicular to *B*
L : Density gradient scale length

Figure II-2.8: Schematic illustration of the gradient-drift instability.

field in the $-z$ direction, the plasma is unstable and the geometry is favorable for the growth of the initial plasma density perturbation. The linear growth rate of the density fluctuation γ is proportional to the plasma velocity V_0 and inversely proportional to the scale length of the background plasma density gradient, L ; i.e., $\gamma \propto V_0/L$, where $V_0 = E_0/B$, $L = n_0/\nabla n_0$. B is the magnitude of the geomagnetic field, E_0 is the magnitude of the electric field in the plane perpendicular to \mathbf{B} , and n_0 is the background plasma density. Therefore when we discuss the formation process of FAIs based on the gradient-drift instability, it is important to pay attention to the direction and amplitude of both the background electric field and the plasma density gradient.

2.5.2 Source Region of DUSE

If we consider the formation process of DUSE on the basis of the gradient-drift instability, several models could be proposed. Here we set forth three models and discuss their possibility. Schematic illustrations of the models proposed here are summarized in Figure II-2.9.

Model A.

First, we consider only the plasma density gradient produced by solar EUV radiation and the ambient electric field. The EUV-related plasma density gradient is directed sunward around sunrise and sunset. Ruohoniemi *et al.* (1988) reported that the plasma velocity associated with DUSE is about 200 m s^{-1} , which consists of sunward ($\approx 150 \text{ m s}^{-1}$) and poleward ($\approx 50 \text{ m s}^{-1}$) components. Thus the ambient electric field is mainly directed poleward in this region. The relationship between ∇n_e and E_0 is illustrated in Figure II-2.9 model A. In this scheme, the direction of the density gradient and the background electric field is favorable for the growth of FAIs. However, a plasma density gradient due to solar EUV exists at all latitudes of the polar ionosphere, which contradicts the fact that DUSE appears only at the intersection of sunset and the midlatitude trough. Moreover, the density gradient of solar EUV has no connection to the level of geomagnetic disturbance, so the dependence of the location of DUSE on the Kp index cannot be explained. Regarding the case of dawnside scatter event, solar EUV density gradient and dominant convective flow are again directed sunward, which

is also favorable for the formation of FAIs. Statistical analysis, however, revealed that there exists a strong asymmetry of scattering occurrence between dawn and dusk. The reasons listed above would be enough to discount the model A.

Model B.

Next, we choose the density gradient at the poleward edge of the trough and small eastward electric field. The midlatitude trough has a steep poleward density gradient at its poleward edge. Ruohoniemi *et al.* (1988) reported that convective drift has a small poleward component (associated electric field directed eastward) in this region. The configuration of these parameters is illustrated in Figure II-2.9 model B. In this case, the geometry is also favorable for the occurrence of the gradient-drift instability. Ruohoniemi *et al.* (1988) suggests the possibility that large-scale FAIs (more than 100 m) are generated in this process and damped into small-scale FAIs which can be observed by the SuperDARN radars. Statistical results, however, show that DUSE occurs within a few hours local time on the eveningside of sunset. If we assume that convective drift within the trough has a poleward component only around sunset, this mechanism can explain the localized appearance of DUSE. It is, however, difficult to consider that a poleward component of the convective flow is seen only at the intersection of sunset and the midlatitude trough. Hence we suppose that this formation process cannot explain the statistical results completely.

Model C.

Finally, we propose another mechanism which has not been previously considered. Regarding our statistical results, the region where DUSE occurs closely corresponds to the sunset edge of the midlatitude trough. The sunset edge of the trough has a steep plasma density gradient directed sunward. Assuming that this density gradient and sunward plasma flow are dominant within the trough, the situation is also favorable for the growth of FAIs. The geometry of these parameters is schematically described in Figure II-2.9 model C. Since the plasma density gradient employed in this model exists only within the intersection of the midlatitude trough and sunset, this mechanism has no contradiction with the statistical results.

We found out several statistical results which support this model. Our statistical study shows that DUSE in fact appears at earlier local times during disturbed condition. Halcrow and Nisbet (1977) and Whalen (1989) pointed out that the sunward edge of the trough extends further into the dayside with increasing Kp . This trough feature was also reproduced by Sojka *et al.* (1990) using the Utah state University time-dependent ionospheric model (TDIM). Such characteristics of the trough can explain the Kp dependence of DUSE activity.

Furthermore, strong asymmetry in occurrence percentage between DUSE and DASE is identified in our statistics. There could be several factors creating this asymmetry. One is the difference in magnitude of plasma density gradient between the sunrise and sunset edge of the trough. In fact, Halcrow and Nisbet (1977) indicated that the sunward plasma density gradient at the sunset edge of the trough is twice as sharp as that at the sunrise edge. The other is the difference in the occurrence of density gradient related to the trough wall between dawn and dusk. Whalen (1987) investigated the characteristics of the sunrise and sunset edges of the trough using the global ionosonde network and reported that all ionosonde stations within a specific longitude range (110° W to 75° E) principally observed the density gradient associated with the sunset edge of the trough while sites outside this range mainly observed the density gradient at the sunrise edge of the trough. They suggested that this longitude dependence arose from the offset of the geomagnetic coordinate from the geographic coordinate. Since all radars used in the statistics are well inside the longitudes between 100° W and 75° E, the longitudinal

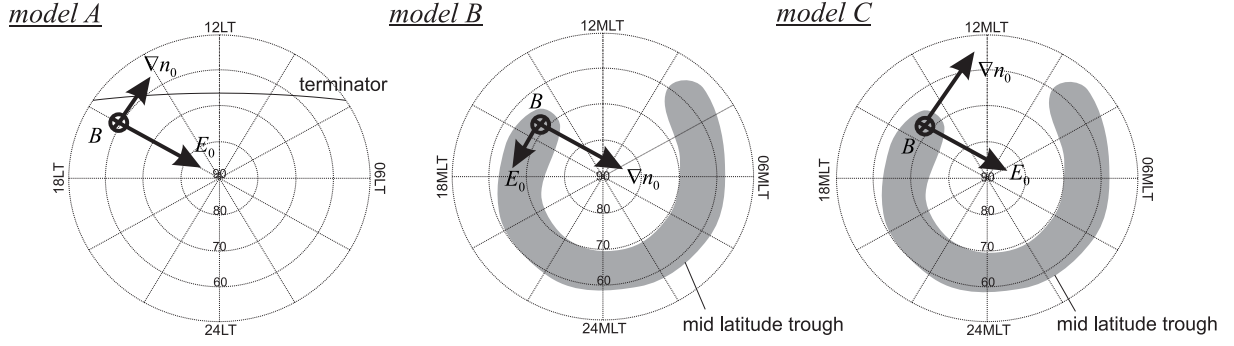


Figure II-2.9: Schematic illustration of the possible formation mechanisms of DUSE based on the gradient-drift instability.

dependence in the occurrence of density gradient could cause the occurrence asymmetry between DUSE and DASE.

Our statistical results exhibits a strong UT dependence such that the activity of DUSE is more pronounced for universal times corresponding to dusk on the prime magnetic meridian (0° longitude). The modeling result by Sojka *et al.* (1990) demonstrates that the sunward-directed density gradient at the sunset edge of the trough is steepest around the prime magnetic meridian (which corresponds to the eastern part of Canada). They showed that this dependence is also due to the offset between the geographic and geomagnetic poles. This longitude dependence of the density gradient is in good agreement with the UT dependence of DUSE activity as seen in our statistics.

2.5.3 Estimation of the Linear Growth Rate of FAIs

In this section, we estimate the linear growth rate of FAIs for all three mechanisms proposed in section 2.5.2. and determine which provides the most favorable conditions for the generation of FAIs. The linear growth rate of the plasma density fluctuation by the gradient-drift instability has already been presented in section 2.5.1. However, the formula does not contain the effect of plasma diffusion. In practice, the growth of FAIs is opposed by plasma diffusion. The complete growth rate of FAIs by the gradient-drift instability, γ_c , is

$$\begin{aligned}\gamma_c &\propto \frac{V_0}{L} - k^2 D \\ &= \frac{E_0}{B} \cdot \frac{\nabla n_0}{n_0} - k^2 D\end{aligned}$$

where k is the wave number of FAIs, and D is the diffusion coefficient. Here we use the same diffusion coefficient as that used in Ruohoniemi *et al.* (1988) for comparison,

$$D = \frac{2k_B T_e \nu_{ei} m_e}{e^2 B^2}$$

where k_B is the Boltzmann constant, and e , T_e , and m_e are the electron charge, temperature, and mass, respectively. Now we discuss the F region FAIs, so the collision frequency between electrons and ions is considered (Kelley, 1989):

$$\nu_{ei} = [34 + 4.18 \ln (T_e^3 / n_e)] n_e T_e^{-3/2}$$

These equations mean that if the complete growth rate γ_c is greater than zero, FAIs whose wave number equals to k ($\lambda = 2\pi/k$ is equivalent to the scale of the FAIs) can grow by overcoming the diffusion effect. In

	n_0 (m^{-3})	∇n_0 (m^{-4})	L (m)	V_0 (m s^{-1})	E_0 (mV m^{-1})	k_{max} (m^{-1})	λ_{min} (m)
model A	3.0×10^{11}	8.0×10^4	3750	150	9.0	0.017	370
model B	1.0×10^{11}	1.3×10^5	770	50	3.0	0.049	129
model C	1.0×10^{11}	2.4×10^5	416	150	9.0	0.114	54

Table II-2.2: Summary of the estimated parameters in the formation models of DUSE

short, large-scale FAIs are resistant to diffusion, and small-scale FAIs are easily diffused. Assuming γ_c is zero, we can obtain the maximum wave number, k_{max} and associated minimum wavelength, λ_{min} , of the FAIs which can grow in this region. Backscatter of radar radio wave \mathbf{k}_r occurs from FAIs with wave vector, \mathbf{k} , which satisfy the condition $\mathbf{k} = \pm 2\mathbf{k}_r$. Since the radar frequency is set anywhere from 8 to 20 MHz, the wavelength ($\lambda = 2\pi/2k_r$) of the FAIs which can be observed by the SuperDARN radar ranges from approximately 8 to 18 m. If the calculated minimum wavelength, λ_{min} , is shorter than 18 m, the SuperDARN radars can observe the FAIs generated directly by the gradient-drift instability.

In all models, the electron temperature T_e is set to 1.5×10^3 K as specified in the International Reference Ionosphere 1990 (IRI 90) model (Bilitza, 1990), and the geomagnetic field B is 6.0×10^4 nT (from the International Geomagnetic Reference Field 2000 model). Ruohoniemi *et al.* (1988) reported that the plasma velocity associated with DUSE is about 200 m s^{-1} , which consists of sunward ($\approx 150 \text{ m s}^{-1}$) and poleward ($\approx 50 \text{ m s}^{-1}$) components. Hence we estimate the sunward convection velocity $V_{\text{sun}} = 150 \text{ m s}^{-1}$ and poleward velocity $V_{\text{pole}} = 50 \text{ m s}^{-1}$. Assume that the plasma flows with the $\mathbf{E} \times \mathbf{B}$ drift velocity in this region, the associated electric fields are $E_{\text{pole}} = 9.0 \text{ mV m}^{-1}$ and $E_{\text{east}} = 3.0 \text{ mV m}^{-1}$.

In model A, a background electron density, $n_e = 3.0 \times 10^{11} \text{ m}^{-3}$, and gradient, $\nabla n_e = 8.0 \times 10^4 \text{ m}^{-4}$, are obtained from IRI 90 model. The calculated maximum wave number is $k_{\text{max}} = 0.017 \text{ m}^{-1}$ and minimum wavelength is $\lambda_{\text{min}} = 370 \text{ m}$. Considering model B, we assume $n_e = 1.0 \times 10^{11} \text{ m}^{-3}$ and $\nabla n_e = 1.3 \times 10^5 \text{ m}^{-4}$ at the poleward and sunset edge of the trough. These values are estimated from the result in Halcrow and Nisbet (1977). As a result, $k_{\text{max}} = 0.049 \text{ m}^{-1}$ and $\lambda_{\text{min}} = 129 \text{ m}$. In the last case, model C, input values are also obtained from the model of Halcrow and Nisbet (1977), $n_e = 1.0 \times 10^{11} \text{ m}^{-3}$ and $\nabla n_e = 2.4 \times 10^5 \text{ m}^{-4}$. The result of the calculation is $k_{\text{max}} = 0.114 \text{ m}^{-1}$ and $\lambda_{\text{min}} = 54 \text{ m}$. The results of the calculation are summarized in Table II-2.2. It is found that the background condition of model C is most favorable for the growth of FAIs in this region. The calculated minimum wavelength, however, does not match the scale of FAIs observed by the SuperDARN radars even in model C. Small-scale FAIs tend to be generated by the electron density gradients at the edges of large-scale FAIs (Tsunoda, 1988), which causes the cascade process from large-scale FAIs into small-scale FAIs. Therefore, it is suggested that the cascade process of FAIs is working also in the case of DUSE.

As claimed in the previous section, model C can explain the morphological features of DUSE completely. In particular, only this model can interpret the characteristics of DUSE during disturbed conditions, the asymmetry of FAI occurrence between sunrise and sunset, and the UT dependence of the DUSE activity consistently. Estimation of linear growth rate of FAIs indicates that model C is most favorable for the growth of FAIs responsible for DUSE. Since the density gradient at the sunrise edge of the trough and the ambient plasma convection are directed sunward, the situation is basically the same in the case of dawn scatter event. Hence we can account for the appearance of DASE assuming the model C. Finally, we can conclude that the gradient-drift instability that is driven by the sunward plasma density gradient at the sunward edge of the trough and the

ambient poleward electric field is responsible for the localized enhancement of FAIs around sunrise and sunset in the subauroral F region.

2.6 Summary

In this chapter, we have investigated the scattering occurrence of the Northern Hemisphere SuperDARN radars and estimated the spatial distribution of FAIs in the subauroral F region. We identified the morphological feature of the ‘dusk scatter event’ (DUSE, first reported by Ruohoniemi *et al.*, 1988) and clarified its relation to the boundaries of the plasma density in the subauroral F region. The findings from the statistical analysis are as follows:

1. The statistical signature of DUSE can be found in the observations of the six Northern Hemisphere radars used in this study. The scale of DUSE ranges from 20° to 30° in longitude.
2. A peak in scattering occurrence percentage associated with DUSE is obtained throughout the year. DUSE is most clearly seen around the period centered on the summer and winter solstices.
3. There exists a clear UT effect in the characteristics of DUSE, such that activity of DUSE is more pronounced for universal times corresponding to dusk on the prime magnetic meridian (0° geomagnetic longitude), which is equivalent to the UT hours from 0100 to 0300 UT in summer and from 2200 to 2400 UT in winter.
4. An enhancement in scattering occurrence is also seen around sunrise (called ‘dawn scatter event’ and termed DASE). Its percentage of scattering occurrence is rather small in comparison with that of DUSE, i.e., a clear asymmetry of FAI occurrence exists between sunrise and sunset.
5. The region where DUSE occurs is located within a few hours of local time on the eveningside of the SZA 90° line and moves with the SZA 90° lines month by month.
6. In all months, the signature of DUSE appears on the dusk meridian where the magnetic latitude is slightly lower than the equatorward edge of the auroral oval, which corresponds to the plasma density depleted structure known as the midlatitude trough.
7. The region where DUSE appears has a close relationship with the sunset edge of the trough modeled by Halcrow and Nisbet (1977). Appearance of DASE is also associated with the sunrise edge of the trough.
8. In disturbed conditions, the signature of DUSE appears at earlier local times compared with those of quiet conditions. The scattering occurrence percentage is considerably enhanced in disturbed conditions.

Three models based on the gradient-drift instability were discussed. It was found that the model which is based on the sunward plasma density gradient at the sunward edge of the midlatitude trough and ambient poleward electric field (referred to as model C in the text) is most favorable for the formation of DUSE. Consequently, we strongly suggest that DUSE and DASE are observed within the local time sectors where the sunward edges of the midlatitude trough are located.

Chapter 3

Simultaneous Measurement of Subauroral Irregularities from SuperDARN Radar and EISCAT UHF System

3.1 Introduction

In the previous chapter, we extended the work of Ruohoniemi *et al.* (1988) by analyzing the scattering occurrence percentage of the Northern Hemisphere SuperDARN radars in a statistical fashion. In all months, the dusk scatter event (DUSE) appears within a few hours of local time on the eveningside of sunset, where the magnetic latitude is slightly lower than the equatorward edge of the auroral oval. The most significant finding is that the region where DUSE occurs has a close relationship with the duskside end of the midlatitude trough in longitudinal direction (which is termed the sunward edge of the trough in this thesis), where the sunward directed steep plasma density gradient exists. It is also found that the signature of DUSE appears at earlier local time during disturbed conditions compared with those during quiet conditions. Halcrow and Nisbet (1977) pointed out that the location of the sunward edge of the trough is highly controlled by the solar zenith angle and the level of geomagnetic disturbance as estimated by the Kp index. In short, the sunward edge of the trough is located at evening side of local sunset during quiet conditions and it extends further into the dayside with the Kp index increasing. This feature is confirmed by the other observations (Whalen, 1987, 1989, 1994) and by the modeling work (Sojka *et al.*, 1990). Based on these characteristics of DUSE and the midlatitude trough, we have suggested that the electron density gradient at the sunward edge of the trough is a key parameter for the generation of DUSE and then have proposed a model of DUSE generation mechanism which is based on the gradient-drift instability.

Figure II-3.1 demonstrates a schematic illustration of the model proposed in chapter 2. The poleward and equatorward edges of the auroral oval are plotted and the gray-shaded region located just outside of the auroral oval indicates the midlatitude trough. At the sunward edge of the trough, a sunward directed, steep, density gradient exists. The model employs this sunward plasma density gradient, downward geomagnetic field and ambient poleward electric field in the subauroral region. Assuming that DUSE is produced in gradient-drift instability, the geometry of these parameters is favorable for the growth of the initial plasma density fluctuation (see Keskinen and Ossakow, 1983 in detail). This model is consistent with all statistical characteristics of DUSE during both quiet and disturbed conditions. However, the SuperDARN radars can not observe the electron density and plasma temperature in the vicinity of DUSE. Hence, we could not discuss the validity of the model in detail. In order to confirm validity of the model, we have investigated two DUSE events which had been observed by the CUTLASS Finland radar and the EISCAT UHF system simultaneously. The EISCAT mainland UHF system has a common volume with the CUTLASS Finland radar (eastern most radar of the Northern Hemisphere SuperDARN chain) and can provide background parameters of DUSE such as the two-

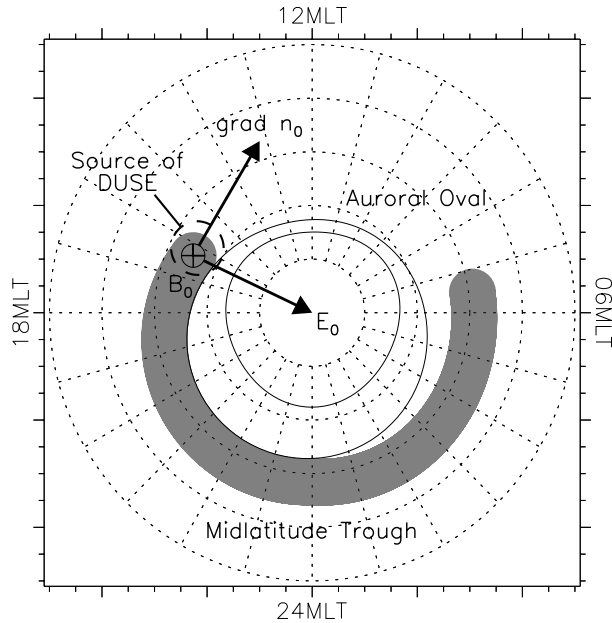


Figure II-3.1: Schematic illustration of the model proposed in chapter 2. The poleward and equatorward edges of the auroral oval are plotted and the gray-shaded region located just outside of the auroral oval indicates the midlatitude trough. Source of DUSE is shown by the dashed circle at the duskside edge of the midlatitude trough (see the text in detail).

dimensional electric field, electron density, and plasma temperature. Using these background parameters, we can closely discuss the relationship between the appearance of DUSE and the electron density gradient at the sunward edge of the midlatitude trough.

Previous studies of the trough (Knudsen, 1974; Knudsen *et al.*, 1977; Spiro *et al.*, 1978) suggested that the midlatitude trough is primarily created by an ordinary loss through recombination in darkened regions of stagnated plasma flow (stagnation trough theory). At subauroral latitudes, the atmospheric corotation and ionospheric convection compete, which produces region of stagnated plasma flow in the evening sector. Flux tubes containing F region plasma are confined to this stagnation region and spend many hours. The decay of ionization in these flux tubes then leads to the formation of the trough. Other authors (Evans *et al.*, 1983; Holt *et al.*, 1983; Providakes *et al.*, 1989) have reported that the trough is formed by an enhanced recombination in regions of rapid subauroral plasma drift through ion-frictional heating (Schunk *et al.*, 1975) (enhanced recombination trough theory). These high speed plasma drifts in the subauroral F region ionosphere could be originated from the occurrence of substorms and might correspond to a feature known as the subauroral ion drift (SAID, Galperin *et al.*, 1973; Smiddy *et al.*, 1977; Anderson *et al.*, 1991, 1993, 2001; Karlsson *et al.*, 1998). As is already noted, we have demonstrated that the local time where DUSE appears extends further into the dayside with the Kp index increasing. This feature must be discussed in relation to the proposed formation mechanisms of the trough during disturbed conditions (i.e., under the occurrence of geomagnetic substorms). Since two DUSE events examined in this paper occurred during moderately disturbed conditions (Kp index ranges from 3 to 4–), we are able to discuss this point in terms of the formation process of the trough during disturbed conditions and its association with the other substorm-related subauroral phenomena.

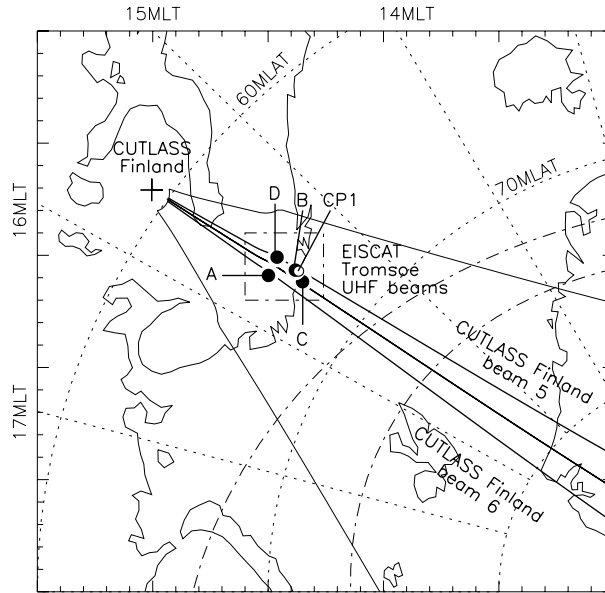


Figure II-3.2: Map showing the location of the fields-of-view of the instruments used for this study in geomagnetic coordinate system (geomagnetic latitude and magnetic local time in the AACGM coordinates) at 1320 UT. Fan-shaped area indicates the field-of-view of the CUTLASS Finland radar. White circle depicts the tristatic position of the EISCAT CP-1 mode at 278km altitude. Four black circles from A to D indicate the EISCAT CP-2 beam positions at 250km altitude. Two dot-dashed lines indicate the equatorward and poleward edges of the auroral oval (Feldstein and Starkov, 1967) as modeled by Holzworth and Meng (1975) for $K_p = 3$.

3.2 Experimental Arrangements

This chapter presents two separate intervals of simultaneous observation of DUSE from the CUTLASS Finland radar and the EISCAT UHF system. This section contains a brief description of the two radar systems and the data sets therefrom. Figure II-3.2 depicts the field-of-view of the Co-operative UK Twin Located Auroral Sounding System (CUTLASS) (Milan *et al.*, 1997) Finland radar mapped into the Altitude Adjusted Corrected Geomagnetic (AACGM) coordinate system (based on Baker and Wing, 1989) at 1320 UT. The CUTLASS Finland radar is the easternmost radar of the SuperDARN network (Greenwald *et al.*, 1995) in the Northern Hemisphere. The magnetic latitude of the Finland radar is relatively low (59.21°), which is suitable for the detection of DUSE. The radar can operate at specific frequencies between 8 MHz and 20 MHz, although the operating frequency is typically near 10 MHz, which corresponds to a wavelength of the scattering FAIs of 15 m. During both intervals of this study, the CUTLASS Finland radar was running in normal scan mode. The radar scans through 16 azimuthal beams in every two minutes and the dwell time on each beam is approximately 7 s. Each beam is separated into 75 range gates that are 45 km in length with a distance to the first gate of 180 km.

The European Incoherent SCATter (EISCAT) radars (Rishbeth and Williams, 1985) have also been employed in this work. The EISCAT UHF incoherent scatter radar facility, which operates at frequencies around 931 MHz, comprises three antennas, one sited at Tromsø, Northern Norway, which combines both transmit and receive capabilities and two remote site receivers, at Kiruna in Sweden and Sodankyla in Finland. In this study, we employed data from the EISCAT UHF common programs, CP-1 and CP-2 (e.g. Rishbeth and Williams, 1985). Specifically, we used estimates of the electron density, ion and electron temperature, and 2-dimensional electric field. In the EISCAT CP-1 mode, the beam from the UHF transmitter is aligned along the local F region magnetic field direction which is at an elevation of around 77° and a geographic azimuth of 182° . In

CP-2, the transmitter performs a four position scan, one position of which is field-aligned, another vertical and the remaining two, directed south and eastward, respectively. The dwell time for each position of the scan is 90 s, giving a total cycle of 6 min.

The locations of the F region tristatic volume for EISCAT CP-1 and the four pointing directions of CP-2 are overplotted in Figure II-3.2. White circle shows the position of CP-1 mode at 278 km altitude (magnetic latitude is 66.48°) and four black circles from A to D indicate the positions of CP-2 mode at 250 km altitude (magnetic latitude is 65.54° , 66.34° , 66.90° and 65.36° , respectively). For the field-aligned direction (CP-1 and position B of CP-2), the F region intersection volume lies within range gate 16 (corresponding radar range of 900 km) of beam 5 in the CUTLASS Finland radar field-of-view (see Davies *et al.*, 1999 for the detail). DUSE normally appears at the radar range of 600-1500 km in the field-of-view of the SuperDARN radars. Thus, the configuration of the CUTLASS Finland radar and the EISCAT UHF system is suitable for the simultaneous observation of DUSE.

3.3 Observations

As noted before, this paper presents two simultaneous observations of DUSE from the CUTLASS Finland radar and the EISCAT UHF system. One occurred on February 14th, 1996 (hereinafter referred as Event A) and the other on October 12th, 1996 (hereinafter referred as Event B). In this section, we first introduce two DUSE events observed by the CUTLASS Finland and the EISCAT UHF system. Next, we briefly check background conditions obtained from the EISCAT when DUSE does not appear in the field-of-view of the CUTLASS Finland radar for comparison. Finally, a relationship between the appearance of DUSE and the occurrence of geomagnetic substorms is examined using ground magnetic field variations obtained from the magnetometers located on the nightside.

3.3.1 CUTLASS Finland Observations

Event A : February 14th, 1996

The upper six panels of Figure II-3.3 show the set of the maps of the line-of-sight Doppler velocity illustrating the development of DUSE on February 14th, 1996. The data are mapped into the AACGM geomagnetic latitude and MLT coordinates. The closed circle indicates the field-of-view of the EISCAT CP-1 beam at F region altitudes. In the second map (1240 UT) the patch of backscatter emerges from near the coast of Scandinavia. Twenty minutes earlier (the first map: 1220 UT), there is no such activity in this area. These echoes are due to backscatter from FAIs in the ionosphere at radar ranges of 900-1300 km. In the SuperDARN observations, the radar echoes whose range is larger than 900 km are generally defined to be F region scatter, hence, these echoes are considered to be from F region FAIs. The fourth (1320 UT) and fifth (1340 UT) maps show that this scatter consolidates into a region that spans the entire range of radar azimuths. By the time of the last map (1400 UT) the scatter has disappeared on the eastern beams. The shifting continues until the image moves entirely off the western edge of the field-of-view at 1425 UT. This example illustrates the general development of DUSE. In short, the activity turns on in the space of several minutes at dusk, develops into a latitudinally confined region extending through about 1 hour in longitudinal direction, and decays by a westward movement that eventually takes it out of the radar field-of-view. The time from first appearance to complete departure is approximately 115 minutes in this case, which is slightly longer than the typical duration of 1-1.5 hours suggested by Ruohoniemi *et al.* (1988).

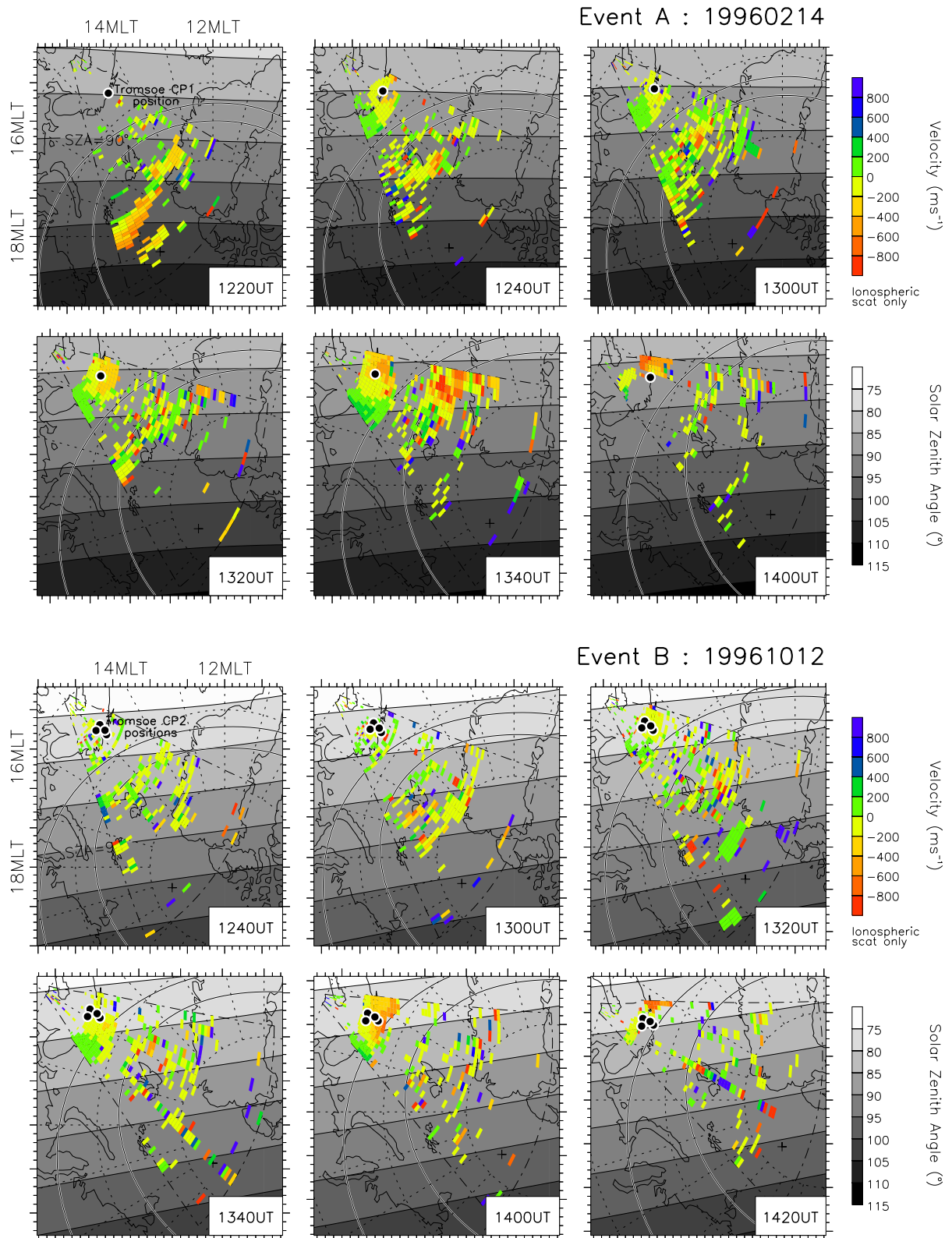


Figure II-3.3: Summary of the observations by the CUTLASS Finland radar for the two intervals of interest. The upper six panels show the set of the maps of the line-of-sight Doppler velocity illustrating development of DUSE activity for Event A (February 14th, 1996), and the lower six panels for Event B (October 12th, 1996), where motion of plasma away from the radar is negative, and toward the radar is positive. The poleward and equatorward edges of the Feldstein auroral oval (Feldstein and Starkov, 1967) as modeled by Holzworth and Meng (1975) are overplotted as $Kp = 3$ for Event A and as $Kp = 4$ for Event B. The background gray-scaled colours display the contour of solar zenith angle.

The poleward and equatorward edges of the Feldstein auroral oval (Feldstein and Starkov, 1967) as modeled by Holzworth and Meng (1975) for $Kp = 3$ (Kp value for the period 1200-1500 UT was 3+) are illustrated by the black on white lines. Ruohoniemi *et al.* (1988) pointed out that the source of DUSE is closely related to the structure of the midlatitude trough. Also in this case, DUSE appears just equatorward of the average position of the auroral oval, which is quite consistent with the previous observations. The background gray-scaled colours display the contour of solar zenith angle on the day of this event. DUSE appears for a solar zenith angle ranging 85° - 92° . Ruohoniemi *et al.* (1988) pointed out that DUSE generally occurs when the solar zenith angle is near 95° . In this case, the solar zenith angle where DUSE appears is smaller in comparison with typical DUSE events. In the previous chapter, we have indicated that DUSE appears at earlier local times (for a smaller solar zenith angle) in magnetically disturbed conditions compared with those in quiet conditions. Since geomagnetic activity during this interval was moderately disturbed, the appearance of DUSE for a smaller solar zenith angle is consistent with the characteristics of DUSE revealed in the previous chapter.

Moving now to the line-of-sight Doppler velocities in Figure II-3.3, we note that positive (negative) values represent irregularity towards (away from) the radar. Then the pattern observed at the time of the fifth panel (1340 UT) is a smooth variation from negative values ($\approx -500 \text{ m s}^{-1}$) on the most westerly beams, through zero on the most central beams, to positive values ($\approx 400 \text{ m s}^{-1}$) on the most easterly beams. Ruohoniemi *et al.* (1988) demonstrated that DUSE typically exhibits low ($\leq 200 \text{ m s}^{-1}$) line-of-sight Doppler velocities, indicative of small ($\leq 50 \text{ m s}^{-1}$) poleward drift across L-shell contours and small ($\leq 150 \text{ m s}^{-1}$) sunward drift. The Doppler velocity values obtained in this event are larger than those reported by Ruohoniemi *et al.* (1988). This difference could be due to the difference in the level of geomagnetic disturbance, which will be discussed in detail later. Finally, we note that width of the Doppler spectra is narrow ($\leq 200 \text{ m s}^{-1}$) throughout the interval, which is also consistent with the result of Ruohoniemi *et al.* (1988).

Event B : October 12th, 1996

The lower six panels of Figure II-3.3 show a set of the maps of the line-of-sight Doppler velocity on October 12th, 1996. The format is the same as the upper six panels, but in this case four solid circles indicate the fields-of-view of the four beam directions of the EISCAT CP-2 mode at F region altitudes. DUSE first appears on the eastern beams in the third map (1320 UT), then intensifies and covers all radar azimuths by the time of fourth (1340 UT) and fifth (1400 UT) map, and finally moves off the western edge of the field-of-view (sixth map: 1420 UT). This example is also consistent with the general development and disappearance of DUSE described by Ruohoniemi *et al.* (1988). The poleward and equatorward edges of the Feldstein auroral oval for $Kp = 4$ (Kp value for the period 1200-1500 UT was 4-) are overplotted as the black on white lines. Again, the poleward edge of DUSE is located at equatorward edge of the auroral oval, which is consistent with Ruohoniemi *et al.* (1988). The Doppler velocity and spectral width observed during this interval are similar to those observed in Event A. As noted before, the background gray-scaled colours display the contour of solar zenith angle. In this case, the solar zenith angle where DUSE appears is further smaller (77° - 83°) than that in Event A, which again is consistent with our statistical investigation. In this event, the time from first appearance to complete departure is approximately 65 minutes, which is shorter than that in Event A. Next, we will discuss what defines the duration of DUSE referring the observation of background parameters from the EISCAT.

3.3.2 EISCAT Observations

During the interval of Event A, CP-1 mode was running in the EISCAT mainland system and during the interval of Event B, CP-2 mode was running. The observations are summarized in Figure II-3.4 together with the latitude-time-parameter plots of the CUTLASS Finland line-of-sight Doppler velocity.

Event A : February 14th, 1996

The left top panel shows the line-of-sight Doppler velocity observed by the CUTLASS Finland radar beam 5 on February 14th, 1996. The data are plotted as a function of geographic latitude and universal time. EISCAT CP-1 mode has a F region intersection volume inside of range gate 16 of the Finland radar beam 5, which is indicated by the horizontal dashed line. The two vertical lines indicate the duration of DUSE from 1230 UT to 1425 UT. EISCAT CP-1 beam is located well within DUSE and thus is able to provide information on the background ionospheric parameters.

The observations of the EISCAT are summarized in the left middle four panels of Figure II-3.4. Altitude versus UT plots of the electron density, ion and electron temperature for the altitudes from 150 to 500 km, and single time-series of the electron density at F region altitude (300 km) are presented. In the panel of the electron density at 300 km altitude, variation of electron density derived from IRI 90 model (Bilitza, 1990) is overplotted as a background shadow. Before the onset of DUSE, the electron density seems to be controlled by the solar illumination. Soon after the onset of DUSE, the electron density starts to decrease and some 30 minutes after the disappearance of DUSE the electron density stops decreasing, which is most clearly seen in the panel of the electron density at 300 km altitude. The level of the electron density reduction is apparently larger than that estimated by the IRI 90 model. This suggests that the field-of-view of the EISCAT CP-1 beam crosses the sunward edge of the trough during the interval of DUSE. The other signature worth noting is an increase of ion temperature between 1330 UT and 1520 UT. Previous studies of the trough (e.g. Rodger *et al.*, 1992) indicated that plasma temperature is normally high within the midlatitude trough. Hence, this increase of ion temperature also suggests that the field-of-view of the EISCAT enters the midlatitude trough through its duskside edge. In general, the midlatitude trough moves equatorward with increasing MLT (Collis and Haggstrom, 1988; Rodger *et al.*, 1992). Hence the beam of the EISCAT CP-1 mode is considered to move out of the trough and enter into the auroral oval after 1520 UT when the enhancement of ion temperature ends.

The left bottom two panels display the geographic northward and eastward components of the electric field obtained from the EISCAT tristatic velocity measurements at 278 km altitude. Following the appearance of DUSE, the northward electric field starts to increase from $\approx 20 \text{ mV m}^{-1}$ to $\approx 50 \text{ mV m}^{-1}$, while there is little variation in the eastward component. Collis and Haggstrom (1988) and Haggstrom and Collis (1990) demonstrated an observation of sunward extension of the midlatitude trough with a rapid westward plasma drift and an enhancement of ion temperature. Their observation has been reproduced numerically by Namgaladze *et al.* (1996). They concluded that the sunward movement of the duskside edge of the trough is caused by an increase of loss rate through the ion-frictional heating due to an enhanced relative velocity between the ion and neutral populations (for the detail of the ion-frictional heating, see Rees and Walker, 1968; Schunk *et al.*, 1975; Schunk and Sojka, 1982). In our observation, the parameters observed by the EISCAT radar exhibit a very similar behavior to those reported by Collis and Haggstrom (1988) and Haggstrom and Collis (1990). Based on this similarity, the increase of ion temperature and the reduction of electron density in our observation seem to be a manifestation of the ion-frictional heating due to the strong northward electric field. These strong electric field signatures in the subauroral F region could be originated from the occurrence of substorm and

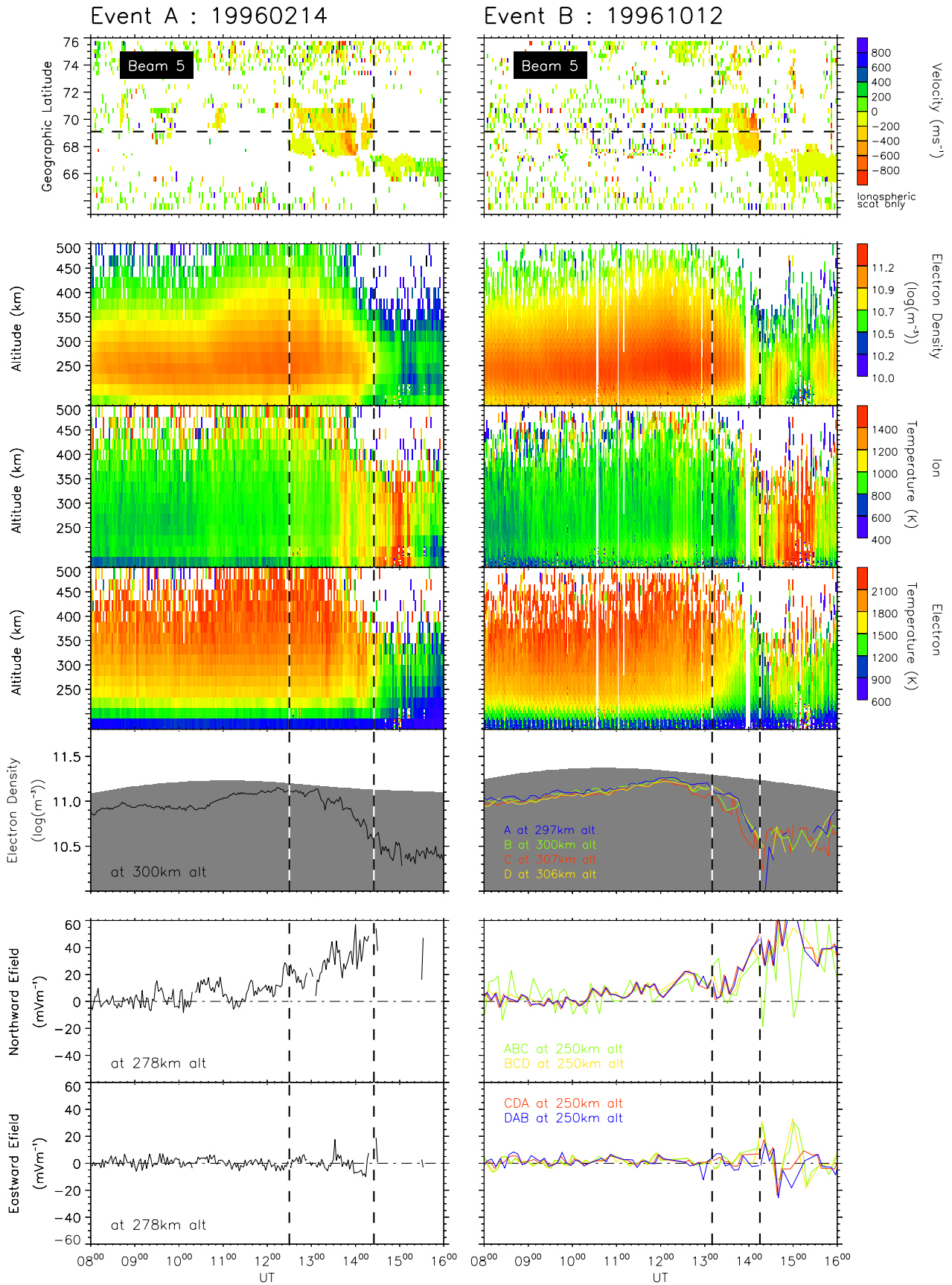


Figure II-3.4: Summary of the observations from the CUTLASS Finland and the EISCAT UHF system for Event A (left) and Event B (right). See the text in detail.

might correspond to a feature known as the subauroral ion drift (SAID, Galperin *et al.*, 1973; Smiddy *et al.*, 1977; Anderson *et al.*, 1991, 1993, 2001; Karlsson *et al.*, 1998). Detailed discussion on generation mechanism of the trough responsible for DUSE during this interval and its association with the strong northward electric field will be given later.

Event B : October 12th, 1996

The top right panel of Figure II-3.4 shows the line-of-sight Doppler velocity observed by the CUTLASS Finland radar beam 5 from 0800 UT to 1600 UT on October 12th, 1996. The format is same as before. For the field-aligned pointing beam of EISCAT CP-2 mode, an F region intersection volume lies within range gate 16 of the Finland radar beam 5, which is indicated by the horizontal dashed line. The two vertical lines indicate the duration of DUSE, which is 65 minutes from 1310 UT to 1415 UT. The fields-of-view of the EISCAT CP-2 beams are located within the region of DUSE, and hence it is again possible to compare the observations of the Finland radar and the EISCAT CP-2 mode directly.

The right middle four panels indicate the observation of EISCAT CP-2 mode during this interval, where altitude profiles of the electron density, ion temperature, electron temperature for altitude range from 150 to 500 km, and single time-series of the electron density at F region altitude are shown. Here, data from all beams of the CP-2 mode are plotted together. Electron density variation predicted by the IRI 90 model is also displayed as a shadow in the panel of the electron density at 300 km altitude. During the period of DUSE, the EISCAT observed significant decrease of electron density. Also, a clear increase of ion temperature was observed after the disappearance of DUSE. These signatures suggest that the EISCAT CP-2 beams start to encounter the sunward edge of the trough at the time of DUSE onset and after the disappearance of DUSE the EISCAT CP-2 beams are located completely within the trough. What is worth noting is that the duration of the electron density decrease is quite similar to that of DUSE, which means that the duration time of DUSE is defined by the scale of the electron density gradient at the sunward edge of the trough.

The bottom right two panels display the geographic northward and eastward components of the electric field determined by a beam-swinging technique using the data of three beams out of four CP-2 beams at 250 km altitude. During this interval, the data of the remote sites (Kiruna and Sodankyla) contain large error, then the tristatic velocity determination could not be applied. Following the appearance of DUSE, the northward electric field starts to increase from $\approx 10 \text{ mV m}^{-1}$ to 45 mV m^{-1} , while there is no considerable variation in the eastward component. The parameters observed during this event exhibit a behavior quite similar to those during Event A, which indicates that the background conditions of DUSE presented here is a reproducible feature within these local times. Again the large values of the electric field imply that the trough observed during this interval could be associated with the rapid convection in the subauroral ionosphere during substorm. A relationship of this intense electric field with the occurrence of substorm will be discussed employing data of ground magnetic field variation on the nightside in the later part of this section.

Background Parameters in the Absence of DUSE

We have examined a behavior of background parameters of DUSE and have confirmed the model proposed in chapter 2. In short, steep electron density gradient in a longitudinal direction, which corresponds to the sunward edge of the trough, has been observed in the vicinity of DUSE. But, we have demonstrated no evidence that the electron density gradient identified by the EISCAT radar is absolutely responsible for the generation of DUSE. Hence, we need to show how background parameters behave when DUSE does not appear. Figure II-3.5 displays

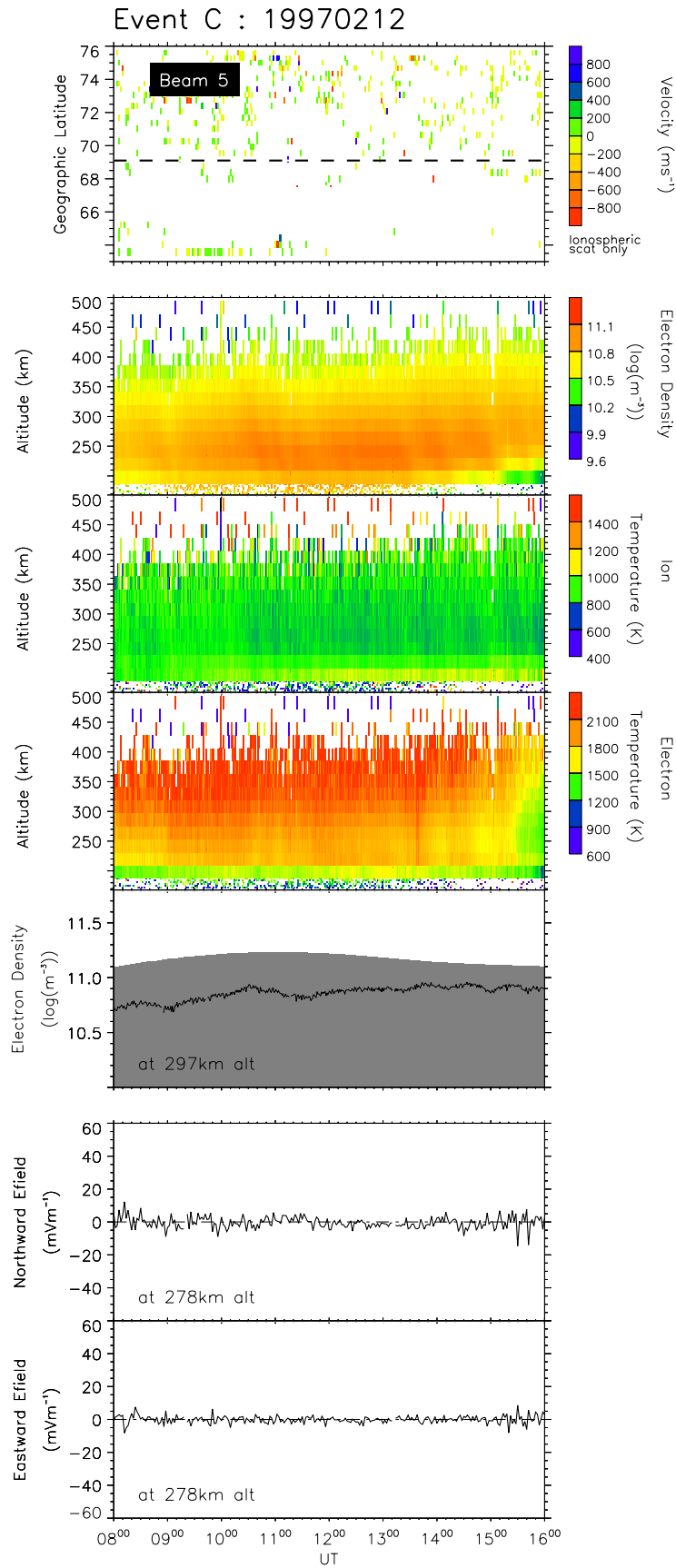


Figure II-3.5: Summary of the observations from the CUTLASS Finland and the EISCAT UHF system for Event C (February 12th, 1997), in which DUSE was not observed by the CUTLASS Finland radar.

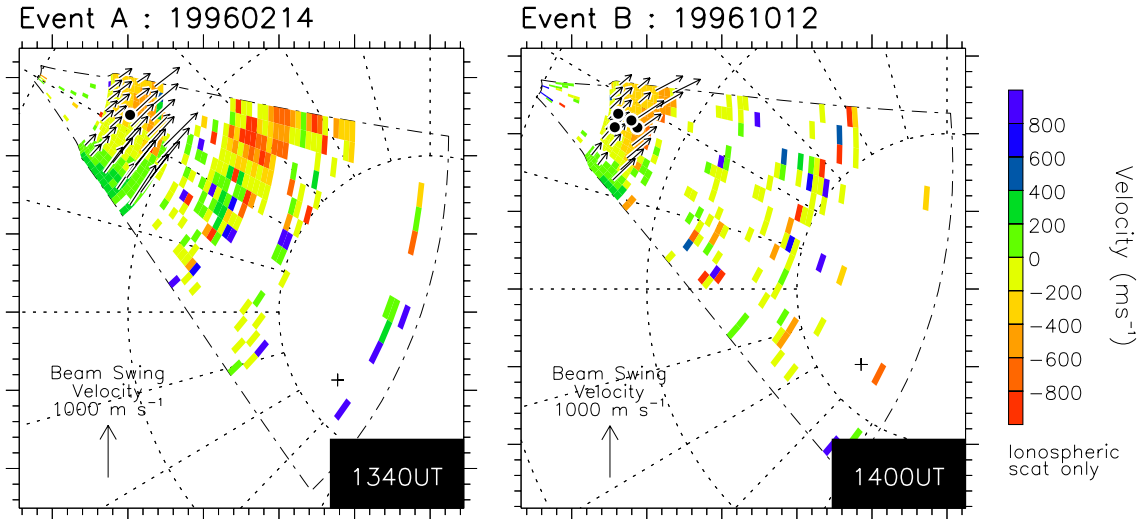


Figure II-3.6: Line-of-sight Doppler velocity measurements from the CUTLASS Finland radar for selected scans from both intervals (1340 UT for Event A and 1400 UT for Event B, respectively), superimposed on which are 2-dimensional velocity vectors estimated by applying a beam-swinging technique on the line-of-sight Doppler velocities.

observations from the CUTLASS Finland and the EISCAT UHF system on February 12th, 1997 (hereinafter referred as Event C). On this day, DUSE did not appear in the field-of-view of the CUTLASS Finland radar (see top panel of Figure II-3.5). Background parameters observed by the EISCAT UHF system CP-1 mode are displayed in the bottom six panels of Figure II-3.5 in the same format as Figure II-3.4. The observation shows that there exists no specific variation in electron density, ion temperature and electric field. This strongly suggests that the plasma density gradient and the poleward electric field observed during Event A and B play an indispensable role for the generation of DUSE.

3.3.3 Plasma Drift Observation by the CUTLASS Finland Radar

During the intervals of Event A and B, the EISCAT radar observed large northward directed electric field up to 50 mV m^{-1} in the vicinity of DUSE. Here, we compare the velocity measurement from the CUTLASS Finland radar with the electric field observation from the EISCAT radar. Purpose of this comparison is to confirm a consistency of the simultaneous observation from the radars of different scattering techniques. Figure II-3.6 displays the line-of-sight velocity measurements from the CUTLASS Finland radar for selected scans of both intervals (1340 UT for Event A and 1400 UT for Event B, respectively), superimposed on which are 2-dimensional velocity vectors estimated by a beam-swinging technique (see Ruohoniemi *et al.*, 1989; Freeman *et al.*, 1991; Milan *et al.*, 2000). When a beam-swinging technique is applied, it is assumed that the flow within each backscatter region is uniform across the field-of-view. In other word, the zonal and meridional components relative to the local L shell are constant at all points. Within the region of interest, convective flow is expected to be zonal (westward), then the estimated 2-dimensional velocities are considered to be reliable. In the same manner as Figure II-3.3, the closed circles indicate the field-of-view of the EISCAT beams at F region altitudes. There were comprehensive comparisons of the velocities obtained from the CUTLASS Finland radar and from the EISCAT radar (Davies *et al.*, 1999, 2000). The authors concluded that there is an overall reasonable correspondence between these two measurements. At the time of the scans presented in Figure II-3.6, 2-dimensional velocity determined from the line-of-sight Doppler velocity of the Finland radar is approximately

600 m s⁻¹ westward (corresponding electric field is approximately 30 mV m⁻¹ northward) within the field-of-view of the EISCAT beams, which is in good agreement with the electric field measurement by the EISCAT UHF system presented in Figure II-3.4. This good agreement supports a validity of our simultaneous measurement of DUSE using two different techniques.

3.3.4 Ground Magnetometer Observations

During both intervals of this study, the EISCAT observed an enhanced subauroral electric field in the vicinity of DUSE. In general, these high speed plasma drifts in the duskside subauroral region are connected with the occurrence of geomagnetic substorm on the nightside ionosphere. One famous signature of these high speed plasma flows associated with substorm is a feature known as the subauroral ion drift (SAID). We can not determine whether the strong northward electric field observed during the intervals of this study is the SAID or not. However, there still exists a possibility that this large electric field results from substorm activity. Here, we check the occurrence of substorm using the data of magnetometer stations from the Canadian Auroral Network for the OPEN Program Unified Study (CANOPUS) network (as described by Samson *et al.*, 1992) and discuss a relationship between the electric field enhancement and substorm activity. Figure II-3.7 shows X-component magnetograms and bandpass filtered data of the DAWS station (magnetic latitude is 65.93°) conveniently located on the nightside for the three intervals of interest.

In the case of Event A (top panel), a substorm occurs at 1120 UT (DAWS is located at 0035 MLT), which is 70 minutes before the onset of DUSE. The occurrence of the substorm is confirmed by large negative bay in the X-component and the presence of Pi2 pulsations indicating the expansion phase onset of substorm. In the case of Event B (middle panel), two substorm signatures are identified. The first substorm occurs at 1035 UT and the second at 1312 UT (DAWS is located at 2351 MLT and 0058 MLT, respectively). The negative bay in the X-component is deeper in Event B than that in Event A. This means that the level of geomagnetic disturbance is more severe in Event B than that in Event A, which is consistent with the *Kp* indices. The bottom panel shows the observation of the DAWS station during Event C in which DUSE was not observed by the CUTLASS Finland radar. There can be found no clear signature of substorm breakup, which is consistent with the lack of the large northward electric field in the duskside subauroral region and the absence of DUSE in the field-of-view of the CUTLASS Finland radar.

3.4 Discussion

3.4.1 The Model

In order to confirm the generation mechanism of DUSE proposed in chapter 2, we have investigated two examples of DUSE which had been commonly observed by the CUTLASS Finland radar and the EISCAT UHF system. As a result, when DUSE appeared in the field-of-view of the CUTLASS Finland radar, the EISCAT observed a sunward directed density gradient in the vicinity of DUSE. This density gradient was rather steeper than those created only by the solar illumination around sunset. Also, after the passage of DUSE, EISCAT observed an enhancement in ion temperature, which suggested that the EISCAT entered the midlatitude trough through its sunward edge. In addition, a strong northward electric field, which is identical to westward plasma drift, was identified during the intervals of interest. These observations show that the geometry of the background parameters around DUSE is quite consistent with the model proposed in the previous chapter.

Here, we discuss the generation of DUSE by estimating the growth rate of FAIs quantitatively. In chapter 2, we have calculated the growth rate of FAIs responsible for DUSE using values from several empirical models.

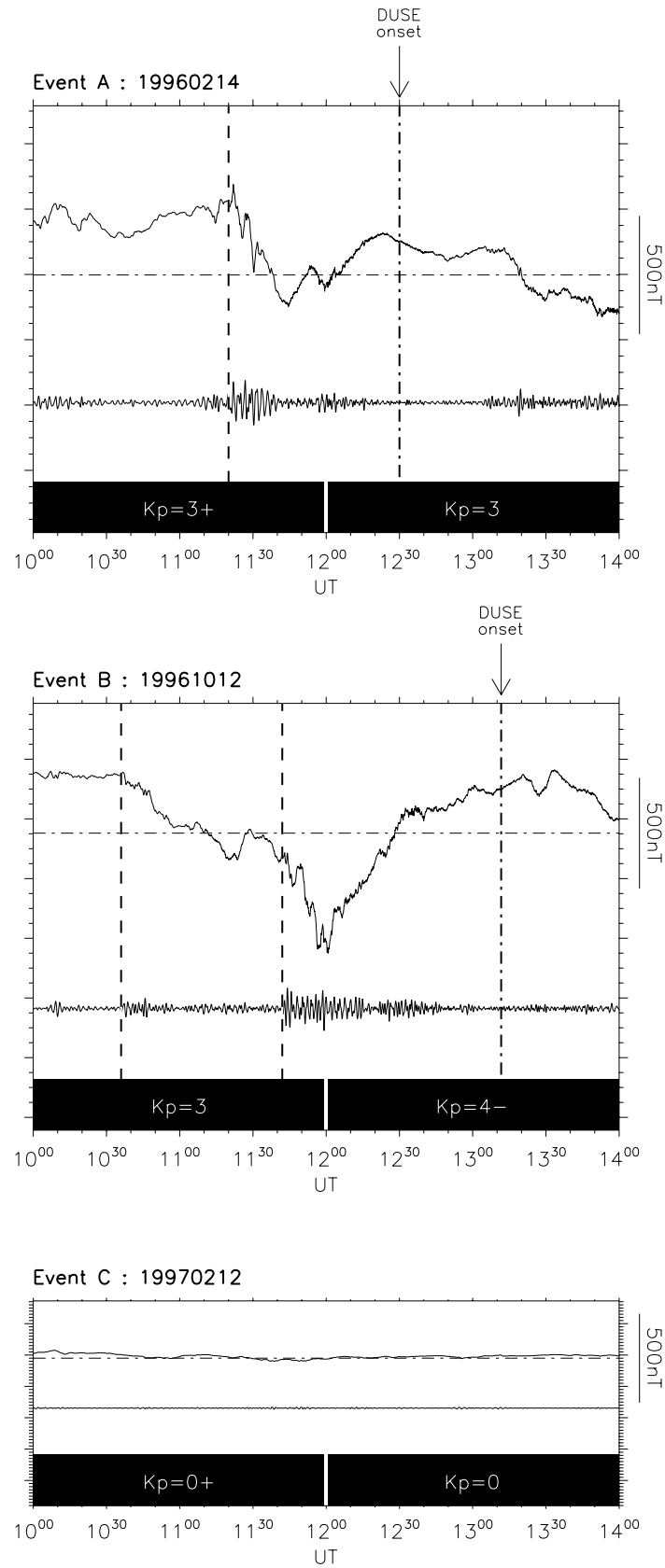


Figure II-3.7: X-component magnetograms from the DAWs station of the CANOPUS networks, along with filtered data showing Pi2 activity (scaled by a factor of 5 for clarity) for the three intervals of interest in this paper. Vertical dashed lines indicate the onset of substorm breakup and vertical dash-dotted lines the onset of DUSE.

Then, it was suggested that a cascade process of FAIs from larger scale to smaller scale is needed for the generation of DUSE. However, we could not carry out a growth rate calculation of DUSE using observed background parameters. Here, we employ the background parameters observed by the EISCAT and clarify whether the cascade process is still required or not. For comparison, we use the same equations as those used in chapter 2. For both events, the geomagnetic field is set to 4.56×10^4 nT (from the International Geomagnetic Reference Field 2000 model) as a value over Tromsø. When we calculate ∇n_e , it is assumed that the electron density variation observed by the EISCAT is predominantly spatial. In the case of Event A, calculation is carried out using observations at 1330 UT, at which $n_e = 9.37 \times 10^{10} \text{ m}^{-3}$, $\nabla n_e = 1.01 \times 10^5 \text{ m}^{-4}$ (variation in n_e between 1310 UT and 1350 UT is divided by the length of the movement of the EISCAT), $T_e = 2006 \text{ K}$, and $E = 38.5 \text{ mV m}^{-1}$, giving a maximum wave number $k_{\text{max}} = 0.151 \text{ m}^{-1}$ and minimum wavelength $\lambda_{\text{min}} = 41.54 \text{ m}$. In the case of Event B, observations at 1350 UT are used for the calculation, at which $n_e = 9.59 \times 10^{10} \text{ m}^{-3}$, $\nabla n_e = 1.53 \times 10^5 \text{ m}^{-4}$ (variation in n_e between 1330 UT and 1410 UT is employed), $T_e = 1546 \text{ K}$, and $E = 24.5 \text{ mV m}^{-1}$, giving a maximum wave number $k_{\text{max}} = 0.137 \text{ m}^{-1}$ and minimum wavelength $\lambda_{\text{min}} = 45.72 \text{ m}$. During both intervals, the calculated minimum wavelength is still larger than the scale of FAIs which can be observed by the SuperDARN radars. This result suggests that a cascade process from larger scale FAIs into smaller scale is also working during these events and, most likely, is always needed to explain the generation of DUSE.

3.4.2 Generation Mechanisms of the Trough

Both of Ruohoniemi *et al.* (1988) and the statistical study in chapter 2 pointed out that the source of DUSE lies at magnetic latitudes associated with the midlatitude trough. Previous studies proposed that the primary cause of the formation of the trough during quiet geomagnetic condition is a loss through recombination in darkened regions of stagnated plasma (stagnation trough theory) (Knudsen, 1974; Knudsen *et al.*, 1977; Spiro *et al.*, 1978). Competition between the earth corotation and ionospheric convection forms region of stagnated plasma in the evening sector. Flux tubes of F region plasma have long trajectories in darkness before being transported into sunlit and then the trough is formed by a loss through ordinary recombination in darkness. If we assume this mechanism, the sunward edge of the trough is expected to be located at the evening side of the local sunset (i.e., the trough is formed in the dark hemisphere). Since DUSE normally appears when the solar zenith angle is near 95° , DUSE during quiet condition can be explained by the stagnation trough theory.

On the other hand, the present observation demonstrated that local time where DUSE appears extends further into the dayside across the terminator during disturbed conditions. Also, the sunward edge of the trough, where a steep sunward electron density gradient exists, is shifted to the earlier local time sector together with DUSE. These features are in good agreement with the results of the statistical analysis in the previous chapter. In addition, the EISCAT UHF system observed elevated ion temperature and strong poleward electric field (up to 50 mV m^{-1}) in the vicinity DUSE. Then the question addressed here is how the sunward edge of the trough responsible for DUSE is formed at the earlier local time sector in our observations. There are at least two possible mechanisms which could contribute to this sunward extension of DUSE and trough.

One of them employs an enhanced advection of low density plasma from the stagnation region in darkness into the sunlit hemisphere by substorm-induced subauroral convection. As geomagnetic activity increases, the northward electric field in the subauroral region, which corresponds to the westward convective return flow in the dusk sector, also increases. Therefore, plasma that has been stagnated in darkness can be transported to the sunlit hemisphere across the terminator before it becomes filled in with local solar production. Sojka *et al.*

(1983) simulated the dayside extension of the trough numerically and suggested that the extension can be due to transports of low density nightside flux tubes to the sunlit region. In practice, it is difficult to estimate to what degree this effect contributes to the sunward extension of the trough only from the present observations. However, observed westward flow (1 km s^{-1} at maximum) is comparable to that used in the calculation by Sojka *et al.* (1983), which suggests that the effect of the substorm-related enhanced advection should not be ignored.

The other employs an enhanced recombination trough theory (Evans *et al.*, 1983; Holt *et al.*, 1983; Providakes *et al.*, 1989). These authors have reported that the trough is formed by an enhanced recombination in regions of rapid subauroral plasma drift associated with substorm activity through ion-frictional heating. Schunk *et al.* (1975) have numerically estimated the effect of electric field on the electron density depletion in the F region through an interaction between ions and neutrals. They have pointed out that electric field in a rest frame of neutrals $\approx 50 \text{ mV m}^{-1}$ substantially reduces electron density in the F region altitudes. For the case of Event A, electric field observation was terminated before EISCAT entered the trough. Hence, we cannot know whether the electric field within the trough is sufficient for the frictional-heating to occur. However, the electric field observation in Event B shows that there exist occasions when the northward electric field exceeds 50 mV m^{-1} (between 1440 UT and 1510 UT). During this period elevated ion temperature up to 1500 K is also observed at 300 km altitudes. Although we do not have exact information on the neutral wind velocity on that occasions, combination of the strong northward electric field and the elevated ion temperature suggests a possibility that the density depletion within the trough during our observations is connected to an enhancement of recombination caused by the ion-frictional heating. Davies *et al.* (1997) have performed a statistical investigation of the occurrence of the ion-frictional heating observed by the EISCAT UHF system. They demonstrated that the ion-frictional heating occurs predominantly in the dusk sector rather than in the dawn sector. It was also reported that the region where the heating is observed by the EISCAT gradually moves to the earlier local time sector with the Kp index increasing. These statistical results also support our suggestion that the dayside displacement of DUSE can be caused by the sunward extension of the trough due to the loss through the ion-frictional heating process associated with the fast ion drift.

3.4.3 Relationship with the Other Phenomena

We cannot decide which of the above mechanisms primarily contributes to the sunward extension of the trough in our observation. However, both of them commonly assume the existence of the enhanced electric field, which implies that the enhanced electric field is the key to explain the sunward extension of the trough and DUSE. Here we discuss the origin of this large electric field. There have been a number of observations of the rapid convective flows in the duskside subauroral region (e.g., Anderson *et al.*, 1991, 1993; Freeman *et al.*, 1992; Shand *et al.*, 1998a). Since these signatures, referred to as the subauroral ion drift (SAID) or substorm associated radar auroral surge (SARAS), were suggested to occur well after the substorm onset (most clearly seen in statistical analysis of the SAID by Karlsson *et al.*, 1998). Then, the SAID/SARAS were interpreted as indicating an ionospheric response that would be established after development of the substorm expansion (Freeman *et al.*, 1992; Anderson *et al.*, 1993, 2001). The definition of the SAID in Spiro *et al.* (1979, pp.659) is ‘the portion of the sunward flow equatorward of the auroral zone that exceeds 500 m s^{-1} ’, that of Anderson *et al.* (1991, pp.5786) is ‘westward plasma flow exceeding 1000 m s^{-1} ’, and that of Karlsson *et al.* (1998, pp.4328) is ‘poleward electric field exceeding 30 mV m^{-1} ($\approx 600 \text{ m s}^{-1}$ in these latitudes)’. Owing to the lack of the observation in the other local time sector of the subauroral latitudes, especially pre-midnight sector, we can not provide a clear evidence

that the high speed westward flow reported in this paper belongs to the category classified as the SAID/SARAS. However, there exist occasions when the northward electric field exceeds 50 mV m^{-1} ($\approx 1 \text{ km s}^{-1}$ westward drift) and the occurrence of the substorm is evidenced by a large negative bay and the presence of Pi2 pulsations in the CANOPUS magnetometers on the nightside before the onset of DUSE. These observational facts suggest a possibility that the strong electric field could be classified as the category of the SAID/SARAS.

Now we turn to discuss how the morphological feature of DUSE (degree of the sunward extension, etc.) can be utilized as a tool for estimating condition of the magnetosphere-ionosphere coupling system within the subauroral latitudes. Discussion is on the assumption that the enhanced electric field due to the SAID/SARAS type phenomenon forms the trough responsible for DUSE through the frictional-heating process. As noted in the previous section, the degree of the sunward extension of DUSE is larger in Event B than that in Event A. Furthermore, the magnitude of the geomagnetic field variation is found to be larger in Event B than that in Event A. Although we just examine the difference between these two DUSE events, however, the comparison implies that degree of the sunward movement of DUSE tells us how far the high speed convective flow associated with the SAID/SARAS penetrates into the earlier local time sector. Southwood and Wolf (1978) suggested that the SAID is generated as a result of the establishment of low-latitude shielding of substorm-enhanced electric fields. An increase in the cross-tail magnetospheric electric field induces an electric field between the inner edges of the electron and proton ring currents when their separation is small. Recently, De Keyser *et al.* (1998) and De Keyser (1999) pointed out that the SAID is ionospheric footprint of a localized intense electric field generated on a current sheet that separates the cold corotating plasma from the energetic particles penetrating into the inner magnetosphere during substorm. If we assume that the strong northward electric field detected in the present observations belongs to the SAID/SARAS, the idea proposed by De Keyser and colleagues leads us to suspect that the location where DUSE appears can be used as a diagnostic tool to estimate how far the energetic particles penetrate into the inner magnetosphere from the plasma sheet during substorm. There have been direct observations of this particle penetration close to 1800 MLT in the magnetosphere (e.g. Ejiri *et al.*, 1980). In order to know whether this speculation is true or false, a relationship between an enhancement of the subauroral electric field and particle penetration into the inner magnetosphere must be investigated in relation to the appearance of DUSE.

Stable auroral red (SAR) arc is one of the other outstanding phenomena in the subauroral ionosphere. Relationship between the SAR arc and the trough has been clearly shown by Mendillo *et al.* (1987). Foster *et al.* (1994) have demonstrated that the SAR arc is collocated with the trough and a region of enhanced westward convection of similar width. They indicated that the convection feature seen in association with the SAR arc has many of the characteristics of the SAID. These observational facts suggest that the SAR arcs are also caused by the ion-frictional heating process due to the intense electric field (possibly SAID). If we examine optical observation during the intervals of this study, DUSE might appear at the sunward edge of the visible SAR arc. Recently, Parkinson *et al.* (2002) have identified a signature of strong sunward flow channel (maximum velocity is approximately 1.3 km s^{-1}) in the SuperDARN data at subauroral latitudes well after the substorm expansion phase onset. They concluded that this flow satisfies all of the criteria defining the SAID. To acquire more conclusive results, coordinated observation of the subauroral phenomena such as DUSE, SAID/SARAS and SAR arcs using various kinds of instruments is desired.

3.5 Summary

In order to evidence the model proposed in chapter 2, we have investigated two DUSE events (referred as Event A and B in the text) which had been observed by the CUTLASS Finland radar and the EISCAT UHF system simultaneously. When DUSE is observed by the Finland radar, the EISCAT observed sunward directed density gradient in the vicinity of DUSE. This density gradient was steeper than that produced only by the solar illumination. Also, after the passage of DUSE, the EISCAT observed ion temperature enhancement. These signatures imply that the sunward density gradient was observed at the duskside edge of the midlatitude trough. Then, it is confirmed that geometry of the parameters around DUSE is quite consistent with the model proposed in chapter 2. We employed substantial background parameters observed by the EISCAT and calculated linear growth rate of DUSE. During both intervals, the calculated minimum wavelength of FAIs is still larger than the scale of FAIs observed by the Finland radar. This result suggests that cascade process from larger scale FAIs to smaller scale is also working during these events and is still needed to explain the generation of DUSE.

During both intervals, DUSE appeared at earlier local time and the sunward edge of the trough was found to extend into the dayside. It is impossible to determine which process cause the dayside extension of DUSE and the trough. However, the EISCAT observed an enhancement of poleward electric field around DUSE. In addition, a signature of substorm breakup was identified by the ground magnetometer on the nightside. These observations suggest that the dayside extension of the midlatitude trough during the intervals of interest was primarily caused by an enhanced recombination due to the substorm-induced rapid subauroral convection through the ion-frictional heating.

Chapter 4

Conclusions, Speculations, and Future Directions

At the first step, we have investigated spatial distribution of the subauroral F region FAIs in a statistical fashion. Consequently, we have found that a distinct backscatter feature known as the dusk scatter event (DUSE, first explored by Ruohoniemi *et al.*, 1988) has a close relationship with the duskside end (i.e., sunward edge) of the midlatitude trough. This suggests that an electron density gradient at the sunward edge of the trough is most important factor for the generation of DUSE. Three models based on the gradient-drift instability were put forward. Then, it was found that the model which employs the sunward density gradient at the sunward edge of the trough together with an ambient poleward electric field is most favorable for the generation of DUSE. The other important finding was that in disturbed conditions DUSE appears at earlier local times compared with those in quiet conditions, which is schematically illustrated in Figure II-4.1 (a). This implies that the trough also extends into the dayside across the terminator during disturbed conditions as shown in Figure II-4.1 (b) and (c).

In order to testify the picture deduced from the statistical analysis, we have examined two DUSE events that occurred during disturbed conditions. Background electron density, electric field and plasma temperature obtained from the EISCAT incoherent scatter radar were employed. Consequently, when DUSE appeared in the field-of-view of the SuperDARN radar, the EISCAT observed sunward directed density gradient and poleward electric field in the vicinity of DUSE. This evidenced that geometry of the parameters is quite consistent with the proposed model. During the interval of both events, DUSE appeared at earlier local time and the sunward edge of the trough was found to extend into the dayside. This suggests that DUSE can be used as a tracer of the sunward edge of the trough during both quiet and disturbed conditions. The other important finding

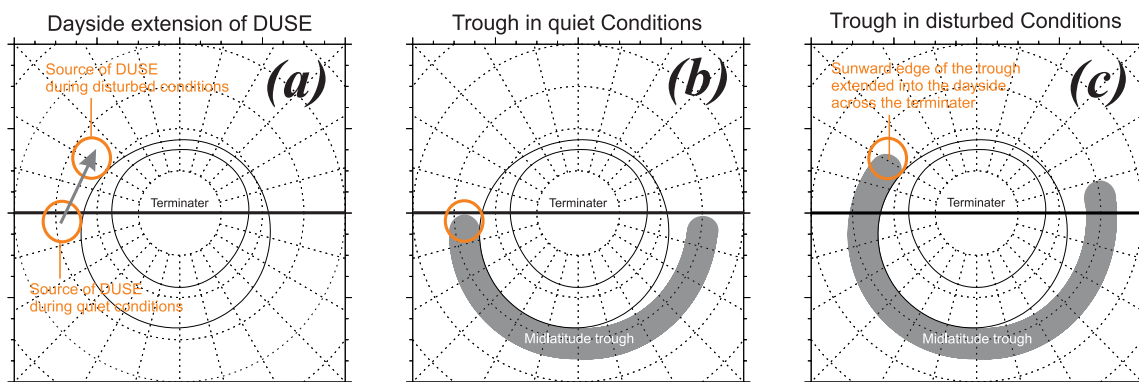


Figure II-4.1: (a) Schematic illustration of the dayside extension of DUSE during disturbed conditions. (b) picture of the midlatitude trough during quiet geomagnetic conditions, and (c) during disturbed conditions.

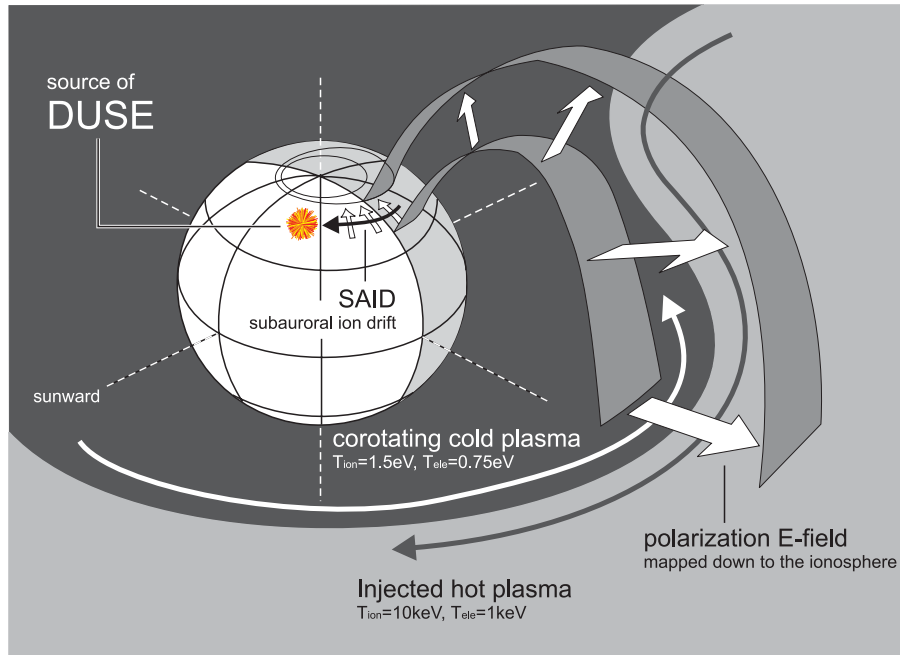


Figure II-4.2: Schematic picture of the hypothesis explaining the dayside extension of DUSE and trough during disturbed conditions (see text in detail).

was that the electric field observed by the EISCAT was more intense than that expected. In addition, the ion temperature was significantly enhanced in the region of the strong electric field. This suggests a possibility that an enhanced recombination in the region of intense electric field through the ion-frictional heating contributes to the dayside extension of the midlatitude trough and DUSE.

The origin of this intense electric field is unclear at this moment. However, subauroral ion drift (SAID) is one of the possible candidates. There are many distinct theories for the SAID generation. Recently, De Keyser *et al.* (1998) proposed that an intense radial electric field is generated by a thermoelectric effect due to strong temperature gradient across the interface between cold corotating plasma and hot plasma injected from the plasma sheet well after the substorm onset. They claimed that this radial electric field can be mapped into the subauroral ionosphere and the SAID is formed. If we adopt the SAID hypothesis including De Keyser's generation mechanism, the story could be illustrated like as Figure II-4.2. At first, polarization electric field is generated across the interface of two plasma populations after the substorm expansion. At the footprints of these polarization fields, strong poleward electric field due to the SAID reduces the electron density through the ion-frictional heating. Then, the midlatitude trough extends further into the dayside across the terminator. The region where the SAID terminates corresponds to the sunward edge of the midlatitude trough, i.e., source of DUSE. This picture might allow us to speculate that DUSE can be used not only as a tracer of the sunward edge of the midlatitude trough but also an diagnostic tool for detecting the electric field penetrating from the magnetosphere into the subauroral ionosphere.

In order to know whether this speculation is true or false, a relationship between an enhancement of the subauroral electric field and the injection of hot plasma into the inner magnetosphere must be investigated in relation to the appearance of DUSE. The SuperDARN community is now planning to construct the other network of coherent HF radars in the subauroral latitudes. If the new radars were operative at the lower latitudes in near future, more detailed and coordinated study of the subauroral FAIs could be carried out.

Part III

Dayside High-Latitude Irregularities as a Proxy for the Polar Cap Boundary

Chapter 1

Overview

As is introduced in section I-5.2, the dayside high-latitude region is one of the most active sources of the field-aligned irregularities (FAIs) observed by the SuperDARN coherent HF radars. Doppler spectra of the backscatters from these FAIs are known to have distinct characteristics in comparison with those observed in the other ionospheric regimes. The analysis presented in this part is aimed at improving our understanding of the dayside high-latitude FAIs and how they can be used to identify ionospheric and magnetospheric regions and processes, specifically the use of the frequently observed latitudinal boundary in Doppler spectral populations.

1.1 Geophysical Characteristics within the Dayside Ionosphere

There exist various kinds of structures within the dayside high-latitude ionosphere because several magnetospheric regimes are converged onto this region along the Earth's magnetic field lines. Most major feature among them is the cusp, which is generally defined as the neutral point in which the magnetic field lines change from closed to open based on the framework of the open magnetosphere model. In addition, the dayside low-latitude boundary layer (LLBL) and the mantle (boundary layer with open field lines in the magnetotail) are also mapped into the dayside high-latitude and their footprints surround the cusp. The dayside high-latitude has been investigated with various kinds of observations, both from the ground and with the satellites. In this section, geophysical characteristics seen in the vicinity of the cusp are introduced.

1.1.1 Structures Defined with Particle Precipitation

Many spacecrafts have observed the cusp and structures around the cusp at both high and low altitudes. The term cusp have not been defined correctly until the recent work of Newell and Meng (1988). They defined the cusp on the basis of the particle precipitation:

The low-altitude cusp is the dayside region in which the entry of magnetosheath plasma to low altitudes is more direct. Entry into a region is considered more direct if more particles make it in (the number flux is higher) and if such particles maintain more of their original spectral characteristics (Newell and Meng, 1988, pp.14,550).

Newell and Meng (1988, 1992) and Newell *et al.* (1991) employed over 60,000 satellite overpasses through the high-latitude dayside ionosphere and provided definitions of the cusp precipitation as well as other regions surrounding the cusp such as the LLBL and the mantle. A statistical map of the average dayside ionospheric precipitation pattern that they have produced is schematically illustrated in Figure III-1.1. Particle precipitation characteristics of the regimes shown in Figure III-1.1 are summarized as follows:

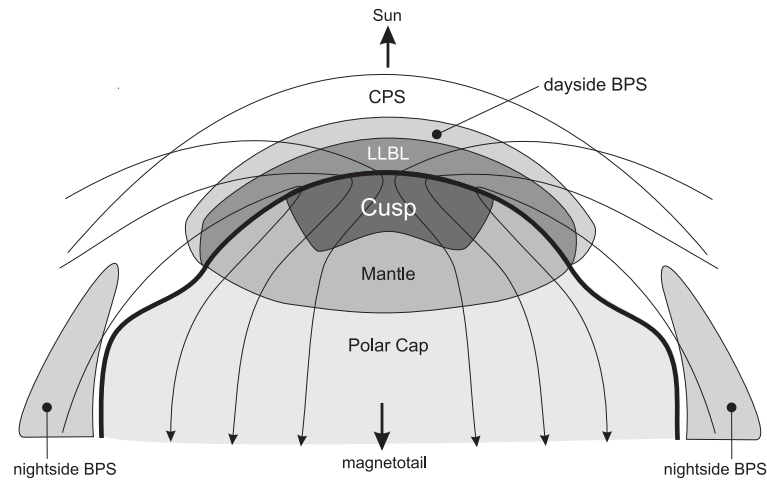


Figure III-1.1: Schematic illustration of relationship of the open/closed field line boundary to the dayside precipitation regions and the pattern of convective flow during southward IMF conditions (after Lockwood, 1997). Thick line indicates the position of the open/closed field line boundary.

- mantle: de-energized magnetosheath ions in comparison with the cusp and thus the point of lowest ion average energy among particle precipitation regions observed on the dayside high-latitude. Ion average energies are usually no more than a few hundred eV. Densities are also much lower than in the cusp or even LLBL.
- cusp: characterized by very high fluxes, particularly for ions. Typically the ions have a spectral peak of 10^8 eV/cm² s eV sr or more, which is higher than anywhere else in the polar ionosphere. Average energy of ions is approximately 1 keV.
- LLBL: average energies are similar to the cusp, but usually ion densities are about a factor of 5 smaller than those in the cusp. Peak of the energy spectra in the ion flux is also about a factor of 10 smaller ($\approx 10^7$ eV/cm² s eV sr) than that in the cusp.
- dayside BPS: precipitation which closely resembles the poleward portion of the nightside auroral oval. The electrons have a typical energies of about 600 eV, somewhat higher than the LLBL.
- CPS: hard zone of electron precipitation on the dayside. These precipitating electrons have been injected into the near Earth region on the nightside and subsequently drift around the Earth. Typical energies of electrons are above 1 keV.

The left panels of Figure III-1.2 show an example of the DMSP particle measurement that Newell and colleagues employed to categorize the dayside precipitation regimes. The bottom panels show the spectrogram of differential energy flux from the DMSP satellite overpassing the dayside structures from higher to lower latitudes. The top two panels show integral energy flux (eV/cm² s sr) and averaged energy (eV), respectively. The right panels are temporally expanded plots of the left panels, where the automated identification of the structures using a neural network method is displayed at the bottom of the panels.

Another important feature that characterizes the cusp is the energy dispersion of the ions, i.e., ion energy falls with increasing latitudes. This signature is clearly seen in the example presented in Figure III-1.2. This is due to the fact that ions of different field-aligned velocity, injected simultaneously across the magnetopause, have different flight times along the field line. Hence, they have different arrival times in the ionosphere and

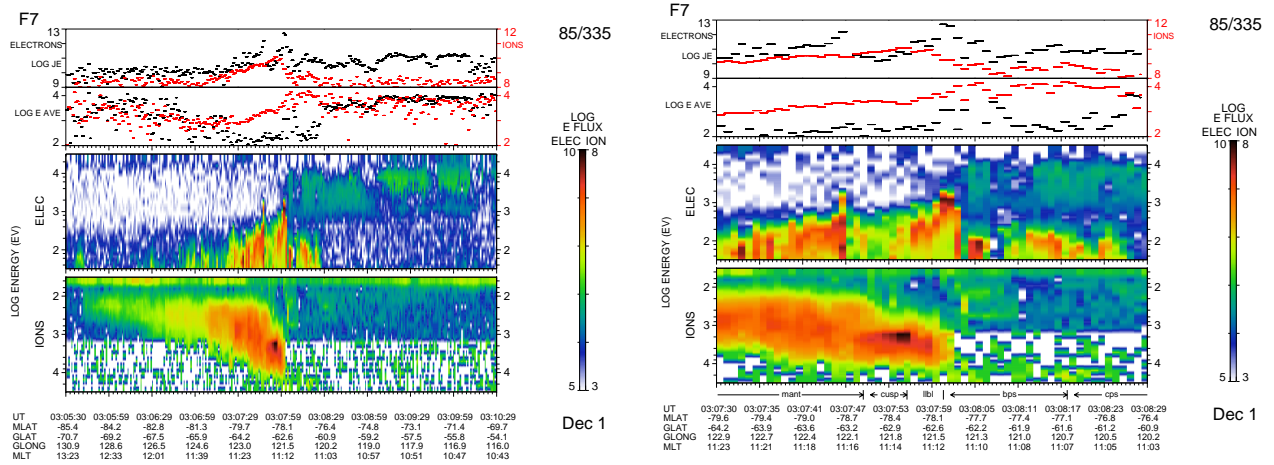


Figure III-1.2: (Left) the bottom two panels show the spectrogram of differential energy flux from the DMSP satellite overpassing the dayside structures from higher to lower latitudes. The energy scales go from 32 eV to 30 keV, and differential energy flux is colour-scaled in units of $\text{eV}/\text{cm}^2 \text{ s eV sr}$. Note that the ion energy scale is inverted then the lowest energies lie near the center of the spectrogram for both electrons and ions. The top two panels show integral energy flux ($\text{eV}/\text{cm}^2 \text{ s sr}$) and averaged energy (eV), respectively. (Right) temporally expanded plots of the left panels, where the automated identification of the structures using a neural network method is displayed at the bottom of the panels (taken from online spectrogram at sd-www.jhuapl.edu/Aurora/spectrogram/).

are spatially dispersed along the convecting field lines. For the case of the southward IMF, the field lines are convected anti-sunward, then the ions of highest energy arrive first in the ionosphere and are observed at the lowest latitude. This feature is known as the velocity filter effect first discussed by Rosenbauer *et al.*, (1975), which is now regarded as the characteristics of precipitation on newly-reconnected field lines for the southward IMF conditions on the open magnetosphere concepts (Smith and Lockwood, 1996).

The location of the boundary between open and closed field lines is particularly important for the study of the energy transfer from the solar wind into the magnetosphere-ionosphere system via reconnection. The region of open field lines is termed as the polar cap and its size is primarily controlled by the balance between the dayside and nightside reconnection. The question is where the open/closed field line boundary (OCFLB) lies in relation to the particle signatures described by Newell and Meng (1992). Lockwood (1997) have shown the situation that is expected on the basis of the closed magnetosphere model, which is reproduced in Figure III-1.1. The OCFLB is located between the cusp and the LLBL. Conversely, Lockwood (1997) also showed the situation more likely if we consider the open magnetosphere model with reconnection occurring at the dayside magnetopause. In that picture, the finite poleward convection velocity of recently reconnected flux tubes leads the bulk of the cusp particles to the region some distance poleward of the true OCFLB at ionospheric altitudes. Then, the OCFLB should be located at the region some distance equatorward of the boundary between the cusp and the LLBL. Rodger and Pinnock (1997) assumed that the cusp particle precipitation travels at speed of the ions, and then estimated this offset to be ≈ 150 km near noon.

1.1.2 Dayside Auroral Morphology

Precipitating energetic particles give rise to auroral luminosity, which can be detected with ground or space-based optical imagers. Harder (≈ 10 keV) and softer (≈ 1 keV) electrons produce green (557.7 nm) and red line (630.0 nm) emissions in the E and F region ionospheres, respectively. On the dayside, red line (630 nm) aurora is often observed poleward of the auroral oval dominated by green line emissions (Whalen *et al.*, 1971; Murphree

et al., 1980; Elphinstone *et al.*, 1992). These red line auroral emissions are excited by electrons with energies of order 100 eV. These electrons satisfy the energy characteristics of unaccelerated cusp plasma of magnetosheath origin on newly opened field lines (Lockwood *et al.*, 1993; Sandholt *et al.*, 1998). Hence, the OCFLB can be determined as the poleward edge of luminosity dominated by green line and the equatorward edge of red line luminosity (Lockwood *et al.*, 1993). A very clear example of the coincidence of the poleward boundary of the trapped high-energy particle with the boundary between red and green line dominated aurora is presented by Lorentzen *et al.* (1996).

1.1.3 The Cusp as a Source of Intense Electric and Magnetic Field Fluctuations

The cusp is normally defined by a high density plasma injected from the magnetosheath. However, it is often referred as an active source of the intense electric and magnetic field fluctuations. Curtis *et al.* (1982) and Maynard (1985) have reported broadband electrostatic noise activity in the ULF/ELF frequency band (from a few Hz to kHz) associated with the cusp. The electric field amplitude is found to be of the order of a few tens of mV m^{-1} but can sometimes reach 100 mV m^{-1} . Later, Maynard *et al.* (1991) detected a low-frequency ($< 1 \text{ Hz}$) fluctuations in both the electric and magnetic field. By using the particle data, they found that these electric field structures correspond to the equatorward edge of the cusp particle precipitation. Erlandson and Anderson (1996) also found that the power spectral density of the electric field in the Pc1 frequency band sharply increases at the equatorward edge of the cusp particle precipitation. At higher altitude, Matsuoka *et al.* (1991, 1993) have found a similar electromagnetic wave activity in the EXOS-D satellite data, and they showed that the electric field fluctuations in the cusp are more intense than those observed in the dayside auroral region. They showed a very good correlation between the increase of the power spectral density in the Pc1-Pc2 frequency band and the increase of the magnetosheath particle flux in the cusp.

Origin of these fluctuating field is still a considerable debate. Two competing models have been put forward. The first one assumes that the fluctuations are observed due to the orbital motion of the satellite through small-scale quasi-static field-aligned current structures embedded in the large-scale field-aligned current (Smiddy *et al.*, 1980; Sugiura *et al.*, 1982; Ishii *et al.*, 1992). The second one suggests that disturbances in the distant magnetosphere are transmitted to the ionosphere as Alfvén waves (Lysak and Dum, 1983). Matsuoka *et al.* (1993) emphasized from the EXOS-D measurement that the electric to magnetic field ratios in the frequency range of 0.5-3 Hz agree well with the Alfvén velocity at the observation point. In general, it is almost impossible to distinguish temporal and spatial variations in the satellite observation. However, Ishii *et al.* (1992) demonstrated that the Alfvén wave model is applicable to variations of scale lengths less than 4.0 s, while effect of the quasi-static model becomes increasingly dominant for scale length greater than 8.0 s.

1.2 Coherent HF Radar Observation of the Cusp

1.2.1 Broad Doppler Spectral Width

It has been well known that the precipitating electrons at energies below 300 eV within the region around the cusp is associated with significantly enhanced and intense targets of the HF radar backscatter (Yeoman *et al.*, 1997; Milan *et al.*, 1998). Papers by Baker and colleagues in 1990 and 1995 have investigated these backscatters with the SuperDARN Goose Bay and Halley radars in relation to the coincident particle measurements by the DMSP spacecraft (Baker *et al.*, 1990; 1995). By referring the location of the cusp as identified in the particle measurements on a single pass through the radar field-of-view, Baker *et al.* (1990) have demonstrated that the spectral width within the cusp is typically larger than 150 m s^{-1} , with values often exceeding 750 m s^{-1} , while

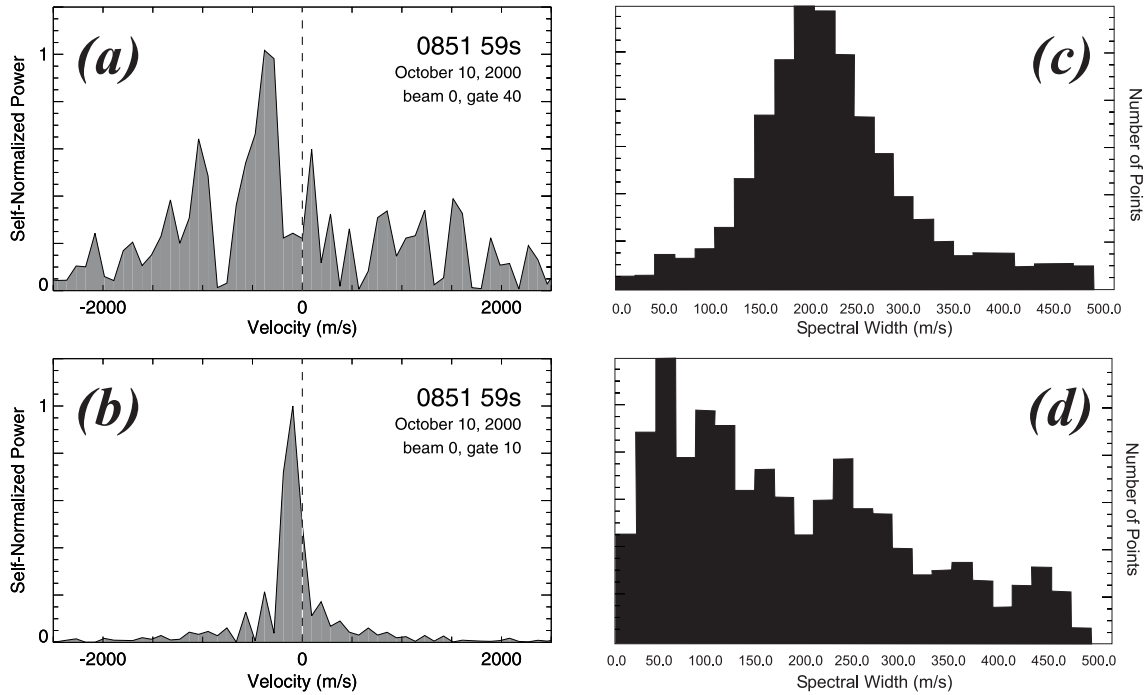


Figure III-1.3: (Left) typical example of the radar Doppler spectra observed in a region associated with the ionospheric cusp (a), and the LLBL (b) (taken from Syowa-East radar data). (Right) distribution of spectral widths for 8 different passes associated with the cusp (c) and 8 different passes associated with the LLBL (d) (taken from Baker *et al.*, 1995).

elsewhere outside of the cusp the widths are approximately 100 m s^{-1} or less. They also presented that the ion velocity measurements by the DMSP in the region of the cusp are highly variable, with rapid and large velocity variations compared to those in the other regions on the spacecraft track.

A more detailed analysis has been made using a number of DMSP passes through the radar field-of-view by Baker *et al.* (1995). In their work, there was an attempt not only to identify spectra associated with the cusp but also to separate them from those associated with the LLBL. Typical example of the Doppler spectra within the cusp is shown in Figure III-1.3 (a). The spectra are multi component and vary considerably with range gate, which is clearly different from the spectra at similar latitudes but a different local time. Comparing these spectra with those observed in regions identified as the LLBL, some major differences are found. Typical example of the spectra within the LLBL is shown in Figure III-1.3 (b). The spectra are relatively narrow and have a single component. The spectral width is typically between 100 and 150 m s^{-1} . However, it is not always the case that the spectral width which is mapped into the regions of closed magnetic field lines, or the LLBL, is single peaked and narrow. Multi component spectra which look like so-called cusp spectra can also occur on closed field lines (Baker *et al.*, 1995).

Baker *et al.* (1995) analyzed the HF radar data for 8 cusp events and 8 LLBL events in a statistical fashion. They reported that the statistical distribution of observed spectral widths in the cusp is significantly different from that in the LLBL. Right panels of Figure III-1.3 show the statistical distribution of the spectral width within the cusp (c) and LLBL (d) reported by Baker *et al.* (1995). The distribution of spectral widths within the cusp is a broad Gaussian shaped distribution, whose average is around 220 m s^{-1} . In contrast, the distribution in the LLBL is more similar to an exponential distribution with the peak occurring at about 50 m s^{-1} .

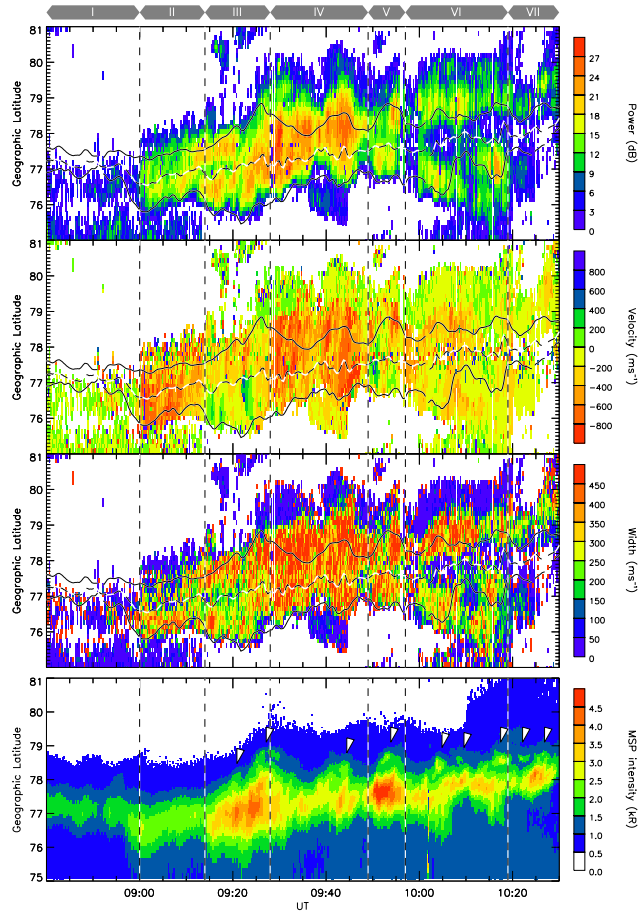


Figure III-1.4: The backscatter power (top), line-of-sight Doppler velocity (second panel), and spectral width (third panel) observation by the SuperDARN Finland radar. Also illustrated in the bottom panel is 630 nm (red line) optical emission intensity observed by the meridian scanning photometer at Ny Alesund. The locations of the equatorward 1.5 kR isocontour, the peak intensity and the poleward 1.5 kR isocontour of the red line emission are superimposed on the radar data for comparison (taken from Milan *et al.*, 1999).

1.2.2 Relationship between the Broad Spectra and Other Features

As introduced in the previous section, the cusp is characterized by several kinds of observations such as the particle precipitation, auroral emission, wave activities. The broad Doppler spectral width obtained from the coherent HF radars also has a distinct characteristics within the cusp. In this section, relationship between the broad Doppler spectral width and the signatures of the cusp in other observations are briefly overviewed.

As Baker *et al.* (1995) reported, there exists a close relationship between the cusp particle precipitation and the broad Doppler spectral width. This relationship has been confirmed by Milan *et al.* (2002b) which compared the low altitude particle precipitation and the HF radar broad Doppler spectral width in the course of estimation of the polar cap area during substorm cycle. Equatorward boundary of the broad Doppler spectral width is corresponding to the equatorward boundary of the dispersed ion signature and poleward boundary of the high-energy particles trapped on closed field lines. They also have found that this relationship is not clear during the intervals of the northward IMF.

Several attempts have been made to compare HF radar spectral width and optical signature of the cusp. Rodger *et al.* (1995) found the equatorward boundary of the broad spectral widths to be located at equatorward boundary of the optical cusp for the negative IMF conditions. Yeoman *et al.* (1997) demonstrated a fine

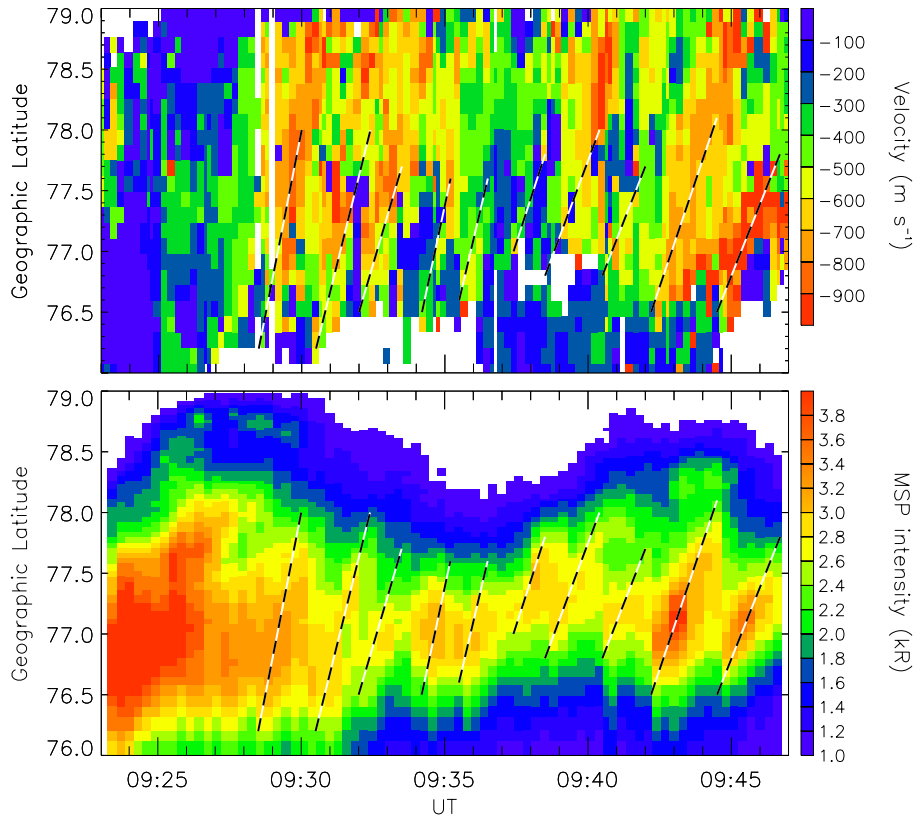


Figure III-1.5: Radar and meridian scanning photometer observations of the poleward moving forms. The top panel shows the line-of-sight Doppler velocity and the bottom panel shows the red line optical emissions. The dashed lines in both panels indicate the optical poleward moving transients and the radar flow bursts (taken from Milan *et al.*, 1999).

collocation of strong HF backscatter power, poleward moving auroral forms, and energy dispersed ions for a DMSP overpass through the cusp. Milan *et al.* (1999) demonstrated a good correlation between HF backscatter and dayside 630 nm aurora along the meridian swept by the scanning photometer. Summary of their observation is shown in Figure III-1.4, where radar backscatter power, Doppler velocity and spectral width are shown in the upper three panels, and intensity of the red line aurora is presented in the bottom panel. They found a rather good collocation between the equatorward boundaries of the broad spectral width region and the auroral luminosity. However, Moen *et al.* (2001) reported that this close relationship breaks down for northward IMF conditions.

1.2.3 Application of the Broad Doppler Spectral Width

Previous studies have shown that the equatorward boundary of the broad Doppler spectral width is fairly coincident with the low latitude limits of the cusp particle precipitation and red line auroral emissions. These observational results allow us to use the equatorward boundary of the broad spectral width region as a proxy for the open/closed field line boundary (OCFLB) at the ionospheric altitudes. Then, we can locate the area of polar cap by using the broad Doppler spectral width within the dayside ionosphere.

Nature of the reconnections (i.e. steady or bursty ?) is still one of the most frequently discussed issues. For the reconnections in the magnetotail, they are explosive and their manifestation is well known as the substorm expansion. Also for the case of the dayside reconnections, there exist a lots of observations of transient feature indicating their bursty nature. Haerendel *et al.* (1978) reported the first observations at the magnetopause

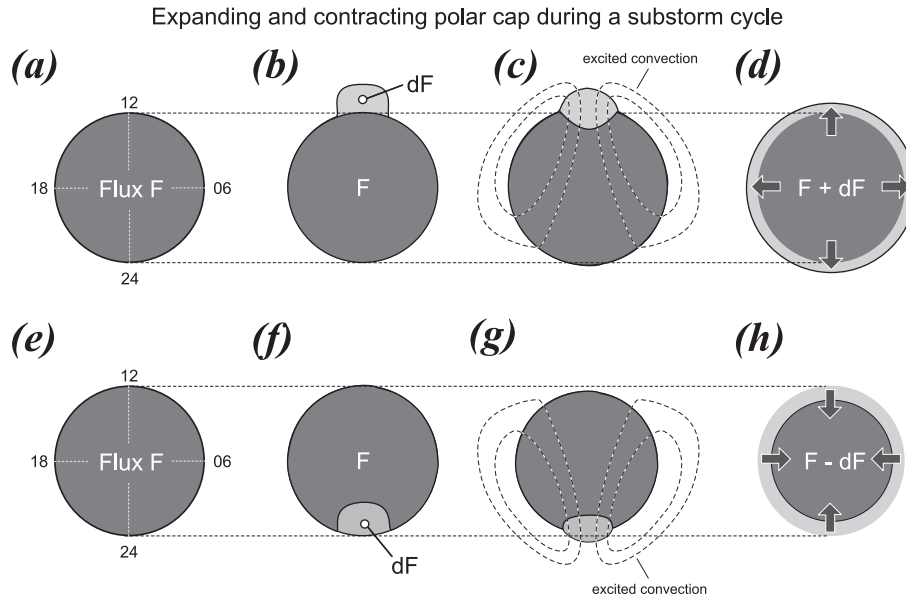


Figure III-1.6: Schematic diagram of the expanding and contracting polar cap during substorm cycle outlined by Cowley and Lockwood (1992). Initially it is assumed that the open and closed flux in the polar cap is in a state of equilibrium (a). In response to a burst dayside reconnection, a region of closed flux adjacent to the pre-existing dayside polar cap boundary is opened (b). The OCFLB moves equatorward to encompass the new open flux (c)-(d). Conversely, during the substorm expansion phase, magnetotail reconnection closes pre-existing open flux, then the boundary moves poleward as the polar cap shrinks (e-h).

boundary layer suggesting small-scale, transient reconnections. A bipolar variation in the normal component of the magnetic field at the magnetopause is interpreted as a highly kinked newly reconnected flux tube passing through the spacecraft. Later on, they have been studied by many authors (Russell and Elphic, 1978; Lockwood and Wild, 1993; Kuo *et al.*, 1995) and have come to be known as flux transfer events (FTEs). Series of poleward moving auroral forms (PMAFs) at the polar cap boundary are believed to be the optical manifestation of the magnetospheric FTEs at the ionospheric altitudes (e.g., Fasel, 1995). The aurora is believed to be directly excited by plasma precipitating from the reconnection region to the ionosphere along newly reconnected field lines. These poleward moving signatures are also detectable with the coherent HF radars (Pinnock *et al.*, 1995; Provan *et al.*, 1998, 1999; Milan *et al.*, 1999, 2000). One of the clearest example of such features observed simultaneously with meridian scanning photometer and coherent HF radar is presented in Figure III-1.5 (taken from Milan *et al.*, 1999).

In general, size of the polar cap varies in response to the creation and destruction of the open magnetic flux due to the dayside and nightside reconnections (Siscoe and Huang, 1985). Cowley and Lockwood (1992) illustrated an expanding/contracting polar cap model in which they described the ionospheric flow as a distributor of the magnetic flux newly created by the dayside and nightside reconnections. Figure III-1.6 gives a schematic illustration of their model. Initially it is assumed that the open and closed flux in the polar cap is in a state of equilibrium and that the polar cap is circular, containing some amount of open flux F (state a). In response to a burst of dayside reconnection, a region of closed flux adjacent to the pre-existing dayside polar cap boundary is opened (state b). The OCFLB, the boundary which encloses open flux, moves equatorward to encompass the new open flux (state c-d). Conversely, during the substorm expansion phase, magnetotail reconnection closes pre-existing open flux, then the boundary moves poleward as the polar cap shrinks (e-h). This model is an ionospheric projection of the magnetospheric convection known as the Dungey cycle, although

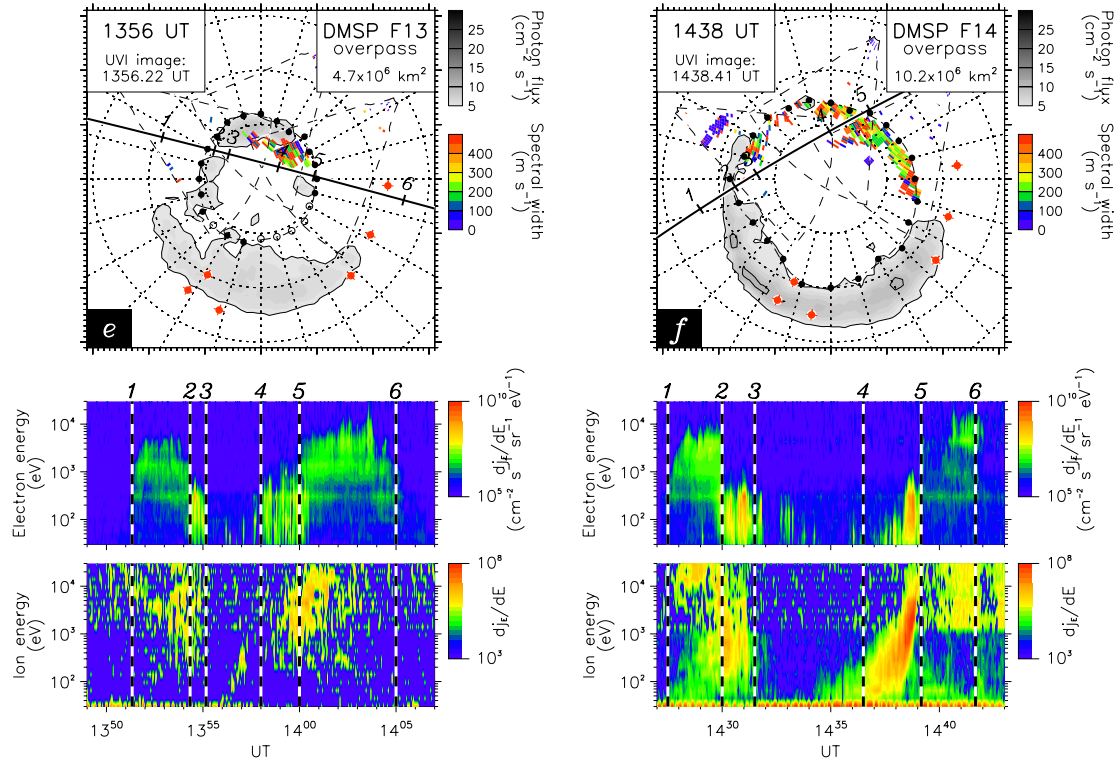


Figure III-1.7: Estimation of the polar cap area with SuperDARN broad spectral width, Polar UVI auroral image, and low-altitude particle precipitation data by the DMSP satellite. Filled dots indicate estimated location of the equatorward boundary of the polar cap area at each MLT meridian. The dot-dashed line is a smoothed fit to these points (taken from Milan *et al.*, 2002b).

it contains a concept of the bursty reconnection.

One of the most successive application of the broad spectral width were made by Milan *et al.* (2002b). They have estimated region of open magnetic flux (i.e., polar cap) and its temporal variation by using the SuperDARN broad spectral width in combination with the low altitude particle precipitation and Polar UVI auroral emission data. The upper panels of Figure III-1.7 are composite plots of the Polar UVI auroral luminosity (grey scale) and radar spectral width (colour scale) on magnetic latitude and MLT coordinates. Filled dots indicate estimated location of the OCFLB at each MLT meridian. The dot-dashed line is a smoothed fit to these points, i.e., indicating a rough estimate of the location of the open/closed field line boundary. Superimposed is the track of the overpassing spacecraft, tick marks indicating the location of boundaries 1-6 identified in the lower panels. The lower panels show electron and ion measurements from the overpassing DMSP satellites. In the right panel, during the interval of the negative IMF Bz, equatorward boundaries of the broad spectral width and the dispersed ion signature are in good agreement, locating the polar cap boundary within the dayside ionosphere. They applied this method for two substorm cycles and obtained the result that are very consistent with the framework illustrated by Cowley and Lockwood (1992).

Baker *et al.* (1997) attempted to estimate electric potential across the magnetopause reconnection X-line from the ionospheric plasma convection across the OCFLB as determined by the spectral width. This potential drop, or corresponding reconnection electric field along the reconnection line, is one of the most important driver to generate cross polar cap potential within the high-latitude ionosphere. They compared the radar observations with the results from AMIE (assimilative mapping of ionospheric electrodynamics, Richmond, 1992) procedure

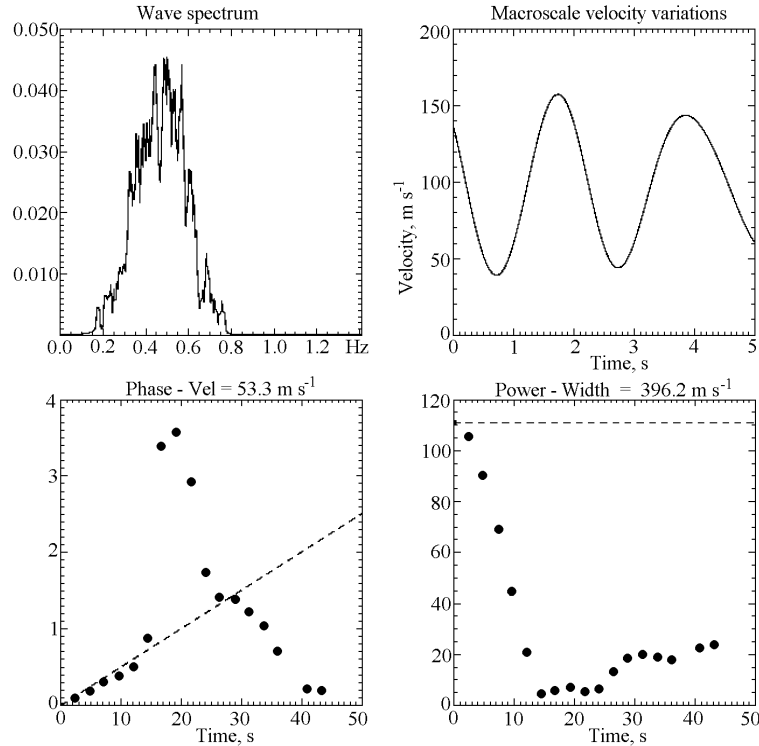


Figure III-1.8: (Top left) spectrum of the wave inputted, (top right) velocity variations during the radar integration time, (bottom left) phase and (bottom right) power of the simulated ACF (taken from André *et al.*, 2000b).

and reported that a majority of the cross polar cap potential is generated by the contribution of the dayside reconnection electric field unless the substorm does not occur.

1.3 Cause of the Broad Doppler Spectra: Theoretical Approach

Previous studies have shown that the spectral width is very useful tool to locate the geophysical boundaries around the dayside ionosphere. However, it is still unclear what physical mechanism broaden the Doppler spectra within the dayside. Baker *et al.* (1995) suspected that spectra with multiple components and associated broad spectral widths within the cusp could be attributed to the variability of the electric field both in time and space. Actually, the radar has a limit for the frequency of changes in plasma flow to be picked up, then it is very natural to consider that the multi-peak spectra are a result of undersampling. This speculation has been testified by André *et al.* (1999, 2000a, 2000b) by using theoretical approach. Figure III-1.8 shows an example of their simulation. The upper panels show the spectrum of the fluctuating electric field used as an input (left) and the corresponding temporal variation of the velocity field (right). The lower panels show resulting temporal evolution of the auto-correlation function (ACF) phase (left) and ACF power (right). The dashed line shows the expected ACF without the wave. Here, the plasma is moving with a constant velocity of 100 m s^{-1} , modulated by a wave characterized by an amplitude of 40 m s^{-1} and a frequency of 0.5 Hz . This example shows that the temporal evolution of both the phase and the power of the ACF are modulated. This implies that the associated spectrum contains more than one component and spectral width deduced from the fitting procedure is very broad. They concluded that all of the features seen in the cusp spectra can be explained by the presence of a broadband wave in the Pc1/Pc2 frequency range (see section III-1.1.3). Later on, André *et al.* (2000a) demonstrated that even a monochromatic electric field variation can cause apparently turbulent behavior in the

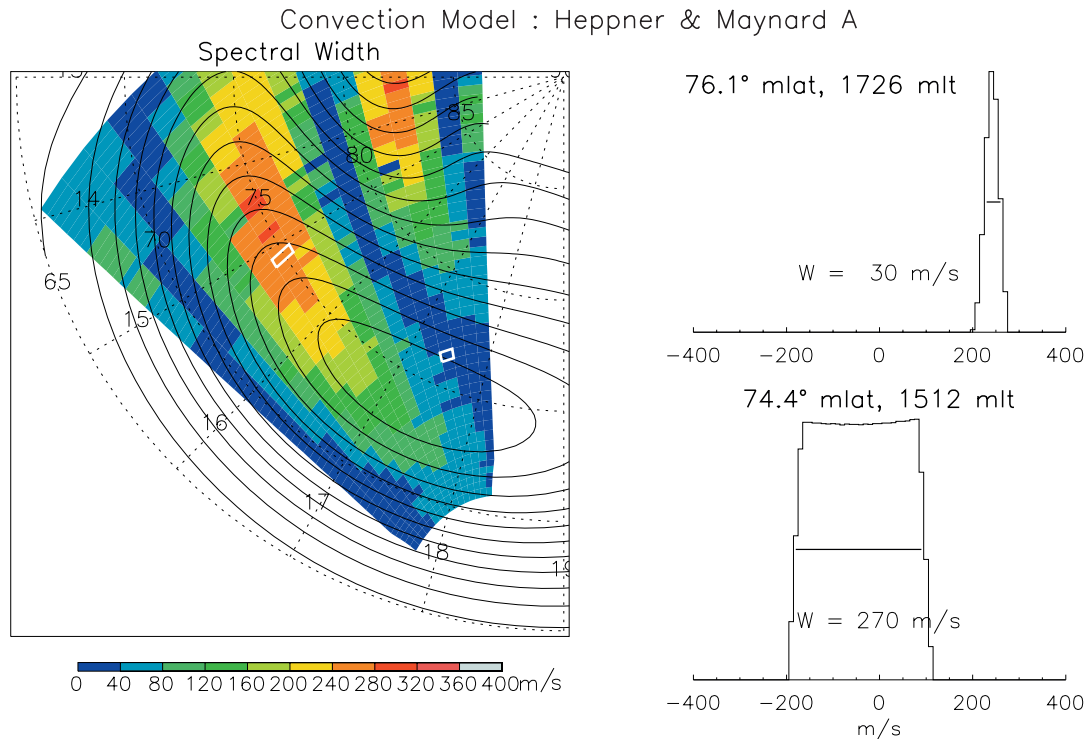


Figure III-1.9: (Left) estimated spectral width in the radar field-of-view coded in colours. The isocontours of the ionospheric convection model are shown by the black lines. (Right) examples of velocity distribution functions obtained in the constant velocity area (upper) and inside the convection reversal (lower) (taken from André *et al.*, 2000b).

ACF, suggesting multi-peak spectra and broad spectral width. Their simulations also demonstrated that low amplitude waves are sufficient to broaden the spectral width if the frequency of the electric field variation is high enough.

Two physical sources other than the wave activities were simulated to estimate their impact on the spectral width by André *et al.* (2000b). These are the presence of a convection reversal and a vortex within a single range/beam cell. Two oppositely directed velocities exist within one range cell around the convection reversal. The ACF would reflect this with the power spectrum that has two peaks. It has been reported by Barthes *et al.* (1998) that the probability of finding multi-component spectra is strongly enhanced at convection reversals. André *et al.* (2000b) employed empirical convection model by Rich and Maynard (1989) to generate velocity vector in a range gate and computed how the ACFs respond to the convection reversal. The left panel of Figure III-1.9 shows the estimated spectral width in the Iceland-West radar field-of-view at 1900 UT. Black lines represent isocontours of the employed convection model. At this time, the radar is looking mainly at the convection reversal. Two examples of the computed velocity distribution are also displayed in the right panel. When the radar is looking in a region where there is no large velocity gradient (upper right panel), the velocity distribution is narrow, and the associated spectral width is negligible. In contrast, when the range gate is inside a large velocity gradient (lower right panel), the spectral width can be as large as 250 m s^{-1} . However, the averaged impact of this process on the spectral width is approximately 150 m s^{-1} and therefore not capable of explaining the spectra within the cusp which often exceed 500 m s^{-1} . Villain *et al.* (2002) also investigated the effect of flow reversals on the spectral width by performing simulations using the convection model by Heppner and Maynard (1987). Their calculation also demonstrated that the contribution of the flow reversal to the broad

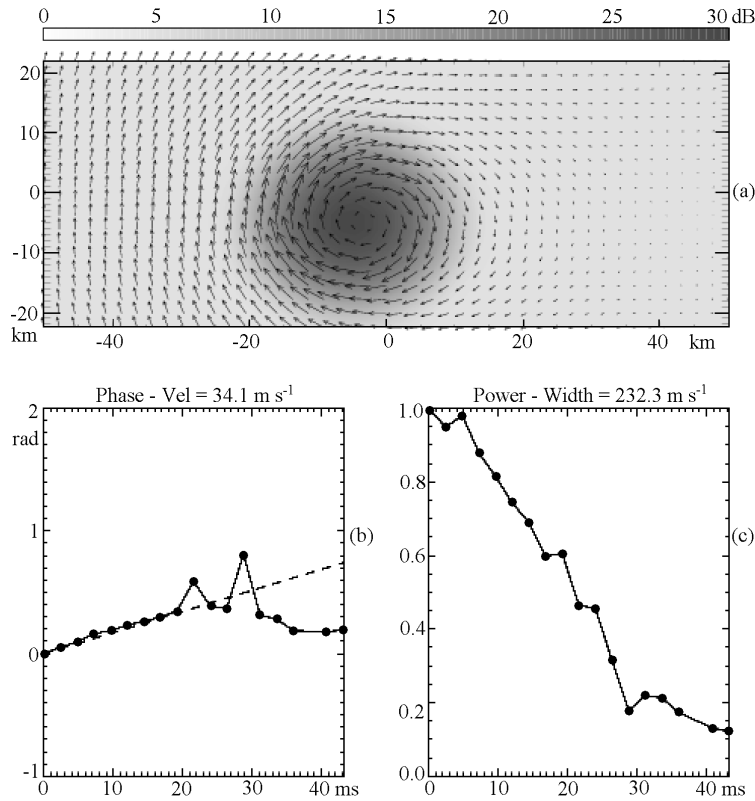


Figure III-1.10: (Upper) velocity vectors with vortex structure inputted in the simulation, superimposed on the backscattered power coded in gray scale. (Lower) temporal evolution of the ACF phase (left) and power (right) (taken from André *et al.*, 2000b).

spectral widths is insufficient to explain the values observed.

Small scale velocity vortices of the order of the range/beam cell were also simulated by André *et al.* (2000b). The vortex is related to structures that can be created by filamentary field-aligned currents (FACs) (Borovsky, 1993). The current closure in the conducting layer will generate a divergent electric field structure, then small-scale velocity vortex is formed. A vortex in a plane perpendicular to the magnetic field is assumed and its impact on the ACF is simulated. Figure III-1.10 shows the result of the calculation. The upper panel shows velocity vectors with small-scale vortex inputted in the calculation. The lower panels display the simulated phase and power of the ACF. The phase does not present a linear behavior, which suggests a multi-component spectrum. Schiffler *et al.* (1997) have found a large number of double-peaked spectra in the radar data obtained within the LLBL. They suggested that these double-peaked spectra could arise from filamentary currents generated by structured soft electron precipitation observed by satellites at the same time. These currents could generate small-scale vortices (scale size of 10 km), such as the one modeled by André *et al.* (2000b). Kataoka *et al.* (2002) have shown that the radar observes broadened Doppler spectra in conjunction with the traveling convection vortices as detected with the ground magnetometer array. These observational facts confirm that the small-scale vortex structure in convection field can contribute to the production of the broad spectral width. However, the radar actually observes the broad Doppler spectral width even in the absence of these vortex structures. This implies that this process is not a primal cause of the broad spectra observed routinely within the dayside ionosphere.

André and co-workers have evaluated a number of factors which condition the Doppler spectral width

as observed by the SuperDARN HF radars through computer simulations. They have demonstrated that the Doppler spectral width is a complex convolution of (i) Pc1/Pc2 wave activities, (ii) geometry of the radar with respect to the large scale convection velocity (large-scale velocity shear), (iii) the presence of velocity shears of the scale size of a range/beam cells (small scale velocity vortex). They concluded that the wave activity is the dominant parameter in the case of the dayside high-latitude region. However, there has been no observational evidence supporting their calculations.

1.4 Interhemispheric Study: What is Conjugacy?

In chapter 2 and 4, behavior of the broad Doppler spectral width is compared between the Northern and Southern Hemisphere. In this section, meaning of the ‘conjugate’ or ‘conjugacy’ is defined and such a studies using the SuperDARN radar are overviewed.

In the study of the magnetosphere ionosphere coupling system, the terms ‘conjugate study’ and ‘conjugacy’ are frequently used. Magnetically conjugate phenomena is defined to occur on a single magnetic field line or flux tube. In this sense a low altitude satellite passing over a ground station can be magnetically conjugate. Then, strictly speaking, phenomena in opposite polar caps with open field lines should not be termed as ‘conjugate phenomena’. However, the term magnetic conjugacy is sometimes loosely used to describe phenomena in opposite hemisphere at locations which would be approximately conjugate if the Earth’s main field were the only magnetic field. Since target of the study presented in chapter 4 appears on the boundary between the open and closed field lines, then the term ‘conjugate study’ should not be used. However, the term ‘conjugacy’ is sometimes loosely used also in our studies. We hope readers to keep in mind that the term ‘conjugacy’ used in this thesis means how the phenomena that occur in two hemispheres match.

It is only worth studying conjugate phenomena if it adds new insights to our understanding of the physics. In other words, if phenomena are simply mapped from one hemisphere into the other, there would no need to do the conjugate study. First conjugate study using the coherent HF radar was made by Greenwald *et al.* (1990). They examined the effect on convection of the By component of IMF. They employed beam-swinging technique (Ruohoniemi *et al.*, 1989) to estimate the vector velocity from the line-of-sight Doppler velocities for each radar. They were able to relate the interhemispheric difference in the convection patterns to those deduced theoretically for different IMF By conditions. They also studied reconfiguration of these patterns as By changed. Chisham *et al.* (2000) have measured a time delay in the ionospheric response to changes in IMF By between the Northern and Southern Hemispheres using conjugate radar pair. The radar in the Northern Hemisphere observed reconfiguration of the dayside convection pattern in response to the changes in IMF By about 3-4 min before the radar in the Southern Hemisphere. This difference can be interpreted as a consequence of the location of the dominant reconnection site on the magnetopause, which is closer to the northern ionosphere than to the southern ionosphere due to the dipole tilt of the magnetosphere and the orientation of the IMF Bx component.

Milan and Lester (2001) have investigated conjugacy of the signature of the bursty reconnection as observed by the coherent HF radars. They have found that radar observes poleward-moving backscatter features in the Northern Hemisphere, as believed to be the signature of the flux transfer events (FTEs) at the dayside magnetopause, with a repetition rate of 9 min. In contrast, the Southern Hemisphere radar does not observe any significant signatures of bursty reconnection. The convection flow patterns at the footprint of the reconnection X-line in the two hemispheres are found to be considerably different. The azimuthal component of the plasma drift is near 0 km s⁻¹ in the Northern Hemisphere and near 1.2 km s⁻¹ in the Southern Hemisphere. They

suggested that the magnetopause reconnection site is closest to the cusp footprint in the Southern Hemisphere because of the negative B_x dominating conditions. Pinnock *et al.* (1999) estimated reconnection electric field in both hemispheres using the same procedure as used by Baker *et al.* (1997), i.e., the electric field is estimated by the ionospheric flow perpendicular to the OCFLB as determined by the spectral width observations. They also investigated an interhemispheric difference of the latitude of the OCFLB. However, the observation was made in summer, then they could not discuss interhemispheric difference in detail because of the bias due to the effect of the dipole tilt.

1.5 Organization of This Part

Organization of this part is as follows: In chapter 2, characteristics of the spectral width distribution within the dayside ionosphere are investigated in a statistical fashion, then general link to geophysical structures is discussed. In chapter 3, Doppler spectral width observed by the SuperDARN radars and magnetic field fluctuations observed by the Oersted satellite magnetometer are compared during an interval of the negative IMF B_z conditions. Then, validity of the theoretical prediction by André *et al.* (1999, 2000a, 2000b) is verified. In chapter 4, the boundaries between narrow and broad spectral width obtained from the conjugate radar pair are compared and interhemispheric difference in their temporal variation is discussed.

Chapter 2

Statistical Characteristics of Doppler Spectral Width as Observed by the Conjugate SuperDARN Radars

2.1 Introduction

The dayside auroral zone provides a good target for HF radars (Milan *et al.*, 1998). A relationship between the magnetospheric cusp particle precipitation into the ionosphere and the HF radar backscatter from the ionospheric F region has been reported by a number of authors (Baker *et al.*, 1990, 1995; Rodger *et al.*, 1995; Yeoman *et al.*, 1997). They demonstrated that the equatorward edge of radar backscatter showing broad Doppler spectral widths is coincident with the equatorward edge of the cusp particle precipitation. Furthermore, the equatorward edge of these regions of HF radar backscatter appear to correspond closely to the equatorward edge of the 630 nm (red line) aurora during the period of negative IMF Bz (Rodger *et al.*, 1995; Milan *et al.*, 1999; Moen *et al.*, 2001). Baker *et al.* (1995) analyzed the HF radar data for 8 cusp events and 8 low-latitude boundary layer (LLBL) events which were identified by the DMSP satellite. They reported that the distribution of observed spectral widths in the cusp is significantly different from that observed in the LLBL. The distribution of spectral widths within the cusp is a broad Gaussian shaped distribution, whose average is around 220 m s^{-1} (termed cusp-type distribution in this paper). In contrast, the distribution of spectral widths in the LLBL is more similar to an exponential distribution with the peak occurring at about 50 m s^{-1} (termed LLBL-type distribution in this paper). The boundary between these two types of spectral width distribution has been considered to be the open/closed field line boundary (OCFLB) in the HF radar observation, though it is possible that there is a displacement of radar signature of the OCFLB from the real OCFLB (for a discussion see Lockwood, 1997).

A number of previous papers have examined the HF radar spectral width signatures around the dayside ionosphere through case studies. However, there have been only a few simultaneous observations of the cusp and the OCFLB using the data from magnetic conjugate radars (Pinnock *et al.*, 1999; Milan and Lester, 2001). These conjugate studies employed the data of the Polar Anglo-American Conjugate Radar Experiment (PACE) radars located at Goose Bay, Canada, and Halley, Antarctica which are a part of the SuperDARN chain (Greenwald *et al.*, 1995). In this paper, we employed another magnetic conjugate radar pair in the SuperDARN chain which is composed of the Iceland-East radar of the Coordinated U.K. Twin-Located Auroral Sounding System (CUTLASS) and Syowa-East radar of Syowa-South & East HF Radars of NIPR for SuperDARN (SENSU). For the first time, statistical characteristics of spectral width distributions in magnetically conjugate ionospheres have been compared. Consequently, significant interhemispheric differences in the characteristics of spectral width distribution are found and the statistical locations of the cusp and the OCFLB were determined in both hemispheres.

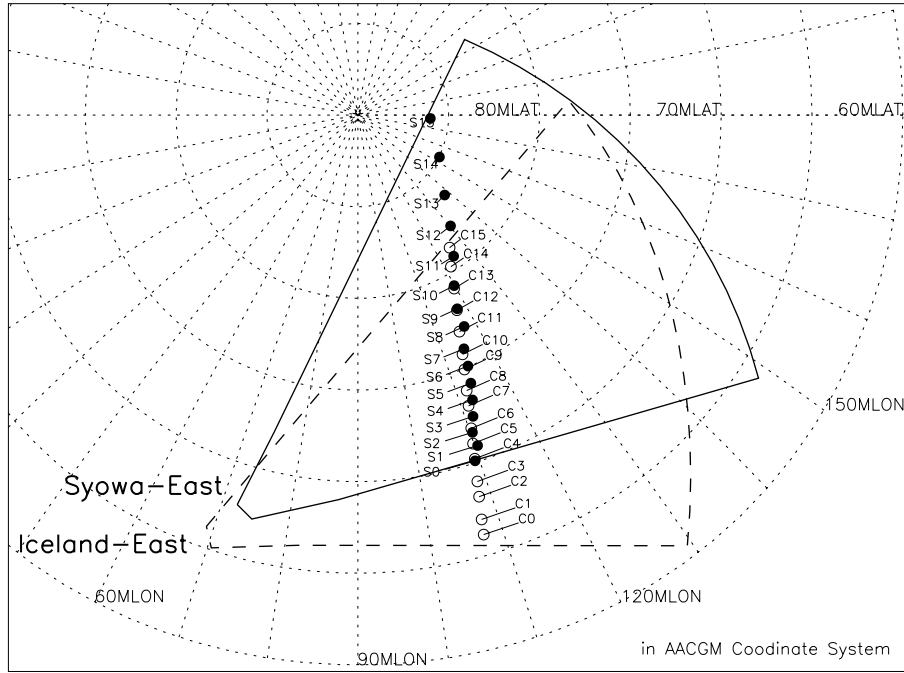


Figure III-2.1: The location of the summary point arrays within the field-of-view of CUTLASS Iceland-East and SENSU Syowa-East radars which are mapped into the AACGM coordinate system in the Northern Hemisphere. The solid fan-shaped area indicates the field-of-view of Syowa-East and dashed indicates that of Iceland-East. The summary points and the field-of-view of Syowa-East radar are mapped into the Northern Hemisphere using IGRF 95 model. Open circles indicate the summary points of Iceland-East from C0 to C15 and filled circles indicate those of Syowa-East from S0 to S15.

2.2 Database and Analysis

2.2.1 Statistics Database

Common time operation data of CUTLASS Iceland-East in the Northern Hemisphere and SENSU Syowa-East in the Southern Hemisphere have been employed for this study. In the current version of common time operation normal scan mode, the radar scans through 16 beams, each beam being binned into 75 range gates (70 range gates in the case of SENSU radars). Hence, one complete scan, which is obtained every 2 minutes, covers a fan-shaped area with 1200 cells (1120 cells for SENSU radars). To allow statistical analysis of long periods of observations, Milan *et al.* (1997) designated 16 cells from the total of 1200 as ‘summary points’ and created a database for the CUTLASS radars. In a similar way, we determined summary points and constructed a database for the SENSU Syowa-East radar. In the statistical analysis, we used the 36 months of data from January 1998 to December 2000 of CUTLASS Iceland-East and SENSU Syowa-East radars.

Figure III-2.1 presents the location of the summary point arrays in the field-of-view of CUTLASS Iceland-East and SENSU Syowa-East, which are mapped into the AACGM coordinate system (based on Baker and Wing, 1989) in the Northern Hemisphere. The summary points and the field-of-view of Syowa-East are mapped into the Northern Hemisphere using the IGRF95 model. Open circles indicate the summary points of Iceland-East (from C0 to C15) and filled circles indicate those of Syowa-East (from S0 to S15). We emphasize that the Syowa-East summary points from S0 to S11 are determined to be located to the magnetic conjugate point of the Iceland-East summary points from C4 to C15. Intersection of the two summary point arrays ranges from 70° to 81° in magnetic latitude, which lies from the average position of the LLBL to the polar cap through the

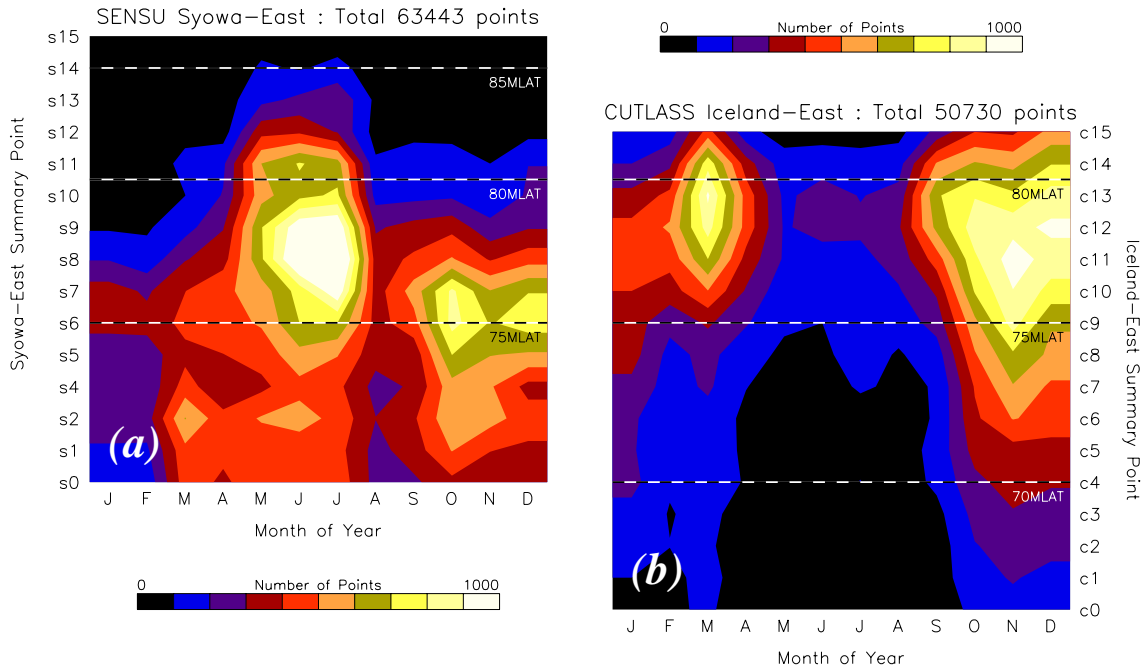


Figure III-2.2: The number of data points as a function of month obtained by (a) SENSU Syowa-East radar and (b) CUTLASS Iceland-East radar during the interval of our statistical analysis. The vertical axis indicates the summary points from S0 to S15 for Syowa-East and C0 to C15 for Iceland-East, and the horizontal axis is the month of year.

OCFLB and the cusp around the dayside ionosphere.

To clarify the characteristics of spectral width distribution in the dayside high-latitude ionospheres, we used the radar data taken in 6 hours of the magnetic local time centered at local magnetic noon (09-15 MLT). Echoes that are considered to be ground scatter were excluded on the basis of FITACF (Villain *et al.*, 1987; Baker *et al.*, 1995) analysis. Furthermore, echoes which do not have sufficiently strong signal (< 3 dB signal-to-noise ratio) were eliminated in order to remove much of the ghost scatter due to radio interference. After the elimination of non-ionospheric backscatter, we classified the spectral widths into twenty five bins covering $0-500 \text{ m s}^{-1}$, each with a range of 20 m s^{-1} , and investigated the occurrence distribution of the spectral widths.

2.2.2 Geophysical Bias

For the time interval from January 1998 to December 2000, we obtained 63,443 observations of spectral width at the summary points of the Syowa-East radar in the Southern Hemisphere and 50,730 at those of the Iceland-East radar in the Northern Hemisphere. Syowa-East radar observes about 25% more backscatter than Iceland-East radar. The occurrence of ionospheric backscatter is strongly affected by HF propagation condition mainly associated with ionospheric electron density structure (Milan *et al.*, 1997). Thus, the difference in the data points between two radars might be due to the difference in propagation condition between two hemispheres. Although there is a slight difference in the data points between two radars, the number of the data points is large enough to illustrate the average characteristics of the spectral width distribution in both hemispheres. When we process a large dataset in a statistical manner, it is very important to characterize the database. Here, geophysical biases in our database due to season and magnetic local time are examined and their effects on our statistical analysis are estimated.

All of the SuperDARN HF radars have an enhanced probability of observing ionospheric scatters around

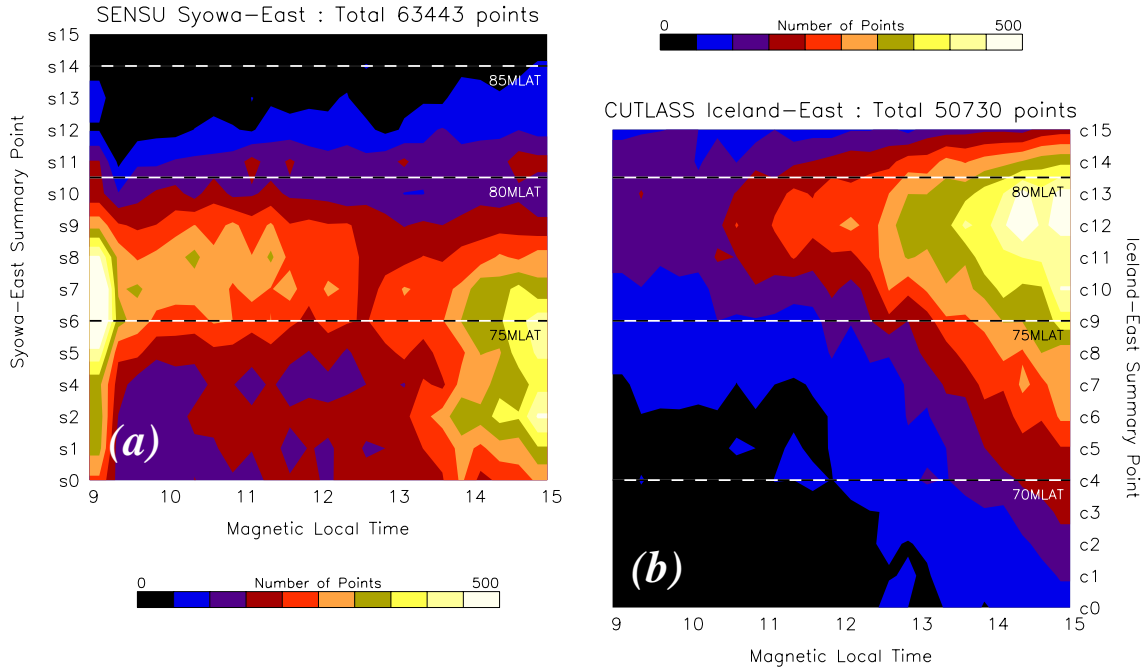


Figure III-2.3: The number of data points as a function of magnetic local time obtained by (a) SENSU Syowa-East radar and (b) CUTLASS Iceland-East radar during the interval of our statistical analysis. The vertical axis indicates the summary points from S0 to S15 for Syowa-East and C0 to C15 for Iceland-East, and the horizontal axis is the magnetic local time from 09 to 15 MLT.

dayside local time sector during winter months (Ruohoniemi and Greenwald, 1997; Milan *et al.*, 1997). This winter effect might be caused by the differences of propagation condition in sunlit and dark hemispheres or the difference in growth rate of the gradient-drift instability process which creates FAIs as a target of the HF radar backscatter (Milan *et al.*, 1997). Figure III-2.2 displays the number of data points as a function of month obtained by (a) the SENSU Syowa-East radar and (b) the CUTLASS Iceland-East radar during the interval of our statistical study. The vertical axis shows the summary points from S0 to S15 for Syowa-East (data of S3 are not displayed in this figure, because S3 has no corresponding summary point in Iceland-East) and C0 to C15 for Iceland-East, and the horizontal axis is the month of year. Since the summary points of Syowa-East are located at relatively higher latitudes compared with those of Iceland-East, Figure III-2.2 (a) is shifted by 4 summary points upward along the vertical axis. Our statistical database also exhibits an enhancement of backscatter occurrence during winter months in both hemispheres. Hence, the statistical results obtained in this study are considered to be dominated by the data observed during the winter months. However, the coverage of the data employed in this study extends from January 1998 to December 2000 and hence both radars cover three winters commonly. This suggests that this winter effect cannot be a major bias on our statistical analysis of the spectral width. On the other hand, summer data are mainly obtained by the Syowa-East at magnetic latitudes below s8 (approximately 77°). It could affect interhemispheric comparison at low latitude part of the summary point array but not within the average latitudes of the cusp.

Figure III-2.3 gives the number of data points as a function of magnetic local time, between 09 and 15 MLT, and summary points obtained by (a) SENSU Syowa-East radar and (b) CUTLASS Iceland-East radar. A large amount of data points is obtained in the postnoon sector for the case of the Iceland-East radar. This tendency is consistent with the backscatter occurrence statistics of Iceland-East radar provided by Milan *et al.* (1997). In contrast, the distribution of the data points in the Syowa-East radar is more uniform with magnetic

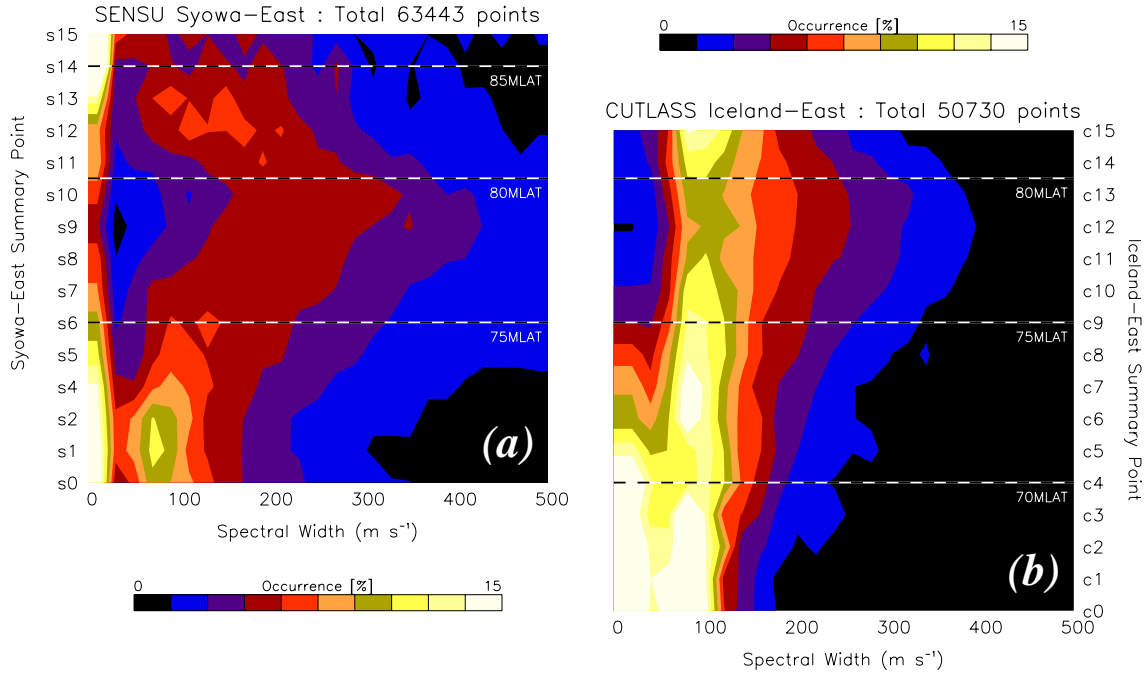


Figure III-2.4: The occurrence distribution of spectral widths observed by (a) SENSU Syowa-East radar and (b) CUTLASS Iceland-East radar. The vertical axis indicates the summary points from S0 to S15 for Syowa-East and C0 to C15 for Iceland-East, and the horizontal axis is the spectral width.

local time than that in Iceland-East. This result suggests that there is a considerable difference in data point distribution between two radars and we must keep in mind the possibility this could introduce a bias on the interhemispheric statistical analysis of spectral width. The effect of this bias on the spectral width distribution is also discussed in the next section.

2.3 Statistical Results

2.3.1 Latitudinal Variation of the Spectral Width Distribution

Figure III-2.4 gives the occurrence distribution of spectral widths observed by (a) the SENSU Syowa-East radar and (b) the CUTLASS Iceland-East radar within the magnetic local times from 09 to 15 MLT. The vertical axis shows the summary points and the horizontal axis is the spectral width. The percentage occurrence distribution for each summary point is normalized by the total number of points at that summary point. Coverage of the summary points extends from 70° to 86° for Syowa-East and from 66° to 81° for Iceland-East. Hence, the region where we can directly compare the spectral width distributions of both radars ranges from S0 to S11 in Syowa-East and C4 to C15 in Iceland-East, which corresponds to the magnetic latitudes range of 70° - 81° . One thing we must note is that the peaks of the occurrence at first spectral width bins (0 - 20 m s^{-1}) in Syowa-East data are mainly due to a contamination of ground scatter and are out of interest of this paper. This means that there exist backscatter echoes from the ground whose Doppler velocity is larger than the criterion for identifying ground scatter in FITACF procedure.

Figure III-2.4 (b) shows that the occurrences are fairly localized around the spectral width values less than 150 m s^{-1} at the magnetic latitudes below 70° , which is equivalent to the summary points between C0 and C4 in Iceland-East. Also within the magnetic latitudes between 70° and 72° , which correspond to the summary points between S0 and S2 of Syowa-East and between C4 and C6 of Iceland-East, narrow spectral width values less than

200 m s⁻¹ are dominant in both radars. These features correspond to the LLBL-type spectral width distribution as identified by Baker *et al.* (1995). Above 72° magnetic latitude, the form of the distribution gradually changes as the magnetic latitude increases and another type of distribution appears around magnetic latitudes centered at S9 in Syowa-East and C12 in Iceland-East, that is approximately 78°. Around this magnetic latitude, the occurrence rate of narrow spectral width becomes lower and spectral widths are distributed in broader range. This type of distribution is considered to correspond to the cusp-type distribution described in Baker *et al.* (1995). Transition from the LLBL-type spectral width distribution to the cusp-type is seen around the magnetic latitudes from 74° to 76° in both hemispheres. It is also worth noting that the narrow spectral width values tend to be dominant again above 80° in magnetic latitude. This tendency is most clearly seen in the Syowa-East, although there is some evidence for this in the data from Iceland-East. These observations suggest that another type of spectral width distribution exists above 80° in magnetic latitude. This type of distribution has similarities to the LLBL-type spectral width distribution, but, there exist clear differences in their characteristics. The details of these three types of spectral width distribution will be discussed in the later part of this section.

2.3.2 Longitudinal Variation of the Spectral Width Distribution

As noted in the previous section, bias due to the data point distribution with magnetic local time could affect the statistical results shown in Figure III-2.4, because we merged the data measured in the interval from 09 to 15 MLT in Figure III-2.4. Figure III-2.5 shows the variation of spectral width distribution with magnetic local time for both radars. The distributions are shown in a similar form of contour as Figure III-2.4 for three magnetic local time sectors, prenoon sector (09-11 MLT, top panels), noon sector (11-13 MLT, middle panel) and postnoon sector (13-15 MLT, bottom panels), respectively. Although the number of the data points is different between magnetic local time sectors, the general trend of the spectral width distribution is common among all magnetic local time sectors. This fact suggests that bias due to the data point distribution with magnetic local time does not affect the spectral width distribution drastically, which allows us to investigate the characteristics of spectral width around dayside ionosphere using the data obtained within the magnetic local time from 09 to 15 MLT.

2.3.3 Form of the Spectral Width Distribution

The most significant finding in Figure III-2.4 is that the spectral width distributions obtained in conjugate hemispheres exhibit the same general trend with latitude. However, the distribution of spectral widths measured by Syowa-East within the average position of the cusp (around a few degrees magnetic latitude centered on 78°) differs from that at Iceland-East. The bottom two panels of Figure III-2.6 show the histograms of the spectral width distribution at (c) S1 in Syowa-East and (d) C5 in Iceland-East. The magnetic latitudes of these summary points are approximately 71°, a latitude at which the LLBL-type distribution dominates. The distribution of spectral widths exhibits the approximate form of an exponential distribution in both hemispheres, with most values lying within the range 0 to 200 m s⁻¹. One difference at these magnetic latitudes is that the Syowa-East data have a large peak in the first spectral width bin, 0-20 m s⁻¹. This peak is due to the contamination of the backscatter echoes from the ground and has no relation to the geophysical structures in the ionosphere. Hence, there exists no considerable difference in the characteristics of the spectral width distribution between the two radars at these magnetic latitudes.

The upper two panels of Figure III-2.6 show the distribution of spectral width at (a) S9 in Syowa-East and

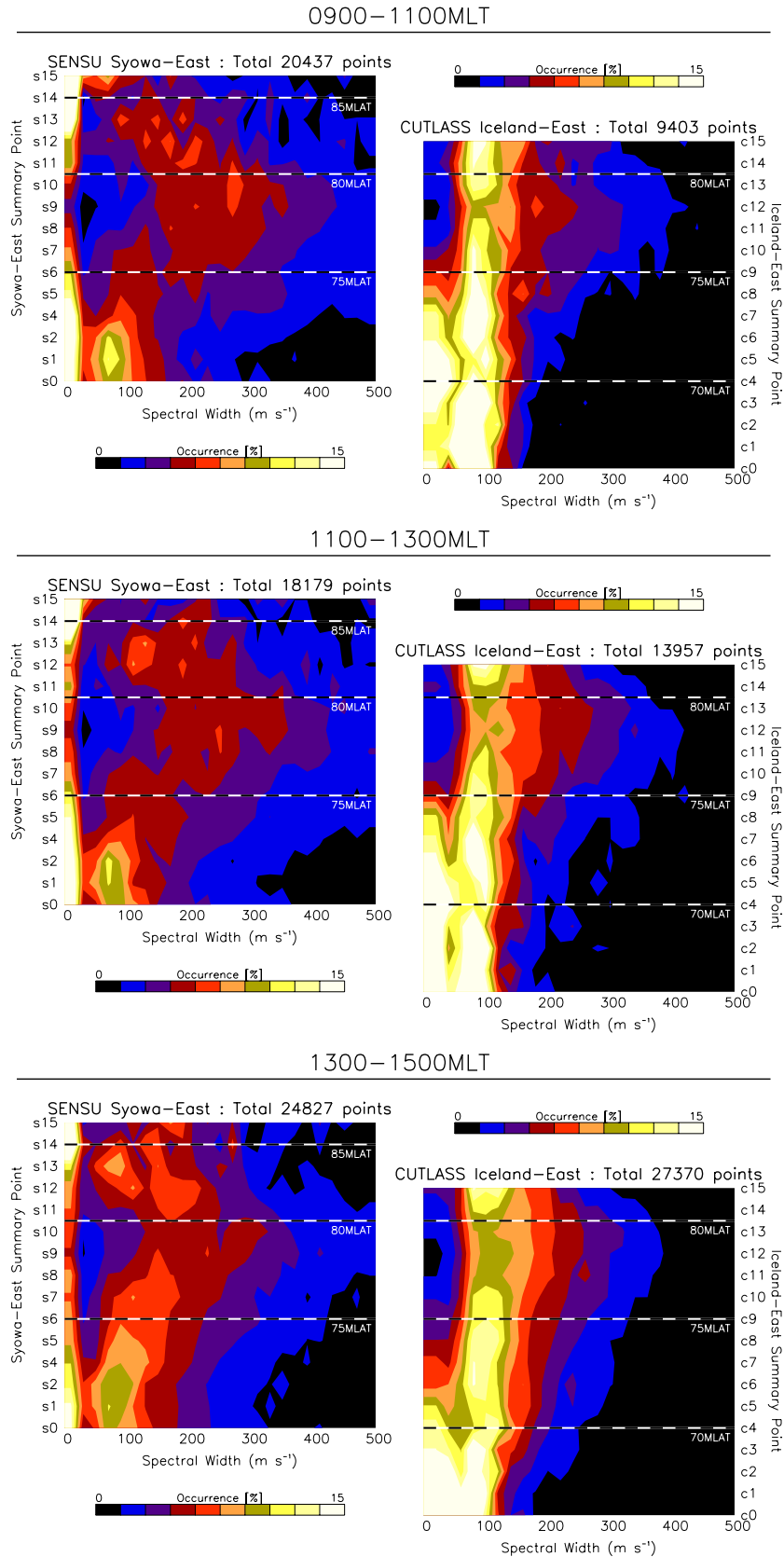


Figure III-2.5: Variation of spectral width distribution with magnetic local time. The distributions are shown in same form of contour as Figure III-2.4 for three magnetic local time sector, prenoon sector (09–11 MLT; top panel), noon sector (11–13 MLT; middle panel), and postnoon sector (13–15 MLT; bottom panel), respectively.

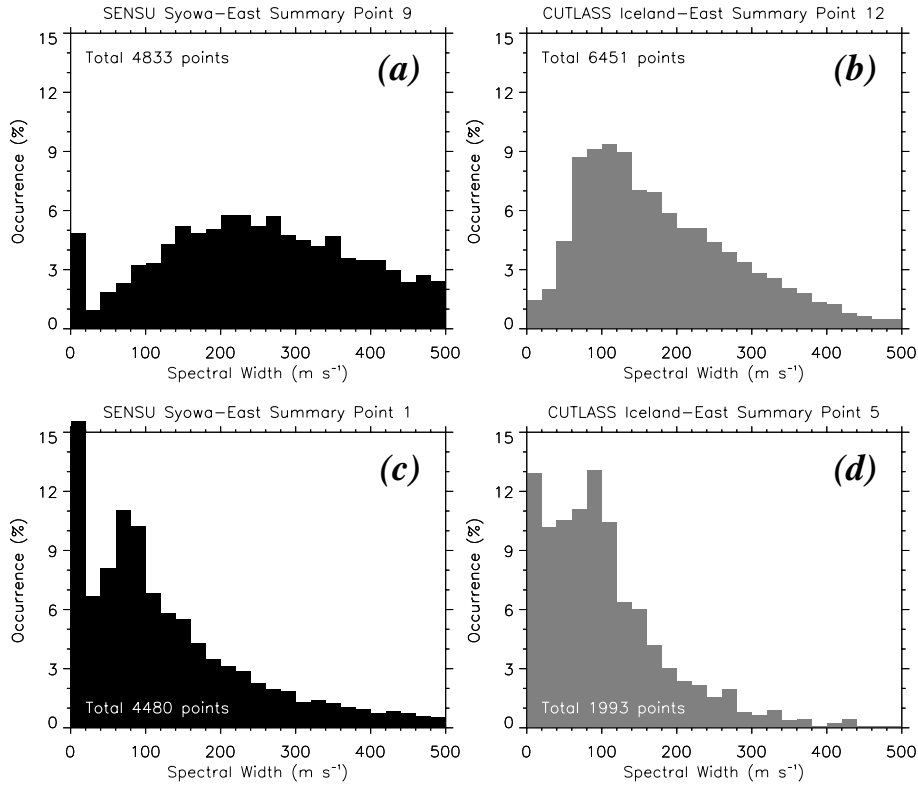


Figure III-2.6: The histogram of the spectral width distribution at (a) S9 in Syowa-East, (b) C12 in Iceland-East, (c) S1 in Syowa-East and (d) C5 in Iceland-East.

(b) C12 in Iceland-East. The magnetic latitude of these summary points is about 78° . In the case of Syowa-East, the distribution of the spectral widths is a broad Gaussian shape with the peak at about 220 m s^{-1} , which is in good agreement with the cusp-type spectral width distribution found by Baker *et al.* (1995). However, the distribution is slightly wider in comparison with the one found by Baker *et al.* (1995), i.e., percentage of very high spectral width ($> 350 \text{ m s}^{-1}$) is higher. This is because spectral width values used in this study are computed with a different version of the FITACF program than the one Baker *et al.* (1995) used in their study. Indeed, the spectral widths observed by Iceland-East are distributed in broad range from 50 to 400 m s^{-1} , however, the peak is found at 100 m s^{-1} . The spectral width values obtained from Iceland-East tend to be rather smaller than those obtained from Syowa-East and by Baker *et al.* (1995). The reason why the distributions of Iceland-East is quite different from that of Syowa-East within the cusp is discussed in the next section.

As displayed in Figure III-2.4, another type of spectral width distribution exists above 80° in magnetic latitude. This tendency is clearly seen in the Syowa-East, although there is some evidence for this in the data from Iceland-East. Figure III-2.7 shows the histograms of the spectral width distribution at S1 (shaded) and S13 (black line) in Syowa-East. This distribution has similarities to the LLBL-type spectral width distribution, but, there are the following clear differences, (i) the occurrence of broader spectral width values (above 200 m s^{-1}) is higher, (ii) the maximum of the distribution is found around above 100 m s^{-1} , slightly greater than that of the LLBL-type distribution, and (iii) the occurrence of low spectral width values (less than 100 m s^{-1}) is smaller. This feature has not been identified in previous studies and an interpretation of this type of distribution will be discussed in the next section.

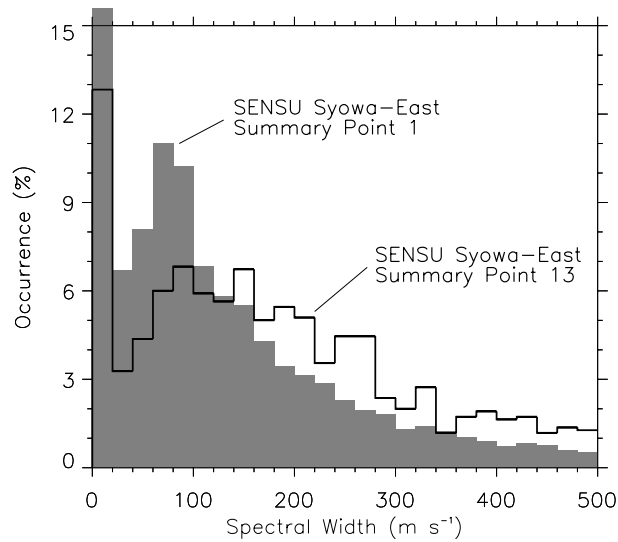


Figure III-2.7: The histogram of the spectral width distribution at S1 (shaded) and S13 (black line) in Syowa-East.

2.4 Discussion

2.4.1 Generation Mechanisms of Broad Spectral Width

To investigate the spectral width characteristics in detail, the median value of the distribution is computed for both radars and presented in Figure III-2.8. The results from Syowa-East are displayed with filled circles and those from Iceland-East are displayed with open circles, respectively. The latitudinal transition of the median value exhibits basically the same trend between conjugate hemispheres. Namely, the median of the distribution steadily increases from S0 to S10 for Syowa-East and from C0 to C12 for Iceland-East, and decreases from S10 to S14 for Syowa-East and C12 to C15 for Iceland-East. Recently, André *et al.* (1999, 2000a, 2000b) have proposed that high frequency (Pc1) wave activity associated with the cusp contains highly variable electric fields which broaden the HF radar spectra. Most of these waves are attributed to electromagnetic ion cyclotron waves generated at the dayside magnetopause in the equatorial plane. André *et al.* (2000a) also pointed out that small scale vortices of ionospheric convection, which are generated by the field-aligned current with structured soft electron precipitation from the dayside magnetosheath (Schiffler *et al.*, 1997; Huber and Sofko, 2000), can broaden the spectra around the dayside ionosphere. Since both of these activities, wave and particle precipitation, are considered to propagate into the conjugate ionospheres along the magnetic field line, the ideas proposed by André *et al.* (1999, 2000a, 2000b) can explain the interhemispheric similarity in the latitudinal trend of spectral width distribution consistently.

Present statistical analysis has also shown that there exists another type of spectral width distribution in the higher magnetic latitudes (above 80°). This distribution has similarities to the LLBL-type spectral width distribution found in the lower latitudes (below 72°), however, occurrence of broad spectral width values clearly tends to be higher. There are two possible interpretation of this distribution. One is that this distribution represents characteristics of particle precipitation peculiar to the domain poleward of the cusp, that is mantle region. Mantle region consists of very low energy ions, with a low density (Newell *et al.*, 1991). This specific nature of particle precipitation might produce the spectral width feature different from the LLBL-type and cusp-type distributions. The other is that it is a result of the ionospheric signature of the cusp precipitation

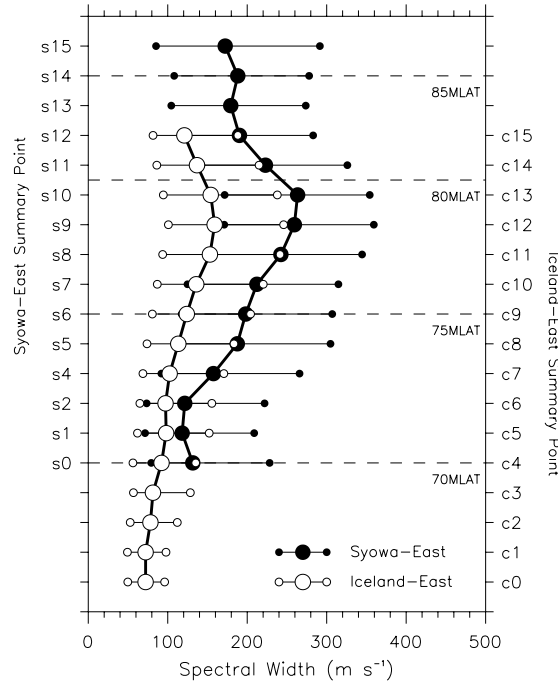


Figure III-2.8: The median value of the spectral width distribution for Syowa-East and Iceland-East. The results from Syowa-East is displayed as a line with filled circles, those from Iceland-East being displayed as a line with open circles. Filled small circles indicate the upper quartile and lower quartile, respectively.

during northward IMF. During the period of northward IMF, the cusp is generally located at higher magnetic latitude and characteristics of the cusp precipitation is also expected to be different from that for southward IMF case. Since our statistical analysis merged northward and southward IMF conditions, this might affect the spectral width distribution at the higher latitude regime.

2.4.2 Interhemispheric Differences in Spectral Width Values

As shown in Figure III-2.6 and Figure III-2.8, there exists a interhemispheric difference in the spectral width characteristics around the average latitudes of the cusp, although the latitudinal trend of the spectral width distribution exhibits basically the same behavior. The form of the distribution is slightly different and the median of the distribution obtained from Syowa-East is larger than that from Iceland-East, in particular the difference reaches 100 m s^{-1} around 78° . This kind of interhemispheric asymmetry in the spectral width characteristics was also reported on a case study basis by Milan and Lester (2001). They employed the other conjugate radar pair composed of SuperDARN Goose Bay and Halley radars and demonstrated that spectral width values obtained in the Southern Hemisphere are larger than those in the Northern Hemisphere.

First, we discuss the possibility of instrumental effects, such as the difference in beam width or noise level, on this interhemispheric asymmetry. If the interhemispheric difference in our statistics is due to an instrumental effect, the difference has to be found commonly at all magnetic latitudes. However, the difference in spectral width values is smaller around the magnetic latitude below 72° , differences in median values being approximately less than 30 m s^{-1} . Also, form of the distributions within the lower magnetic latitudes of the summary point arrays are quite similar between two hemispheres. This fact suggests an instrumental effect does not make a significant contribution to the interhemispheric asymmetry in spectral width distributions.

Next, we discuss the effect of contamination by non F region backscatters. SuperDARN radars often observe

the spectra that includes several sources such as F region scatter, E region scatter and ground scatter. Milan *et al.* (1997) reported that Type I E region backscatter echoes as well as F region backscatter can be observed at far radar ranges during winter months. Barthes *et al.* (1998) demonstrated that if the spectra is composed of both ionospheric and ground scatter, spectral width value derived from FITACF analysis contains error. Chisham and Pinnock (2002) also pointed out that contamination by non F region backscatter contributes to the velocity determination of SuperDARN observations. In our statistical analysis, however, interhemispheric difference of median value is up to 100 m s^{-1} (see Figure III-2.8), which is considered to be too large to be explained only by the contamination of non F region backscatters. Also, as is not shown in this paper, contaminations by ground and E region backscatters are commonly found in the observations of Iceland-East and Syowa-East, which also confirms that the effect of non F region backscatter makes minor contribution on the interhemispheric difference in spectral width distribution.

The other possibility is that the spectral width distribution around 78° magnetic latitude in the Northern Hemisphere is a mixture of the cusp-type and LLBL-type distributions while that in the Southern Hemisphere is dominated only by the cusp-type spectral width distribution. The summary points of Iceland-East and Syowa-East are magnetically conjugate, however, their geographic latitudes and longitudes are slightly different. This displacement could cause the difference in radio wave propagation path or scattering condition. Hence, Iceland-East radar could observe LLBL-type spectral width feature even in the average latitude of the cusp.

In addition to the contribution by the high frequency wave activity and small scale convection vortex created by soft particle precipitation, gradient in velocity distribution which results from geometry of the radar with respect to the large scale convection pattern also broaden the HF radar spectra (Barthes *et al.*, 1998; André *et al.*, 2000b). Milan *et al.* (2001) demonstrated that the dayside convection pattern could exhibit considerable asymmetries between summer and winter hemispheres as a consequence of the biases in the reconnection geometries available at the subsolar magnetopause. Pinnock *et al.* (1999) also presented there exists a considerable interhemispheric difference in convection velocity around dayside ionosphere. These observational facts are confirmed by modeling work by Coleman *et al.* (2000). This effect is imposed by the tilts of the dipole and rotation axes relative to the Sun-Earth line. As mentioned before, the summary points of Iceland-East and Syowa-East are magnetically conjugate, however, their geographic latitudes and longitudes are different, which might cause an interhemispheric asymmetry in plasma convection patterns observed by the conjugate radars. If the plasma convection has an asymmetry between both hemispheres, observed spectral widths also could exhibit considerable difference between conjugate ionospheres by the effect of gradient in velocity distribution estimated by André *et al.* (2000b). However, we investigated three whole years of spectral width observation in a statistical fashion. Hence, it is still an open question whether difference of ionospheric convection could contribute to the interhemispheric asymmetry of spectral width characteristics even in statistical description. Statistical analysis of spectral width using other conjugate radar pair is needed for the further understanding of this interhemispheric difference.

2.4.3 Comparison with the Other Observations

We now turn to the identification of the cusp and the OCFLB from the HF radar spectral width characteristics. In Figure III-2.8, the median of the distribution has its maximum at S10 of Syowa-East and C12 of Iceland-East, where magnetic latitude $\approx 78^\circ$. This could be regarded as the statistical location of the cusp center as determined by the HF radar spectral width characteristics, which is in good agreement between conjugate hemispheres. Newell and Meng (1992) employed the data of DMSP satellites dayside passes and clarified the average position

of the cusp statistically. They found that the particle precipitations peculiar to the cusp are observed in a region between latitudes of 75° and 82° , with the center approximately 78° . The statistical location of the cusp center identified by the HF radar and the DMSP is fairly consistent in both hemispheres. Furthermore, the latitude at which the spectral width distribution begin to return to exponential-like distribution again is similar to the poleward limit of the particle precipitation cusp. These facts confirm that the identification of the cusp using HF radar spectral width characteristics is valid for the study of magnetosphere-ionosphere coupling process in addition to the other observations such as the particle precipitation and the aurora.

In the study of case examples (e.g., Baker *et al.*, 1997; Pinnock *et al.*, 1999), well-defined boundary between narrow spectra at lower latitude and broad spectra at higher latitude has been used as a proxy for the OCFLB. This suggests that the transition region between the LLBL-type and the cusp-type spectral width distributions is considered to be the dayside OCFLB in a statistical sense. It is, however, still considerable debate whether the LLBL is on open or closed field lines (for a discussion see Lockwood, 1997). Hence, we must keep in mind that our statistical estimation of the OCFLB location using spectral width is on the assumption that the LLBL is on closed field line. The latitudinal location of the OCFLB is highly controlled by the state of the dayside reconnection at the magnetopause triggered by the north-south component of the IMF. Also, magnetic latitude of the OCFLB is expected to vary with magnetic local time mainly by the effect of east-west component of IMF (Rodger, 2000). Hence, the exact location of the OCFLB cannot be determined by the present statistical analysis because the data have not classified by the IMF orientation and magnetic local time sector. However, we can roughly estimate the magnetic latitudes where the OCFLB is normally formed. On the basis of the statistical results from Syowa-East, the distribution starts to change remarkably at the magnetic latitude between S5 and S7. These summary points correspond to the magnetic latitudes between 74° and 76° .

2.5 Summary

Characteristics of the spectral width distribution were investigated using the conjugate radar pair composed of CUTLASS Iceland-East in the Northern Hemisphere and SENSU Syowa-East in the Southern Hemisphere.

Three types of spectral width distribution were identified, (i) an exponential-like distribution in the lower magnetic latitudes (below 72°), (ii) a Gaussian-like distribution around a few degrees magnetic latitude centered on 78° , and (iii) another type of distribution in the higher magnetic latitude (above 80°). The first two are considered to represent the LLBL and the cusp respectively because they are similar to the spectral width distributions within the LLBL and the cusp classified by Baker *et al.* (1995). The distribution found poleward of the cusp has been clarified for the first time in this study. This distribution has similarities to the exponential-like distribution in the lower latitude part of the radar observation, however, there exist clear differences in their characteristics.

These features were commonly identified in conjugate hemispheres. The latitudinal transition of the distribution exhibits basically the same trend between two hemispheres, but, there is an interhemispheric difference in the form of the distribution within the cusp such that the spectral width values obtained from Syowa-East are larger than those from Iceland-East. Average locations of the cusp and the open/closed field line boundary (OCFLB) are determined from the spectral width characteristics. The average position of the cusp center is found to be 78° in magnetic latitude which is consistent with the result from the DMSP satellite observation by Newell and Meng (1992). Also, the OCFLB is identified to be positioned within the magnetic latitudes between 74° and 76° .

Chapter 3

Origin of the SuperDARN Broad Doppler Spectra: First Observational Evidence from Oersted Satellite Magnetometer

3.1 Introduction

The HF coherent scatter radars of the Super Dual Auroral Radar Network (SuperDARN, Greenwald *et al.*, 1995) often observe broad, complex Doppler spectra within the dayside and nightside high-latitude ionosphere. Baker *et al.* (1995) pointed out that the dayside polar cusp as defined by low-altitude satellite particle precipitation data (e.g., Newell and Meng, 1991) is characterized by these broad and complex Doppler spectra in the coherent HF radar observations. They also showed that regions equatorward of the cusp are usually found to have narrow Doppler spectra dominated by a single component. The equatorward edge of these HF radar backscatters with broad spectra appears to correspond closely to the equatorward edge of the red line (630 nm) aurora during the period of negative IMF Bz (Rodger *et al.*, 1995; Milan *et al.*, 1999; Moen *et al.*, 2001). These observational facts enable recent studies to use the boundary between narrow and broad Doppler spectral widths (hereinafter referred to as spectral width boundary: SWB) as a proxy for the open/closed field line boundary (OCFLB) within the dayside ionosphere. This relationship has been widely employed to estimate several geophysical parameters such as (i) reconnection electric field (Baker *et al.*, 1997; Pinnock *et al.*, 1999); (ii) the form and size of polar cap (Chisham *et al.*, 2001; Milan *et al.*, 2002b); (iii) the creation and destruction rate of open magnetic flux associated with the dayside and nightside reconnection. However, our knowledge about the origin of the HF radar broad Doppler spectra is still not sufficient.

In general, these broad spectra could be related to both temporal variability of the convection electric field and spatial inhomogeneity of the plasma convection within a single radar range cell. André *et al.* (1999, 2000a, 2000b) theoretically modeled the impact of various kind of physical processes on the width of the HF radar Doppler spectra. They concluded that the broad spectral widths observed in the dayside high-latitude ionosphere result predominantly from time-varying electric field in the Pc1-2 frequency range, whereas the other factors such as the velocity shears within the radar cells and micro-scale turbulence also make an additional contributions. The fluctuating electric field employed in their modeling and accompanying magnetic field fluctuations are continuously observed in vast area of the dayside high-latitude region by low-altitude (e.g., Maynard *et al.*, 1982; Maynard, 1985; Maynard *et al.*, 1991; Erlandson and Anderson, 1996) and polar-orbiting (e.g., Matsuoka *et al.*, 1991; 1993) satellites. However, one to one relationship between the HF radar broad spectral width and the electric and magnetic field fluctuations has not been confirmed by substantial observations. In this study, we have investigated high-resolution magnetic field observation from the Oersted satellite in conjunction with the broad spectral width as observed by the SuperDARN Syowa-East radar in Antarctica. Consequently, we have found very close relationship between the broad spectral width and the magnetic field fluctuations within

the dayside ionosphere during an interval of negative IMF Bz.

3.2 Instrumentations

This paper presents a single event of the SWB observation from the SENSU (Syowa-East radar of Syowa-South & East HF Radars of NIPR for SuperDARN) Syowa-East radar in Antarctica (69.01°S; 39.61°E). The radar is a part of the SuperDARN, which covers a vast portion of the Northern and Southern auroral zones and polar cap. On the day presented in this paper (January 22, 2000), the radar was operating in a normal scan mode. In the current version of this scan mode the radars carry out azimuthal sweeps through discrete beam pointing directions that are numbered 0-15 with a step in azimuth of approximately 3.33°. It takes approximately 7 s to integrate backscatter returns in one direction and about 2 min are needed to do a scan of all directions. In SENSU radars, 70 range gates are sampled for each beam with a pulse length of 300 μ s, which is equivalent to a gate length of 45 km, and a lag to the first gate of 1200 μ s (180 km). In this configuration the maximum range of the radars is approximately 3550 km. Hence, the radar field-of-view in each scan contains 1120 cells (70 ranges \times 16 beams). A seven pulse scheme is transmitted and analysis of the auto-correlation function (ACF) of the returned signals (FITACF; see Baker *et al.*, 1988 and Villain *et al.*, 1987) yields backscatter power, Doppler velocity and spectral width.

The Oersted satellite was launched on February 23, 1999 into a polar orbit whose inclination is 96.5°. The ascending node was initially located at 1411 LT. The orbital plane drifts at a rate of -0.88 min per day. The initial perigee and apogee were 638 km and 849 km, respectively. The orbital period is about 100 min. The magnetometer data used in this analysis are the radial (r), southward (θ), and eastward (ϕ) components sampled at every 39.25 ms (approximately 25 Hz). The original data are described in the geographic coordinates and the data used in this analysis are transformed into the geomagnetic dipole coordinates. The residuals (ΔB_r , ΔB_θ and ΔB_ϕ) from the geomagnetic main field were calculated by using the Oersted (10c/99) model. The Oersted (10c/99) model is a geomagnetic main field model which consists of the OIFM (the Oersted initial field model, Olsen *et al.*, 2000) and secular variation.

3.3 Observations

The top panel of Figure III-3.1 shows variation of the IMF Bz monitored by ACE spacecraft located upstream of the Earth's magnetosphere ($X_{\text{gsm}}=239.79$, $Y_{\text{gsm}}=14.70$, $Z_{\text{gsm}}=18.98$). An approximate solar wind velocity of 380 km s $^{-1}$ measured by the spacecraft gives a delay of 74 minutes between the observation of IMF feature and their incidence on the Earth's magnetopause (calculation is based on the method outlined by Khan and Cowley, 1999). The IMF Bz component was predominantly negative for the entire interval, except for a brief positive excursion at 0632 and 0650 UT.

The bottom panel presents the spectral width observed along beam 5 of the SENSU Syowa-East radar from 0530 to 0730 UT on January 22, 2000, where only backscatters from the ionospheric irregularities are shown (i.e., echoes regarded as a ground scatter have been eliminated). The spectral width is colour-coded with blue representing the narrowest spectral widths and red indicating the widest. Vertical dashed line indicates the time when the Oersted satellite traversed the radar field-of-view at 0622 UT. During the interval of the Oersted overpass, the broad spectral width region at higher latitude (characterized by a mixture of the colours such as yellow and red) is clearly distinct from the narrow spectral width region at lower latitude (characterized by an almost uniform blue appearance), and well-defined SWB can be identified.

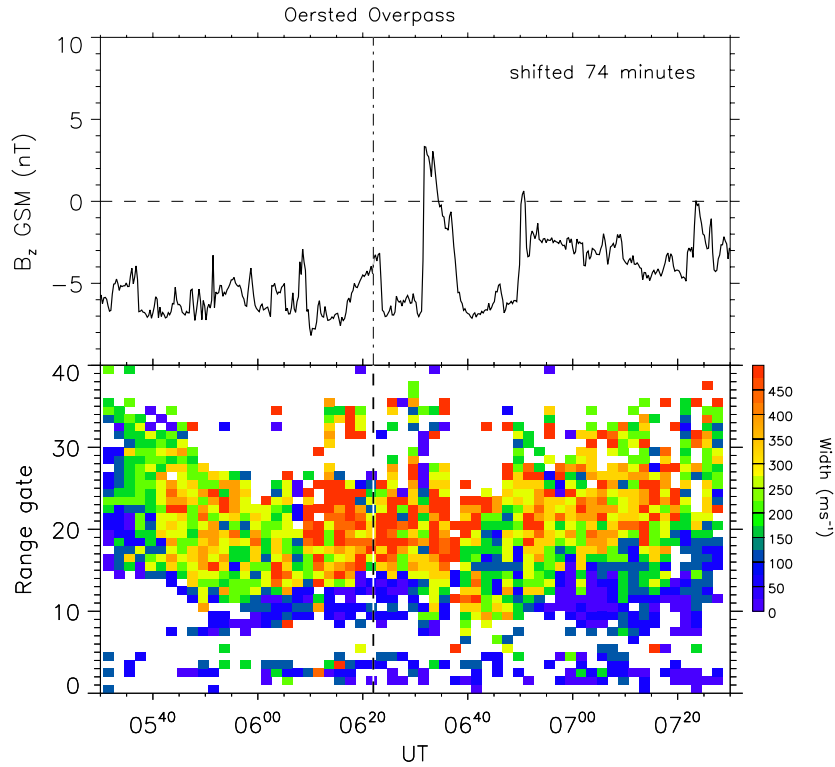


Figure III-3.1: (Top) B_z component of the IMF as measured by the ACE spacecraft lagged to the magnetopause. (Bottom) spectral width observed along beam 5 of the SENSU Syowa-East radar during the interval of the present study, 0530 to 0730 UT, January 22, 2000. Vertical dashed line indicates the time of the Oersted crossing of the spectral width boundary at 0622 UT.

Figure III-3.2 displays map of the spectral width at 0622 UT in a magnetic latitude and local time coordinate system (AACGM geomagnetic coordinate system based on Baker and Wing, 1989) as observed by all of the beams of the SENSU Syowa-East radar. Overlaid is the footprints of the Oersted spacecraft mapped down to the altitude of the SuperDARN observations (assumed to be 400 km in this case) using Tsyganenko 96 model (Tsyganenko, 1995). SWB is observed in the dawn meridian between 0620 and 0820 MLT, and it clearly exhibits L-shell aligned structure. Dashed line traces approximate position of the SWB, magnetic latitude being approximately 71.5° . The spacecraft is flying from high-latitude region to the low-latitude and crosses the SWB at 0622 UT (magnetic local time ≈ 0745 MLT). In the next part of this section, we compare the magnetic field data obtained from Oersted and structure of the SWB for the interval of the approach of the satellite to the SWB.

Figure III-3.3 shows three components of high time resolution magnetic field observation from the Oersted spacecraft around the crossing of the SWB (from 0617 to 0626 UT). Grey-shaded bars at the bottom of each panel display standard deviation of the variation calculated for every 2 seconds duration (i.e., 50 samples). Vertical dashed line indicates the time when Oersted crosses the SWB. It is found that fluctuating magnetic field is observed before the crossing of the SWB. These fluctuations suddenly cease just after the SWB crossing. This sudden change is most clearly seen in the variation of the standard deviation. Fluctuations are observed in all components, however, they are more prominent in θ (north-south) and ϕ (east-west) components rather than that in the r (radial) component.

The other thing worth noting is that the level of fluctuations are also low in the highest latitude part of the Oersted track. Because there exists a data gap from 0618 50 s UT to 0619 32 s UT, we can not determine

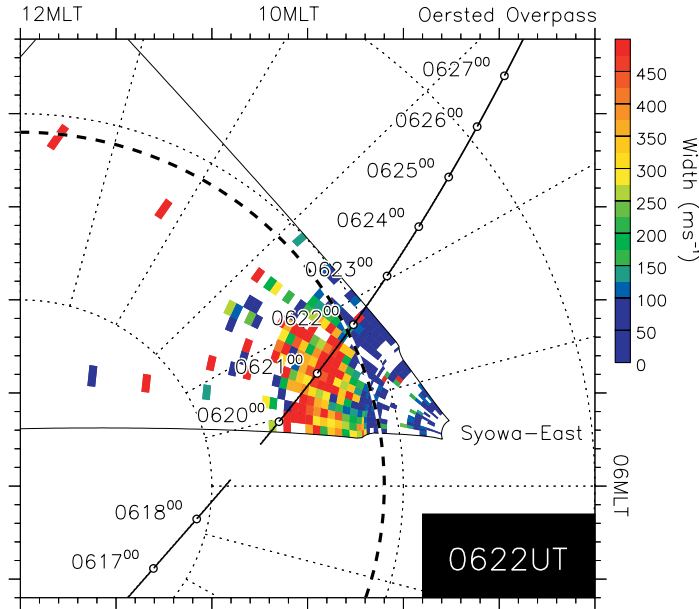


Figure III-3.2: Map of spectral width as observed by all of the beams of the SENSU Syowa-East radar at 0622 UT in a magnetic latitude and magnetic local time coordinate system. Overlaid black line is the footprints of the Oersted spacecraft mapped down to the altitude of the SuperDARN observations using Tsyganenko 96 model. Dotted circle traces an approximate location of the spectral width boundary.

when the fluctuation started to be observed exactly. However, large amplitude fluctuating magnetic fields are not seen in the magnetic latitude above 80° . This characteristic is consistent with the past observations of the fluctuating electric field (e.g., Maynard *et al.*, 1991; Matsuoka *et al.*, 1993). Another point is that the magnetic field fluctuations and large-scale field aligned current structure seem to have a relationship. Large positive variation is identified in the east-west component around the SWB, which suggests that a large-scale field-aligned current pair exists near the boundary of the fluctuation and spectral width. The changes in ΔB_θ are small compared with those in ΔB_ϕ , indicating that the current sheet is nearly parallel to the L-shell.

In order to clarify the dominant frequency band of the fluctuations seen in the Oersted observation, dynamic spectra of ΔB_θ component in frequency range between 0.2 Hz and 5 Hz are displayed in the bottom panel of Figure III-3.4, where the Fourier transform interval is 10.08 s (corresponding to 256 samples). An expanded plot of ΔB_θ component around the SWB (1 minute interval from 0621 30 s to 0622 30 s UT) is also presented in the top panel of Figure III-3.4 for comparison. Vertical dashed line in each panel gives the time when the satellite traverses the SWB. It is again clearly found in the top panel that the fluctuation suddenly terminates when the satellite crosses the SWB. Equatorward boundary of the fluctuation is considerably sharp, which is consistent with the previous observations (e.g., Maynard *et al.*, 1991). Spectral characteristics of these fluctuations have no distinct frequency peak and tend to be broadband, however, contribution becomes smaller as the frequency increases. This feature is basically in good agreement with the previous studies of the fluctuating electric field within the cusp (e.g., Maynard *et al.*, 1985).

3.4 Discussion

Intense electric and magnetic field fluctuations in Pc1 frequency range have been observed over the dayside cusp by low-altitude, polar-orbiting satellites (Sugiura *et al.*, 1982; Maynard *et al.*, 1982; Maynard, 1985; Maynard *et al.*, 1991; Matsuoka *et al.*, 1991; Ishii *et al.*, 1992; Matsuoka *et al.*, 1993; Erlandson and Anderson, 1996).

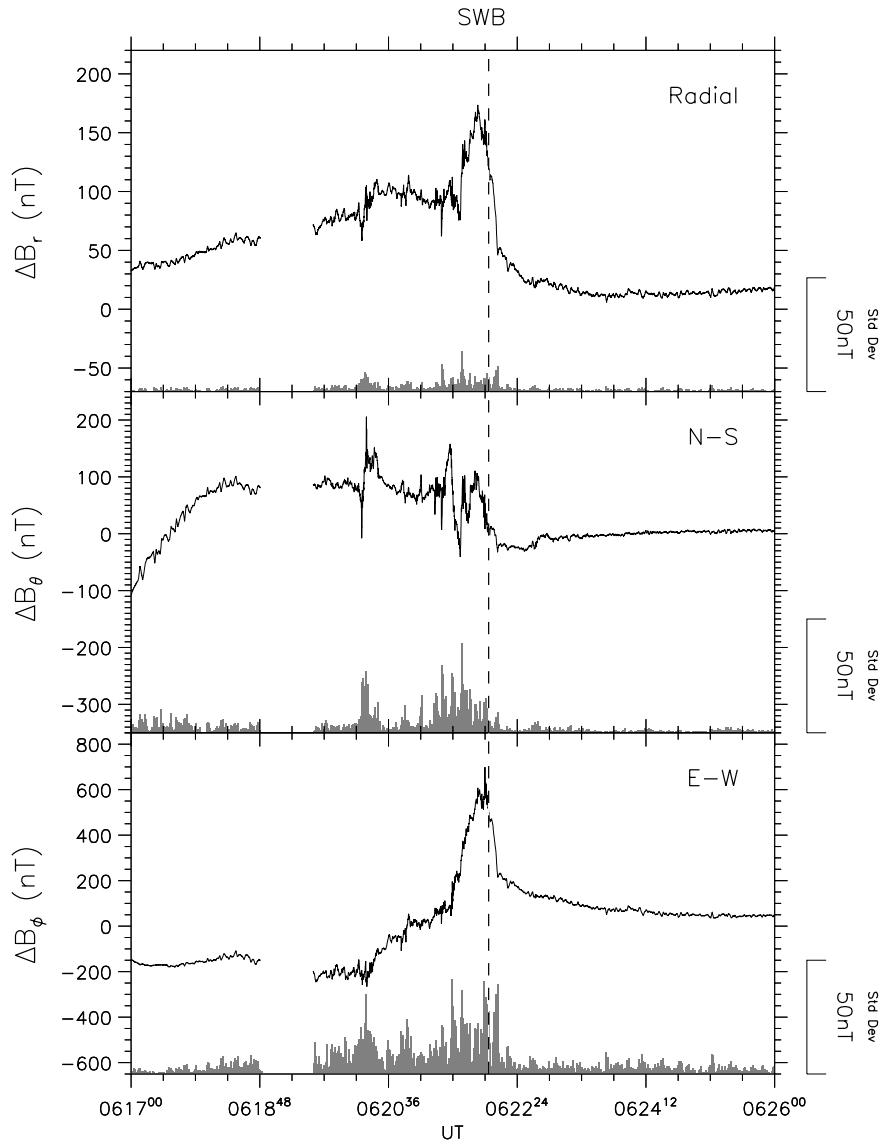


Figure III-3.3: Three components of high time resolution magnetic field observation from the Oersted satellite around the crossing of the spectral width boundary, from 0617 to 0626 UT. Grey-shaded bars at the bottom of each panel display standard deviation of the variation calculated for every 2 seconds duration (i.e., 50 samples). Vertical dashed line indicates the time when the Oersted crosses the spectral width boundary.

These observations indicate that the orthogonal components of the magnetic and electric field perturbations are highly correlated. The present observation has shown that highly fluctuating magnetic field is observed in the vicinity of the broad spectral width region. Especially, equatorward boundary of the fluctuation is closely corresponding to the SWB in the radar observations. These observational facts are suggesting that HF radar broad spectral width is likely to be associated with the same kind of fluctuations in electric field.

The other important issue to be discussed is that the level of magnetic field fluctuation is low also in the magnetic latitudes above 80° . In the previous chapter, we have carried out a statistical analysis of HF radar spectral width and have reported that the spectral width is small above 80° magnetic latitudes. McWilliams *et al.* (2001) investigated poleward moving pulsed ionospheric flows (PIFs) in the HF radar data and pointed out that the spectral widths are relatively high at the equatorward edge of the PIFs, but decrease with increasing latitude. Milan *et al.* (2002a) analyzed HF radar polar patches and clearly showed that spectral width within

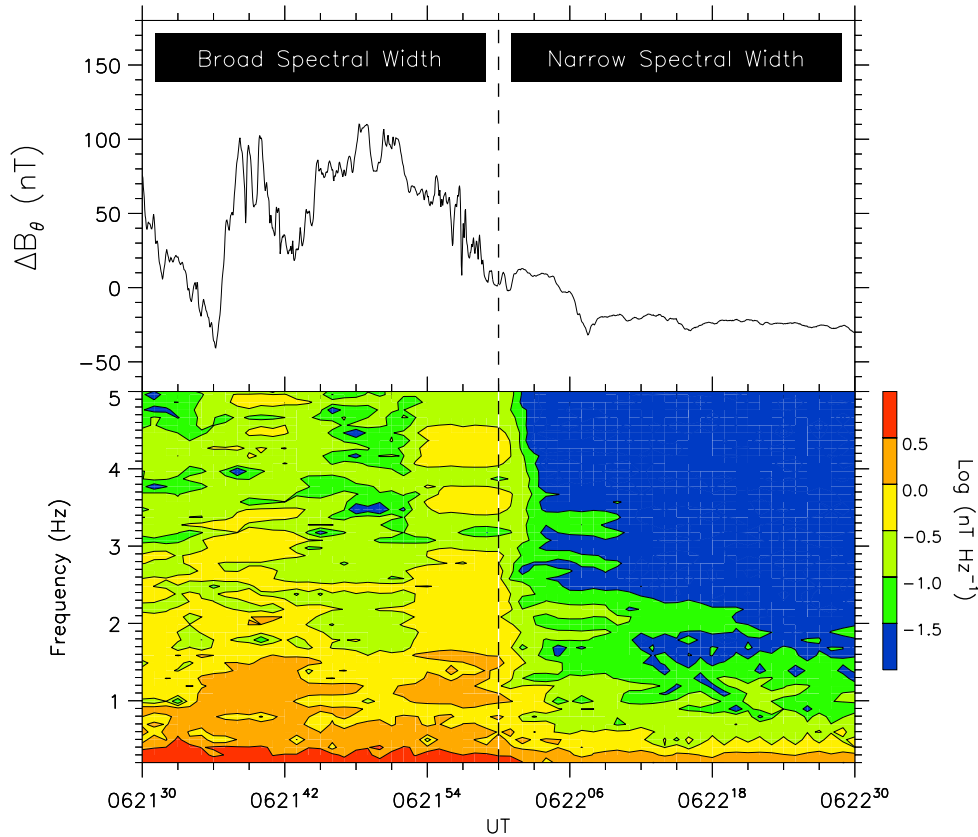


Figure III-3.4: (Top) an expanded plot of ΔB_θ component (1 minute interval from 0621 30 s to 0622 30 s UT). (Bottom) dynamic spectra of ΔB_θ component in frequency range between 0.2 and 5 Hz. Vertical dashed line indicates the time when Oersted crosses the spectral width boundary at 0622 UT.

the patch becomes considerably narrow as it moves poleward. The nature of the fluctuating magnetic field observed in the present study is in good agreement with the low spectral widths at the highest part of the HF radar observation commonly identified in the previous studies.

Origin of these fluctuating field is still considerable debate. Two models for the generation of these fluctuations have been put forward. The first one assumes that the fluctuations are observed due to the orbital motion of the satellite through small-scale quasi-static field-aligned current structures embedded in the large-scale field-aligned current (Smiddy *et al.*, 1980; Sugiura *et al.*, 1982; Ishii *et al.*, 1992). This is a space and time ambiguity in the satellite observation, not an actual wave in the ionosphere. As for the frequency range of 0.6 Hz (one of the dominant frequency band in Figure III-3.4), spatial scale length of the fluctuations is approximately 11 km. This length is well below the size of a radar range cells (≈ 45 km). These small-scale FACs are capable of producing small-scale vortex structure in the convective flow pattern of the ionosphere plasma. Some previous studies of HF radar spectra have attributed double-peaked spectra to vortices less than the scale size of the radar range cells (Schiffler *et al.*, 1997; Huber and Sofko, 2000). André *et al.* (2000b) pointed out that the vortices smaller than the size of the radar range cells could also produce broad and complex Doppler spectra.

The second one suggests that disturbances in the distant magnetosphere are transmitted to the ionosphere as Alfvén waves (Lysak and Dum, 1983). Matsuoka *et al.* (1993) emphasized from the polar-orbiting satellite EXOS-D measurement that the electric to magnetic field ratios in the frequency range of 0.5-3 Hz agree well with the Alfvén velocity at the observation point. In general, it is difficult to distinguish between temporal and spatial variation in the satellite observation. However, Ishii *et al.* (1992) demonstrated that the Alfvén wave

model is applicable to variations of scale lengths less than 4.0 s, while effect of the quasi-static model becomes increasingly dominant for scale length greater than 8.0 s. Hence, as for the dominant frequency range of the fluctuation as displayed in Figure III-3.4, primary source of the fluctuation is considered to be the downward propagating Alfvén waves.

Next, we consider a relationship among various kind of observations such as the fluctuating electric and magnetic field, precipitating ion and electron, 630 nm cusp auroral luminosity, and HF radar broad spectral width. Maynard *et al.* (1982) have mentioned that the region of highly variable electric fields observed below 900 km altitudes on the dayside high-latitude region is associated with large fluxes of low energy electrons and field-aligned current structures. Matsuoka *et al.* (1993) have investigated the correlation between wave activities and enhancement of the flux of precipitating ions and electrons simultaneously observed by EXOS-D satellite. They reported that when the latitude of the cusp is low and IMF is expected to be southward the correlation coefficient is high, while the correlation is poor when the latitude of the cusp is high and IMF is expected to be northward. This fact suggests that the waves are observed in association with the injection of particles into the magnetosphere when the IMF B_z is negative and low-latitude reconnection occurs.

On the other hand, previous studies have shown that the equatorward edge of the radar backscatter showing broad Doppler spectral width is coincident with the equatorward edge of the cusp particle precipitation (Baker *et al.*, 1995; Yeoman *et al.*, 1997) and the 630 nm cusp auroral emissions (Rodger *et al.*, 1995; Milan *et al.*, 1999; Moen *et al.*, 2001). However, Moen *et al.* (2001) pointed out from a comparison of dayside auroral activity and HF radar backscatter that this good relationship breaks down for northward IMF conditions. The present observation firstly evidenced that HF radar broad Doppler spectral width is closely connected with time-varying electric and magnetic field possibly associated with particle precipitation during southward IMF B_z conditions. Taking into account of these observational results, we can speculate that HF radar broad Doppler spectral width represents characteristics of cusp particle precipitations and corresponding 630 nm auroral emissions via reconnection-induced electric and magnetic field fluctuation for the case of the southward IMF conditions.

3.5 Summary

Doppler spectral width observed by the SuperDARN radars and magnetic field fluctuations observed by the Oersted satellite magnetometer were compared during an interval of the negative IMF B_z condition. The radar observed L-shell aligned spectral width boundary around the dayside ionosphere. Simultaneously, Oersted observed high-frequency (0.2-5 Hz) magnetic field fluctuation. These magnetic field fluctuations are considered to be Alfvén wave possibly associated with the particle which precipitates into the dayside high-latitude ionosphere when reconnection occurs. It has been theoretically predicted that time-varying electric field is the dominant physical process to produce the broad radar Doppler spectral width (André *et al.*, 2000a). Our observation clearly demonstrated that the boundary between narrow and broad spectral widths is well corresponding to the boundary in the level of the fluctuations, which can provide a direct evidence for the previous theoretical prediction. A close relationship between electric and magnetic field fluctuations and particle precipitations during southward IMF conditions has been confirmed by many authors. We suggest that the boundary between narrow and broad Doppler spectral widths observed in the dayside ionosphere is connected with the signature of the open/closed field line boundary such as the cusp particle precipitations and the red line (630 nm) auroral emissions via electric and magnetic field fluctuations for the case of the negative IMF B_z conditions.

Chapter 4

Interhemispheric Comparison of Spectral Width Boundary as Observed by the SuperDARN Radars

4.1 Introduction

It is very important for the study of magnetosphere-ionosphere coupling processes to identify the location of the open/closed field line boundary (OCFLB) in the ionosphere. Determining the OCFLB around the dayside ionosphere enables us to estimate several geophysical parameters such as (i) the rate of reconnection at the magnetopause; (ii) the size of polar cap; (iii) the creation and destruction of open magnetic flux associated with the dayside and nightside reconnection. In practice, however, the OCFLB can be difficult to locate in the ionosphere continuously. There are a number of signatures which can be employed as proxies for the OCFLB, although some of these still require verification (Rodger, 2000). Direct observations of cusp particle precipitation by low-altitude spacecraft such as DMSP (e.g. Newell and Meng, 1988, 1991) are most widely utilized as a proxy for the OCFLB. The optical auroral signature triggered by the cusp particles precipitation has also been a good guide for the identification of the OCFLB (Sandholt *et al.*, 1998). The dayside auroral zone provides a good target for HF radars (Milan *et al.*, 1998) and a relationship between the magnetospheric cusp particle precipitation into the ionosphere and the HF radar backscatter from the ionospheric F region has been reported by a number of authors (Baker *et al.*, 1990, 1995; Rodger *et al.*, 1995; Yeoman *et al.*, 1997). They demonstrated that the equatorward edge of radar backscatter showing broad Doppler spectral width is coincident with the equatorward edge of the cusp particle precipitation. The equatorward edge of the HF radar backscatter also appears to correspond closely to the equatorward edge of red line aurora and hence the OCFLB (Rodger *et al.*, 1995; Milan *et al.*, 1999), though it is possible that this relationship breaks down for northward IMF (Moen *et al.*, 2001).

Previously, many papers have examined behavior of the spectral width boundary, which is a latitudinal boundary between narrow and broad spectral widths, through case studies (Baker *et al.*, 1997; Chisham *et al.*, 2001) and statistical analysis (Yeoman *et al.*, 2002). However, there have been only a few simultaneous observations of the spectral width boundary using data from magnetic conjugate radars (Pinnock *et al.*, 1999; Milan and Lester, 2001). These authors assumed the spectral width boundary to be a proxy for the true OCFLB and estimated the dayside reconnection electric field from the convection flow across the OCFLB. However, they have not investigated in detail how the behavior of the spectral width boundary is collocated between conjugate hemispheres and how the temporal variation of the spectral width boundary is different between the two hemispheres. All of the previous conjugate studies of spectral width employed the data of Polar Anglo-American Conjugate Radar Experiment (PACE) radars located at Goose Bay, Canada, and Halley, Antarctica which are a part of SuperDARN chain. In contrast, we employed another magnetic conjugate radar

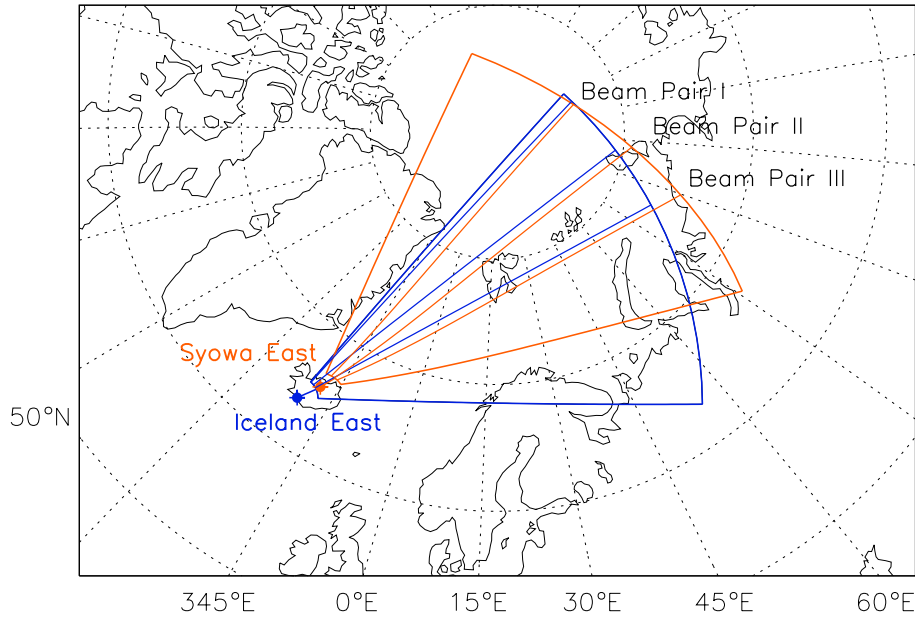


Figure III-4.1: The map of the Northern Hemisphere showing the location of the CUTLASS Iceland-East radar field-of-view (blue line) in geographic coordinate system. Superimposed on this is the field-of-view of the SENSU Syowa-East radar (orange line) as mapped into northern hemisphere. Three beam pairs used in the interhemispheric comparison of the spectral width boundary are displayed on the fields-of-views of both radars. The beams belong to the Iceland-East are indicated as a blue line and those to the Syowa-East as a orange line.

pair in the SuperDARN chain which is composed of the Iceland-East radar of the Cooperative U.K. Twin-Located Auroral Sounding System (CUTLASS) (Milan *et al.*, 1997) and Syowa-East radar of Syowa-South & East HF Radars of NIPR for SuperDARN (SENSU). We directly compared the location and motion of the spectral width boundaries identified in magnetic conjugate ionospheres and investigated the degree of the interhemispheric collocation of the spectral width boundaries. Furthermore, the factors controlling the motion of the spectral width such as interplanetary magnetic field variation and the occurrence of substorm have been examined in detail. Consequently, significant interhemispheric difference in the response time to the occurrence of substorm expansion was identified.

4.2 Experimental Arrangement

We present the data from CUTLASS Iceland-East radar at Pykkibaer, Iceland (63.86°N; 19.20°W) and SENSU Syowa-East radar at Antarctic Syowa Station (69.01°S; 39.61°E). Figure III-4.1 presents the fields-of-view of the CUTLASS Iceland-East and the SENSU Syowa-East mapped into the geographic coordinate system in the Northern Hemisphere. The conjugate fields-of-view overlap considerably and have very similar pointing directions. This allows an almost direct comparison of the backscatter features observed by the two radars. On the day presented in this paper (October 10, 1999), the radars were operating in a high time resolution normal scan mode. In the current version of this mode, the radar scans through 16 beams every 1 minute, with an integration time of 3 s for each beam, which are binned into 75 range gates. We determined three beam pairs that have nearly parallel conjugate beams and used them for this interhemispheric comparison. These conjugate beam pairs are shown in Figure III-4.1. Beam pair I is composed of Iceland-East beam 0 and Syowa-East beam 4, beam pair II is Iceland-East beam 7 and Syowa-East beam 6, beam pair III is Iceland-East beam 10 and Syowa-East beam 6. Coverage of these beam pairs at F region altitude is ranging approximately from 72°

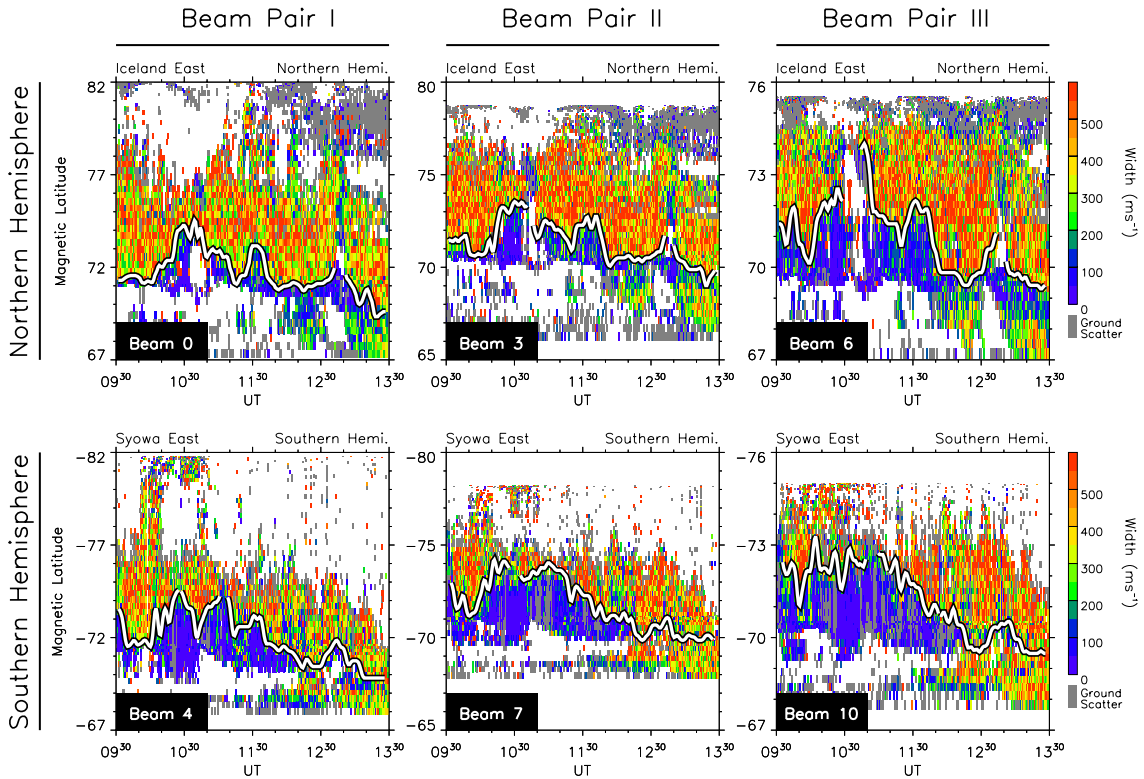


Figure III-4.2: The latitude versus time plot of spectral width for the beams of each conjugate beam pair during the period of the present study, from 0930 to 1330 UT, 10 October 1999 (top panels) for beam 0, 3 and 6 of Iceland-East in the Northern Hemisphere, (bottom panels) for beam 4, 7 and 10 of Syowa-East in the Southern Hemisphere. White line in each panel presents the spectral width boundary estimated using the algorithm described in the text.

to 83° in magnetic latitude around the dayside magnetic local time sector. Beam pair I is pointing closest to the magnetically meridional direction (the angle between the beam direction and the magnetic meridian is approximately 45°), and hence is most favorable for the direct comparison of the latitudinal movement of the spectral width boundary.

4.3 Observations

4.3.1 Determining Spectral Width Boundary

Figure III-4.2 displays the magnetic latitude (AACGM coordinate system, based on Baker and Wing, 1989) versus time plot of spectral width for the beams of each conjugate beam pair I, II and III during the period of the present study, 0930 to 1330 UT, 10 October 1999. The spectral width is colour-coded and grey indicates backscatter from the ground. The top three panels show the observations from the Iceland-East in the Northern Hemisphere and the bottom three panels from the Syowa-East in the Southern Hemisphere. During this UT period, the fields-of-view of the two radars cover the magnetic latitudes ranging from the average latitude of the central plasma sheet (CPS) and low-latitude boundary layer (LLBL) to the polar cap through the cusp around the dayside ionosphere. In each scan, the broad spectral width region (characterized by a mixture of the colours such as green, yellow and red) is clearly distinct from the narrow spectral width region (characterized by an almost uniform blue appearance), and well-defined boundaries between low and high spectral width are identified for all beam pairs.

In order to compare the spectral width boundaries in both hemispheres, we need an algorithm which can estimate the location of the boundaries. Previous studies which have identified the spectral width boundary have placed the boundary in each beam at the first range gate where the spectral width exceeds specific criteria such as 150 m s^{-1} (Baker *et al.*, 1997; Pinnock *et al.*, 1999) and 250 m s^{-1} (Chisham *et al.*, 2001). This method is based on the occurrence distributions of spectral widths in the cusp and the region equatorward of the cusp (such as the LLBL and the central plasma sheet, i.e. normally considered to be the regions of closed field lines) reported by Baker *et al.* (1995). They pointed out that the occurrence distribution of spectral widths within the cusp is a broad Gaussian shaped distribution. The average spectral width is around 220 m s^{-1} , with the majority of the spectra found in the range from about 120 to 320 m s^{-1} . In contrast, the distribution of spectral widths equatorward of the cusp is more similar to an exponential distribution with a peak occurring at about 50 m s^{-1} . In chapter 2, we have carried out a statistical analysis of the spectral width distribution obtained from the Iceland-East and the Syowa-East for the time interval from January 1998 to December 2000. This statistical analysis has shown that 80% of spectral width value obtained within the non-cusp region are less than 200 m s^{-1} in both radars, hence we have used 200 m s^{-1} as a criterion to identify the spectral width boundary in the present study.

An algorithm is then employed which finds the first appearance (in increasing latitude) of two consecutive range cells where the spectral width is greater than or equal to 200 m s^{-1} . The boundary is then determined to be at the start of the first of these cells. The result is temporally smoothed (window for smoothing is 5 min, i.e., 5 samples) and plotted as a white on black line in Figure III-4.2. It is clearly seen that the estimated spectral width boundary provides a clear demarcation line between the narrow spectral width region at lower latitudes and the broader spectral width region at higher latitudes. One thing worth noting is that main part of the narrow spectral width echoes equatorward of the boundaries are not ground scatter, hence the boundaries identified here are not between different scattering targets, e.g. ground and ionospheric scatter. The spectral width boundary is located at magnetic latitudes between approximately -69.5° and -75.0° in the Southern Hemisphere, and between 69.0° and 75.5° in the Northern Hemisphere. The average latitudes where the spectral width boundaries are located closely correspond between two hemispheres.

The accuracy of the backscatter location should be estimated before investigating the behavior of the boundaries in detail. Yeoman *et al.* (2001) investigated simultaneous observation with the CUTLASS radars and EISCAT Tromso heating facility and estimated potential error of the standard algorithm for the determination of the backscatter location employed in the SuperDARN community. They found that the accuracy is within 60 km for one and half hop ionospheric backscatter. They also calculated HF propagation path from the CUTLASS Iceland-East radar for several elevation angle. During the interval of this study, elevation angle is approximately 30° and the spectral width boundaries appear at approximately 1000 km in slant range in Iceland-East radar (facility for angle of arrival determination has not been installed in Syowa-East radar). If we refer the propagation path estimated by Yeoman *et al.* (2001), echoes around the spectral width boundary are considered to be one and half hop ionospheric backscatter. Then, the accuracy is estimated to be ± 60 km in our observation, corresponding to 1.08° in latitude.

4.3.2 Low Latitude Particle Precipitation

In the course of this study, we investigate an interhemispheric similarity and difference in the location of the dayside OCFLB using the radar spectral width boundary as a proxy. The spectral width boundary in the radar data has been widely used as a proxy for the OCFLB in the recent papers. However its validity has not been

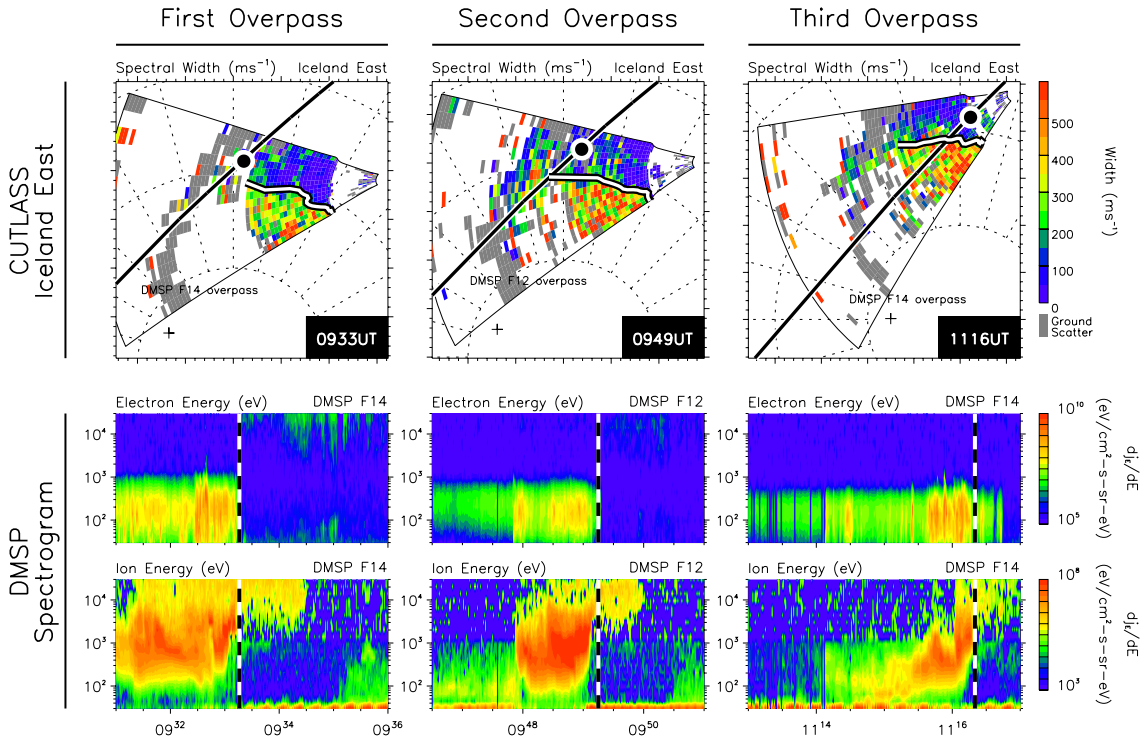


Figure III-4.3: (Top) maps of spectral width observation by Iceland-East on magnetic latitude and MLT coordinates for the time interval of DMSP satellite overpass. Dotted circles represent 60°, 70° and 80° latitudes and radial dotted lines represent MLT meridians, 12 MLT being directed towards the top of the panel. Superimposed black line on white in each panel is the track of the overpassing DMSP satellite. White line on black represents the estimated location of the spectral width boundary and black point on white indicates the point where the DMSP crosses particle trapping boundary. (Bottom) electron and ion measurements from the overpassing DMSP satellite. These are spectrograms between ≈ 10 eV and 30 keV. From these observations, particle trapping boundaries have been identified, which are indicated as a dashed line.

so well established. Hence, the spectral width boundary identified during the interval of this study has to be calibrated using other proxies for the OCFLB. There are a number of signatures which can be employed as proxies for the OCFLB (Rodger, 2000). The most popular one is the trapping boundary of the high energy (≈ 10 keV) particle precipitation (particle trapping boundary, Evans and Stone, 1972). Here, we employ three overpasses of the DMSP F12 and F14 satellite (Hardy *et al.*, 1984) and compare the locations of the spectral width boundary and the particle trapping boundary. The data from the DMSP spacecraft are available only in the Northern Hemisphere during this interval.

The results of the comparison are summarized in Figure III-4.3. The top three panels display the maps of the spectral width observation by the CUTLASS Iceland-East radar for three DMSP overpasses at 0933 UT, 0949 UT and 1116 UT, respectively. The bottom three panels show corresponding spectrograms of electrons (upper) and ions (lower) observed by the DMSP F12 and F14 satellite as they traversed the radar field-of-view. As the satellite approaches the noon sector, a dispersed ion feature is commonly observed in all overpasses. Such features are characteristic of precipitation on newly-reconnected field lines for southward IMF (e.g., Reiff *et al.*, 1977; Woch and Lundin, 1992), the dispersion being a consequence of the velocity filter effect. The lower-latitude cut-off of this ion feature provides a sharp demarcation between high and low fluxes of high energy (> 10 keV) particles, which is considered to be the trapping boundary. Dashed lines in the spectrograms indicate the trapping boundary as identified by the DMSP satellites and black points on the spacecraft overpassed in

the polar map give the location of the spacecrafts when they cross the trapping boundary. White on black lines in the polar map indicate the latitude of the spectral width boundary identified in each scan of the radar.

In all overpasses, spectral width boundaries exhibit L-shell aligned variation with longitude. Although not shown here, in the Southern Hemisphere the variation of the spectral width boundary with longitude is also L-shell aligned. However, the spectral width boundary is located slightly poleward of the particle trapping boundary, the offset being 1-1.5° in magnetic latitude. What is worth noting is that this tendency is found to be the case for all overpasses. Yeoman *et al.* (1997) also demonstrated that the equatorward boundary of the HF radar backscatter is located at slightly higher latitude compared with the trapping boundary identified by the DMSP satellite. André *et al.* (1999, 2000a, 2000b) attributed the cause of the broad spectral widths observed within the cusp to the wave activity observed by polar-orbiting satellites passing through the cusp (e.g. Maynard *et al.*, 1982; Matsuoka *et al.*, 1993). Matsuoka *et al.* (1993) have pointed out that correlation between these wave activities and enhancement of the flux of precipitating cusp ions and electrons is good during the intervals of the southward IMF Bz component. Lockwood (1997) and Rodger and Pinnock (1997) have shown that the finite poleward convection velocity of recently reconnected flux tubes leads the bulk of the cusp particles to the region some distance poleward of the true OCFLB at ionospheric altitudes. Rodger and Pinnock (1997) assumed that the cusp particle precipitation travels at the speed of the ions, and then estimated this offset to be ≈ 150 km near noon. This length of the offset is basically consistent with those seen in the present observation.

Since there is no overpass of the DMSP satellite in the Southern Hemisphere during this interval, we do not know whether or not the offset between the spectral width boundary and the particle trapping boundary exists also in the Southern Hemisphere. Coleman *et al.* (2000) have shown that the ionospheric footprint of the reconnection X-line varies in length with dipole tilt angle. This effect can introduce an interhemispheric difference in ionospheric convection velocities in the solstice conditions, which has been confirmed by Pinnock *et al.* (1999) at the summer solstice. During the interval of this study, however, the effect of the poleward convection of the reconnected flux tubes is expected to have approximately equal impact on both hemisphere because the present observation was done at equinox. This suggests that it is valid to use the spectral width boundary as a proxy for the OCFLB during this interval and that it is possible to discuss their interhemispheric difference, keeping in mind the possibility that we may underestimate the latitude of the OCFLB by a small amount.

4.3.3 Interhemispheric Comparison of the Spectral Width Boundary

For better understanding of the behavior of the spectral width boundaries in both hemispheres, we projected the spectral width boundary identified in the Northern Hemisphere into the Southern Hemisphere using the Tsyganenko 89 magnetic field model (Tsyganenko, 1989) and compared directly the locations of the boundaries in both hemispheres. The middle three panels of Figure III-4.4 show the latitudes of the spectral width boundaries identified in both hemispheres for each conjugate beam pair. In each panel, the blue line indicates the boundary identified in the Iceland-East radar and the orange line indicates the boundary identified by the Syowa-East radar. Attached grey bars indicate uncertainties of the boundary location as estimated in section 4.3.1 (1.08° in latitude). The lack of the spectral width boundary for Iceland-East between 1035 UT and 1045 UT in beam pair I is caused by the fact that field lines can not be traced from the Northern Hemisphere into the Southern Hemisphere because they are defined to be open by Tsyganenko 89 model.

The magnetic latitude of the spectral width boundary follows the same general equatorward trend in both

hemispheres throughout the interval. It is difficult to determine whether this variation is purely temporal or not. In general, the equatorward edge of the polar cap (ideally this corresponds to the poleward edge of the auroral oval) is not a circle. Latitudes are slightly different against magnetic local time. If we refer the model of the auroral oval (e.g., Feldstein and Starkov, 1967), the latitude of the poleward edge of the oval found to be highest at magnetic local noon. Hence, the boundary seems to shift poleward (equatorward) as it moves from dawnside (noon) to noon (duskside). This apparent variation could be a considerable bias when we estimate how the polar cap is expanding and contracting in association with the IMF orientations and substorm activities. In the middle panels of Figure III-4.4, approximate UT of magnetic local noon is indicated by an open black triangle. The large scale equatorward trend of the boundaries is found to be independent on the variation of the MLT, which suggests that the bias introduced by the longitudinal variation of the form of the polar cap boundary is negligible during the interval of this study.

To illustrate the degree of collocation of the spectral width boundaries in both hemispheres, Figure III-4.5 presents scattergrams and histograms of the magnetic latitudes of the spectral width boundaries identified in both hemispheres for each conjugate beam pair. Linear fits to the variations are indicated by solid lines, and correlation coefficients are shown at the bottom of the scattergrams. Dashed-lines on the scattergrams indicate a hypothetical equality of the boundaries identified in both hemispheres for comparative purposes. It is clear that the latitudes of the spectral width boundaries are highly collocated between both hemispheres, where correlation coefficients are larger than 0.70 for all beam pairs and occurrence histograms are considerably overlapping between two hemispheres. However, the boundary in the Syowa-East field-of-view tends to be at higher latitude compared with that in the Iceland-East, where the differences as large as 2° latitude can be identified on individual points. In general, magnetic latitude of the cusp varies with dipole tilt angle (e.g., Newell and Meng, 1989). When the dipole tilt angle is directed positive, the latitude of the cusp is higher in the Northern Hemisphere than that in the Southern Hemisphere. In order to estimate how the tilt of dipole contributes to the interhemispheric difference in the latitude of the boundaries, information on the dipole tilt angle is added as a colour-scale in the upper three panels of Figure III-4.5. It is found that the interhemispheric difference is larger when the dipole tilt angle is larger (blue and green points) while the difference is almost negligible when the angle is close to zero (orange and red points).

4.3.4 Response to the IMF and Substorm Activity

Returning to the middle three panels of Figure III-4.4, the magnetic latitude of the spectral width boundary follows the same general equatorward trend in both hemispheres throughout the interval, which means the OCFLB is gradually expanding around the dayside ionosphere. The other thing worth noting that the latitude of the spectral width boundary in both hemispheres shows short-lived poleward excursions superposed on the general equatorward trend. In order to clarify what causes these poleward and equatorward movements of the spectral width boundary, we have examined the variation of the interplanetary magnetic field and the occurrence of substorms during the interval. The former would contribute to the expansion of the OCFLB through the reconnection at the magnetopause, while the latter would contribute to the contraction of the OCFLB through the reconnection of open field in the tail, most likely as a part of the substorm process.

During the interval of the present study, the ACE spacecraft was located upstream of the magnetosphere at $X_{\text{gsm}} \approx 228 R_E$ and the Wind spacecraft was located at $X_{\text{gsm}} \approx 49 R_E$. An approximate solar wind velocity of 530 km s^{-1} measured by both spacecrafts during this interval gives a delay of some 50 minutes for ACE and 14 minutes for Wind between the observation of IMF features and their incidence on the Earth's magnetopause.

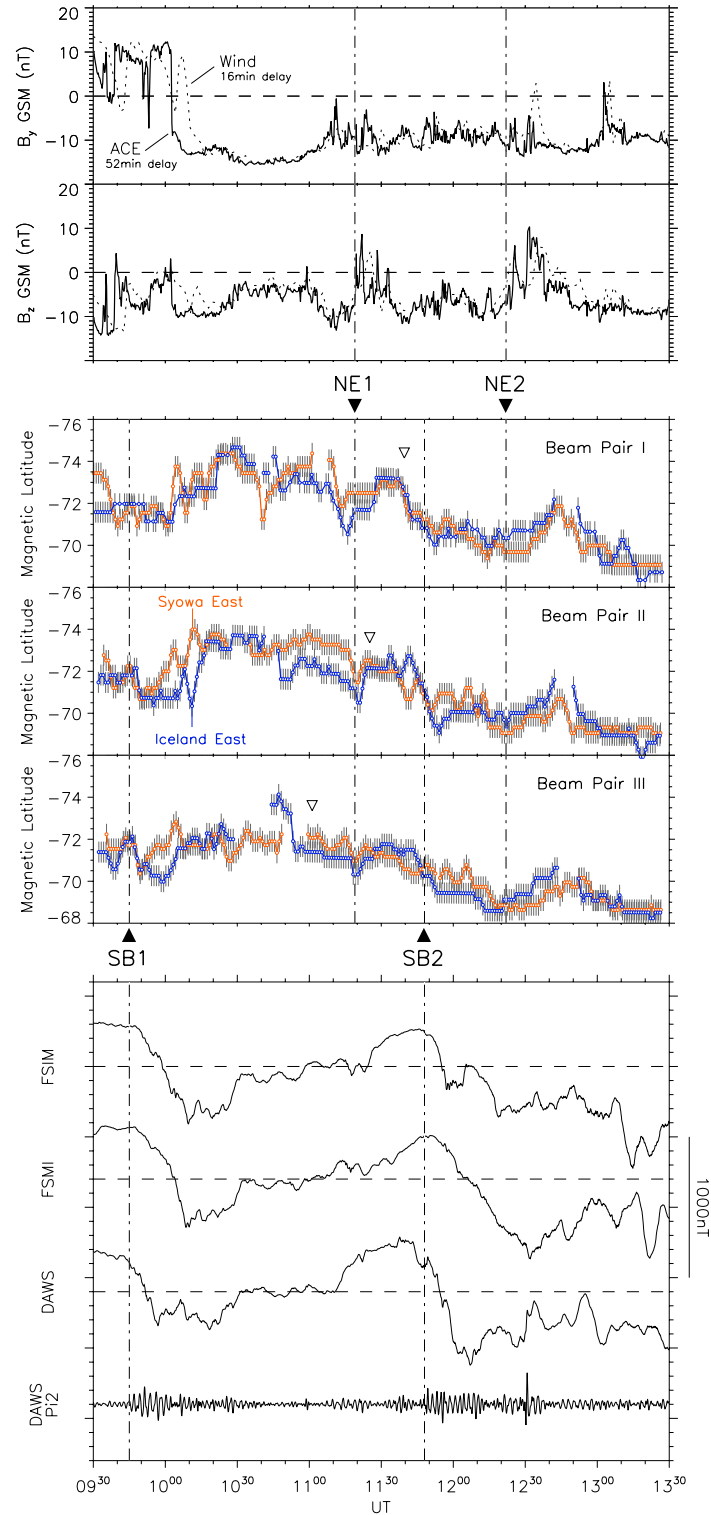


Figure III-4.4: (Top two panels) B_y and B_z components of the IMF as measured by the ACE and Wind spacecraft (solid and dashed line, respectively), lagged to the magnetopause. Two vertical dashed lines indicate the time of the northward excursion of the IMF B_z ('NE1' and 'NE2'). (Middle three panels) the magnetic latitude of the spectral width boundaries identified for each conjugate beam pair, respectively. In each panel, blue line indicates the boundary identified in the Iceland-East and orange line indicates the boundary identified in the Syowa-East. Attached grey bars indicate uncertainties of the boundary latitude. (Bottom panel) H-component magnetograms from the CANOPUS networks, along with filtered data showing Pi2 activity (scaled by a factor of 5 for clarity). Vertical dashed lines indicate the onset of the two substorm breakup ('SB1' and 'SB2').

The calculation is based on the technique of Khan and Cowley (1999). An additional two minutes must be added to account for the propagation time of Alfvén waves from the subsolar magnetopause to the dayside high-latitude ionosphere. A total solar wind propagation time delay of 52 minutes for ACE and 16 minutes for Wind appears to give the best correlation between the variations observed in the IMF and the behavior of the spectral width boundary observed by the radars. The IMF B_y and B_z components as measured by the spacecraft, including the estimated propagation time of 52 minutes for ACE and 16 minutes for Wind, are displayed in the top two panels of Figure III-4.4, data from ACE being represented by the solid line and those from Wind by the dashed line. During first 30 minutes from the start of the interval, IMF B_y is strongly positive, but turns negative at 1000 UT, after which it has a strong negative value (≈ -10 nT). In the case of the B_z component, negative values are dominant throughout the interval, with excursions to close to zero around 1118 UT ('NE1') and 1222 UT ('NE2'), which are presented as dot-dashed lines.

As is already noted, the magnetic latitude of the spectral width boundary exhibits a general equatorward trend in both hemispheres. This trend is found to be related to the continuous negative B_z component of the IMF. Following each of the two northward excursions of the IMF, the spectral width boundary moved poleward in both hemispheres. The response of spectral width boundary to these northward excursion is rapid (response time is less than 5 minutes) and occurs simultaneously in both hemispheres. Duration of these poleward motions of the boundaries is similar to that of the northward excursion of the IMF. When the B_y component of the IMF suddenly changes, the magnetic latitudes of the spectral width boundaries are also expected to move. Cowley *et al.* (1991) pointed out that in the Northern Hemisphere the OCFLB shifts towards dusk during the interval of positive B_y and towards dawn for the B_y negative case. The situation is reversed in the Southern Hemisphere. At the time of the large B_y change (1000 UT), the radars observe the spectral width boundary between 1000 MLT and 1200 MLT in both hemispheres. Hence, this change in IMF B_y is expected to create poleward displacement of the spectral width boundary in the Northern Hemisphere and equatorward in the Southern Hemisphere. However, our observation does not support this prediction. Although there could be found an evidence that the spectral width boundary in the Northern Hemisphere shifts poleward in response to the B_y change, corresponding equatorward movement of the spectral width boundaries can not be identified in the Southern Hemisphere.

Two substorms occur during the interval of interest, the progress of which are monitored by three magnetometer stations from the Canadian Auroral Network for the OPEN Program Unified Study (CANOPUS) network (as described by Samson *et al.*, 1992). These stations are FSIM, FSMI and DAWS, which are located between 2230 MLT and 0400 MLT at the times of the substorm expansion phase onsets. The H-component magnetograms from the three stations and bandpass filtered data from DAWS are shown in the bottom panel of Figure III-4.4. The first substorm occurs at 0945 UT ('SB1') and the second at 1148 UT ('SB2'), both of which are confirmed by large negative bay in H-component and the presence of Pi2 pulsations indicating the expansion phase onset of the substorms. Following the expansion phase onset of the substorms (as indicated by the dot-dashed lines, respectively), the spectral width boundary starts to move poleward or stops its equatorward motion. This response is more clearly seen at the time of the first substorm onset (degree of the displacement is approximately 3° in magnetic latitude), although there is some evidence for this at the time of the second substorm onset (degree of the movement is less than 1° in beam pair I and II, and the boundary remains at a constant latitude in beam pair III). In short, degree of the poleward movement of the spectral width boundary is larger following the first substorm onset than in the second. In addition, at the time of the first substorm breakup, there is an interhemispheric difference in the response of spectral width boundary to the substorm.

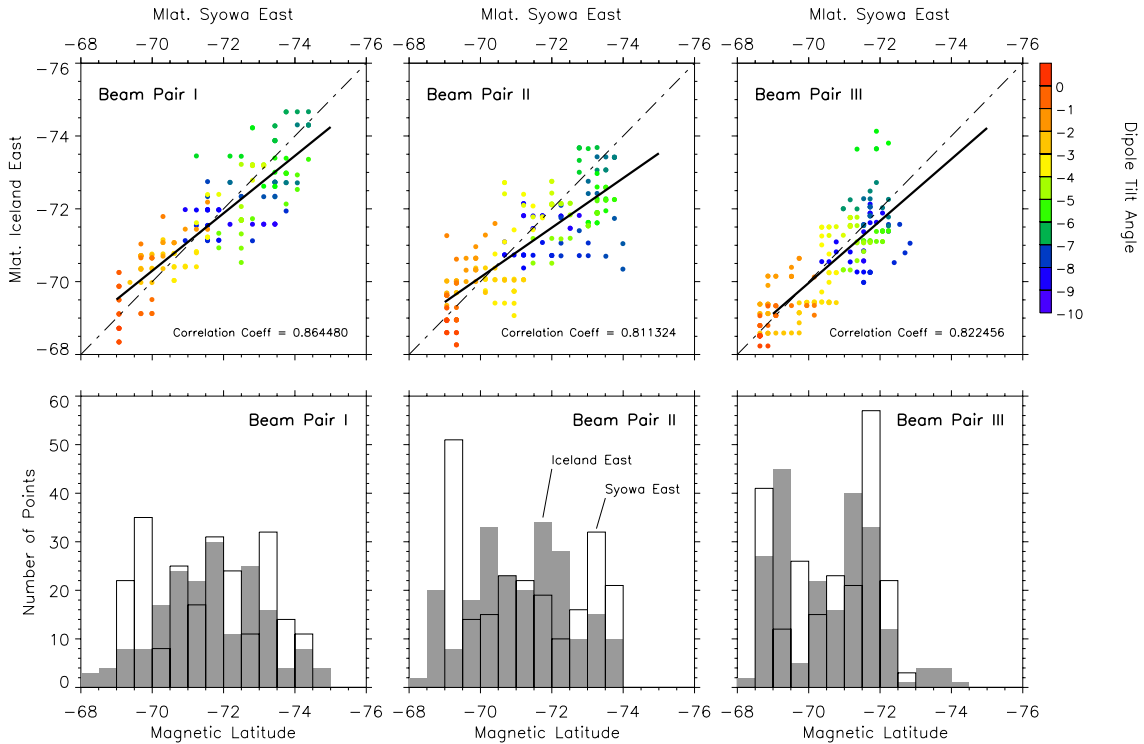


Figure III-4.5: (Top three panels) the scattergram of the magnetic latitudes of the spectral width boundaries identified in both hemispheres for each conjugate beam pair, respectively. Vertical axis is the magnetic latitude of the Iceland-East and horizontal is the that of the Syowa-East. Dot-dashed line in each panel indicates a hypothetical equality of the boundaries identified in both hemispheres for comparative purposes. Linear fits to the variations are indicated by solid lines, and correlation coefficients are shown at the bottom of the panels. Dipole tilt angle is shown in colour-scale. (Bottom three panels) the histograms of the magnetic latitudes of the spectral width boundaries identified in the Iceland-East (grey bars) and the Syowa-East (open bars) for each conjugate beam pair, respectively.

The spectral width boundary starts to move poleward 5 minutes after the onset of the substorm in the Southern Hemisphere, while it takes approximately 15 minutes to respond in the Northern Hemisphere. On the other hand, no interhemispheric difference can be found in the response time to the second substorm. Cause of this interhemispheric difference will be discussed in later section.

4.4 Discussion

4.4.1 Interhemispheric Collocation of the Boundaries

First we discuss the collocation of the spectral width boundaries in both hemispheres. The present observation suggests that the magnetic latitude of the spectral width boundary is similar in both hemispheres, and the correlation coefficients between both latitudes are larger than 0.70 for all beam pairs. Newell and Meng (1989) investigated a large data set of DMSP satellite crossing of the cusp and concluded that the position of the cusp is about 4° lower in winter than that in the summer hemisphere and approximately symmetric around equinox. The first interhemispheric observation of the spectral width boundaries by Pinnock *et al.* (1999) exhibited the difference in the latitude of the boundaries (up to 4° in magnetic latitude) between both hemispheres. Their observation was carried out during summer in the Northern Hemisphere, hence they argued that the interhemispheric difference of the boundary location is caused by the seasonal asymmetry of the dayside structure related to the dipole tilt angle effect. On the other hand, the present observation was done during equinoctial

conditions when the effect of dipole tilt angle on the interhemispheric difference is minimized, which can, therefore, be the reason for the good collocation of the spectral width boundary between both hemispheres.

Though the spectral width boundaries coincide on average between both hemispheres, there is a slight difference such that the spectral width boundary identified in the Syowa-East field-of-view tends to be at higher latitude compared with that in the Iceland-East (2° in maximum). There are two possible reasons for this difference. One candidate is again the effect of the dipole tilt angle. Tilt angle of the dipole varies not only with season but also with UT. During the interval of this study, the dipole tilt angle changes from -9.33° (0930 UT) to 0.76° (1330 UT). As clearly shown in Figure III-4.5, there exists a good correlation between the dipole tilt angle and the interhemispheric difference of the boundary latitudes. This suggests that the primary cause of the interhemispheric difference in the latitude of the boundaries is the effect of the dipole tilt angle. Newell and Meng (1989) have shown that 17° of dipole tilt angle is required to shift the cusp by 1° of latitude. -9.33° of dipole tilt angle shifts the cusp equatorward (poleward) by 0.55° in the Northern (Southern) Hemisphere. Then, an interhemispheric difference in boundary latitude is estimated to be 1.1° , which is roughly consistent with the present observation. Although the observation was carried out close to the equinox, it was not under pure equinox conditions (about a half month after the equinox). According to the statistical analysis of Newell and Meng (1989), such a shift from the equinox is enough to create a small difference in the average latitude of the dayside structure. The other possible factor producing the interhemispheric difference is the effect of IMF By. Apart from the first 30 minutes of the interval, IMF By is predominantly negative. The IMF By component imposes a strong skewing force on the high-latitude convection pattern (e.g. Cowley, 1981) which results, within the Northern Hemisphere, in anti-sunward flow being dragged towards the morning sector for IMF By positive and towards the evening sector for By negative (e.g. Reiff and Burch, 1985). Variation of dayside OCFLB with longitude could also have a dependence on the IMF By, which might create a difference of spectral width location around the dayside.

We again stress our finding, that is the spectral width boundaries identified in both hemispheres are highly collocated. Milan *et al.* (1998) shows that the HF radar technique can be relatively insensitive to the variations in the propagation environment of the high-latitude ionosphere and that dayside auroral backscatter exhibits a true geophysical structure. Furthermore, Yeoman *et al.* (1997) employed a swept-frequency radar mode to demonstrate that the equatorward boundary of the cusp backscatter was independent of the radio wave frequency and any variations in propagation. Our observational results also suggest that the spectral width boundary is not affected by the local conditions in a hemisphere and are strongly controlled by factors common to both hemispheres. André *et al.* (1999, 2000a, 2000b) have postulated that high frequency (Pc1) wave activity associated with the cusp results in highly variable electric fields which broaden the spectra. Most of these waves are attributed to electromagnetic ion cyclotron waves generated at the dayside magnetopause in the equatorial plane. Since this wave activity is considered to propagate into the conjugate ionospheres from the equatorial plane, the interhemispheric collocation of the spectral width boundaries in our observation can be explained by this mechanism.

4.4.2 Response to the Changes of IMF Bz and Substorm

We have seen that the spectral width boundary appears to move equatorward or poleward in response to the changes in the IMF and the occurrence of substorm. We now discuss the influence of the IMF Bz and the occurrence of substorm on the variation of the spectral width boundary. The size of the area of open flux is controlled by both the dayside and nightside reconnection rates (Siscoe and Huang, 1985). Cowley and

Lockwood (1992) illustrated an expanding/contracting polar cap model in which they described the ionospheric flow as a consequence of both dayside and nightside reconnection rates. Initially it is assumed that the open and closed flux in the polar cap is in a state of equilibrium and that the polar cap is circular, containing some amount of open flux. In response to a burst of dayside reconnection, a region of closed flux adjacent to the pre-existing dayside polar cap boundary is opened. The OCFLB, the boundary which encloses open flux, moves equatorward to encompass the new open flux. For the period analyzed in the present study, negative B_z was dominant throughout the interval. The general equatorward trend of the spectral width boundary is consistent with the gradual accumulation of open flux in the polar cap through magnetopause reconnection, which is expected for southward IMF.

Conversely, during the substorm expansion phase, when reconnection occurs in the magnetotail closing pre-existing open flux, the boundary moves poleward as the polar cap shrinks. Following the onset of two substorm breakups (termed ‘SB1’ and ‘SB2’ in the text) spectral width boundary moves poleward with some delay time, which indicates that the reconnection in the magnetotail is destroying open flux within the polar cap. There is a difference between two poleward excursions associated with the substorm such that the scale of the excursion is larger for the first substorm breakup (SB1) than that for the second substorm breakup (SB2). At the onsets of both substorms, the IMF B_z is oriented southward. However, just after the onset of the first substorm, IMF B_z becomes close to zero, while the IMF continues to be directed southward after the onset of the second substorm. If reconnection occurs in the magnetotail and on the dayside magnetopause simultaneously, the day and nightside reconnection rates are in competition. In the case of the first substorm, the nightside reconnection rate is expected to strongly exceed the dayside reconnection rate, hence, the spectral width boundary shifts poleward by approximately 3° . On the other hand, during the interval of the second substorm breakup, the difference between the reconnection rates at the dayside magnetopause and in the tail is considered to be relatively smaller compared with that at the first substorm breakup, because of the continuing southward IMF. Hence, the scale of the poleward excursion following the second substorm breakup is small (less than 1° or remaining at a constant latitude).

When the IMF has a northward component, reconnection can take place at the high-latitude magnetopause (tailward of the magnetopause entrance to the cusp region). Here, reconnection occurs between the IMF and pre-existing open flux in the magnetotail lobe. These field lines map to the high-latitude side of the ionospheric footprint of the cusp. Hence, no new open flux is created in this process and the amount of open flux in the polar cap remains unchanged if there is no nightside reconnection. In the present observation, however, following the northward excursions of the IMF B_z (termed ‘NE1’ and ‘NE2’ in the text), the spectral width boundary moves poleward in both hemisphere. This suggests that tail reconnection is still continuing. Actually, at the times of both northward excursions, variation of the CANOPUS magnetometers still exhibits the signature of substorm recovery phase. Milan *et al.* (2002b) pointed out that magnetotail reconnection and the associated shrinkage of the polar cap appears to continue from substorm expansion phase onset to the end of the recovery phase, which is about 100 minutes. A similar finding was reported by Khan *et al.* (2001), in which reconnection signatures were observed in the magnetotail some time after significant auroral activity had subsided. Our observation is consistent with their results.

4.4.3 Interhemispheric Asymmetry in Response to the Substorms

Here, we discuss the interhemispheric difference in the response time to the occurrence of substorm expansion. During the period analyzed in this paper, two substorms, SB1 and SB2, occur. Following the onset of both

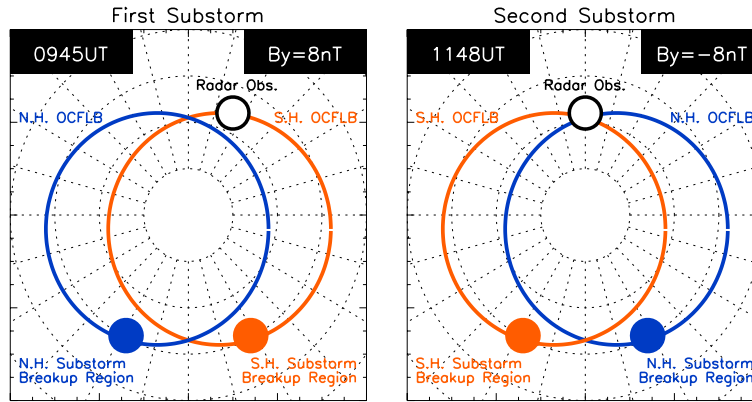


Figure III-4.6: A schematic diagram of the situation accounting for the response of the spectral width boundary to the substorm expansion at the time of the first substorm onset (left panel) and the second substorm onset (right panel). Magnetic local noon is toward the top of the figure.

substorms, the spectral width boundary moves poleward, indicating that reconnection in the magnetotail is destroying open flux in the polar cap. However, there is a difference in response time to the substorm onset between the two substorms. For the first substorm, the spectral width boundary starts to move poleward 5 minutes after the onset of the substorm in the Southern Hemisphere, while it takes approximately 15 minutes to respond in the Northern Hemisphere. The conjugate observation of the spectral width boundary by Pinnock *et al.* (1999) demonstrated that there is an interval of poleward movement of the spectral width boundary suggesting the nightside reconnection rate exceed the dayside rate. However, no interhemispheric difference was discussed in their study. Here, we discuss this difference in terms of interhemispheric asymmetry of the substorm breakup region in the longitudinal direction, associated with the effect of the IMF B_y component.

It is well-known that the B_y component of IMF imposes a skewing force on the convection pattern around the dayside high-latitude ionosphere, which results, within the Northern Hemisphere, in anti-sunward flow being dragged towards the morning sector for IMF B_y positive and towards the evening sector for B_y negative, with an opposite variation produced within the Southern Hemisphere (e.g. Cowley, 1981). This skewing force imposed on the ionosphere also results in the dawn-dusk displacement of the auroral oval, within the Southern Hemisphere in the direction of the imposed B_y component (Holzworth and Meng, 1984). Also in the nightside ionosphere, configuration of the ionosphere depends on the IMF B_y . For example, Rodger *et al.* (1984) described the asymmetric location in MLT of the Harang discontinuity as a function of IMF B_y , with its location within the Northern Hemisphere skewed ≈ 2 hour westwards and the Southern Hemisphere ≈ 2 hour eastwards, for an IMF B_y of ≈ 8 nT. Shand *et al.* (1998b) and Yeoman *et al.* (2000) investigated interhemispheric contrasts in the ionospheric convection in response to variations of the IMF and substorm activity using conjugate SuperDARN radar data on the nightside. They demonstrated that large IMF B_y component generates large-scale non-conjugacy in convections driven by nightside processes. In a recent analysis of conjugate satellite images, Craven and Frank (1996) found indication of a dependence in the substorm expansion phase on the B_y component of the IMF. Stenbaek-Nielsen and Otto (1997) gave an interpretation with the penetration of the IMF B_y causing the observed interhemispheric difference in the behavior of discrete aurora.

In the present observation, IMF B_y is ≈ 8 nT at the onset of the first substorm, and ≈ -8 nT at the onset of the second substorm. At the onset of both substorms, the B_z component of IMF is predominantly negative. If we postulate a motion of the substorm breakup region in a similar fashion to Rodger *et al.* (1984), the

substorm breakup region shifts towards dusk for the case of the first substorm and towards dawn for the second substorm within the Northern Hemisphere, with the situation being reversed in the Southern Hemisphere. At the onset of the first substorm, the conjugate radars are observing spectral width boundaries between 10 MLT and 11.5 MLT, while at the onset of the second substorm, the boundaries in the field-of-view of the radars are located around 12 MLT. The situation described here is summarized in Figure III-4.6. Hence, the breakup region of the first substorm is expected to be closer to the spectral width boundary as identified by the radar in the Southern Hemisphere than in the Northern Hemisphere, while there is no considerable difference in distance from the substorm breakup region to fields-of-view of the conjugate radars for the case of the second substorm. We suggest that this displacement of the substorm breakup region in MLT associated with IMF B_y polarity could create the interhemispheric difference in response of the boundaries to the first substorm. However, whether or not the longitudinal displacement of substorm breakup region is sufficient to create the difference of response time of 10 minutes is still a considerable debate and then more detailed analysis is needed for the further understanding of this interhemispheric difference.

4.5 Summary

The spectral width boundaries obtained from the conjugate radar pair composed of the CUTLASS Iceland-East in the Northern Hemisphere and the SENSU Syowa-East in the Southern Hemisphere were compared. Correspondence between the magnetic latitudes of the boundaries in both hemispheres is generally remarkable. Correlation coefficients between the latitudes of the boundaries are larger than 0.70 for all conjugate beam pairs employed in this study. This high correlation would be due to the fact that the observation was carried out around equinox when the effect of dipole tilt angle on the location of the cusp is minimized. The temporal variation of the magnetic latitude of the spectral width boundary follows the same equatorward trend in both hemispheres. This signature is consistent with the accumulation of open flux in the polar cap by magnetopause reconnection, expected when IMF B_z is negative. Boundaries in both hemispheres also exhibit short-lived poleward motions superposed on the general equatorward trend, which follow both the onset of substorm expansion phases and temporary northward excursions of IMF B_z during substorm recovery phase. This signature suggests that the nightside reconnection rate exceeds the dayside reconnection rate and the polar cap contracts during these intervals. In addition, there is an interhemispheric difference in response time to the substorm occurrence between two hemispheres such that the spectral width boundary in the Southern Hemisphere starts to move poleward 10 minutes earlier than that in the Northern Hemisphere. We discuss this difference in terms of interhemispheric asymmetry of the substorm breakup region in the longitudinal direction associated with the effect of IMF B_y .

Chapter 5

Conclusion and Future Directions

At the first step, statistical characteristics of the spectral width distribution were investigated using data from the conjugate radar pair composed of the Iceland-East radar in the Northern Hemisphere and the Syowa-East radar in the Southern Hemisphere. Three types of spectral width distribution were identified in both hemispheres, (i) an exponential-like distribution in the lower magnetic latitudes (below 72°), (ii) a Gaussian-like distribution around a few degrees magnetic latitude centered on 78° , and (iii) another type of distribution in the higher magnetic latitudes (above 80°). The first two correspond to the spectral width distributions within the LLBL and the cusp classified by Baker *et al.* (1995). Most important finding was that the spectral width is also narrow in the region poleward of the cusp (above 80°). These spectral width features are obtained in wide magnetic local time sector of at least 6 hours from 09 to 15 MLT.

Next we have tried to disclose the origin of these broad Doppler spectral widths on the dayside polar region. Simulation study by André *et al.* (1999, 2000a, 2000b) pointed out that the broad spectral widths observed in the dayside high-latitude ionosphere result predominantly from time-varying electric field in the Pc1-2 frequency range. However, no substantial observation has supported their prediction. We have performed a case study of a favorable conjunction of overpass of the Oersted satellite with the field-of-view of the SuperDARN Syowa-East radar during an interval of the southward IMF B_z . At the time, the radar observed L-shell aligned boundary in the spectral width around the dayside ionosphere. High-frequency (0.2-5 Hz) magnetic field fluctuations were simultaneously observed by the Oersted satellite high time resolution magnetometer. These magnetic field fluctuations are considered to be Alfvén wave possibly associated with the particle which precipitates into the dayside high-latitude ionosphere when magnetic reconnection occurs. The boundary between narrow and broad spectral widths (spectral width boundary) was well corresponding to the boundary in the level of the fluctuations. Thus, our observation can provide a direct evidence for the previous theoretical prediction. A close relationship between electric and magnetic field fluctuations and cusp particle precipitations during southward IMF conditions has been confirmed by many authors. The present observation suggests that the boundary between narrow and broad Doppler spectral widths observed in the dayside ionosphere is connected with the signature of the open/closed field line boundary such as the cusp particle precipitations and the red line (630 nm) auroral emissions via electric and magnetic field fluctuations for the case of the negative IMF B_z conditions.

Figure III-5.1 shows a picture illustrating how the electric and magnetic field fluctuations are propagating from the equatorial magnetopause into the dayside ionosphere and how they relate to the broad Doppler spectral width observed by the radar. Assuming that these fluctuations originate from dayside magnetopause reconnection, the boundary between narrow and broad Doppler spectral width region can be used as a proxy for the open/closed field line boundary in the dayside ionosphere although small offsets could exist due to the finite Alfvén traveling time from the magnetopause to the ionosphere. We have presented a case study which

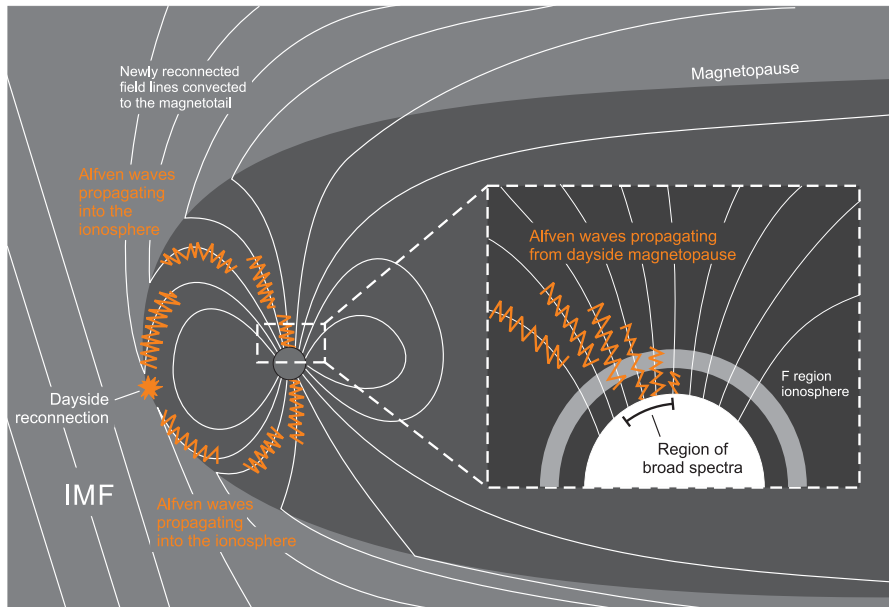


Figure III-5.1: Picture illustrating how the electric and magnetic field fluctuations are propagating from the equatorial magnetopause into the ionosphere and how they relate to the broad spectra observed by the radar.

employed magnetically conjugate SuperDARN coherent HF radars and made an interhemispheric comparison of the location and variation of the spectral width boundaries. Agreement between the magnetic latitudes of the boundaries in both hemispheres was remarkable. Correlation coefficients between the latitudes of the boundaries were larger than 0.70 for all conjugate beam pairs employed in this study. The temporal variation of the magnetic latitude of the spectral width boundary followed the same equatorward trend in both hemispheres. This signature is consistent with the accumulation of open flux in the polar cap by the dayside low latitude magnetopause reconnection, which is expected when IMF B_z is negative. Boundaries in both hemispheres also exhibited short-lived poleward motions superposed on the general equatorward trend, which followed the onset of substorm expansion phase and temporary northward excursion of IMF B_z during substorm recovery phase. These characteristics can be interpreted as a manifestation of the expanding and contracting polar cap due to the dayside and nightside reconnections (e.g., Cowley and Lockwood, 1992). In addition, there was an interhemispheric difference in response time to the substorm occurrence between two hemispheres. The spectral width boundary in the Southern Hemisphere started to move poleward 10 minutes earlier than that in the Northern Hemisphere. We have discussed this difference in terms of interhemispheric asymmetry of the substorm breakup region in the longitudinal direction associated with the effect of IMF B_y component. This case study has confirmed that the Doppler spectral characteristics of the FAIs is very useful to study the boundaries and processes in the dayside ionosphere.

Our study has clarified the statistical properties, origin and practical usage of the broad Doppler spectral width observed by the SuperDARN radars around the dayside ionosphere. Broad spectral width echoes are also observed on the nightside ionosphere. Their statistical properties have been investigated by Woodfield *et al.* (2002c) in detail. However, it is still unclear whether or not the broad spectra on the nightside are also related to the electric and magnetic field fluctuations in Pc1/Pc2 frequency ranges. It is also a considerable debate how they can be used to locate the geophysical boundaries on the nightside (Lester *et al.*, 2001; Woodfield *et al.*, 2002a, 2002b). These issues must be examined by using various kinds of instruments in near future.

Part IV
Mesospheric Irregularities
as an Indicator of the Global Climate Change

Chapter 1

Overview

1.1 Polar Mesosphere Summer Echoes: PMSE

The polar mesosphere has become a region of increasing interest in recent years. Temperature at the solstices is significantly different from those expected from radiative equilibrium, which is presumably because of the effect of gravity wave driving pole to pole meridional circulation (e.g., McIntyre, 1989). Temperature measurements by rocket experiment have shown that summer polar mesosphere is the coldest region on the Earth (von Zahn and Meyer, 1989; Lübken and von Zahn, 1991). The cold temperature leads to the formation of ice particles near the mesopause which are visible as noctilucent clouds (NLCs) from the ground. The observational fact that NLCs have been observed only in the last 100 years leads to speculation that the summer polar mesosphere is a manifestations of global environmental change (Thomas, 1996).

The other important feature that is also associated with the cold polar summer mesosphere temperature is Polar Mesosphere Summer Echoes (PMSE). PMSE are unexpected strong radar backscatters from mesospheric heights which are regularly observed during summer months at polar latitudes. Detail of PMSE is precisely described in reviews by Cho and Kelley (1993) and Cho and Röttger (1997) and references therein. The first observations were made by Ecklund and Balsley (1981) with the 50 MHz VHF radar at Poker Flat in 1979. Later on, the Arctic PMSE have been observed at higher frequencies of 224 MHz (Röttger *et al.*, 1988), 500 MHz (Hall and Röttger, 2001), 933 MHz (Röttger *et al.*, 1990), and 1.29 GHz (Cho *et al.*, 1992b). Recent observations demonstrated that PMSE can be detected at even lower frequency ranges of 8-9 MHz (Karashtin *et al.*, 1997) and of 3.3-7.6 MHz (Kelley *et al.*, 2002), which evidenced that radars at HF frequencies are also powerful tool for the study of PMSE. Bremer *et al.* (1996) identified distinct characteristics in 2.78 MHz MF radar signal-to-noise ratio data and associated them with PMSE through comparison with a collocated VHF radar. However, it is still a considerable debate whether or not this signature is actually related to PMSE.

In contrast to the Arctic PMSE, observational history of the Antarctic PMSE is very short. This could be due to lack of the facilities suitable for the PMSE observation or lower occurrence probability of PMSE itself in the Southern Hemisphere. The first clear observation was made with a 50 MHz radar in 1994 by Woodman *et al.* (1999). However, the echoes were much weaker than the Arctic PMSE. Balsley and Huaman (1997) and Huaman and Balsley (1999) discussed this interhemispheric difference in terms of possible difference in temperatures and water vapor concentrations. However, recent rocket measurements in Antarctica (Lübken *et al.*, 1999) pointed out that there is no significant interhemispheric difference in summer mesopause temperatures. Clearly, further detailed analysis is required to estimate the degree to which conditions in the opposite hemispheric polar mesospheres differ. A problem is that only a small number of VHF radar are operative in Antarctica.

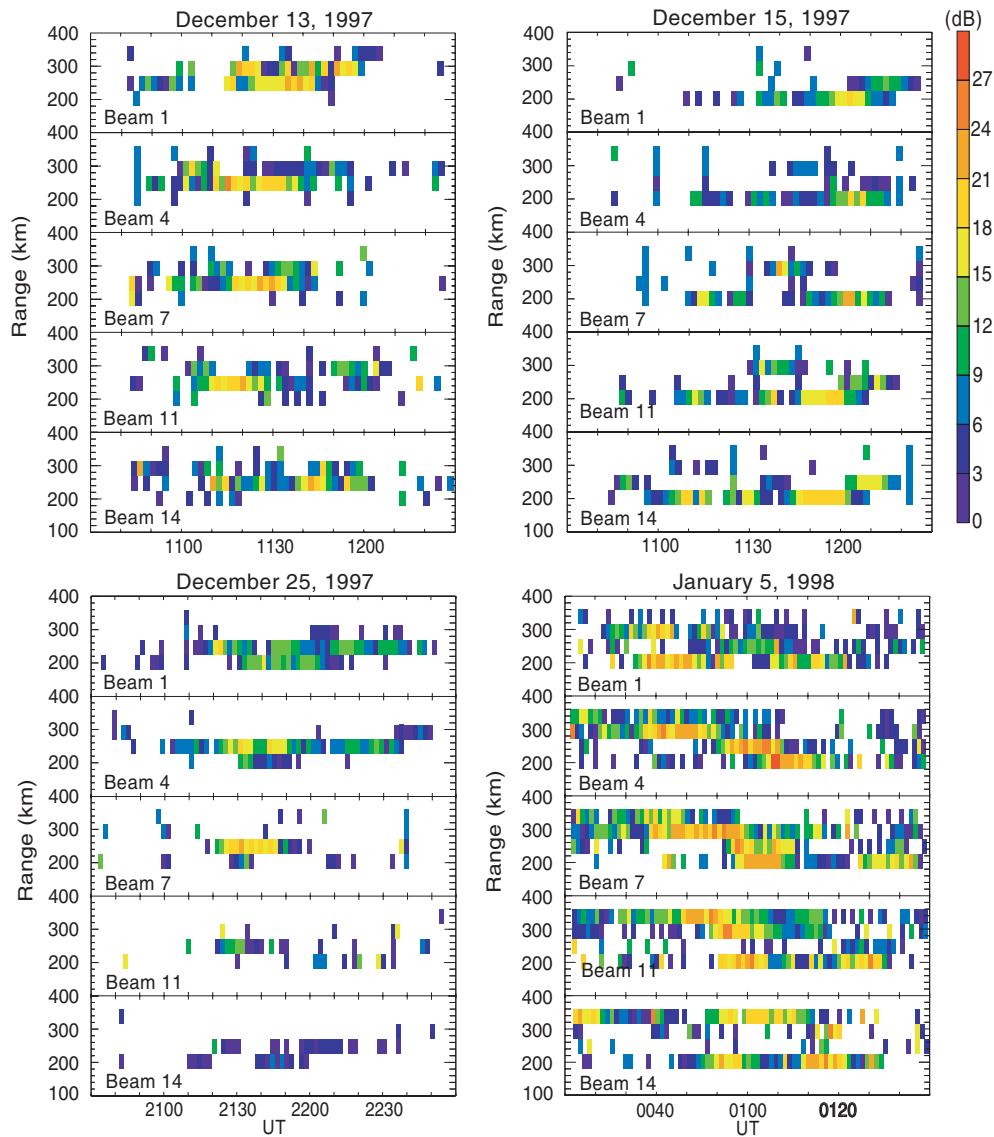


Figure IV-1.1: A collection of the 4 peculiar near range echoes explored by Ogawa *et al.* (2002a) in the SuperDARN Syowa-East radar data. Time and slant range distributions of echo power on 5 beams (beams 1, 4, 7, 11, 14) are shown (provided by Prof. T. Ogawa at Solar-Terrestrial Environment Lab., Nagoya Univ.).

1.2 Peculiar Near Range Echoes Detected with SuperDARN

Ogawa *et al.* (2001) have performed a statistical analysis of 11 months data of the SuperDARN Syowa-East radar in 1997 and have found that there are peculiar echoes with considerable low Doppler velocity (typically $\leq 100 \text{ m s}^{-1}$) backscattered from ranges very near the radar site. In order to clarify the origin of this kind of backscatters, Ogawa *et al.* (2002a) surveyed low Doppler velocity echoes appearing within the near ranges of the SuperDARN Syowa-East radar under very quiet geomagnetic conditions. As a result, they identified peculiar HF echoes that cannot be explained by a backscatter from the field-aligned E region irregularities. Figure IV-1.1 is a collection of the events that Ogawa and co-workers explored in the Syowa-East radar data. Time and slant range distributions of echo power on 5 beams (1, 4, 7, 11, 14) are shown. The echoes appear mostly at slant ranges of 180-225 km (first range gate) and at some time intervals, at 180-315 km (first to third gate). The main characteristics of the echoes are as follows: (1) radar echoes continue for about 80 min with

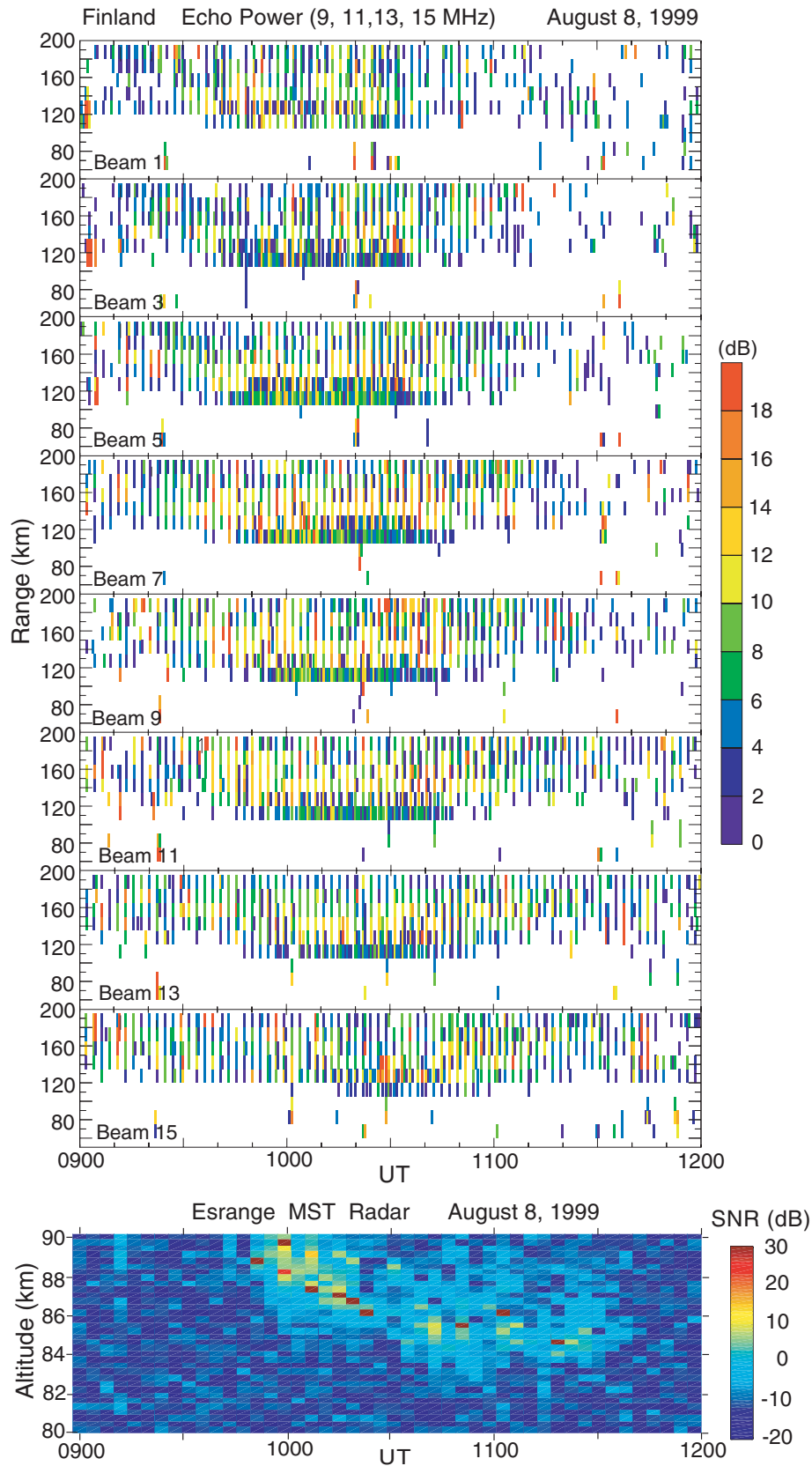


Figure IV-1.2: (Top 8 panels) time and slant range distributions of echo power observed at four frequencies on 8 beams (beams 1, 3, ..., 15) of the SuperDARN Finland radar. (Bottom) time and altitude distribution of echo power observed with the Esrangle MST radar between 0900 and 1200 UT on August 8, 1999 (taken from Ogawa *et al.*, 2002b).

intermittent subsidence, (2) echo groups have duration of 5-40 min, (3) they move across the radar beams, (4) velocity and power exhibit quasi-periodic oscillations with periods of 5-20 min, (5) velocities are between -40 to 20 m s^{-1} and the power are less than 25 dB, and (6) no particular correlation exists between the power and velocity amplitudes. The spectral widths are very narrow, less than 40 m s^{-1} . Relying on the fact that their morphological features are very similar to those of the Arctic PMSE, Ogawa and colleagues concluded that this is the first observation of the Antarctic PMSE by using the SuperDARN HF radars.

Very recently, Ogawa *et al.* (2002b) have succeeded in observing peculiar near range echo similar to those in Ogawa *et al.* (2002a) simultaneously with SuperDARN radar at Hankasalmi, Finland and VHF MST radar at Erange, Sweden. Duration during which the echoes appeared is quite similar between two radars. The upper panels of Figure IV-1.2 display time and slant range distributions of the echo power observed at four frequencies on 8 beams (beams 1, 3, ..., 15) of the SuperDARN Finland radar from 0900 to 1200 UT on August 8, 1999. The lower panel of Figure IV-1.2 shows distribution of the echo power observed at altitudes of 80-90 km with the Erange VHF MST radar. Clear PMSE appeared at 89 km. A comparison between the upper and lower panels of Figure IV-1.2 indicates that the HF echoes at 105-135 km in range are well coincident with the VHF PMSE although the HF and Erange radar sites are 650 km apart. This suggests that the peculiar near range echo detected with the SuperDARN Finland radar is PMSE at HF frequencies. Angle-of-arrival measurements of the HF radar indicates that echoes are located 80-100 km altitudes, which is also consistent with the PMSE altitudes. These two papers by Ogawa and co-workers are very suggestive of the possibility that the near range observations of the SuperDARN radars contain PMSE. However, more detailed analysis of the echo characteristics is needed to acquire more conclusive results.

1.3 Organization of This Part

In chapter 2, we extend the work of Ogawa *et al.* (2002a) by analyzing the data of longer period. Especially, seasonal variation and local time distribution of the echo occurrence are presented. Also, long-term variability of the echo appearance is investigated on the basis of the 46 months of the SuperDARN Syowa-East radar data.

Chapter 2

A Statistical Study of Antarctic Polar Mesosphere Summer Echoes Observed with the Syowa Station HF Radar

2.1 Introduction

Polar Mesosphere Summer Echoes (PMSE) in the Northern Hemisphere have been detected with ground-based radars whose frequency ranges from HF to UHF. In contrast to the Arctic PMSE, our understanding of the Antarctic PMSE is still poor because of short observation history which may be due to the warm summer mesopause in the Southern Hemisphere or a lack of radar facilities suitable for PMSE observation. Radars in HF band had been considered not to be suitable for PMSE detection. However, recent observations by Karashtin *et al.* (1997) and Kelley *et al.* (2002) identified signatures of PMSE in HF frequencies, which demonstrated that HF radars are also powerful tool for the detection of PMSE. Ogawa *et al.* (2002a) explored peculiar near range echoes that cannot be explained by backscatters from field-aligned E region plasma irregularities. Relying on the fact that their morphological features are very similar to those of the Arctic PMSE, they concluded that this is the first observation of the Antarctic PMSE by using the SuperDARN HF radars. Very recently, Ogawa *et al.* (2002b) have succeeded in observing PMSE simultaneously with SuperDARN Finland radar and VHF MST radar at ESRANGE, Sweden. These two papers by Ogawa and co-workers are very suggestive of the possibility that the near range observations of the SuperDARN radars contain PMSE. However, amount of dataset surveyed in Ogawa *et al.* (2002a) was just 4 months in June, July, December and January 1997, which is not sufficient to confirm the PMSE hypothesis and to disclose the echo characteristics. We extended the work of Ogawa *et al.* (2002a) and searched 46 months of SuperDARN Syowa-East radar data from March 1997 to December 2000. Primary aim of this study is to clarify seasonal variation and local time distribution of the echo occurrence probability in a statistical fashion on the basis of the large amount of dataset. Long-term variability of the echo occurrence is also computed and its reliability is discussed in relation to the past observations.

2.2 Brief Description of the Radar

Data from the Super Dual Auroral Radar Network (SuperDARN) Syowa-East radar in Antarctica (69.01°S, 38.61°E) are employed in this analysis. The radar beam in the normal operation mode is sequentially scanned from beam 0 to beam 15 with a step in azimuth of 3.33°. It takes approximately 7 s to integrate backscatter returns in one direction and about 120 s is needed to complete a scan of all directions. The first range gate is set to 180 km, a range resolution of 45 km. Most of PMSE have been detected by using vertical incidence radars with short altitude resolution (minimum \approx 150 m), which is due to strong aspect sensitivity and thin layer of PMSE. Range resolution of the SuperDARN radar is set to 45 km, which is obviously thicker than the PMSE layer. However, radars of the SuperDARN employ oblique sounding system, in which maximum sensitivity occurs at

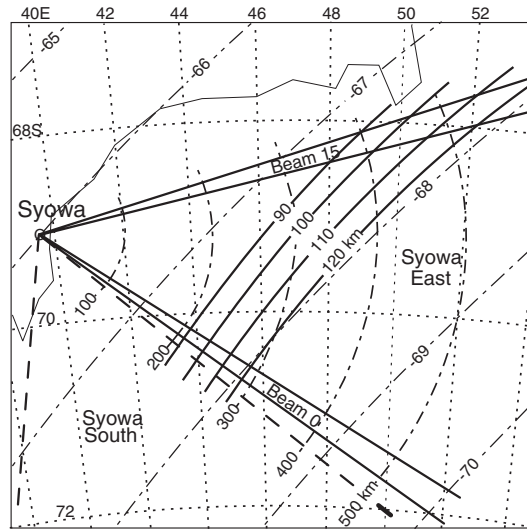


Figure IV-2.1: Field-of-view of the Syowa-East HF radar covered with 16 narrow beams. Geomagnetic latitude and ground ranges (100 km step) from Syowa Station are shown by the dot-dashed curves. Contour lines of angle ($=90^\circ$) between radar wave and the geomagnetic field vectors at altitudes of 90, 100, 110, and 120 km are shown by the solid curves (taken from Ogawa *et al.*, 2002a).

elevation angles of 15° - 35° depending on frequency (Greenwald *et al.*, 1985). This oblique incidence enables the radars to detect the echoes at mesospheric altitudes in spite of the disadvantage in altitude resolution. Ogawa *et al.* (2002b) demonstrated that angle of arrival of the peculiar near range echoes is consistent with this configuration.

Geometry of the Syowa-East radar in relation to the local geomagnetic field is displayed in Figure IV-2.1. Primary target of the SuperDARN radars is field-aligned irregularities (FAIs) in the E and F region ionosphere. Coherent radar echoes due to the E region FAIs are most strongly backscattered from an area where the angles between radar wave and the local geomagnetic field vectors are close to 90° (normality condition). Ogawa *et al.* (2002a) pointed out that the strong E region backscatter echoes (altitude is approximately 100-120 km) are expected to come from slant ranges of 250-320 km on beam 0 (western-most beam), while on beam 15 (eastern-most beam) they come from slant ranges of 400-500 km. This dependence of the ranges where the normality condition is satisfied on the beam direction becomes a key when we distinguish the echoes of present interest from E region FAIs, i.e., ranges where the echoes appear do not depend on beam number but are almost constant for all the beams.

2.3 Event Selection

We looked for echoes similar to those reported by Ogawa *et al.* (2002a) (hereinafter termed as Ogawa's PMSE) by eye inspection in the Syowa-East radar data of 46 months from March 1997 and December 2000. Data obtained from all operation modes (common time, special time, and discretionary time, see Greenwald *et al.*, 1995 in detail) were surveyed. There exist three classes of dominant backscatter target in the near range (say 180-500 km in slant range) observations of the SuperDARN radars. Those are (i) meteor trails, (ii) E region FAIs and (iii) Ogawa's PMSE. In the course of this research, backscatters from E region FAIs and meteor trail must be correctly distinguished from Ogawa's PMSE. Figure IV-2.2 shows the typical examples of these three kinds of backscatter features. Left panels show range versus time plots of backscatter power of meteor

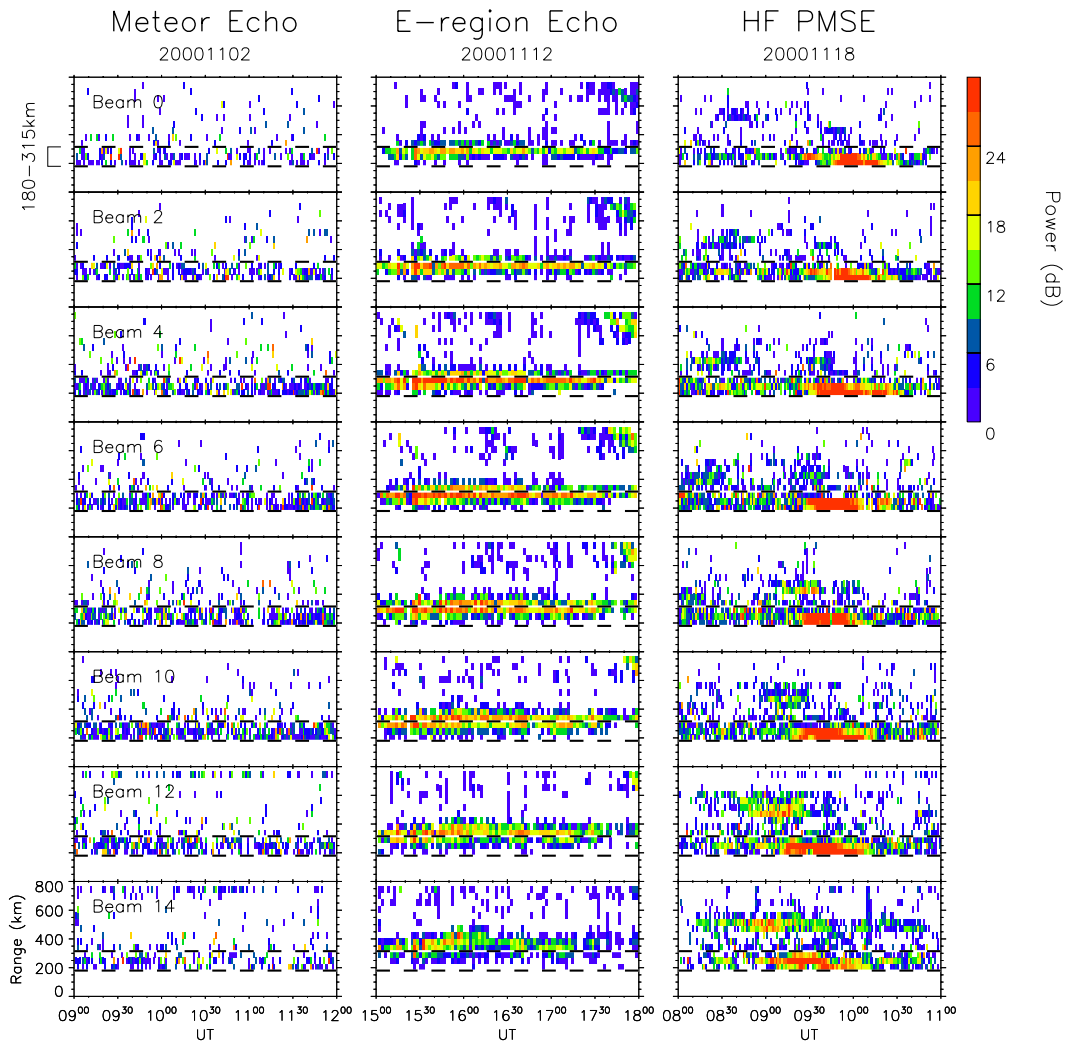


Figure IV-2.2: Typical examples of the three dominant echoes that appear in the near range observation of the SuperDARN radars, (left) meteor echoes, (middle) E region irregularities, and (right) the peculiar near range echoes (Ogawa’s PMSE). Time and slant range distributions of echo power on 8 beams (beams 0, 2, 4, ..., 14) are shown.

echoes observed by the SuperDARN Syowa-East radar, middle panels of typical E region backscatter and right panels of Ogawa’s PMSE, in which beams of even number are displayed. The power is colour-coded with blue representing the smallest power and red representing the greatest. Two horizontal dashed lines indicate a band of slant range between 180 and 315 km, where Ogawa *et al.* (2002a) identified Ogawa’s PMSE in the Syowa-East radar data.

In general, radars observe E region FAIs when their field-of-view intersects the region of auroral electrojet. These electrojet-related E region FAIs can be excluded by comparing echo appearance with local geomagnetic field observations. K index and H-component magnetogram at Syowa Station are employed in this study. In addition, the slant range where E region FAIs appear systematically changes with beam number increasing in the Syowa-East radar. These two diagnostic checks are firstly applied to the dataset. At last, we cautiously omitted near range echoes which are accompanied by apparent E region backscatters at farther ranges.

Meteor trails are also one of the major targets in near range observations of the SuperDARN radars, which have been used to measure surrounding neutral wind velocity (Hall *et al.*, 1997; Yukimatu and Tsutsumi, 2002). The slant ranges where they appear are very similar to those of Ogawa’s PMSE and average characteristics of

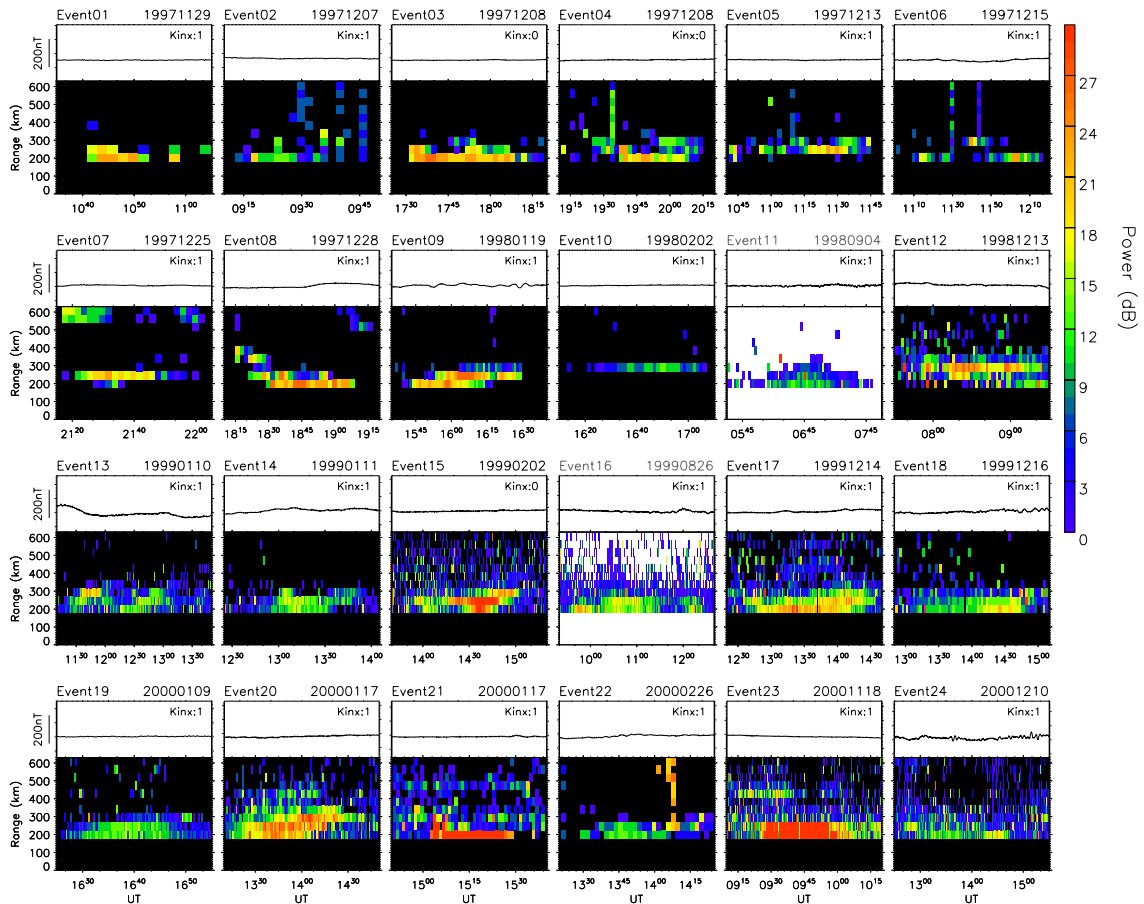


Figure IV-2.3: A collection of range versus time backscatter power plots of the selected events. H-component magnetogram from Syowa Station and local K index are attached. The panels with black background indicate the events that occurred during summer months from November to February.

the parameters (power, Doppler velocity and spectral width) are also similar. However, when we compare them with naked eyes, there exists clear difference in their characteristics. Meteor echoes appear randomly both in time and space because they tend to be short-lived (2 min, which is comparable to the scan repeat time of the radar) and range-isolated. In contrast, Ogawa's PMSE last longer than at least 20 minutes in a fixed range. Hence, meteor echoes can be accurately excluded by eye inspection.

We have selected echoes satisfying the following conditions simultaneously: (1) geomagnetic condition is quiet (local K index is 0 or 1, and no corresponding variation in H-component magnetogram at Syowa Station), (2) echoes existing somewhere between 180 to 315 km in slant ranges, (3) no random appearance in time and space, (4) no dependence of ranges where the echo appears on beam direction, and (5) no E region backscatters together with. As a result, total 24 events were identified during 46 months from March 1997 to December 2000. Figure IV-2.3 is a collection of range versus time backscatter power plots of these events, in which H-component magnetogram from Syowa Station and local K index are attached. Most of the events (22 events) occurred in summer months from November to February, which are displayed as a panel of black background. Two echoes that appeared in spring months (August and September) passed the criteria (Event 11 and Event 16). After this, seasonal, local time and long-term variations of echo occurrence probability will be investigated mainly based on the 22 events observed during summer months.

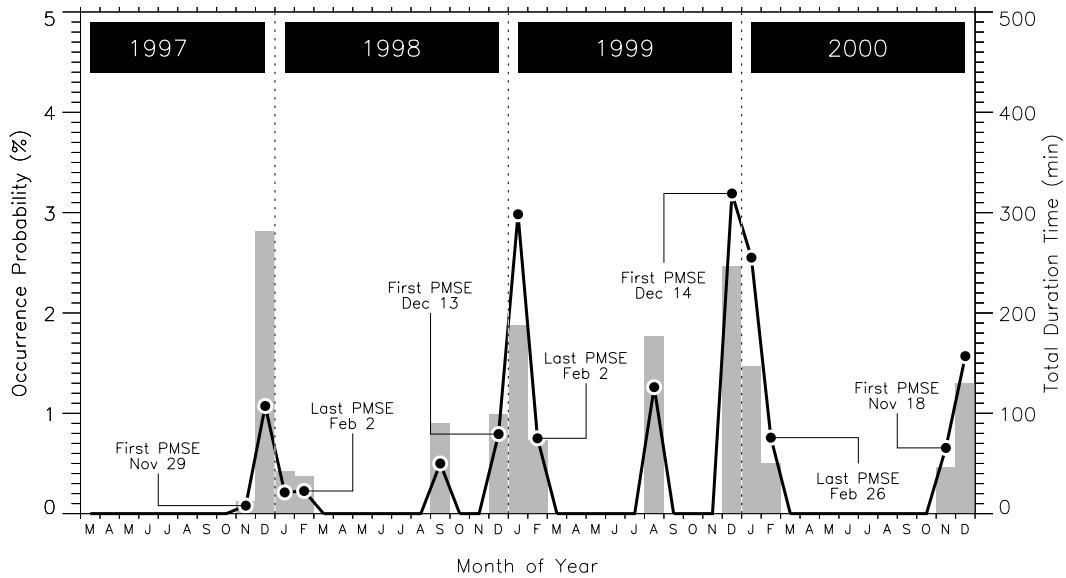


Figure IV-2.4: Seasonal occurrence probability of the echoes summarized in Figure IV-2.3. Histogram indicates the total duration in minutes binned into monthly intervals. The solid line with closed circle indicates the occurrence probability in percentage.

2.4 Seasonal Dependence

Primary objective of this study is to clarify the occurrence distribution of Ogawa's PMSE with season. Occurrence probability is estimated by using the total duration time of the events in minutes. It might be helpful to use the number of the day when the echoes appeared binned into monthly intervals. However, the number of the events identified is just 22, which is clearly insufficient to discuss the occurrence probability on the basis of the number of the days. Figure IV-2.4 shows seasonal occurrence probability of the 24 echoes summarized in Figure IV-2.3. Histogram indicates the total duration time in minutes binned into monthly intervals. If there are two consecutive samples whose backscatter power is greater than 3 dB within at least one range gate between 180 and 315 km, they are counted as a duration. This policy for computing a duration time makes some events to be divided into two or three parts (e.g., Event 2, 5, and 6). The solid line with closed circle indicates the occurrence probability in percentage, which was derived from dividing the total duration by the period of quiet geomagnetic conditions (local K index is 0 or 1). It is found that occurrence probability greatly enhances in summer months, while there is no clear peak in other seasons except for September 1998 and August 1999.

The seasonal variation presented in Figure IV-2.4 is in good agreement with the strong seasonal dependence of PMSE reported in the previous studies (Palmer *et al.*, 1996; Kirkwood *et al.*, 1998; Woodman *et al.*, 1999; Bremer *et al.*, 2002). The first and last dates when PMSE were observed in each season are also indicated in Figure IV-2.4. Bremer *et al.* (2002) have investigated 7 years of Andenes VHF radar data and have reported that averaged date of the first seasonal appearance of PMSE is May 19 (Julian day 139), and that of the last appearance is August 28 (Julian day 240). These dates are corresponding to November 19 and February 27 in the Southern Hemisphere, respectively. All of the 22 events detected with the Syowa-East radar during summer months are well inside of this period (hereinafter termed as PMSE season).

Kirkwood *et al.* (1998) have investigated PMSE detected with the ESRANGE MST radar at 68° N, 20° E in 1997. They have shown that the daily prevalence of PMSE rapidly increases at the beginning of the PMSE season. It took only 8 days until the prevalence reaches almost saturation. In contrast, the decay of PMSE from

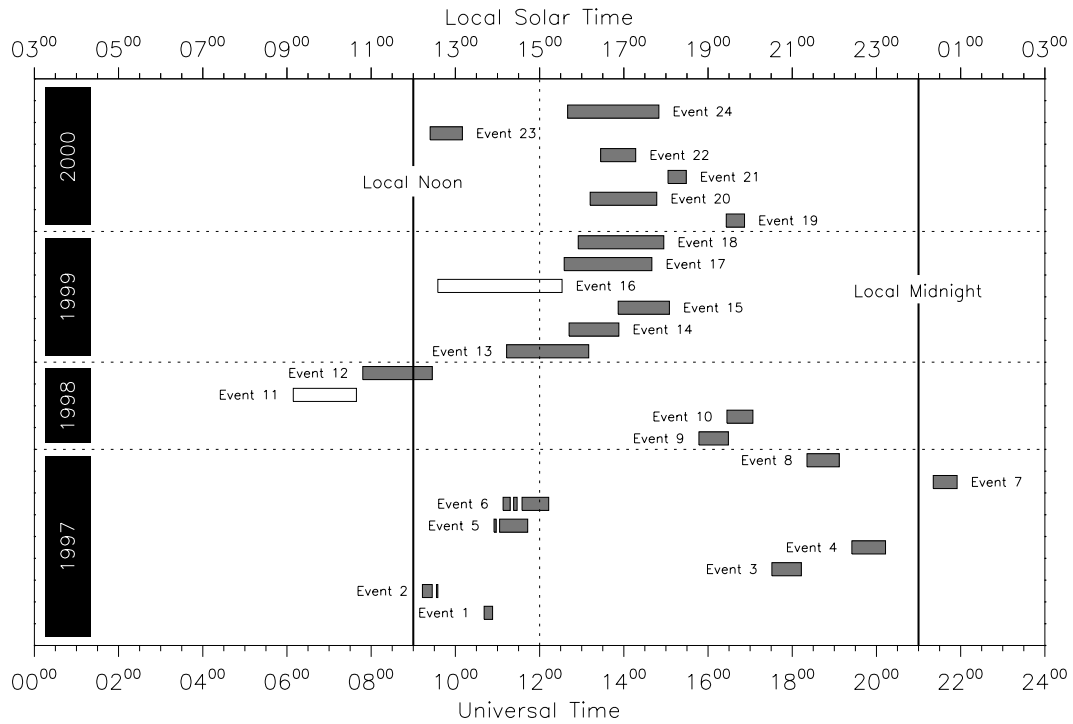


Figure IV-2.5: Occurrence distribution of the echoes listed in Figure IV-2.3 with UT and local time. Filled bars indicate duration of events that occurred in the PMSE seasons, and open bars showing that of the events in the other seasons.

maximum values to the end of the PMSE season took a whole month. This tendency has also been confirmed by Bremer *et al.* (2002). Also in the present dataset, the gradient of the increase of the occurrence probability is likely to be pronounced than the gradient of the decrease for all the PMSE seasons. Since Ogawa *et al.* (2002a) investigated only four months of data, seasonal characteristics of the echoes have not been investigated in detail. Our results strongly support the PMSE hypothesis by Ogawa *et al.* (2002a), and suggest that near range observations of the SuperDARN radar actually contain PMSE.

We have found two echoes that occurred in spring months. Balsley *et al.* (1983) have identified mesospheric echoes in winter months which appeared to be correlated with the high-energy particle precipitation into the mesospheric altitudes. These echoes have been further studied by Czechowsky *et al.* (1989). They reported that the echoes were detectable only during periods when electron densities were enhanced by energetic particle precipitation. Recently, Kirkwood *et al.* (2002) observed winter time mesospheric echoes in the polar region during several recent solar proton events. Then, the two spring echoes in the present study are expected to be due to the high-energy particle precipitation. During the intervals of the two spring echoes, however, enhancement of proton flux was not observed by the geosynchronous satellites GOES and no signature of radio wave absorption was identified by the Riometer at Syowa Station. These facts lead us to conclude that the two near range echoes in spring are not associated with the high-energy particles precipitation. The origin of these echoes is not clear at the moment, and more detailed study is needed.

2.5 Local Time Dependence

Figure IV-2.5 shows how the occurrence of the echoes listed in Figure IV-2.3 varies with UT and local time. Filled bars indicate duration of the events that occurred in the PMSE season, open bars showing that of the

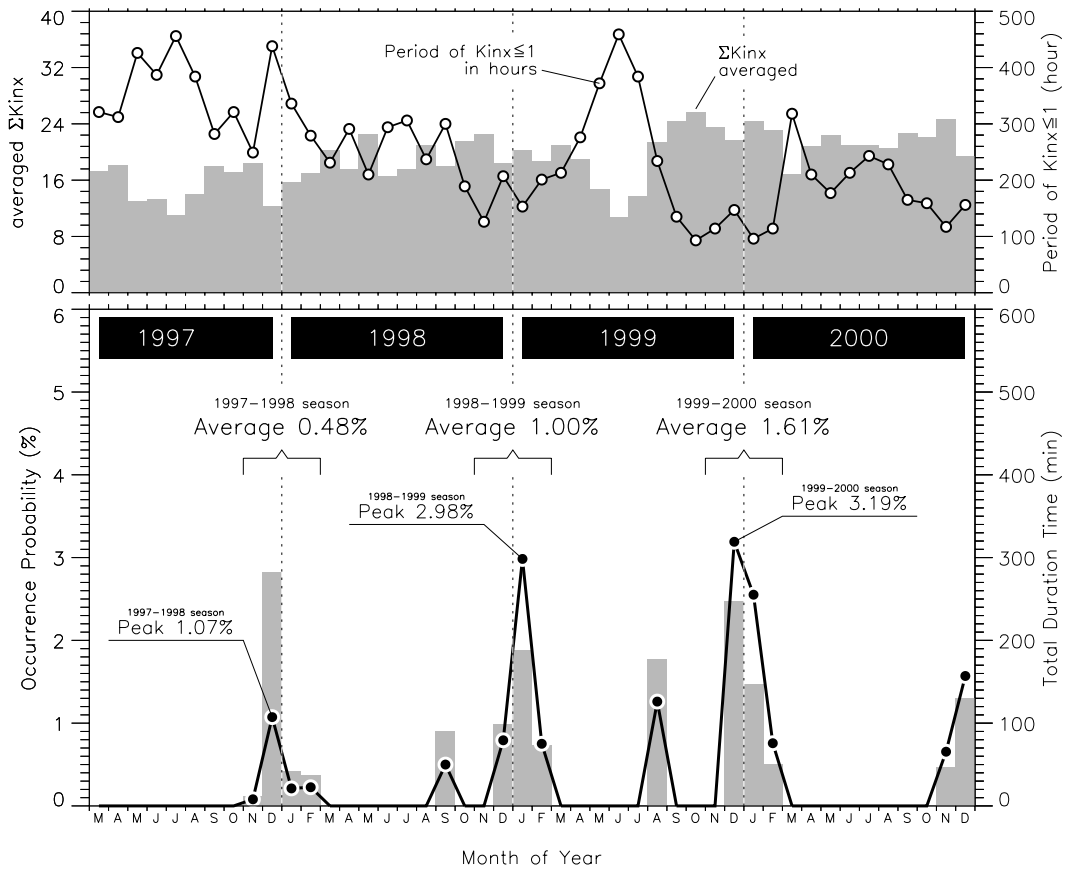


Figure IV-2.6: (Upper) variation of the averaged ΣK index (histogram) and period of K index ≤ 1 in hours (line with open circle). (Lower) seasonal occurrence probability of the echoes summarized in Figure IV-2.3. Histogram indicates the total duration in minutes binned into monthly intervals. The solid line with closed circle indicates the percentage of the occurrence probability. Peak and average values of the occurrence percentage for each PMSE season are also presented.

events in the other seasons (Event 11 and Event 16). Most of the echoes in the PMSE season are found to appear between 12 and 18 LT, although some of them appear before local midnight (between 19 and 01 LT).

Balsley *et al.* (1983) reported that the occurrence of PMSE has its maximum value just after the local noon and that secondary peak appears around the local midnight in most cases. They also have shown that there exists a prominent minimum near 20 LT. This semi-diurnal pattern is confirmed by many authors (Czechowsky *et al.*, 1989; Williams *et al.*, 1995; Palmer *et al.*, 1996). Our result is basically consistent with the results of the previous studies. However, the secondary peak around the midnight is not so prominent, especially for the interval from 1998 to 2000. This could be due to the fact that we have eliminated near range echoes that had appeared together with the E region FAIs. The E region FAIs are predominantly nighttime phenomena and their occurrence is enhanced as the solar activities are increasing. Then, some PMSE echoes on the nightside might be filtered out together with the E region FAIs during years from 1998 to 2000. This implies that the occurrence of PMSE on the nightside could be underestimated in this analysis. The other point is that few events occur before local noon. Meteor echoes are generally observed in the dawn hemisphere (for the detail of the occurrence distribution of the meteor echoes at Syowa Station, see Ogawa *et al.*, 1985). This suggests that our selection criteria were successful in eliminating a contamination of the meteor echoes.

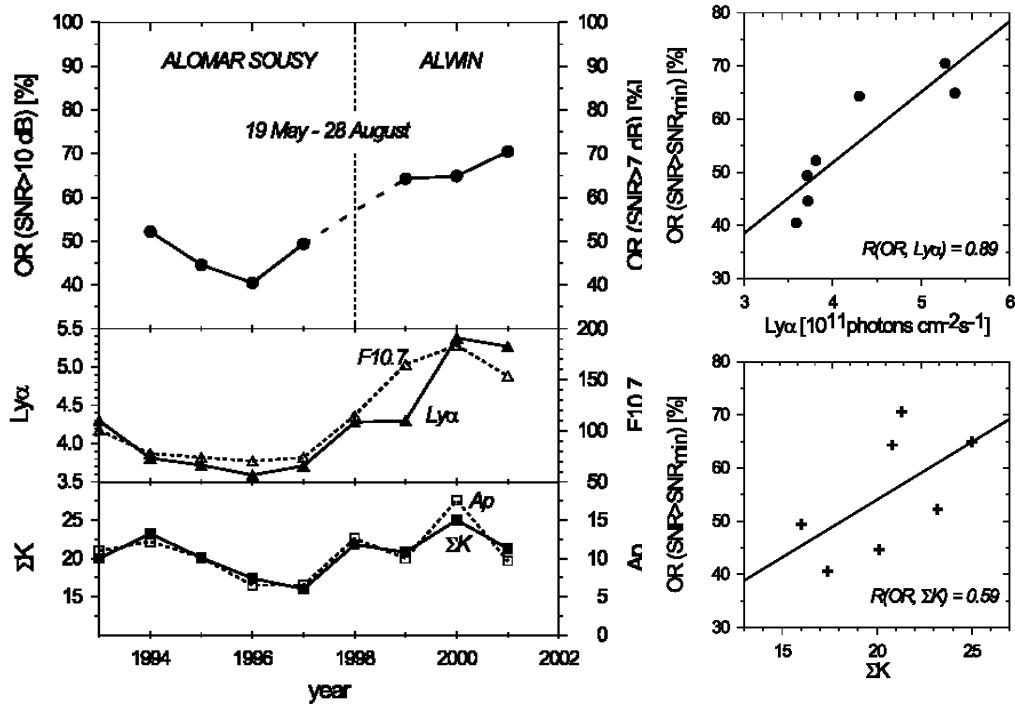


Figure IV-2.7: (Left) comparison of long-term variation of yearly PMSE occurrence rates with two VHF radars in Andenes, Norway with corresponding variations of the solar wave radiation (Lyman α and 10.7 cm radio flux) and of geomagnetic activity (global Ap and local ΣK index). (Right) correlation of yearly PMSE occurrence rate with corresponding solar Lyman α radiation data (upper) and geomagnetic ΣK values (lower) (taken from Bremer *et al.*, 2002).

2.6 Long-Term Variabilities

The lower panel of Figure IV-2.6 displays the same statistical results as Figure IV-2.4, but peak and average values of the monthly occurrence probability for the three individual PMSE seasons are presented. The occurrence is found to increase year by year. The peak values from 1997 to 2000 are 1.07%, 2.98% and 3.19%, respectively. Occurrence percentages averaged for each complete PMSE season are also likely to increase (0.48%, 1.00% and 1.61%).

There are many distinct theories for PMSE generation. However, it is thought that PMSE is a small-scale structures which are allowed to be maintained due to the reduction of the diffusivity by the effect of charged ice particles and aerosols (Kelley *et al.*, 1987; Kelley and Urwick, 1998; Cho *et al.*, 1992a). This theory comes from the fact that appearance of PMSE is closely related to the mesopause temperature and water vapor concentration (Balsley and Huaman, 1997; Kirkwood *et al.*, 1998). Based on this theory, it might be speculated that increasing tendency of the PMSE occurrence in our dataset might suggest that the mesopause temperature and water vapor concentration are becoming more favorable for PMSE generation in recent years. This speculation could allow us to use PMSE as a diagnostic tool for the global climate change. This is because water vapor in the mesosphere is believed to come from the photo-dissociation and oxidation of upwardly transported methane and a drop in mesopause temperature could result from an anthropogenic increase in CO_2 . However, care must be taken when we interpret the long-term variabilities of the PMSE occurrence because period of the data used in this study is less than 4 years and this period is well overlapping the phase of increasing solar activities.

Long-term variation of PMSE occurrence is investigated using VHF radars at Norway by Bremer *et al.*

(2002). Their results are summarized in Figure IV-2.7. They presented that the occurrence is gradually increasing during the period from 1996 to 2001. However, this trend is found to positively correlated with the mesospheric ionization level indexed by solar indices (F10.7 and Lyman α) and geomagnetic indices (Ap and local K index). They pointed out that amount of the database (6 years) is not enough to estimate long-term increasing trend due to the global change of the Earth's environment. Also during the interval of the present study (1997-2000), mesospheric ionization level is expected to be increasing. Then, even if occurrence of PMSE is actually increasing by the effect of the global environmental change, their signature would be hidden by the bias due to the increasing trend of the mesospheric ionization level.

At the top panel of Figure IV-2.6, monthly averaged ΣK index (histogram) and period of K index ≤ 1 in hours (line with open circle) are presented. We have sampled PMSE which appeared during quiet geomagnetic conditions (local K index ≤ 1), i.e., we have filtered out PMSE that occurred during disturbed conditions. The number of these uncounted echoes is expected to be larger in 1999-2000 PMSE season than that in 1997-1998 season because the period of K index ≤ 1 is decreasing. This could be another bias when we consider the long-term variabilities of PMSE occurrences. Because of the two biases described above, it can be concluded that the increasing trend of PMSE shown in Figure IV-2.6 does not have a significant meaning in terms of the relationship with the global environmental change. In order to acquire more reliable and conclusive result, PMSE occurrence must be investigated by using the data of longer period.

2.7 Summary

We have looked for echoes, similar to those reported by Ogawa *et al.* (2002a), by eye inspection in 46 months of the SuperDARN Syowa-East radar data from March 1997 to December 2000. Although strict criteria were applied to distinguish the echoes of the present interest from the E region backscatters and meteor echoes correctly, total 24 events pass the criteria. Most of them (22 events) appeared during summer months from November to January, maximum being located in December or January. The local time distribution of the echoes has its maximum value just after the local noon and secondary peak around the local midnight, and thus follows a semi-diurnal pattern. These characteristics are well consistent with those of Polar Mesosphere Summer Echoes (PMSE), which confirms that the peculiar near range echo in the SuperDARN Syowa-East radar does correspond to PMSE. Two events occurred in spring (August and September, respectively), whose origin is not clear at the moment. Echo occurrence rate seems to increase year by year, which might suggest that conditions for generating PMSE (the mesopause temperature and water vapor concentration) are becoming more favorable in the recent years. However, amount of the data employed in this study is clearly not sufficient to extract essential long-term trend of PMSE due to the contamination of the biases such as the increasing mesospheric ionization level. Then, long-term trend of PMSE occurrence is still controversial.

Chapter 3

Conclusion and Future Directions

We have investigated statistical characteristics of the peculiar near range echoes that are firstly identified by Ogawa *et al.* (2002a). Most important finding is that the echoes appeared predominantly in summer months from November to February. This strong seasonal dependence is consistent with those of Polar Mesosphere Summer Echoes (PMSE). It is also reported that local time distribution of the echo appearance is basically similar to that of PMSE. Ogawa *et al.* (2002a) concluded that these peculiar near range echoes correspond to PMSE at HF frequencies, because they could not explained them by the other backscatter targets such as the E region FAIs and meteor trails. However, amount of the dataset was clearly insufficient to acquire final conclusion. Our study indicated that statistical characteristics of the echoes are quite consistent with those of PMSE. Then, it was confirmed that the peculiar near range echoes are actually PMSE.

PMSE have been investigated by using various kinds of instruments such as the ground-based radar and in-situ measurements by rockets. Previous studies pointed out that there exist two outstanding questions that have not been answered. Those are

- Is there an interhemispheric difference in PMSE activities ?
- Is the occurrence of PMSE increasing in the recent years ?

The former issue has been discussed since Woodman *et al.* (1999) made the first observation of the Antarctic PMSE in 1994. They have presented surprising result that the Antarctic PMSE were much weaker than the Arctic PMSE. Balsley and Huaman (1997) and Huaman and Balsley (1999) discussed this interhemispheric difference in terms of possible difference in temperatures and water vapor concentrations. However, Lübken *et al.* (1999) reported that there is no major difference in summer mesopause temperatures between two hemispheres. Further detailed investigations are needed to estimate how activities of PMSE differ between two hemispheres. However, it is difficult to do an interhemispheric comparison of PMSE activities because of the small number of VHF radar in the Southern Hemisphere. Our statistical analysis has shown that the peculiar near range echoes in the SuperDARN radar are actually corresponding to PMSE at HF frequencies. Then, SuperDARN radars can be added to the list of the radars available for PMSE detection. 15 SuperDARN radars that have common instrumental design are currently operative in both hemisphere (9 radars in the Northern and 6 radar in the Southern Hemisphere). If we detect PMSE by using all of the SuperDARN radars in both hemisphere, we can estimate quantitatively how activity of PMSE differ between two hemispheres.

Long-term variability of PMSE occurrence is the other important issue to be discussed. Some authors have a speculation that occurrence of PMSE have connection with global environmental change through the decrease of mesospheric temperature and water vapor concentration. They expect that PMSE can be used as an indicator of the global environmental change like as noctilucent clouds (NLCs). Our statistical result

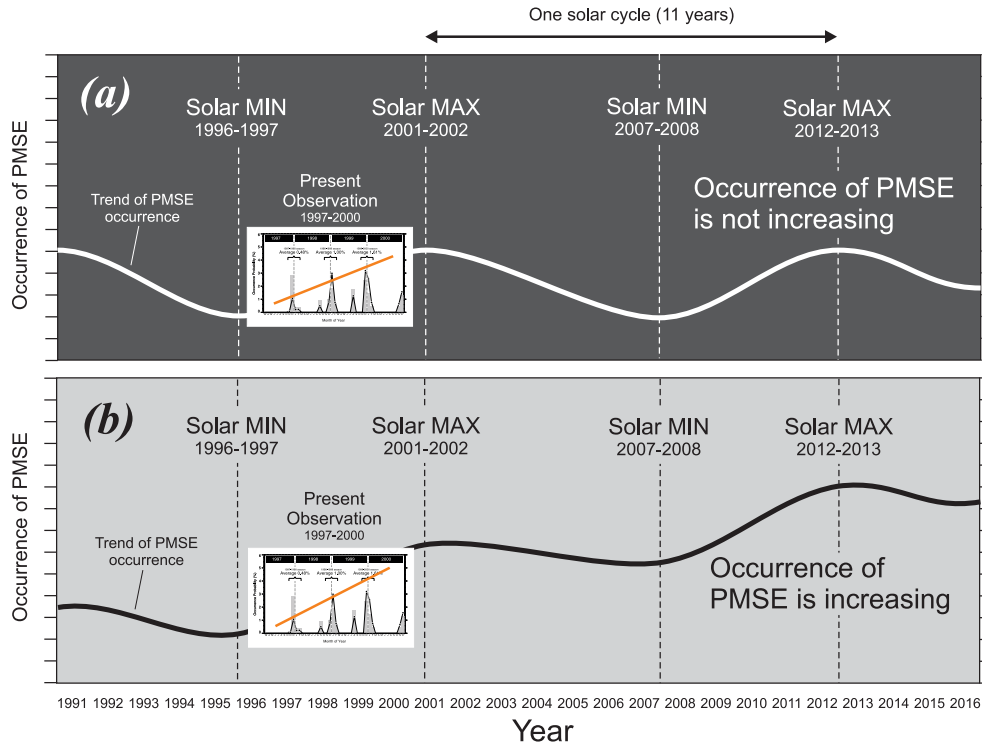


Figure IV-3.1: Pictures illustrating how the occurrence of PMSE will be in the coming decade. Two competing predictions are shown. The upper panel shows the case in which the occurrence of PMSE is not increasing, while the lower panel shows the other case where the occurrence of PMSE is gradually increasing (see text in detail).

exhibited increasing trend of the echo occurrence probability. However, period of the analysis corresponds to the period of increasing solar activities. The first study of long-term variabilities of PMSE was made by Bremer *et al.* (2002) using 7 years of VHF radar data from 1994 to 2001. They have pointed out that activities of PMSE is primarily controlled by the solar and geomagnetic activities and it is difficult to extract the effect of the global environmental change. This difficulty also appears when we attempt to interpret of our statistical results. Increasing trend is likely to be correlated with the increasing solar activities during the period of this study. Thus, it is concluded that occurrence probability must be investigated over the period longer than at least one solar cycle (11 years) in order to extract pure long-term trend of PMSE. If long-term variability of PMSE occurrence were investigated using the dataset longer than one solar cycle, two different results would be expected. Schematic pictures of them are shown in Figure IV-3.1. Upper panel shows the case in which the occurrence of PMSE is not increasing but just modulated in correlation with the solar activities of 11 years. Lower panel shows the other case, where the occurrence of PMSE is gradually increasing although the biases due to the solar activities are modulating the trend. We have to determine which of these two pictures is correct by using dataset of longer period.

We now plan to develop an algorithm that picks up the SuperDARN PMSE automatically. There would be some difficulties in eliminating contaminations from E region FAIs and meteor scatter. However, if it is done, we can easily estimate how interhemispheric difference and long-term variabilities of PMSE activities are. Then, relationship between PMSE activity and mesospheric temperature would be disclosed and PMSE might be used as an indicator of the global environmental change.

Part V
Appendix

Appendix A

Techniques for Doppler Spectral Analysis of Coherent Backscatters in the High-Latitude Ionosphere

A.1 Introduction

A number of parameters can be estimated from the backscattered signal received by the SuperDARN radars. There are three important parameters for the purpose of the study of the ionospheric plasma. They are (i) the intensity of the backscatter signal, (ii) the mean Doppler velocity, and (iii) the width of the Doppler power spectrum. A relationship between these parameters and the Doppler spectrum is presented in Figure V-A.1. Doppler velocity is widely utilized as a diagnostic of the bulk plasma motion of the ionosphere under the influence of the convection electric field. In this thesis, we have focused on a characteristics of the Doppler spectral width obtained from the SuperDARN radars and have reported that the spectral width is also useful for the identification of the geophysical boundaries and processes within the dayside high-latitude ionosphere. Thus, further detailed introduction on the Doppler spectral analysis might be needed to help the readers to understand our analysis. Here, we review the techniques for the Doppler spectral analysis applied for the data production in the SuperDARN community.

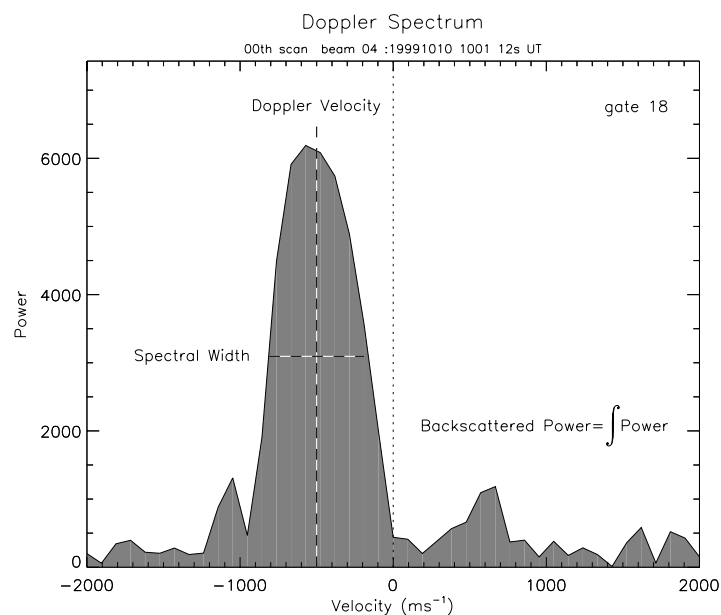


Figure V-A.1: An example of the Doppler spectrum obtained from the SuperDARN radar observation.

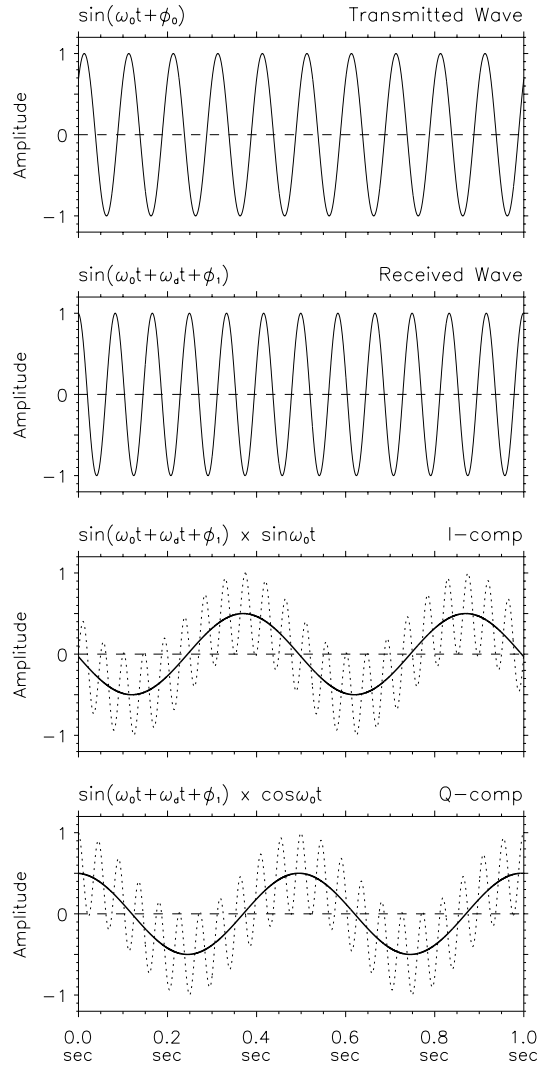


Figure V-A.2: Plots illustrating how the Doppler component is extracted from the backscattered signal. (Top two panels) forms of the transmitted wave and received backscattered signal, respectively. (Bottom two panels) extracted I and Q -components that include information about the Doppler frequency ω_d .

A.2 Extraction of Doppler Component (in analog part)

Frequency of the electromagnetic waves used in the SuperDARN observation is ranging from 8 to 20 MHz, normally set to around 10 MHz. Typical drift velocity of ionospheric plasma within the high-latitude F region is an order of 10^1 - 10^3 m s⁻¹. Corresponding Doppler shift imposed on the backscattered signal ranges from 0.7 Hz to 70 Hz when the frequency of the transmitted wave is assumed to be 10 MHz. Information that is essential for the estimation of the ionospheric plasma drift is the Doppler frequency, then, component of the Doppler frequency must be extracted from the backscattered signal within the receiver before sampling (i.e. before digitalization).

Let us assume that the form of the transmitted wave, S_T , and that of the received wave, S_R , are

$$S_T = A_T \sin[\omega_0 t + \phi_0] \quad (\text{A.1})$$

$$S_R = A_R \sin[(\omega_0 + \omega_d)t + \phi_1] \quad (\text{A.2})$$

where ω_0 is angular frequency of the transmitted wave, ω_d is a Doppler shift imposed on the received wave, ϕ_0

and ϕ_1 are initial phases of the transmitted and received wave, respectively. Here, let us consider a product $S_R \cdot \sin \omega_0 t$,

$$S_R \times \sin \omega_0 t = A_R \sin[(\omega_0 + \omega_d)t + \phi_1] \times \sin \omega_0 t \quad (\text{A.3})$$

$$= \frac{1}{2} A_R \{ \cos[\omega_d t + \phi_1] - \cos[(2\omega_0 + \omega_d)t + \phi_1] \} \quad (\text{A.4})$$

$$= \frac{1}{2} A_R \{ \cos[2\pi f_d t + \phi_1] - \cos[(4\pi f_0 + 2\pi f_d)t + \phi_1] \} \quad (\text{A.5})$$

where f_0 is frequency of the transmitted wave and f_d is the Doppler frequency. Since the difference in frequency between the first and second terms of the right hand side of equation (A.5) is enough large, $A_R \cos(\omega_d t + \phi_1)$, which has an information on ω_d , can be extracted using a bandpass filter in an analog circuit. In a similar manner, a product $S_R \cdot \cos \omega_0 t$ provides $A_R \sin(\omega_d t + \phi_1)$. These signals are sampled with a period of 300 μs as I -component (in phase) and Q -component (quadrature phase), respectively. After the digitalization, we process a complex value, $S(t)$, composed of I and Q -components,

$$S(t) = I + iQ \quad (\text{A.6})$$

$$= A_R \cos(\omega_d t + \phi_1) + iA_R \sin(\omega_d t + \phi_1) \quad (\text{A.7})$$

$$= A_R \exp[i(\omega_d t + \phi_1)] \quad (\text{A.8})$$

Derivation of the I and Q -components is schematically illustrated in Figure V-A.2. Top two panels show the form of the transmitted and received waves. Solid lines in the bottom two panels indicate I and Q -components extracted through the procedure described above.

A.3 Calculating Auto Correlation Function (ACF)

There exist various kinds of method for an analysis of time-series with periodic or quasi-periodic characteristics (e.g., Fourier analysis, maximum entropy method, wavelet analysis, auto-correlation function analysis). SuperDARN radars transmit electromagnetic waves toward the ionosphere and receive time-series of the signals backscattered from the FAIs. Signal processing technique is based on auto-correlation function (ACF) analysis. There is no easy way to understand the detail of the SuperDARN data production without knowledge of the ACF analysis. In this section, essence of the ACF analysis is briefly introduced, and then how it can be applied for the radar data is described.

A.3.1 Brief Tutorial for Spectrum Analysis Using ACF

If we consider a single time-series $S(t)$, the auto-correlation function (ACF) can be defined as an ensemble average of a product $S(t) \cdot S(t + \tau)$

$$\text{ACF}(\tau) = \langle S(t) \cdot S(t + \tau) \rangle \quad (\text{A.9})$$

$$= \lim_{T \rightarrow \infty} \frac{1}{T} \int_{-T/2}^{T/2} S(t) \cdot S(t + \tau) dt \quad (\text{A.10})$$

where the bracket means an ensemble average (it can be replaced with temporal average for single time-series: Ergodic hypothesis) and τ is a lag. What is worth noting is that the ACF is not a function of t but a function of lag τ . When we consider time-series that are defined continuously between $-\infty$ and ∞ , it might be helpful to use ACF normalized by a value of zero lag ACF, which is called auto-correlation function coefficient (here we

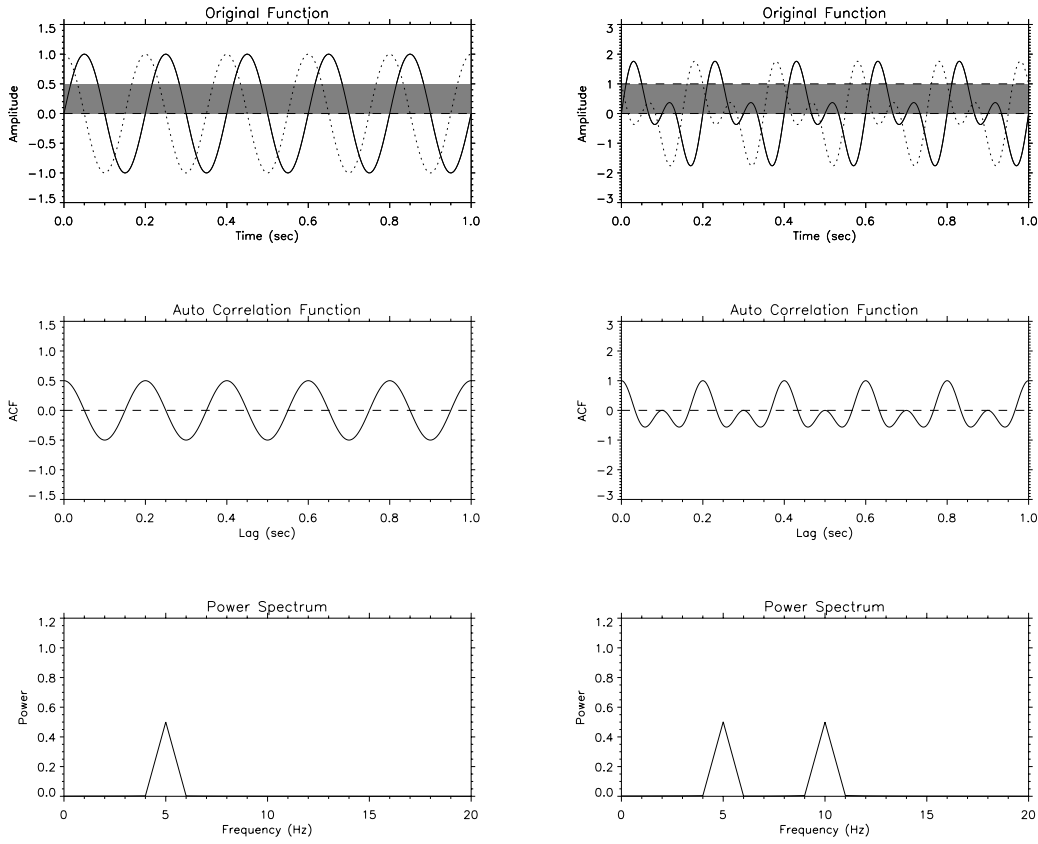


Figure V-A.3: Samples of the ACF analysis. (Left) the top panel shows the original sine wave with frequency of 5 Hz (i.e., $\sin 10\pi t$) where averaged power is presented as a shadow. The middle panel is the corresponding ACF ($\frac{1}{2} \cos 10\pi t$). The bottom panel gives a Fourier transformation of the ACF shown in the middle panel, which is equal to the power spectrum of the original sine wave. (Right) the other example in which the original wave is a summation of the sine waves whose frequencies are 5 and 10 Hz.

name it ACFC). If $\sin \omega t$ is considered for example, ACFC can be obtained as follows:

$$\text{ACFC}(\tau) = \lim_{T \rightarrow \infty} \int_{-T/2}^{T/2} \sin \omega t \cdot \sin \omega(t + \tau) dt / \lim_{T \rightarrow \infty} \int_{-T/2}^{T/2} \sin \omega t \cdot \sin \omega t dt \quad (\text{A.11})$$

$$= \cos \omega \tau \quad (\text{A.12})$$

When we consider non-continuous time-series data, the ACF can be defined as follows:

$$\text{ACF}(\tau) = \frac{1}{N} \sum_{n=1}^N S(t_n) \cdot S(t_n + \tau) \quad (\text{A.13})$$

The left panels of Figure V-A.3 demonstrate one of the simplest examples. The top panel shows the original sine wave with frequency of 5 Hz (i.e., $\sin 10\pi t$) where averaged power is presented as a shadow. The middle panel is the corresponding ACF ($\frac{1}{2} \cos 10\pi t$). Comparison between these two curves provides us physical meaning of the ACF, that is, the ACF has its maximum when the lag is equal to an integer multiple of the period of the original time-series. Another point to be noted is that the Fourier transform of the ACF corresponds to a power spectrum of the original time-series. This fact is well known as Wiener-Khintchine's theorem and widely utilized in the spectrum analysis. The bottom panel gives a Fourier transformation of the ACF shown in the middle panel. Dominant frequency of the original sine wave (5 Hz) is correctly detected and its power is also equal to the averaged power of the original wave. The other example is shown in the right panels of Figure V-A.3, which is slightly complicated. Original wave is a summation of the waves whose frequencies are 5 and 10 Hz. Also

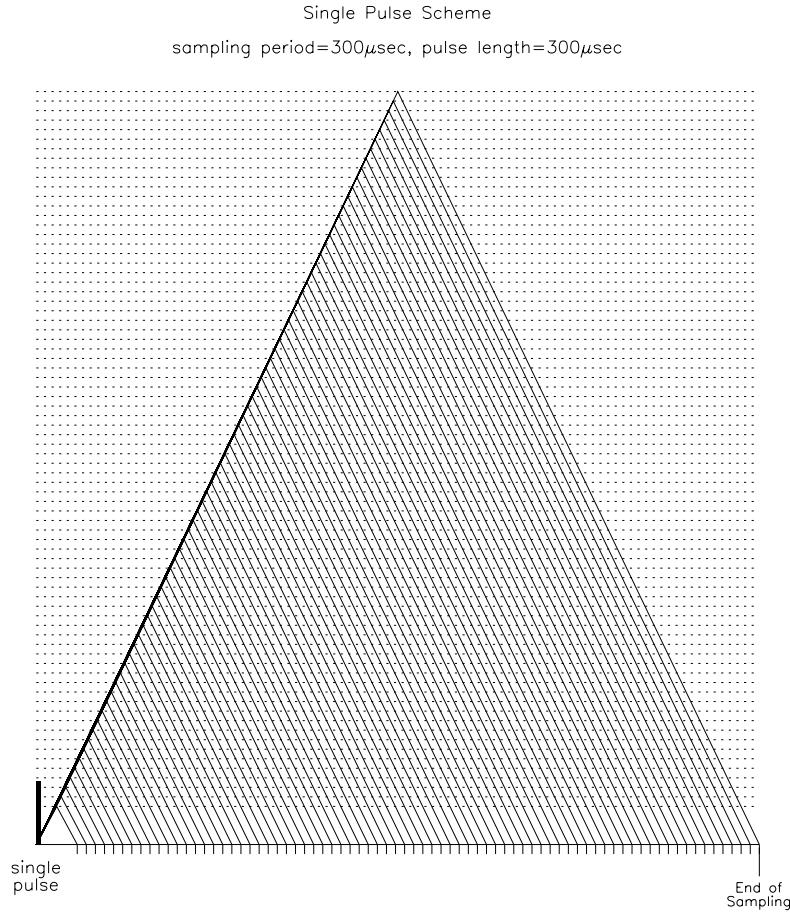


Figure V-A.4: Schematic diagram illustrating how the single pulse is backscattered in the ionosphere and is sampled by the receiver. Horizontal axis is time and vertical axis is range.

in this case, we can see that the ACF analysis obtained two dominant frequencies (i.e., peaks are found to be located at 5 and 10 Hz).

A.3.2 Single Pulse Observation

Multipulse observation (coded pulse) is employed in the SuperDARN observations. Here, however, we start with a description of single pulse observation as an introduction, and then we will turn to the multipulse observation. Here, single pulse means HF band (8-20 MHz, period is about 0.1 μ s) electromagnetic wave whose length is approximately 300 μ s (containing 3000 periods). Signal is sampled as a form of the IQ -output, $S(t)$, with a period of 300 μ s,

$$S(t) = A \exp^{i\omega at} \exp^{i\phi_1} \quad (\text{A.14})$$

Figure V-A.4 schematically illustrates how the transmitted single pulse is backscattered in the ionosphere and is sampled by the receiver. Range from which the received signal comes can be determined directly from arrival time of the signal. In practice, a number of single pulses are needed for the calculation of the ACF, hence one set of single pulse scheme contains large number of the single pulses (typically 70 subsets). In addition, interval between the pulses must vary in order to calculate the ACF for various lags. When a set of single pulses is completed, we can calculate the ACF of accumulated IQ -outputs for each range gates for various lags. Since

the IQ -output is a complex form, then the ACF of $S(t)$ is generally,

$$\text{ACF}(r, \tau) = \langle S(r, t) \cdot S(r, t + \tau)^* \rangle \quad (\text{A.15})$$

$$= \langle A(r) \exp^{i(\omega_d(r)t + \phi_1(r))} \cdot A^*(r) \exp^{-i(\omega_d(r)t + \omega_d(r)\tau + \phi_1(r))} \rangle \quad (\text{A.16})$$

$$= A(r) \cdot A^*(r) \exp^{-i\omega_d(r)\tau} \quad (\text{A.17})$$

Once the ACF is calculated, we can employ Wiener-Khintchine's theorem and derive the power spectrum from the Fourier transformation of the ACF.

A.3.3 Correlation Time

At first glance, the single pulse observation is likely to be valid for the observation of the ionosphere. In practice, however, this kind of pulse scheme is never employed in the radar observations of the FAIs. Here, we introduce a concept of 'correlation time' and discuss the reason why the single pulse observation is never used in our observations. Correlation time is defined as an interval during which correlation dominated by common physical process is maintained in time-series data. ACF analysis is based on a correlation between two points in single time-series. If the sampling period is larger than the correlation time, we can not obtain substantial power spectra from the ACF analysis. In our case, the correlation time is corresponding to an interval during which nature of the scattering medium in the ionosphere is preserved. Typical correlation time of the FAIs within the high-latitude E and F region ionosphere ranges approximately 2-30 ms. Physically, it may be due to the finite lifetime of the individual irregularity structures and the random or turbulent velocities that exist in the scattering volume. If we attempt to obtain backscatter echo over the horizon (i.e. 3000 km in range), sequence of the single pulse must approximate 20 ms. This could be longer than the correlation time of the scattering medium, then the ACF with effective lag will not be obtained. If we apply the ACF analysis for Doppler spectrum derivation, temporal resolution of the sampling should be much shorter than the correlation time of the scattering volume that we expect. This is the reason why the multipulse observation is employed in the SuperDARN observations.

A.3.4 Multiple Pulse Observation

The basic principle of the multipulse observation is to transmit a sequence of pulses such that intervals between any two pulses of the sequence are different. This pulse scheme was initially proposed by Farley (1969) and was precisely described in Farley (1972). One of the multipulse schemes currently used by the SuperDARN radars (7-pulse scheme) is shown in Figure V-A.5. The pulse length is 300 μs , giving a resolution of 45 km in radar range. The backscattered signal is digitized with a sampling period of 300 μs , equal to the pulse length. Time separation between pulses is an integer multiple of $\tau_0 = 2.4$ ms (equal to 8 sampling periods). From the 7-pulse sequence, 17 delays of the ACF are calculated. The total signal received at a given time is the sum of the signals backscattered from different range gates and corresponding to the pulses previously transmitted.

For instance (illustrated in Figure V-A.6), 33 ms after the start of the pulse sequence, the received signal will be the sum of the echoes backscattered at ranges 1710 km (from the second pulse of the sequence) and 630 km (from the third pulse). The echo backscattered from the range 4950 km (first pulse) can be neglected, because echoes returning from ranges over 3500 km are usually too faint. The received signal, S_0 , can be written,

$$S_0 = A_1 \exp^{i\omega_1 t_0} + A_2 \exp^{i\omega_2 t_0} \exp^{i\phi_2} \quad (\text{A.18})$$

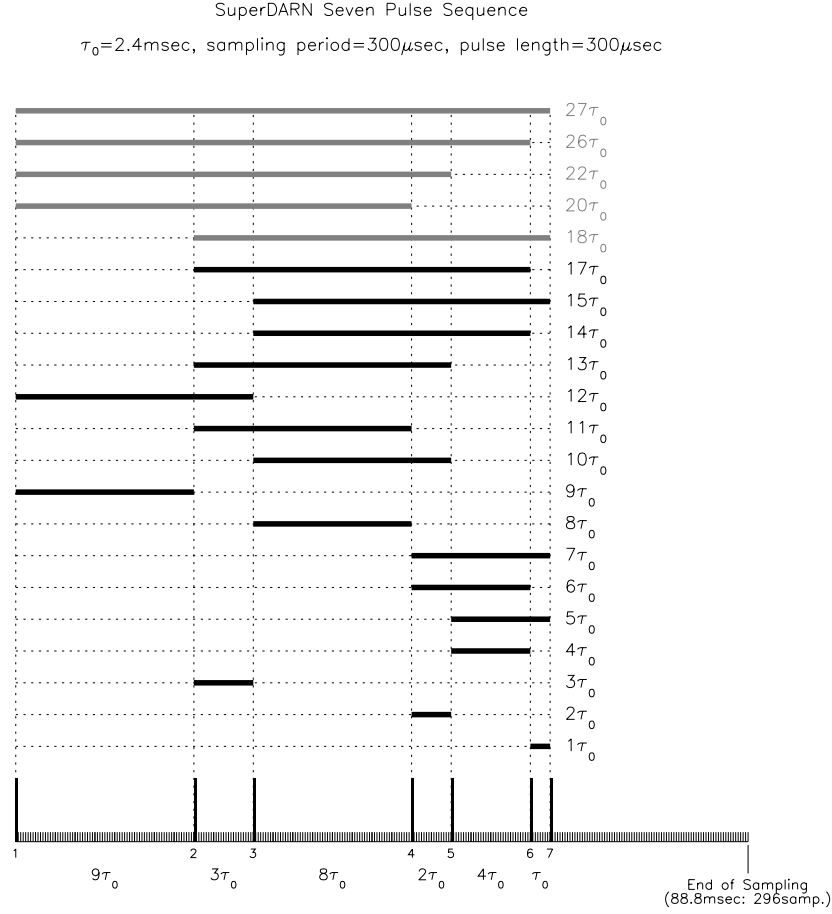


Figure V-A.5: Multi pulse scheme (7-pulse) currently used in the SuperDARN observations.

where t_0 is the time of the measurement (in this case, 33 ms), ω_1 and ω_2 are the angular frequencies of the signals backscattered from ranges 1710 km and 630 km, respectively, A_1 and A_2 are associated amplitudes, and ϕ_2 is the phase difference between two signals. In order to calculate the ACF for the range 1710 km and for the delay τ (for instance, $\tau = 3\tau_0$), we combine the signal received at time $t_0 + \tau$ (here 40.2 ms), S_τ , with S_0 ,

$$S_\tau = A_1' \exp^{i\omega_1(t_0+\tau)} + A_3 \exp^{i\omega_3(t_0+\tau)} \exp^{i\phi_3} \quad (\text{A.19})$$

This signal is also the sum of two echoes, one from the range 1710 km with the amplitude A_1' (which can be different from A_1 because of the time variation of the scattering fluctuations), and one from the unwanted range 2790 km with the amplitude A_3 and angular frequency ω_3 , in which phase difference between two sources is represented by ϕ_3 . The product $S_0 \cdot S_\tau^*$ is then,

$$\begin{aligned} S_0 \cdot S_\tau^* &= A_1 A_1'^* \exp^{-i\omega_1 \tau} \\ &+ A_2 A_1'^* \exp^{-i(\omega_1 - \omega_2)t_0} \exp^{-i\omega_1 \tau} \exp^{-i\phi_2} \\ &+ A_1 A_3'^* \exp^{-i(\omega_3 - \omega_1)t_0} \exp^{-i\omega_3 \tau} \exp^{-i\phi_3} \\ &+ A_2 A_3'^* \exp^{-i(\omega_3 - \omega_2)t_0} \exp^{-i\omega_3 \tau} \exp^{-i(\phi_3 - \phi_2)} \end{aligned} \quad (\text{A.20})$$

Only the first term in the right-hand side of equation (A.20) represents the ACF for the range 1710 km and for the delay $3\tau_0$. The three remaining terms are cross products between different ranges. Their relative amplitude is reduced by repeating the multiple scheme. The phases ϕ_i are random variables, due to the incoherence of

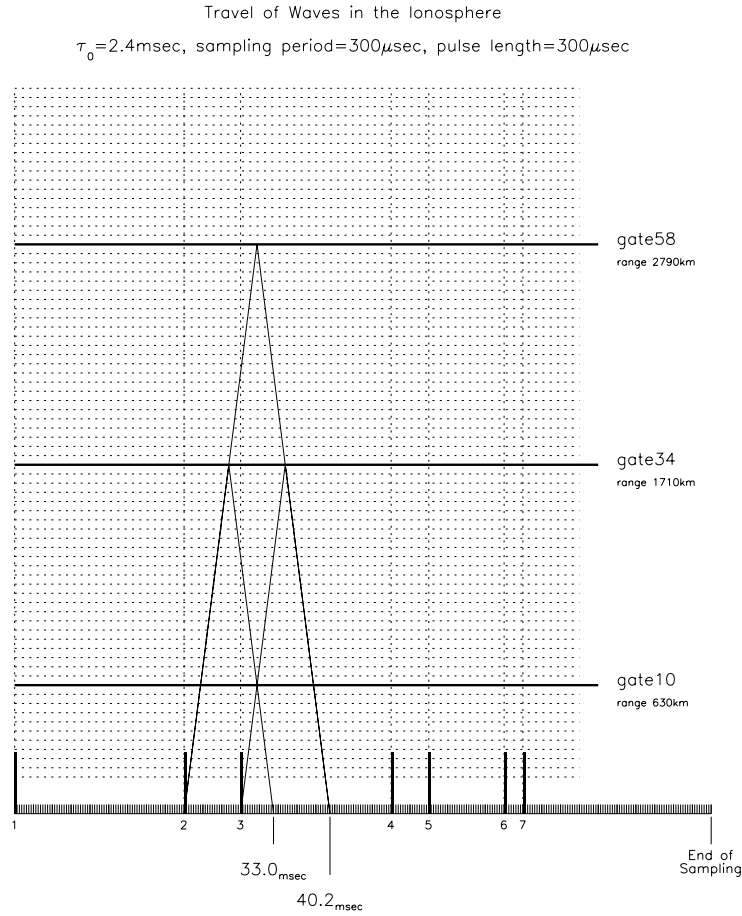


Figure V-A.6: Illustration of how pulses from multipulse scheme travels (see the text in detail).

the phase of the fluctuations which are responsible for the backscatter, at times separated by the delay between successive multipulse sequences., typically 88.8 ms. The damping of these terms is proportional to $N^{1/2}$, where N is the number of multipulse sequences. A relative damping of 8.6 is obtained when the ACF is averaged over 75 multipulses. From here on, only the first term in equation (A.20) will be considered.

$$\text{ACF}(\tau) = \langle S_0 \cdot S_\tau^* \rangle = \langle A_1 A_1'^* \exp^{-i\omega_1 \tau} \rangle \quad (\text{A.21})$$

This technique allows us to obtain 17 points of the complex ACF in each of the 75 range gates for each multipulse sequence. During the 7 s when the radar is transmitting on a specific beam, there are approximately 75 multipulse sequences transmitted. The 75 successive ACFs are averaged to give one mean ACF for the integration period of that beam (the top and middle panel of the left-hand side of Figure V-A.7). As noted before, power spectrum of the radar backscatter can be obtained from Fourier transformation of the obtained ACF (the bottom panel of the left-hand side of Figure V-A.7). In the example shown in the left panels of Figure V-A.7, it is clearly shown that the cross terms in equation (A.20) have no influence on the experimental ACF.

A.4 Fitted Parameter Derivation

The ACF can be converted into Doppler power spectra by a Fourier transform of the complex ACF. From this transformation, Doppler velocity, Doppler spectral width, and backscattered power can be determined. However,

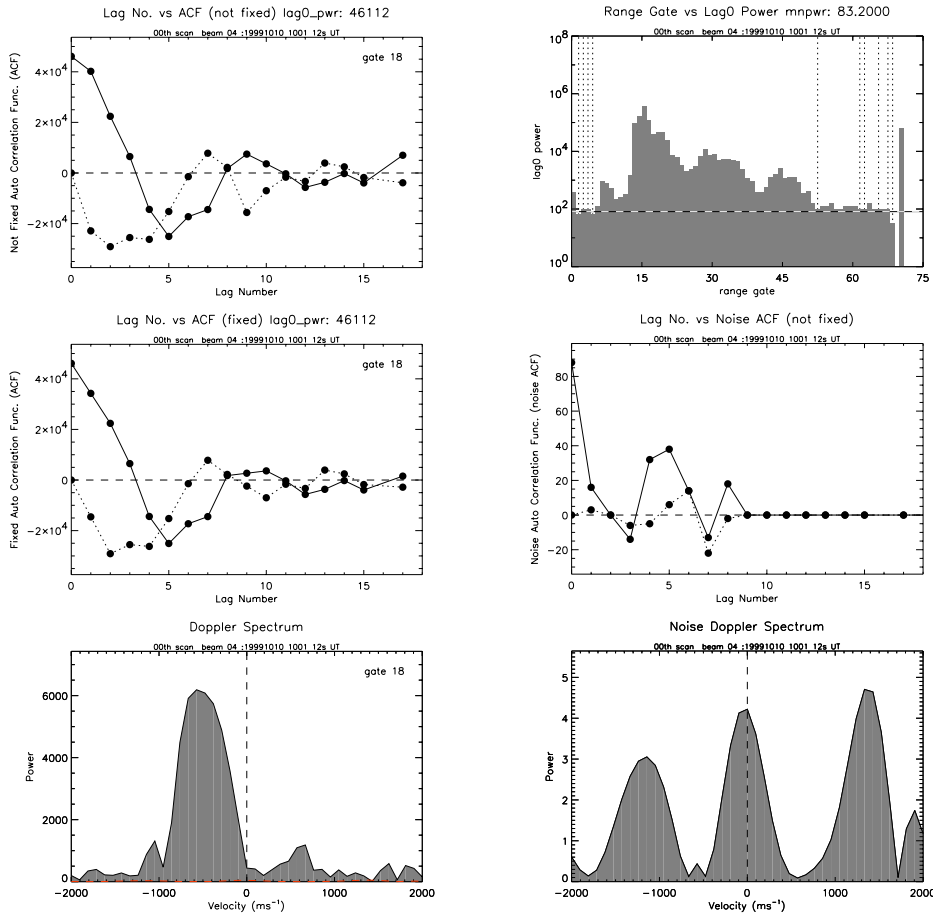


Figure V-A.7: (Left) example of the auto-correlation function and corresponding Doppler power spectrum. (Right) noise reduction process (see text in detail).

it is more efficient to obtain these parameters directly from the ACF rather than to perform the large number of FFTs. Several studies have shown that, for the case of the F region backscatters, the Doppler power spectra are generally Lorentzian in shape and the ACF decays exponentially. Being based on these characteristics of the SuperDARN ACFs, it is possible to fit an assumed functional form to each of the ACFs. The procedure of the direct parameter derivation from the ACF is introduced in this section.

A.4.1 Noise Reduction

There are several sources of noise which complicate the analysis of the radar data. The cosmic HF background noise is relatively constant in time but has a frequency dependence. The multipulse technique causes strong scatter at some ranges to contribute to the noise at other ranges. In addition, there are local sources of HF noise produced by nearby instrument, as well as the inherent noise of the receiver and digitizers. Finally, in the HF frequency band, there are nearly always remote radio transmitters that contribute to the noise. Some of these transmitters are source of CW (continuous wave). The first step to reduce the noise is the determination of the basic noise level and the noise ACF. An initial noise level is determined from the averaged backscattered lag-0 power from the 10 weakest ranges. Next, we select range gates whose lag-0 power is less than 1 dB above the initial noise level. The noise ACF is finally derived from averaging the ACFs of these selected range gates, then is used to reduce the noise for all range gates. In a typical case where there are no external transmitters producing noise, the noise ACF will have a non-zero power at lag-0 and be nearly zero for all other lags. If

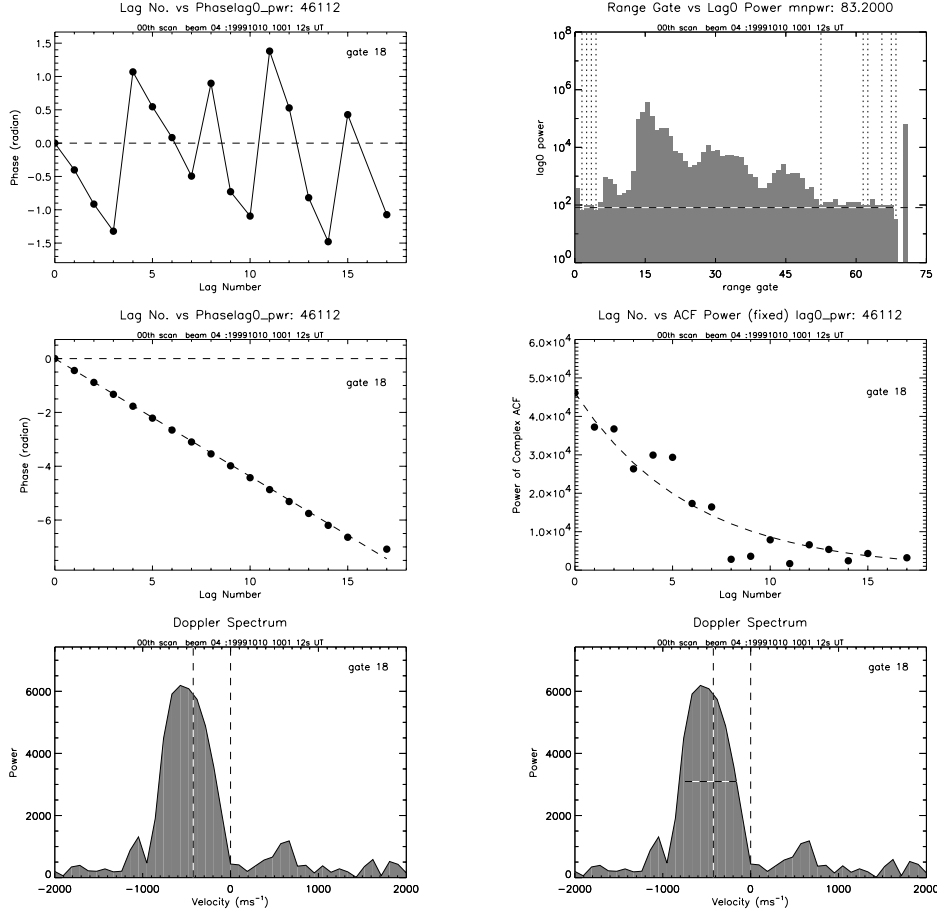


Figure V-A.8: Parameter fitting process for Doppler velocity (left) and Doppler spectral width (right). Two middle panels show how the phase and power of the ACF is fitted by using linear and exponential profiles, respectively.

CW transmitter is present, the noise will be present at all range gates and the noise ACF will show a clear non-zero frequency. In either case, the noise ACF must be subtracted from the raw ACFs before deriving the parameters. The noise reduction process described here is shown in the right panels of Figure V-A.7. Top panel shows a lag-0 power profile with range gate, in which 10 range gates of weakest lag-0 power are indicated by the vertical dotted lines and the initial noise level is indicated by the horizontal dashed line. The middle panel shows the noise ACF and the bottom is the Doppler power spectrum deduced from the noise ACF.

A.4.2 Doppler Velocity

The velocity is derived from the Doppler frequency, deduced from the phase of the ACF by a linear least squares fit. The phase ϕ is given by

$$\phi = \arctan \frac{\text{Im} \text{ ACF}(\tau)}{\text{Real ACF}(\tau)} = \omega_d \tau \pm 2n\pi \quad (\text{A.22})$$

A typical example of the fitting process is shown in the left panels of Figure V-A.8. Top panel shows the phase of the ACF and the middle panel shows the result of the linear least squares fitting. Once the curve of phase and lag is fitted (i.e., ω_d is obtained), corresponding Doppler velocity is automatically estimated by using following equation,

$$V_d = \frac{c}{2\omega_0} \omega_d \quad (\text{A.23})$$

where c is the speed of light and ω_0 is the frequency of the transmitter. Derived Doppler velocity is overplotted on the spectrum in the bottom panel.

A.4.3 Backscatter Power and Doppler Spectral Width

Baker *et al.* (1988) demonstrated that the ACF of the radar backscattered signal can be characterized as a sinusoidal wave in an exponentially decaying envelope. Additional studies of the spectral shapes of the radar Doppler spectrum by Villain *et al.* (1987) and Hanuise *et al.* (1993) pointed out that the Doppler power spectra are generally Lorentzian in shape and the ACF decays exponentially. Then, the Doppler spectral width and backscattered power can be deduced from the time variation of the power of the ACF, $|\text{ACF}(\tau)|$. If the spectra are assumed to be Lorentzian, power of the ACF is characterized as an exponential profile with the damping factor α

$$|\text{ACF}(\tau)| = P \exp^{-\alpha\tau} \quad (\text{A.24})$$

Once least-square fit is performed, width of the Lorentzian spectrum is automatically derived by using following equation.

$$w = \frac{c}{\omega_0} \alpha \quad (\text{A.25})$$

P in equation (A.24) corresponds to the backscattered power. The procedure described here is shown in the right panels of Figure V-A.8. The top panel is the lag-0 power profile with range. The middle panel shows the power of the ACF with lag, where dashed line indicates the least square fit using exponential profile. The bottom panel shows the Doppler power spectrum, where the horizontal dashed line indicates the derived Doppler spectral width.

Appendix B

Linear Theory of Gradient-Drift Instabilities

Here, linear theory of the gradient-drift instabilities is outlined. Gravity plays very little role in the high-latitude ionosphere since \mathbf{g} is essentially parallel to the magnetic field. We therefore concentrate our description on the electric field-driven aspects of the instabilities. A simplified geometry in the high-latitude F region ionosphere is assumed, i.e., vertical magnetic field \mathbf{B} , horizontal density gradient ∇n , and electric field \mathbf{E} perpendicular to \mathbf{B} and ∇n .

B.1 Basic Equations of the Gradient-Drift Instabilities

Basic equations employed in this scheme are, the continuity equations of ions and electrons,

$$\frac{\partial n_e}{\partial t} + \nabla \cdot (n_e \mathbf{v}_e) = 0 \quad (\text{B.1})$$

$$\frac{\partial n_i}{\partial t} + \nabla \cdot (n_i \mathbf{v}_i) = 0 \quad (\text{B.2})$$

momentum equations of ions and electrons,

$$m_e n_e \frac{d\mathbf{v}_e}{dt} = -\nabla P - en_e (\mathbf{E} + \mathbf{v}_e \times \mathbf{B}) + m_e n_e \nu_{en} \mathbf{v}_e + m_e n_e \nu_{ei} (\mathbf{v}_e - \mathbf{v}_i) \quad (\text{B.3})$$

$$m_i n_i \frac{d\mathbf{v}_i}{dt} = -\nabla P + en_i (\mathbf{E} + \mathbf{v}_i \times \mathbf{B}) + m_i n_i \nu_{in} \mathbf{v}_i - m_e n_e \nu_{ei} (\mathbf{v}_e - \mathbf{v}_i) \quad (\text{B.4})$$

and the electric current continuity equation.

$$\nabla \cdot \mathbf{J} = 0 \quad (\text{B.5})$$

In addition to the basic equations from (B.1) to (B.5), we assume charge neutrality,

$$n_e = n_i = n \quad (\text{B.6})$$

and, for the sake of simplicity, the plasma temperatures of ions and electrons are assumed to be equal,

$$T_e = T_i = T \quad (\text{B.7})$$

Now we consider the instability occurring at F region altitudes, so only the collision frequency between electrons and ions is considered,

$$\nu_{en} \ll \nu_{ei} \quad (\text{B.8})$$

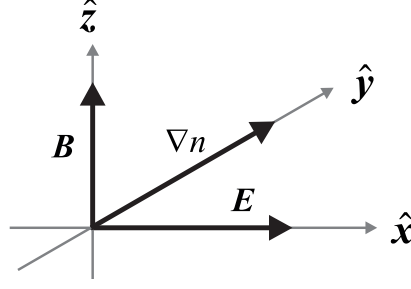


Figure V-B.1: Reference frame used in this scheme.

B.2 Linear Growth Rate of the Gradient-Drift Instabilities

Equation (B.3) and (B.4) become:

$$\mathbf{v}_e = \frac{T}{eB^2} \frac{\nabla n \times \mathbf{B}}{n} + \frac{\mathbf{E} \times \mathbf{B}}{B^2} - \frac{\nu_{ei} C_s^2}{\Omega_e \Omega_i} \frac{\nabla n}{n} \quad (\text{B.9})$$

$$\mathbf{v}_i = -\frac{T}{eB^2} \frac{\nabla n \times \mathbf{B}}{n} + \frac{\mathbf{E} \times \mathbf{B}}{B^2} - \frac{\nu_{ei} C_s^2}{\Omega_e \Omega_i} \frac{\nabla n}{n} + \frac{\nu_{in}}{\Omega_i} \frac{\mathbf{E}}{B} - \frac{\nu_{in} T}{\Omega_i e B} \frac{\nabla n}{n} \quad (\text{B.10})$$

where $C_s = \sqrt{2k_B T/m_i}$ is ion-acoustic speed, $\Omega_i = qB/m_i$ and $\Omega_e = qB/m_e$ are the gyrofrequencies of ions and electrons, respectively. Then, in the reference frame shown in Figure V-B.1, equation (B.1) and (B.2) become:

$$0 = \frac{\partial n}{\partial t} - \nabla n \cdot \frac{\mathbf{E} \times \hat{\mathbf{z}}}{B} - \nabla \cdot \left(\frac{\nu_{ei} C_s}{\Omega_e \Omega_i} \nabla n \right) \quad (\text{B.11})$$

$$0 = \frac{\partial n}{\partial t} - \nabla n \cdot \frac{\mathbf{E} \times \hat{\mathbf{z}}}{B} + \frac{\nu_{in}}{\Omega_i} \nabla \cdot \frac{n \mathbf{E}}{B} - \nabla \cdot \left(\frac{\nu_{ei} C_s^2}{\Omega_e \Omega_i} \nabla n + \frac{\nu_{in}}{\Omega_i} \frac{T_i}{eB} \nabla n \right) \quad (\text{B.12})$$

Small amplitude perturbations are introduced in the system under the form:

$$n = n_0(y) + \tilde{n} \quad (\text{B.13})$$

$$\mathbf{E} = E_0 \hat{\mathbf{x}} - \nabla \tilde{\phi} \quad (\text{B.14})$$

$$\tilde{n} \text{ and } \tilde{\phi} \propto \exp^{-(kx - \omega t)} \quad (\text{B.15})$$

After linearisation and keeping the first order terms, equation (B.11) and (B.12) become:

$$0 = (-i\omega + \frac{\nu_{ei} C_s^2}{\Omega_e \Omega_i} k^2) \tilde{n} - i \frac{k}{B} \frac{\partial n_0}{\partial y} \tilde{\phi} \quad (\text{B.16})$$

$$0 = (-i\omega + ik \frac{\nu_{in}}{\Omega_i} \frac{E_0}{B} + \frac{\nu_{ei} C_s^2}{\Omega_e \Omega_i} k^2 + \frac{\nu_{in}}{\Omega_i} \frac{T}{eB} k^2) \tilde{n} + (-i \frac{\partial n_0}{\partial y} \frac{k}{B} + \frac{\nu_{in}}{\Omega_i} n_0 \frac{k^2}{B}) \tilde{\phi} \quad (\text{B.17})$$

The dispersion relation is obtained by setting the determinant to zero,

$$\omega - \frac{kE_0}{B} - k \frac{1}{n_0} \frac{\partial n_0}{\partial y} \frac{T}{eB} - i \frac{\omega}{k} \frac{1}{n_0} \frac{\partial n_0}{\partial y} + i \frac{\nu_{ei} C_s^2}{\Omega_e \Omega_i} k^2 = 0 \quad (\text{B.18})$$

Finally, the real and imaginary parts are separated, and the growth rate of the gradient-drift instability is given by the following expression.

$$\gamma = \frac{1}{L} \frac{E_0}{B} - D_{\perp} k^2 \quad (\text{B.19})$$

where L is the gradient scale length, and D_{\perp} is the perpendicular diffusion coefficient,

$$\frac{1}{n_0} \frac{\partial n_0}{\partial y} = L^{-1}, \quad \frac{\nu_{ei} C_s^2}{\Omega_e \Omega_i} = D_{\perp} \quad (\text{B.20})$$

Part VI
List of References

- Anderson, P. C., W. B. Hanson, and R. A. Heelis, The ionospheric signatures of rapid subauroral ion drifts, *J. Geophys. Res.*, **96**, 5792, 1991.
- Anderson, P. C., W. B. Hanson, and R. A. Heelis, J. D. Craven, D. N. Baker, and L. A. Frank, A proposed production model of rapid subauroral ion drifts and their relationship to substorm evolution, *J. Geophys. Res.*, **98**, 6069, 1993.
- Anderson, P. C., D. L. Carpenter, K. Tsuruda, T. Mukai, and F. J. Rich, Multisatellite observations of rapid subauroral ion drifts (SAID), *J. Geophys. Res.*, **106**, 29,585, 2001.
- André, R., M. Pinnock, and A. S. Rodger, On the SuperDARN autocorrelation function observed in the ionospheric cusp, *Geophys. Res. Lett.*, **26**, 3353, 1999.
- André, R., M. Pinnock, and A. S. Rodger, Identification of the low-altitude cusp by Super Dual Auroral Radar Network radars: A physical explanation for the empirically derived signature, *J. Geophys. Res.*, **105**, 27081, 2000a.
- André, R., M. Pinnock, J.-P. Villain, and C. Hanuise, On the factors conditioning the Doppler spectral width determined from SuperDARN HF radars, *Int. J. Geomagn. Aeron.*, **2**, 77, 2000b.
- Baker, K. B., R. A. Greenwald, J.-P. Villain, and S. Wing, Spectral characteristics of high frequency (HF) backscatter from high latitude ionospheric irregularities: Preliminary analysis of statistical properties, *Interim Rep.*, RADC-TR-87-284, Rome Air Dev. Cent., Griffis Air Force Base, N. Y., 1988.
- Baker, K. B., and S. Wing, A new magnetic coordinate system for conjugate studies of high latitudes, *J. Geophys. Res.*, **94**, 9139, 1989.
- Baker, K. B., R. A. Greenwald, J. M. Ruohoniemi, J. R. Dudeney, M. Pinnock, P. T. Newell, M. E. Greenspan, and C.-I. Meng, Simultaneous HF radar and DMSP observation of the cusp, *Geophys. Res. Lett.*, **17**, 1869, 1990
- Baker, K. B., J. R. Dudeney, R. A. Greenwald, M. Pinnock, P. T. Newell, A. S. Rodger, N. Mattin, and C.-I. Meng, HF-radar signatures of the cusp and low latitude boundary layer, *J. Geophys. Res.*, **100**, 7671, 1995.
- Baker, K. B., A. S. Rodger, and G. Lu, HF-radar observations of the rate of magnetic merging: a GEM boundary layer campaign study, *J. Geophys. Res.*, **102**, 9603, 1997.
- Balsley, B. B., W. L. Ecklund, and D. C. Fritts, Mesospheric radar echoes at Poker Flat, Alaska: Evidence for seasonally dependent generation mechanisms, *Radio Sci.*, **18**, 1053, 1983.
- Balsley, B. B., and M. Huaman, On the relationship between seasonal occurrence of northern hemispheric polar mesosphere summer echoes and mean mesopause temperatures, *J. Geophys. Res.*, **102**, 2021, 1997.
- Barthes, L., R. André, J.-C. Cerisier, and J.-P. Villain, Separation of multiple echoes using a high resolution spectral analysis in SuperDARN HF radars, *Radio Sci.*, **33**, 1005, 1998.
- Bilitza D., International Reference Ionosphere 1990, National Space Science Data Center, *NSSDC/WDC-A-R&S*, **90-22**, 1990.
- Bilitza D., International Reference Ionosphere - status 1990/1996, *Adv. Space Res.*, **20**, 1751, 1997.
- Borovsky, J. E., Auroral arcs thickness as predicted by various theories, *J. Geophys. Res.*, **99**, 6101, 1993.
- Bremer, J., P. Hoffmann, A. H. Manson, C. E. Meek, R. Rüster, and W. Singer, PMSE observations at three different frequencies in northern Europe during summer 1994, *Ann. Geophys.*, **14**, 1317, 1996.
- Bremer, J., P. Hoffmann, R. Latteck, and W. Singer, Seasonal and long-term variations of PMSE from VHF radar observations at Andenes, Norway, *J. Geophys. Res.*, *in press*, 2002.
- Cerisier, J. C., J. J. Berthelier, and C. Beghin, Unstable density gradients in the high-latitude ionosphere, *Radio Sci.*, **20**, 755, 1985.
- Chisham, G., M. Pinnock, A. S. Rodger, and J.-P. Villain, High-time resolution conjugate SuperDARN radar observations of the dayside convection response to changes in IMF By, *Ann. Geophys.*, **18**, 191, 2000.
- Chisham, G., M. Pinnock, and A. S. Rodger, The response of the HF radar spectral width boundary to a switch in the IMF By directions: Ionospheric consequence of transient dayside reconnection?, *J. Geophys. Res.*, **106**, 191, 2001.
- Chisham, G., and M. Pinnock, Assessing the contamination of SuperDARN global convection maps by non-F-region backscatter, *Ann. Geophys.*, **20**, 13, 2002.

- Cho, J. Y. N., T. M. Hall, and M. C. Kelley, On the role of charged aerosols in polar mesosphere summer echoes, *J. Geophys. Res.*, **97**, 875, 1992a.
- Cho, J. Y. N., M. C. Kelley, and C. J. Heinselman, Enhancement of Thomson scatter by charged aerosols in the polar mesosphere: Measurements with a 1.29-GHz radar, *Geophys. Res. Lett.*, **19**, 1097, 1992b.
- Cho, J. Y. N., and M. C. Kelley, Polar mesosphere summer radar echoes: Observations and current theories, *Rev. Geophys.*, **31**, 243, 1993.
- Cho, J. Y. N., and J. Röttger, An updated review of polar mesosphere summer echoes: Observation, theory and their relationship to noctilucent clouds and subvisible aerosols, *J. Geophys. Res.*, **102**, 2001, 1997.
- Coleman, I. J., M. Pinnock, A. S. Rodger, The ionospheric footprint of antiparallel merging regions on the dayside magnetopause, *Ann. Geophys.*, **18**, 511, 2000.
- Collis, P. N., and I. Haggstrom, Plasma convection and auroral precipitation processes associated with the main ionospheric trough at high latitudes, *J. Atmos. Terr. Phys.*, **50**, 389, 1988.
- Cowley, S. W. H., Magnetospheric asymmetries associated with the Y-component of the IMF, *Planet. Space Sci.*, **29**, 79, 1981.
- Cowley, S. W. H., J. P. Morelli, and M. Lockwood, Dependence of convective flows and particle precipitation in the high-latitude ionosphere on the X and Y components of the interplanetary magnetic field, *J. Geophys. Res.*, **96**, 5557, 1991.
- Cowley, S. W. H., and M. Lockwood, Excitation and decay of solar wind driven flows in the magnetosphere-ionosphere system, *Ann. Geophys.*, **10**, 103, 1992.
- Craven, J. D., and L. A. Frank, The asymmetric substorm expansion phase (abstract), *EOS Trans. AGU*, **77(17)**, Spring Meet. Suppl., 252, 1996.
- Curtis, S. A., W. R. Hoegy, L. H. Brace, N. C. Maynard, M. Sugiura, and J. D. Winningham, DE-2 cusp observations: role of plasma instabilities in topside ionospheric heating and density fluctuations, *Geophys. Res. Lett.*, **9**, 997, 1982.
- Czechowsky, P., Reid, I. M., Ruster, R., and Schmidt, G., VHF radar echoes observed in the summer and polar winter mesosphere over Andoya, *J. Geophys. Res.*, **94**, 5199, 1989.
- Davies, J. A., M. Lester, and I. W. McCrea, A statistical study of ion frictional heating observed by EISCAT, *Ann. Geophys.*, **15**, 1399, 1997.
- Davies, J. A., M. Lester, S. E. Milan, and T. K. Yeoman, A comparison of velocity measurements from the CUTLASS Finland radar and the EISCAT UHF system, *Ann. Geophys.*, **17**, 892, 1999.
- Davies, J. A., T. K. Yeoman, M. Lester, and S. E. Milan, A comparison of F-region ion velocity observations from the EISCAT Svalbard and VHF radars with irregularity drift velocity measurement from the CUTLASS Finland HF radar, *Ann. Geophys.*, **18**, 589, 2000.
- De Keyser, J., M. Roth, and J. Lemaire, The magnetospheric driver of subauroral ion drifts, *Geophys. Res. Lett.*, **25**, 1625, 1998.
- De Keyser, J., Formation and evolution of subauroral ion drifts in the course of a substorm, *J. Geophys. Res.*, **104**, 12,339, 1999.
- Dudeny, J. R., A. S. Rodger, and M. J. Jarvis, Radio studies of the main F region trough in Antarctica, *Radio Sci.*, **18**, 927, 1983.
- Dungey, J. W., Interplanetary magnetic field and the auroral zones, *Phys. Rev. Lett.*, **6**, 47, 1961.
- Dyrud, L. P., M. J. Engebretson, J. L. Posh, W. J. Hughes, H. Fukunishi, R. L. Arnoldy, P. T. Newell, and R. B. Horne, Ground observations and possible source regions of two types of Pc1-2 micropulsation at very high latitudes, *J. Geophys. Res.*, **102**, 27,011, 1997.
- Ecklund, W. L., and B. B. Balsley, Long-term observations of the Arctic mesosphere with the MST radar at Poker Flat, Alaska, *J. Geophys. Res.*, **86**, 7775, 1981.
- Ejiri, M., R. A. Hoffman, and P. H. Smith, Energetic particle penetrations into the inner magnetosphere, *J. Geophys. Res.*, **85**, 653, 1980.
- Elphinstone, R. D., J. S. Murphree, D. J. Hearn, L. L. Cogger, P. T. Newell, and H. Vo, Viking observations of the UV

- dayside aurora and their relation to DMSF particle boundary definitions, *Ann. Geophys.*, **10**, 815, 1992.
- Erlanson, R. E., and B. J. Anderson, Pc1 waves in the ionosphere: A statistical study, *J. Geophys. Res.*, **101**, 7843, 1996.
- Evans, L. C., and E. C. Stone, Electron polar cap and the boundary of open geomagnetic field lines, *J. Geophys. Res.*, **77**, 5580, 1972.
- Evans, J. V., J. M. Holt, W. L., Oliver, and R. H. Wand, The fossil theory of nighttime high latitude F region troughs, *J. Geophys. Res.*, **88**, 7769, 1983.
- Farley, D. T., Incoherent scatter correlation function measurements, *Radio Sci.*, **4**, 935, 1969.
- Farley, D. T., B. B. Balsley, R. F. Woodman, and J. P. McClure, Equatorial spread F: implication of VHF radar observations, *J. Geophys. Res.*, **75**, 7199, 1970.
- Farley, D. T., Multiple-pulse incoherent-scatter correlation function measurements, *Radio Sci.*, **7**, 661, 1972.
- Fasel, G. J., Dayside poleward moving auroral forms: a statistical study, *J. Geophys. Res.*, **100**, 11,891, 1995.
- Fejer, B. G., and M. C. Kelley, Ionospheric irregularities, *Rev. Geophys.*, **18**, 401, 1980.
- Feldstein, Y. I., and G. V. Starkov, Dynamics of auroral belt and polar geomagnetic disturbance, *Planet. Space Sci.*, **15**, 209, 1967.
- Foster, J. C., M. J. Buonsanto, M. Mendillo, D. Nottingham, F. J. Rich, and W. Denig, Coordinated stable auroral red arc observations: relationship to plasma convection, *J. Geophys. Res.*, **99**, 11,429, 1994.
- Foster, J. C., Quantitative investigation of ionospheric density gradients at mid latitudes, *Proc. of Institute of Navigation ION 2000 Conference, January, 2000*.
- Freeman, M. P., J. M. Ruohoniemi, and R. A. Greenwald, The determination of time-stationary two-dimensional convection patterns with single-station radars, *J. Geophys. Res.*, **96**, 15,735, 1991.
- Freeman, M. P., D. J. Southwood, M. Lester, T. K. Yeoman, and G. D. Reeves, Substorm-associated radar auroral surges, *J. Geophys. Res.*, **97**, 12,173, 1992.
- Galperin, Y. I., V. N. Ponomarev, and A. G. Zosimov, Direct measurements of ion drift velocity in the upper atmosphere during a magnetic storm, *Kosm. Issled.*, **11**, 273, 1973.
- Greenwald, R. A., K. B. Baker, and J.-P. Villain, Initial studies of small-scale F-region irregularities at very high latitudes, *Radio. Sci.*, **18**, 1122, 1983.
- Greenwald, R. A., K. B. Baker, R. A. Hutchins, and C. Hanuise, An HF phased-array radar for studying small-scale structure in the high-latitude ionosphere, *Radio Sci.*, **20**, 63, 1985.
- Greenwald, R. A., K. B. Baker, J. M. Ruohoniemi, J. R. Dudeney, M. Pinnock, N. Mattin, J. M. Leonard, and R. P. Lepping, Simultaneous conjugate observations of dynamic variations in high-latitude dayside convection due to changes in IMF By, *J. Geophys. Res.*, **95**, 8057, 1990.
- Greenwald, R. A., K. B. Baker, J. R. Dudeney, M. Pinnock, T. B. Jones, E. C. Thomas, J.-P. Villain, J.-C. Cerisier, C. Senior, C. Hanuise, R. D. Hunsucker, G. Sofko, J. Koehler, E. Nielsen, R. Pellinen, A. D. M. Walker, N. Sato, and H. Yamagishi, DARN/SuperDARN: A global view of high-latitude convection, *Space Sci. Rev.*, **71**, 763, 1995.
- Haerendel, G., G. Paschmann, N. Sckopke, H. Rosenbauer, and P. C. Hedgecock, The frontside boundary layer of the magnetopause and the problem of reconnection, *J. Geophys. Res.*, **83**, 3195, 1978.
- Haggstrom, I., and P. N. Collis, Ion composition changes during F-region troughs, *J. Atmos. Terr. Phys.*, **52**, 519, 1990.
- Halcrow, B. W., and J. S. Nisbet, A model of F2 peak electron density in the main trough region of the ionosphere, *Radio Sci.*, **5**, 815, 1977.
- Hall, G. E., J. W. MacDougall, D. R. Moorcroft, J.-P. St.-Maurice, A. H. Manson and C. E. Meek, Super Dual Auroral Radar Network observations of meteor echoes, *J. Geophys. Res.*, **102**, 14,603, 1997.
- Hall, C. M., and J. Röttger, Initial observations of Polar Mesospheric Summer Echoes using the EISCAT Svalbard Radar, *Geophys. Res. Lett.*, **28**, 131, 2001.
- Hanuise, C., J.-P. Villain, D. Gresillon, B. Cabrit, R. A. Greenwald, and K. B. Baker, Interpretation of HF radar ionospheric Doppler spectra by collective wave scattering theory, *Ann. Geophys.*, **11**, 29, 1993.

- Hardy, D. A., L. K. Schmitt, M. S. Gussenhoven, F. J. Marshall, H. C. Yeh, T. L. Schumaker, A. Huber and J. Pantazis, Precipitating electron and ion detectors (SSJ/4) for the block 5D/Flights 6-10 DMSP satellites: calibration and data presentation, *Rep. AFGL-TR-84-0317*, Air Force Geophysics Laboratory, Hanscom AFB, Mass., 1984.
- Hargreaves, J. K., and C. J. Burns, Electron content measurements in the auroral zone using GPS: preliminary observations of the main trough and a survey of the degree of irregularity in summer, *J. Atmos. Terr. Phys.*, **58**, 1449, 1996.
- Hedin, A. E., Extension of the MSIS thermospheric model into the middle and lower atmosphere, *J. Geophys. Res.*, **96**, 1159, 1991.
- Heelis, R. A., G. J. Bailey, R. Sellek, R. J. Moffet, and B. Jenkins, Field-aligned drifts in subauroral drift events, *J. Geophys. Res.*, **98**, 21,493, 1993.
- Heppner, J. P., and N. C. Maynard, Empirical high-latitude electric field models, *J. Geophys. Res.*, **92**, 4467, 1987.
- Holt, J. M., J. V. Evans, and R. H. Wand, Millstone Hill studies of the trough: Boundary between the plasmopause and magnetosphere or not?, *Radio Sci.*, **18**, 947, 1983.
- Holzworth, R. H., and C. I. Meng, Mathematical representation of the auroral oval, *Geophys. Res. Lett.*, **2**, 377, 1975.
- Hower, G. L., D. M. Ranz, and C. L. Allison, Comparison of HF radar echoes and high-latitude spread-F measurement, *J. Geophys. Res.*, **71**, 3215, 1966.
- Huaman, M. M., and B. B. Balsley, Difference in near-mesopause summer winds, temperatures, and water vapor at northern and southern latitudes as possible causal factors for inter-hemispheric PMSE differences, *Geophys. Res. Lett.*, **26**, 1529, 1999.
- Huber, M., and G. Sofko, Small-scale vortices in the high-latitude F region, *J. Geophys. Res.*, **105**, 20,885, 2000.
- Iijima, T., and T. A. Potemura, Large-scale characteristics of field-aligned currents associated with substorms, *J. Geophys. Res.*, **83**, 599, 1978.
- Ishii, M., M. Sugiura, T. Iyemori, and J. A. Slavin, Correlation between magnetic and electric field perturbations in the field-aligned current regions deduced from DE 2 observations, *J. Geophys. Res.*, **97**, 13,877, 1992.
- Karashtin, A. N., Yu. V. Shlyugaev, V. I. Abramov, I. F. Belov, I. V. Berezin, V. V. Bychkov, E. B. Eryshev, and G. P. Komrakov, First HF radar measurements of summer mesopause echoes at SURA, *Ann. Geophys.*, **15**, 935, 1997.
- Karlsson, T., G. T. Marklund, L. G. Blomberg, and A. Mälkki, Subauroral electric fields observed by the Freja satellite: A statistical study, *J. Geophys. Res.*, **103**, 4327, 1998.
- Kataoka, R., H. Fukunishi, K. Hosokawa, H. Fujiwara, A. S. Yukimatu, N. Sato, and Y.-K. Tung, Transient production of F region irregularities associated with TCV passage, *Ann. Geophys.*, *submitted*, 2002.
- Kelley, M. C., R. C. Livingston, C. L. Rino, and R. T. Tsunoda, The vertical wave number spectrum of topside equatorial spread F: estimates of backscatter levels and implications for a unified theory, *J. Geophys. Res.*, **87**, 5217, 1982.
- Kelley, M. C., D. T. Farley, and J. Röttger, The effect of cluster ions on anomalous VHF backscatter from the summer polar mesosphere, *Geophys. Res. Lett.*, **14**, 1031, 1987.
- Kelley, M. C., and J. C. Ulwick, Large- and small-scale organization of electrons in the high-latitude mesosphere: Implications of the STATE data, *J. Geophys. Res.*, **93**, 7001, 1988.
- Kelley, M. C., *The Earth's Ionosphere*, Academic, San Diego, Calif., 1989.
- Kelley, M. C., M. M. Huaman, C. Y. Chen, C. Ramos, F. Djuth, and E. Kennedy, Polar mesosphere summer echo observation at HF frequencies using the HAARP Gakona Ionospheric Observatory, *Geophys. Res. Lett.*, **29**(12), 10.1029/2001GL013411, 2002.
- Keskinen, M. J., and S. L. Ossakow, Theories of high-latitude ionospheric irregularities: A review, *Radio Sci.*, **18**, 1077, 1983.
- Khan, H., and S. W. H. Cowley, Observations of the response time of high-latitude ionospheric convection to variations in the interplanetary magnetic field using EISCAT and IMP-8 data, *Ann. Geophys.*, **17**, 1306, 1999.
- Khan, H., S. W. H. Cowley, E. Kolesnikova, M. Lester, M. J. Brittacher, T. J. Hughes, W. J. Hughes, W. S. Kurth, D. J. McComas, L. Newitt, C. J. Owen, G. D. Reeves, H. J. Singer, C. W. Smith, D. J. Southwood, and J. F. Wattermann, Observation of two complete substorm cycles during the Cassini Earth swing-by: Cassini magnetometer data in a

- global context, *J. Geophys. Res.*, **106**, 30,141, 2001.
- Kirkwood, S., V. Barabash, P. Chilson, A. Rechou, and K. Stebel, The 1997 PMSE season - its relation to wind, temperature and water vapour, *Geophys. Res. Lett.*, **25**, 1867, 1998.
- Kirkwood, S., V. Barabash, E. Belova, H. Nilsson, T. N. Rao, and K. Stebel, Polar mesosphere winter echoes during solar proton events, *Adv. Polar Upper Atmos. Res.*, *in press*, 2002.
- Knudsen, W. C., Magnetospheric convection and the high-latitude F2 ionosphere, *J. Geophys. Res.*, **79**, 1046, 1974.
- Knudsen, W. C., P. M. Banks, J. D. Winningham, and D. M. Klumper, Numerical model of the convecting F2 ionosphere at high latitudes, *J. Geophys. Res.*, **82**, 4784, 1977.
- Kuo, H., C. T. Russell, and G. Lee, Statistical studies of flux transfer events, *J. Geophys. Res.*, **100**, 3513, 1995.
- Lockwood, M., and M. N. Wild, On the quasi-periodic nature of magnetopause flux transfer events, *J. Geophys. Res.*, **98**, 5935, 1993.
- Lockwood, M., H. C. Carlson, and P. E. Sandholt, The implications of the altitude of transient 630 nm dayside auroral emission, *J. Geophys. Res.*, **98**, 15,571, 1993.
- Lockwood, M., Relationship of dayside auroral precipitations to the open-closed separatrix and the pattern of convective flow, *J. Geophys. Res.*, **102**, 17,475, 1997.
- Lorentzen, D. A., C. S. Deehr, J. I. Minow, R. W. Smith, H. C. Stenback-Nielsen, F. Sigernes, R. L. Arnoldy, K. Lynch, SCIFER-dayside auroral signatures of magnetospheric energetic electrons, *Geophys. Res. Lett.*, **23**, 1885, 1996.
- Lübken, F.-J., and U. von Zahn, Thermal structure of the mesopause region at polar latitudes, *J. Geophys. Res.*, **96**, 20,841, 1991.
- Lübken, F.-J., M. J. Jarvis, and G. O. L. Jones, First in situ temperature measurements at the Antarctic summer mesopause, *Geophys. Res. Lett.*, **26**, 3581, 1999.
- Lysak, R. L., and C. T. Dum, Dynamics of magnetosphere-ionosphere coupling including turbulent transport, *J. Geophys. Res.*, **88**, 365, 1983.
- Matsuoka, A., T. Mukai, H. Hayakawa, Y.-I. Kohno, K. Tsuruda, A. Nishida, T. Okada, N. Kaya, and H. Fukunishi, EXOS-D observations of electric field fluctuations and charged particle precipitation in the polar cusp, *Geophys. Res. Lett.*, **18**, 305, 1991.
- Matsuoka, A., K. Tsuruda, H. Hayakawa, T. Mukai, A. Nishida, T. Okada, N. Kaya, and H. Fukunishi, Electric field fluctuations and charged particle precipitation in the cusp, *J. Geophys. Res.*, **98**, 11,225, 1993.
- Maynard, N. C., J. P. Heppner, and A. Egeland, Intense, variable electric fields at ionospheric altitudes in the high latitude regions as observed by DE-2, *Geophys. Res. Lett.*, **9**, 981, 1982.
- Maynard, N. C., Structure in the DC and AC electric fields associated with the dayside cusp region, in *The Polar Cusp*, edited by J. A. Holtet and A. Egeland, 305, D. Reidel, Norwell, Mass., 1985.
- Maynard, N. C., T. L. Aggson, E. M. Basinka, W. J. Burke, P. Craven, W. K. Peterson, M. Sugiura, and D. R. Weimer, Magnetospheric boundary dynamics: DE-1 and DE-2 observations near the magnetopause and cusp, *J. Geophys. Res.*, **96**, 3505, 1991.
- McIntyre, M. E., On dynamics and transport near the polar mesopause in summer, *J. Geophys. Res.*, **94**, 14,617, 1989.
- McWilliams, K. A., T. K. Yeoman, and S. W. H. Cowley, Two dimensional electric field measurements in the ionospheric footprint of a flux transfer event, *Ann. Geophys.*, **18**, 1584, 2001.
- Mendillo, M., J. Baumgardner, J. Aarons, J. Foster, and J. Klobuchar, Ground-based imaging of detailed arcs, ripples in the diffuse aurora, and patches of 6300Å emission, *Ann. Geophys.*, **5**, 543, 1987.
- Menk, F. W., B. J. Fraser, H. J. Hansen, P. T. Newell, C.-I. Meng, and R. J. Morris, Identification of the magnetospheric cusp and cleft using Pc1-2 ULF pulsations, *J. Atmos. Terr. Phys.*, **54**, 1021, 1992.
- Milan, S. E., T. K. Yeoman, M. Lester, E. C. Thomas, and T. B. Jones, Initial Backscatter occurrence statistics from the CUTLASS HF radars, *Ann. Geophys.*, **15**, 703, 1997.
- Milan, S. E., T. K. Yeoman, and M. Lester, The dayside auroral zone as a hard target for coherent HF radars, *Geophys. Res. Lett.*, **25**, 3717, 1998.

- Milan, S. E., M. Lester, S. W. H. Cowley, J. Moen, P. E. Sandholt, and C. J. Owen, Meridian-scanning photometer, coherent HF radar, and magnetometer observation of the cusp : a case study, *Ann. Geophys.*, **17**, 159, 1999.
- Milan, S. E., M. Lester, S. W. H. Cowley, and M. Brittnacher, Convection and auroral response to a southward turning of the IMF: Polar UVI, CUTLASS and IMAGE signatures of transient flux transfer at the magnetopause, *J. Geophys. Res.*, **105**, 15,741, 2000.
- Milan, S. E., L. J. Baddeley, M. Lester, and N. Sato, A seasonal variation in the convection response to IMF orientation, *Geophys. Res. Lett.*, **28**, 471, 2001.
- Milan, S. E., and M. Lester, Interhemispheric differences in the HF radar signature of the cusp region: A review through the study of a case example, *Adv. Polar Upper Atmos. Res.*, **15**, 159, 2001.
- Milan, S. E., M. Lester, and T. K. Yeoman, HF radar polar patch formation revisited: summer and winter variations in dayside plasma structuring, *Ann. Geophys.*, **20**, 487, 2002a.
- Milan, S. E., M. Lester, S. W. H. Cowley, K. Oksavik, M. Brittnacher, R. A. Greenwald, G. Sofko, and J.-P. Villain, Variation in polar cap area during two substorm cycles, *Ann. Geophys.*, *in press*, 2002b.
- Moen, J., C. Carlson, S. E. Milan, N. Shumilov, B. Lybekk, P. E. Sandholt, and M. Lester, On the collocation between dayside auroral activity and coherent HF radar backscatter, *Ann. Geophys.*, **18**, 1531, 2001.
- Moffet, R. J., and S. Quegan, The mid-latitude trough in the electron concentration of the ionosphere F-layer : A review of observations and modeling, *J. Atmos. Terr. Phys.*, **37**, 161, 1975.
- Moller, H. G., and A. Tauriainen, Observations of intense irregularities in the polar F-region by HF backscatter and satellite scintillation measurements, *J. Atmos. Terr. Phys.*, **37**, 161, 1975.
- Muldrew, D. B., F Layer ionization troughs deduced from Alouette data, *J. Geophys. Res.*, **70**, 2635, 1065.
- Murphree, J. S., L. L. Cogger, C. D. Anger, S. Ismail, and G. G. Shepherd, Large scale 6300A, 5577A, 3914A dayside auroral morphology, *Geophys. Res. Lett.*, **7**, 239, 1980.
- Murphy, D. J., and R. A. Vincent, Amplitude enhancements in Antarctic MF radar echoes, *J. Geophys. Res.*, **105**, 26,683, 2000.
- Namgaladze, A. A., O. V. Martynenko, A. N. Namgaladze, M. A. Volkov, Y. N. Korenkov, V. V. Klimenko, I. V. Karpov, and F. S. Bessarab, Numerical simulation of an ionospheric disturbance over EISCAT using a global ionospheric model, *J. Atmos. Terr. Phys.*, **58**, 297, 1996.
- Newell, P. T., and C. I. Meng, The cusp and the cleft/boundary layer: Low-altitude identification and statistical local time variation, *J. Geophys. Res.*, **93**, 14549, 1988.
- Newell, P. T., and C. I. Meng, Dipole tilt angle effects on the latitude of the cusp and cleft/low-latitude boundary layer, *J. Geophys. Res.*, **94**, 6949, 1989.
- Newell, P. T., W. J. Burke, C.-I. Meng, E. R. Sanchez, and M. E. Greenspan, Identification and observation of the plasma mantle at low altitude, *J. Geophys. Res.*, **96**, 35, 1991.
- Newell, P. T., and C. I. Meng, Ion acceleration at the equatorward edge of the cusp: low-altitude observations of patchy merging, *Geophys. Res. Lett.*, **18**, 1829, 1991.
- Newell, P. T., and C. I. Meng, Mapping the dayside ionosphere to the magnetosphere according to particle precipitation characteristics, *Geophys. Res. Lett.*, **19**, 609, 1992.
- Ogawa, T., N. Nishitani, N. Sato, H. Yamagishi, and A. S. Yukimatu, Implications of statistics of near-range Doppler velocity observed with the Syowa East HF radar, *Adv. Polar Upper Atmos. Res.*, **15**, 82, 2001.
- Ogawa, T., K. Igarashi, Y. Kuratani, R. Fujii, and T. Hirasawa, Some initial results of 50 MHz meteor radar observation at Syowa Station, *Mem. Natl Inst. Polar Res., Spec. Issue*, **36**, 254, 1985.
- Ogawa, T., N. Nishitani, N. Sato, H. Yamagishi, and A. S. Yukimatu, Upper mesosphere summer echoes detected with the Antarctic Syowa HF radar, *Geophys. Res. Lett.*, **29(7)**, 10.1029/2001GL014094, 2002a
- Ogawa, T., N. F. Arnold, S. Kirkwood, N. Nishitani, and M. Lester, Finland HF and Esrange MST radar observation of polar mesosphere summer echoes, *Ann. Geophys.*, *in press*, 2002b.
- Olsen, N., R. Holme, G. Hulot, T. Sabaka, T. Neubert, L. Toffner-Clausen, F. Primdahl, J. Jorgensen, J.-M. Leger, D. Barraclough, J. Bloxham, J. Cain, C. Constable, V. Golovkov, A. Jackson, P. Kotze, B. Langlais, S. Macmillan, M.

- Mandea, J. Merayo, L. Newitt, M. Purucker, T. Risbo, M. Stampe, A. Thomson, and C. Voorhies, Oersted Initial Field Model, *Geophys. Res. Lett.*, **27**, 3607, 2000.
- Palmer, J. R., H. Rishbeth, G. O. L. Jones, and P. J. S. Williams, A statistical study of polar mesosphere summer echoes observed by EISCAT, *J. Atmos. Terr. Phys.*, **58**, 307, 1996.
- Parkinson, M. L., M. Pinnock, H. Ye, M. R. Hairston, J. C. Devlin, P. L. Dyson, R. J. Morris, and P. Ponomarenko, On the lifetime and extent of an auroral westward flow channel (AWFC) observed during a magnetospheric substorm, *Ann. Geophys.*, *submitted*, 2002.
- Providakes, J. F., M. C. Kelley, W. E. Swarts, M. Mendillo, and J. M. Holt, Radar and optical measurements of ionospheric process associated with intense subauroral electric fields, *J. Geophys. Res.*, **94**, 5350, 1989.
- Pinnock, M., A. S. Rodger, J. R. Dudeney, F. Rich, and K. B. Baker, High spatial and temporal resolution observations of the ionospheric cusp, *Ann. Geophys.*, **13**, 919, 1995.
- Pinnock, M., A. S. Rodger, K. B. Baker, G. Lu, and M. Hairston, Conjugate observations of the day-side reconnection electric field: A GEM boundary layer campaign, *Ann. Geophys.*, **17**, 443, 1999.
- Provan, G., T. K. Yeoman, and S. E. Milan, CUTLASS Finland radar observations of the ionospheric signatures of flux transfer events and the resulting plasma flows, *Ann. Geophys.*, **16**, 1411, 1998.
- Provan, G., T. K. Yeoman, and S. E. Milan, Statistical observations of the MLT, latitude and size of the ionospheric signature of flux transfer events with the CUTLASS Finland radar, *Ann. Geophys.*, **17**, 855, 1999.
- Quegan, S., G. J. Bailey, and R. J. Moffett, A theoretical study of the distribution of ionization in the high-latitude ionosphere and the plasmasphere: first results on the mid-latitude trough and the light-ion trough, *J. Atmos. Terr. Phys.*, **44**, 619, 1982.
- Rees, M. H., and J. C. G. Walker, Ion and electron heating by auroral electric fields, *Ann. Geophys.*, **24**, 193, 1968.
- Reiff, P. H., T. W. Hill, and J. L. Burch, Solar wind plasma injection at the dayside magnetospheric cusp, *J. Geophys. Res.*, **82**, 479, 1977.
- Reiff, P. H., and J. L. Burch, IMF By-dependent plasma flow and Birkeland currents in the dayside magnetosphere 2. A global model for northward and southward IMF, *J. Geophys. Res.*, **90**, 1595, 1985.
- Rich, F. J., and N. C. Maynard, Consequences of using simple analytical functions for the high-latitude convection electric field, *J. Geophys. Res.*, **94**, 3687, 1989.
- Richmond, A. D., Assimilative mapping of ionospheric electrodynamics, *Adv. Space. Res.*, **12**, 69, 1992
- Rishbeth, H., and P. J. S. Williams, The EISCAT ionospheric radar: The system and its early results, *Q. J. R. Astron. Soc.*, **26**, 478, 1985.
- Rodger, A. S., S. W. H. Cowley, M. J. Brown, M. Pinnock, and D. A. Simmons, Dawn-dusk(y) component of the interplanetary magnetic field and the local time of the Harang discontinuity, *Planet. Space Sci.*, **8**, 1021, 1984.
- Rodger, A. S., R. J. Moffett, and S. Quegan, The role of ion drift in the formation of ionization troughs in the mid- and high-latitude ionosphere - a review, *J. Atmos. Terr. Phys.*, **54**, 1, 1992.
- Rodger, A. S., S. B. Mende, T. J. Rosenberg, and K. B. Baker, Simultaneous optical and HF radar observations of the ionospheric cusp, *Geophys. Res. Lett.*, **22**, 2045, 1995.
- Rodger, A. S., and M. Pinnock, The ionospheric response to flux transfer events: the first few minutes, *Ann. Geophys.*, **15**, 685, 1997.
- Rodger, A. S., Ground-based imaging of magnetospheric boundaries, *Adv. Space Res.*, **25**, 1461, 2000.
- Rosenbauer, H., H. Gruenwaldt, M. D. Montgomery, G. Paschmann, and N. Sckopke, HEOS-2 plasma observations in the distant polar magnetosphere; the plasma mantle, *J. Geophys. Res.*, **80**, 2723, 1975.
- Röttger, J., R., C. La Hoz, M. C. Kelley, U.-P. Hoppe, and C. Hall, The structure and dynamics of polar mesosphere summer echoes observed with the EISCAT 224-MHz radar, *Geophys. Res. Lett.*, **15**, 1353, 1988.
- Röttger, J., R., M. T. Rietveld, C. La Hoz, T. Hall, M. C. Kelley, and W. E. Swarts, Polar mesosphere summer echoes observed with the EISCAT 933-MHz radar and the CUPRI 46.9-MHz radar, their similarity to 224-MHz radar echoes and their relation to turbulence and electron density profiles, *Radio. Sci.*, **25**, 671, 1990.

- Ruohoniemi, J. M., R. A. Greenwald, K. B. Baker, J. P. Villain, and M. A. McCready, Drift motions of small-scale irregularities in the high-latitude F region: An Experimental comparison with plasma drift motions, *J. Geophys. Res.*, **92**, 4553, 1987.
- Ruohoniemi, J. M., R. A. Greenwald, J.-P. Villain, K. B. Baker, P. T. Newell, and C.-I. Meng, Coherent HF radar backscatter from small-scale irregularities in the dusk sector of the subauroral ionosphere, *J. Geophys. Res.*, **93**, 12,871, 1988.
- Ruohoniemi, J. M., R. A. Greenwald, K. B. Baker, J.-P. Villain, C. Hanuise, and J. Kelly, Mapping high-latitude plasma convection with coherent HF radars, *J. Geophys. Res.*, **94**, 13,463, 1989.
- Ruohoniemi, J. M., and R. A. Greenwald, Statistical patterns of high-latitude convection obtained from Goose Bay HF radar observations, *J. Geophys. Res.*, **101**, 21,743, 1996.
- Ruohoniemi, J. M., and R. A. Greenwald, Rates of scattering occurrence in routine HF radar observations during solar cycle maximum, *Radio Sci.*, **32**, 1051, 1997.
- Russell, C. T., and R. C. Elphic, Initial ISEE magnetometer results: magnetopause observations, *Space Sci. Rev.*, **22**, 681, 1978.
- Samson, J. C., D. D. Wallis, T. J. Hughes, F. Creutzberg, J. M. Ruohoniemi, and R. A. Greenwald, Substorm intensifications and field line resonances in the nightside magnetosphere, *J. Geophys. Res.*, **97**, 8495, 1992.
- Sandholt, P. E., C. J. Farrugia, M. Oieroset, P. Stauning, and W. F. Denig, Auroral activity associated with unsteady magnetospheric erosion: observations on December 19, 1990, *J. Geophys. Res.*, **103**, 2309, 1998.
- Schiffler, A., G. Sofko, P. T. Newell, and R. A. Greenwald, Mapping the outer LLBL with SuperDARN double-peaked spectra, *Geophys. Res. Lett.*, **24**, 3149, 1997.
- Schunk, R. W., W. J. Raitt, and P. M. Banks, Effect of electric field on the daytime high-latitude E and F regions, *J. Geophys. Res.*, **80**, 3121, 1975.
- Schunk, R. W., and J. J. Sojka, Ion temperature variations in the daytime high-latitude F-region, *J. Geophys. Res.*, **87**, 5169, 1982.
- Shand, B. A., M. Lester, and T. K. Yeoman, Substorm associated radar auroral surges: a statistical study and possible generation model, *Ann. Geophys.*, **16**, 441, 1998a.
- Shand, B. A., T. K. Yeoman, R. V. Lewis, R. A. Greenwald, and M. R. Hairston, Inter-hemispheric contrasts in the ionospheric convection response to changes in the interplanetary magnetic field and substorm activity: a case study, *Ann. Geophys.*, **16**, 764, 1998b.
- Sharp, G. W., Mid-latitude trough in the night ionosphere, *J. Geophys. Res.*, **71**, 1345, 1966.
- Siscoe, G. L., and T. S. Huang, Polar cap inflation and deflation, *J. Geophys. Res.*, **90**, 543, 1985.
- Smiddy, M., M. C. Kelley, W. Burke, F. Rich, R. Sagalyn, B. Shuman, R. Hays, and S. Lai, Intense poleward directed electric fields near the ionospheric projection of the plasmopause, *Geophys. Res. Lett.*, **4**, 543, 1977.
- Smiddy, M., W. J. Burke, M. C. Kelley, N. A. Saffekos, M. S. Gussenhoven, D. A. Hardy, and F. J. Rich, Effects of high-altitude conductivity on observed convection electric field and Birkeland currents, *J. Geophys. Res.*, **85**, 6811, 1980.
- Smith, M. F., and M. Lockwood, Earth's magnetospheric cusps, *Rev. Geophys.*, **34**, 233, 1996.
- Sojka, J. J., W. J., Raitt, and R. W. Schunk, A theoretical study of the high-latitude winter F region at solar minimum for low magnetic activity, *J. Geophys. Res.*, **86**, 609, 1981.
- Sojka, J. J., R. W. Schunk, J. V. Evans, J. M. Holt, and R. H. Wand, Comparison of model high-latitude electron densities with Millstone Hill observations, *J. Geophys. Res.*, **88**, 7783, 1983.
- Sojka, J. J., R. W. Schunk, and J. A. Whalen, The longitude dependence of the dayside F region trough : a detailed model-observation comparison, *J. Geophys. Res.*, **95**, 15,275, 1990.
- Southwood, D. J., and R. A. Wolf, An assessment of the role of precipitation in magnetospheric convection, *J. Geophys. Res.*, **83**, 5227, 1978.
- Spiro, R. W., R. A. Heelis, and W. B. Hanson, Ion convection and the formation of the mid-latitude F region ionization trough, *J. Geophys. Res.*, **83**, 4255, 1978.
- Spiro, R. W., R. A. Heelis, and W. B. Hanson, Rapid subauroral ion drifts observed by Atmospherics Explorer C, *Geophys.*

- Res. Lett.*, **6**, 675, 1979.
- Stenbaek-Nielsen, H. C., and A. Otto, Conjugate auroras and the interplanetary magnetic field, *J. Geophys. Res.*, **102**, 2223, 1997.
- Sugiura, M., N. C. Maynard, W. H. Farthing, J. P. Heppner, B. G. Ledley, and L. J. Cahill, Jr., Initial results on the correlation between the magnetic and electric fields observed from the DE-2 satellite in the field-aligned current regions, *Geophys. Res. Lett.*, **9**, 985, 1982.
- Thomas, G. E., Is the polar mesosphere the miners canary of global changes?, *Adv. Space Res.*, **18**, 149, 1996.
- Tsunoda, R. T., High-latitude *F* region irregularities: A review and synthesis, *Rev. Geophys.*, **26**, 719, 1988.
- Tsyganenko, N. A., A magnetospheric magnetic field model with a warped tail current sheet, *Planet. Space Sci.*, **37**, 5, 1989.
- Tsyganenko, N. A., Modeling the Earth's magnetospheric magnetic field confined within a realistic magnetopause, *J. Geophys. Res.*, **100**, 5599, 1995.
- Villain, J.-P., G. Caudal, and C. Hanuise, A SAFARI-EISCAT comparison between the velocity of *F* region small-scale irregularities and the ion drift, *J. Geophys. Res.*, **90**, 8433, 1985.
- Villain, J.-P., R. A. Greenwald, K. B. Baker, and J. M. Ruohoniemi, HF radar observations of *E*-region plasma irregularities produced by oblique electron streaming, *J. Geophys. Res.*, **92**, 12,327, 1987.
- Villain, J.-P., R. André, M. Pinnock, R. A. Greenwald, and C. Hanuise, Statistical study of the Doppler spectral width of high latitude ionosphere *F*-region echoes recorded with SuperDARN Coherent HF Radars, *Ann. Geophys.*, *in press*, 2002.
- von Zahn, U., and W. Meyer, Mesopause temperatures in the polar summer, *J. Geophys. Res.*, **94**, 14,647, 1989.
- Watkins, B. J., A numerical computer investigation of the polar *F*-region ionosphere, *Planet. Space Sci.*, **26**, 559, 1978.
- Whalen, J. A., J. Buchau, and R. A. Wagner, Airborne ionospheric and optical observations of noontime aurora, *J. Atmos. Terr. Phys.*, **33**, 661, 1971.
- Whalen, J. A., Daytime *F* layer trough observed on a macroscopic scale, *J. Geophys. Res.*, **92**, 2571, 1987.
- Whalen, J. A., The daytime *F* layer trough and its relation to ionospheric-magnetospheric convection, *J. Geophys. Res.*, **94**, 17,169, 1989.
- Whalen, J. A., Properties of the *F* layer plasma in the midday throat ridge and trough, *Radio Sci.*, **29**, 219, 1994.
- Williams, P. J. S., G. O. L. Jones, J. R. Palmer, and H. Rishbeth, The association of polar mesosphere summer echo layers with tidal modes, *Ann. Geophys.*, **13**, 454, 1995.
- Woch, J., and R. Lundin, Magnetosheath plasma precipitation in the polar cusp and its control by the interplanetary magnetic field, *J. Geophys. Res.*, **97**, 1421, 1992.
- Woodman, R. F., B. B. Balsley, F. Aquino, L. Flores, E. Vazquez, M. Sarango, M. M. Huaman, and H. Soldi, First observations of polar mesosphere summer echoes in Antarctica, *J. Geophys. Res.*, **104**, 22,577, 1999.
- Yeh, H.-C., J. C. Foster, F. J. Rich, and W. Swider, Storm time electric field penetration observed at midlatitude, *J. Geophys. Res.*, **96**, 5707, 1991.
- Yeoman, T. K., M. Lester, S. W. H. Cowley, S. E. Milan, J. Moen, and P. E. Sandholt, Simultaneous observation of the cusp in optical, DMSP and HF radar data, *Geophys. Res. Lett.*, **24**, 2251-2254, 1997.
- Yeoman, T. K., R. V. Lewis, H. Khan, S. W. H. Cowley, and J. M. Ruohoniemi, Interhemispheric observation of nightside ionospheric electric fields in response to IMF *B_z* and *B_y* changes and substorm pseudobreakup, *Ann. Geophys.*, **18**, 897, 2000.
- Yeoman, T. K., D. M. Wright, A. J. Stocker, and T. B. Jones, An evaluation of range accuracy in the Super Dual Auroral Radar Network over-the-horizon HF radar systems, *Radio Sci.*, **36**, 801, 2001.
- Yeoman, T. K., P. G. Hanlon, and K. A. McWilliams, A statistical study of the location and motion of the HF radar cusp, *Ann. Geophys.*, **20**, 275, 2002.
- Yukimatu, A. S., and M. Tsutsumi, A new SuperDARN raw time series analysis method and its application to mesopause region dynamics, *Geophys. Res. Lett.*, **29**(20), 10.1029/2002GL015210, 2002.

This thesis is based on the following papers.

1. Hosokawa K., T. Iyemori, A. S. Yukimatu, and N. Sato, Source of field-aligned irregularities in the subauroral F region as observed by the SuperDARN radars, *J. Geophys. Res.*, **106**, 24,713-24,731, 2001.
2. Hosokawa K., M. Sugino, M. Lester, N. Sato, A. S. Yukimatu, and T. Iyemori, Simultaneous measurement of duskside subauroral irregularities from the CUTLASS Finland radar and EISCAT UHF system, *J. Geophys. Res.*, *in press*, 2002.
3. Hosokawa K., E. E. Woodfield, M. Lester, S. E. Milan, N. Sato, A. S. Yukimatu, and T. Iyemori, Statistical characteristics of Doppler spectral width as observed by the conjugate SuperDARN radars, *Ann. Geophys.*, **20**, 1213-1223, 2002.
4. Hosokawa K., S. Yamasita, P. Stauning, N. Sato, A. S. Yukimatu, and T. Iyemori, Origin of the SuperDARN broad Doppler spectra: First observational evidence from Oersted satellite magnetometer, *Ann. Geophys.*, *submitted*, 2002.
5. Hosokawa K., E. E. Woodfield, M. Lester, S. E. Milan, N. Sato, A. S. Yukimatu, and T. Iyemori, Interhemispheric comparison of spectral width boundary as observed by the SuperDARN radars, *Ann. Geophys.*, *submitted*, 2002.
6. Hosokawa K., T. Ogawa, N. Sato, A. S. Yukimatu, and T. Iyemori, A statistical investigation of Antarctic polar mesosphere summer echoes observed with the Syowa station HF radar, *Geophys. Res. Lett.*, *to be submitted*, 2002.